Evolution of the gold and base metal mineralization of the Kay Tanda epithermal gold deposit, Lobo, Batangas, Philippines: Insights from fluid inclusion studies, ore mineral chemistry and stable isotope systematics

フィリピン，バタンガス州ロボ，カイタンダ浅熱水金鉱床の金およびベースメタル鉱化作用の進化：流体包有物，鉱石鉱物の化学組成および安定同位体比

Sofia Marah Pascual Frias

ID No. 6516108

Department of Geosciences, Geotechnology and Materials Engineering for Resources

Graduate School of International Resource Science

Akita University, Japan

2019

Department of Geosciences, Geotechnology and Materials Engineering for Resources
Graduate School of International Resource Science
Akita University
Akita City, Japan

ENDORSEMENT

This is to certify that this graduate thesis entitled **Evolution of the gold and base metal mineralization of the Kay Tanda epithermal gold deposit, Lobo, Batangas, Philippines: Insights from fluid inclusion studies, ore mineral chemistry and stable isotope systematics** (フィリピン，バタンガス州ロボ，カイタンダ浅熱水金鉱床の金およびベースメタル鉱化作用の進化：流体包有物，鉱石鉱物の化学組成および安定同位体比) prepared and submitted by Sofia Marah Pascual Frias in partial fulfilment of the requirements for the degree of Doctor of Science, is hereby accepted.

AKIRA IMAI, Ph. D.
Thesis Adviser

RYOHEI TAKAHASHI, Ph. D.
Thesis Adviser

YASUSHI WATANABE, Ph. D.
Thesis Examiner

ANTONIO ARRIBAS JR, Ph. D.
Thesis Examiner

TSUKASA OHBA, Ph. D.
Thesis Examiner

ANDREA AGANGI, Ph. D.
Thesis Examiner

ACKNOWLEDGMENTS

It is an extremely rare and amazing opportunity to have your passion as a profession. Throughout my difficult but extraordinary graduate student life in Akita, I have been blessed by the guidance and support from numerous individuals and institutions.

First, I would like to express my deepest gratitude to my advisers, Dr. Akira Imai and Dr. Ryohei Takahashi, for their continuous guidance, patience, encouragement and wisdom. Dr. Akira Imai opened the opportunity for me to continue my graduate studies in Akita University and he continued to guide my research despite his extremely busy work in Kyushu University. Dr. Ryohei Takahashi patiently guided me throughout my experiments and research updates while managing a laboratory composed of more than 20 students. They have taught me immense knowledge in the field of research and economic geology and for that I am eternally grateful.

I would also like to thank my thesis examiners, Dr. Yasushi Watanabe, Dr. Antonio Arribas, Jr., Dr. Tsukasa Ohba, and Dr. Andrea Agangi for their insightful comments and suggestions. Their comments helped me think beyond my perspective and helped me improve my research. To Dr. Antonio Arribas, I would like to thank you for all the consultations, encouragement and enthusiasm during conference presentations. I hope that I can find the opportunity to work with you in the future. I would also like to thank my other professors, Dr. Daizo Ishiyama, Dr. Mayuko Fukuyama, Dr. Takuya Echigo, Dr. Tokiyuki Sato, Dr. Makoto Yamasaki, Dr. Takashi Hoshide and Dr. Atsushi Shibayama. I gained a lot of knowledge during their classes, laboratory circuit trainings, and fieldworks. I would also like to thank Dr. Hinako Sato, for her patience and support during the chemical experiments. I would also like to thank Dr. Nigel Blamey for the research collaboration. I am also grateful to Dr. Jeffrey Hedenquist, Dr. Keiko Hattori and Dr. Richard Sillitoe for their constructive criticisms and words of encouragement. I would also like to thank Dr. Carla Dimalanta, Dr. Kenzo Sanematsu and another anonymous reviewer for their constructive comments on my first publication.

My sincere thanks to MRL Gold Philippines, Inc. and Egerton Gold Philippines, Inc., for allowing me to continue my study in Kay Tanda and for providing the logistical support for the

fieldwork. I am also truly grateful to Akita University, the Leading Program, and the Japanese Government (MONBUKAGAKUSHO:MEXT) for providing financial assistance for my graduate study in Akita. I would also like to thank the organizers of the 2015 Short Stay Program on Sustainable Resource Development of Akita University and the staff of the International Office of Akita University for introducing me to the graduate program and for helping me adjust to my life in Akita.

I survived all my struggles in Akita because of the people who became my second family. I would like to thank the members of the Kinsho Laboratory for their warm welcome and for their continued support throughout my doctoral study. We all came from different parts of the world but we are connected by our common passion for science and adventure. To my mothers in Akita, Tita Shirley, Tita Minerva, Tita Charina and Watanabe-san, thank you for treating me as your own child. Being away from my family is a struggle and my friends in Akita helped me endure all of it. To Ate Jen, Ate Yojh, Stephanie, Kuya AV, Zedrick, Ate Carmela, Jace, Kuya Darwin, Kuya Lloyd, Amo and Yuika, I cannot find better companions in this crazy journey than you guys. To Ate Pearlyn, thank you for being an inspiration for me to give my best in all I do and for helping me become a better researcher.

Most of all, I am forever grateful to my family and my loved one for their unwavering support and unconditional love. Thank you for understanding all my decisions and for patiently waiting for me to finish my graduate studies. I would not be the person I am today without your guidance and sacrifices, and I cannot thank you enough.

To God be glory!

ABSTRACT

The Kay Tanda epithermal Au deposit in Lobo, Batangas is one of a few known Au deposits in the Batangas Mineral District in southern Luzon, Philippines. It was formed at the southern flank of an inactive volcano located at the southern tip of the Western Luzon Arc, and is less than a kilometer from the coastline of southern Batangas. The geology of Kay Tanda is composed of: (1) the Talahib Volcanic Sequence, a Middle Miocene dacitic to andesitic volcaniclastic sequence which hosts the majority of the epithermal mineralization, (2) the Balibago Diorite Complex, an intrusive complex cogenetic to the Talahib Volcanic Sequence, (3) the Calatagan Formation, a Late Miocene to Early Pliocene volcano-sedimentary sequence overlying the Talahib Volcanic Sequence and hosts minor mineralization, (4) the Dacite Porphyry Intrusives which intruded the older lithologic units, and (5) the Balibago Andesite, a Pliocene post-mineralization volcaniclastic unit.

The mineralization at Kay Tanda evolved from an early-stage extensive epithermal mineralization characterized by Au-Ag-bearing quartz stockworks hosted in the shallower levels of the Talahib Volcanic Sequence, to a late-stage epithermal base metal (Zn, Pb, and Cu) mineralization with local bonanza-grade Au mineralization hosted in veins and hydrothermal breccias at deeper levels. Paragenetic studies defined six mineralization stages. Stage 1 is characterized by the formation of localized quartz ± pyrophyllite ± dickite/kaolinite ± diaspore alteration which was later cut by Au-bearing quartz veins. This was formed due to the intrusion of the Balibago Diorite Complex into the volcaniclastic host rocks. Magmatic volatiles were released from the intrusions and then condensed into the groundwater which generated strongly acidic solutions. Fluid inclusion studies on Stage 1 quartz veins indicate that mixing with meteoric water is the main ore-forming process. With the intrusion of the Dacite Porphyry Intrusives, the hydrothermal system developed over a wider area which formed the pervasive illite ± quartz ± smectite ± kaolinite alteration and the Stage 2 Au-Ag-bearing quartz stockworks. K-Ar dating on two Stage 2 illite samples collected from alteration halos surrounding mineralized Stage 2 quartz veins revealed a mineralization age of 5.9 ± 0.2 to 5.5 ± 0.2 Ma (Late Miocene). Also, a boiling

condition under hydrostatic pressure was estimated around 500 m below the paleowater table. The late base metal mineralization commenced with the deposition of Stage 3 carbonate veins with minor base metal sulfides. Stage 4 is composed of quartz ± adularia ± calcite veins and hydrothermal breccias which host the main base metal and bonanza-grade Au mineralization and is associated to chlorite-illite-quartz alteration. Native gold is the dominant Au-bearing mineral which contains 81.2 to 94.2 atomic% Au. Silver is mainly hosted in native gold (up to 18.8 atomic% Ag), electrum (up to 21.6 atomic% Ag), galena (up to 0.58 atomic% Ag), and Bi-Pb-Cu-Ag minerals (up to 7.5 atomic% Ag) which occur typically as chalcopyrite inclusions. Boiling is the main mechanism of ore deposition in Stage 4 based on the occurrence of rhombic adularia, the heterogeneous trapping of fluid inclusions of variable liquid-vapor ratios, the distribution of homogenization temperatures of measured fluid inclusions, and the ratio of fluid inclusion gas compositions (CO_2/N_2 vs total non-aqueous gas content). Stage 5 is composed of epidote-carbonate veins associated to epidote-calcite-chlorite alteration. Towards the end of the mineralization, the Stage 6 anhydrite/gypsum-base metal veins which contain sub-economic amounts of Au and Ag were formed. Fluid inclusion microthermometry indicates that the temperature of the system increased from the Stage 1 (220-280°C) to Stage 2 (260-310°C), remained at high temperatures towards the Stage 4 (270-310°C) which were attributed to the continuous intrusion of the Dacite Porphyry Intrusives at depth, and then gradually decreased at the Stage 6 (240-290°C). The salinity slightly decreased from 5.8 wt% NaCl equivalent in the Stages 1, 2 and 4 to 4.6 wt% NaCl equivalent in the Stage 6.

Based on the CO_2/CH_4 vs N_2/Ar diagram, Ar/He vs N_2/Ar diagram and N_2/100-10He-Ar ternary diagram derived from the fluid inclusion gas data, meteoric water is an important component of the hydrothermal system. A small amount of arc-type derived magmatic fluid is also suggested from the N_2/100-10He-2Ar ternary diagram. The possibility of incorporation of seawater into the hydrothermal system of Kay Tanda was suggested by the moderate salinity of measured fluid inclusions and the results of oxygen and hydrogen isotope analyses of the two Stage 2 illite samples that were used from K-Ar dating. The calculated $\delta^{18}O_{water}$ and δD_{water} values

of the two Stage 2 illite samples approach the $\delta^{18}O$ and δD value of SMOW. This suggests the incorporation of seawater into the hydrothermal system since the formation of the early mineralization stages. Sulfur isotope analysis on the Stage 2 and Stage 4 sulfides and the Stage 6 sulfide-sulfate pairs also shed light to the evolution of the hydrothermal system. Sulfur isotope analysis was conducted on Stage 2 sulfides (-5.8‰ to +2.8‰), Stage 4 sulfides (-2.1‰ to +3.3‰) and Stage 6 sulfides (+0.1‰ to +2.3‰) and sulfates (+21.6‰ to +22.9‰). Although the sulfur isotopic compositions of the sulfides point to magmatic sulfur as the principal sulfur source, the sulfur isotopic compositions of the Stage 6 sulfates approach that of Late Miocene seawater suggesting incorporation of seawater into the hydrothermal system.

The deposit was formed due to the complex interaction of the volcaniclastic host rocks, the two intrusive rock units at depth, and the circulating hydrothermal fluids with components of magmatic, meteoric and seawater origin. During the early mineralization stages, as the seawater enter the deposit, seawater-derived sulfate minerals precipitate at the recharge zone where the seawater-derived fluids encounter increasing temperatures. The resulting fluids became seawater sulfate-depleted which later circulated in the system. This is consistent with absence of sulfates in the early mineralization stages. However, at the last mineralization stage where the temperature of the system decreased and the meteoric water circulated into the deeper levels, the seawater-derived sulfate minerals started to dissolve which introduced seawater-derived sulfate into the hydrothermal fluids. The mixing of these fluids is an effective mechanism for the co-precipitation of the Stage 6 sulfates and sulfides.

Thermodynamic calculations of physicochemical conditions (pH, $\log fS_2$, $\log fO_2$) during the Stage 4 bonanza grade Au mineralization were also conducted. Ore mineral assemblage and sulfur fugacity determined from the FeS content of sphalerite at temperatures estimated by fluid inclusion microthermometry indicate that the base metal mineralization evolved from a high sulfidation to an intermediate sulfidation condition. Assuming that the system is in equilibrium, the $\log fO_2$ varies from -32.2 to -37.5 atm from T = 300 to 250°C at pH = 5.11 and $\Sigma S = 10^{-2}$ mol/kg. Gold was mainly transported as $Au(HS)_2^-$ complex. In Kay Tanda, evidence of fluid

boiling was observed. Boiling might have caused the removal of H_2S from the hydrothermal fluid, which triggered the decomposition of $Au(HS)_2^-$ complex leading to the precipitation of gold.

TABLE OF CONTENTS

LIST OF FIGURES

Chapter 5: Ore Mineral Chemistry

Chapter 6: Fluid Inclusion Studies

Chapter 7: Stable Isotope Systematics

LIST OF TABLES

CHAPTER 1

INTRODUCTION

1.1 Epithermal deposits: Characteristics, classification and developments in research

Epithermal precious and base metal deposits are hydrothermal ore deposits that form at shallow crustal levels and commonly develop in subaerial volcanic terranes associated with calc-alkaline to alkaline magmatism (Cooke & Simmons, 2000; Simmons et al., 2005). The precious and base metal contents of epithermal deposits vary widely; from Au-rich deposits with Ag/Au ratio <10 (e.g. Hishikari, Japan and Ladolam, Papua New Guinea), to Ag-rich deposits with Ag/Au ratio ~20-200 (e.g. Comstock, United States and La Coipa, Chile); from Cu-As-Sb-rich deposits (e.g. Yanacocha, Peru and Lepanto, Philippines) to Ag-Pb-Zn-rich deposits (e.g. Fresnillo, Mexico) (Simmons et al., 2005). Epithermal deposits form in various volcanotectonic settings which feature any of the following structural regimes: neutral to mildly extensional, extensional leading to rifting, or compressional (Sillitoe & Hedenquist, 2003; Simmons et al., 2005). Epigenetic ore formation occurs at temperatures ranging from approximately 150 °C to about 300 °C at depths approximately less than 1.5 km below the water table (Simmons et al., 2005), although fluid inclusion studies in some epithermal deposits reported homogenization temperatures exceeding 300 °C (Kamilli & Ohmoto, 1977; Ahmad, 1979; Sato et al., 1980). The epithermal environment is characterized by near-hydrostatic conditions, where ore deposition is controlled by changes in the physicochemical conditions of the hydrothermal system (Simmons et al., 2005). Epithermal deposits are commonly hosted by coeval and/or older rocks of either andesitic to dacitic/rhyolitic composition of predominantly calc-alkaline affinity or of tholeiitic bimodal basalt-rhyolite composition (Sillitoe & Hedenquist, 2003; Simmons et al., 2005). Mineralization can be hosted in dilational structures (e.g. veins, vein swarms and stockwork zones

from faults and fractures), in contact planes (e.g. unconformities), in rocks with intrinsic porosity and permeability (e.g. volcaniclastic and sedimentary rocks) and in hydrothermally altered rocks (e.g. intensely leached rocks, diatremes and hydrothermal breccias) (Sillitoe, 1993b; Simmons et al., 2005). These structural controls and lithologic characteristics affect the configuration and extent of the epithermal mineralization (Sillitoe, 1993b; Simmons et al., 2005). Epithermal deposits are typically Tertiary or younger in age because of their poor preservation potential as a consequence of their geologic setting and shallow emplacement (Simmons et al., 2005).

Due to the diversity of epithermal deposits, several classification schemes have been developed throughout the years. These include classification schemes according to metal content (i.e. cinnabar, stibnite, base metal, gold, argentite gold, argentite, gold telluride, gold telluride with alunite, gold selenide) (Lindgren, 1933), according to pH of hydrothermal fluids (i.e. acid and alkaline) (Sillitoe, 1977), according to sulfur content (i.e. high sulfur and low sulfur) (Bonham, 1986, 1988), and according to gangue mineralogy (i.e. acid-sulfate/alunite-kaolinite and adularia-sericite) (Hayba et al., 1985; Heald et al., 1987; Berger & Henley, 1989; Albino & Margolis, 1991). The most recent and widely used classification is according to sulfidation state which describes the oxidation state of the aqueous sulfur species and the stability of sulfur-bearing minerals in terms of sulfur fugacity (i.e. low sulfidation, intermediate sulfidation, and high sulfidation) (Barton & Skinner, 1979; Hedenquist, 1987; Sillitoe, 1989, 1993a; White & Hedenquist, 1990, 1995; Hedenquist & Lowenstern, 1994; White & Poizat, 1995; Hedenquist et al., 2000; Einaudi et al., 2003; Sillitoe & Hedenquist, 2003; Simmons et al., 2005).

Our understanding of the geological characteristics and genesis of epithermal precious and base metal deposits have broadened since Lindgren first introduced the terminology in 1933 as one of the genetic classifications for hydrothermal ore deposits (White & Hedenquist, 1990; Cooke & Simmons, 2000; Simmons et al., 2005). Driven by the increasing prices of gold and silver in the late 1970s, epithermal deposits became attractive targets for exploration because of their shallow depth of formation, wide and distinct alteration footprint, and high gold and silver contents (Cooke & Simmons, 2000; Simmons et al., 2005). Since then, several epithermal deposits have been discovered and developed, especially in the circum-Pacific region (Hedenquist,

1987; Sillitoe, 1995, 2000; White et al., 1995; Garwin et al., 2005). During the 1970s, the developments in the study of epithermal deposits included fluid inclusion studies which reported homogenization temperatures of fluid inclusions from several deposits reaching 300°C (Kamilli & Ohmoto, 1977; Ahmad, 1979; Sato et al., 1980) and stable isotope studies which reported the sources of the hydrothermal fluids and the sulfur of epithermal deposits (O'Neil & Silberman, 1974; Taylor, 1974; Kamilli & Ohmoto, 1977; Sawkins et al., 1979). Experimental and theoretical studies which demonstrated the behavior and solubility of metals and stability of minerals under hydrothermal conditions also contributed to the deeper understanding of metal transport and deposition in epithermal deposits (Seward, 1973; Barton et al., 1977; Barnes, 1979; Barton & Skinner, 1979). Geothermal systems were also found useful in understanding the epithermal environment as they serve as active analogues of these fossil hydrothermal systems (Henley, 1985; White & Hedenquist, 1990; Hedenquist et al., 1992; Simmons et al., 2005). In the 1980s, the Society of Economic Geologists published the first two volumes of *Reviews in Economic Geology*, which presented a thermodynamic approach in dealing with epithermal systems and provided a synthesis of the geological framework of epithermal systems (in Henley et al., 1984; in Berger & Bethke, 1985). Epithermal deposit classification schemes (Sillitoe, 1977; Buchanan, 1981; Ashley, 1982; Giles & Nelson, 1982; Hayba et al., 1985; Bonham, 1986, 1988; Heald et al., 1987; Hedenquist, 1987; Berger & Henley, 1989; Sillitoe, 1989, 1993a; White & Hedenquist, 1990, 1995; Albino & Margolis, 1991; White & Poizat, 1995; Hedenquist et al., 2000; Einaudi et al., 2003; Sillitoe & Hedenquist, 2003; Cooke & Deyell, 2003), and genetic models (Buchanan, 1981; Hayba et al., 1985; Heald et al., 1987; Berger & Henley, 1989; White & Hedenquist, 1990, 1995; White, 1991; Sillitoe, 1993b; Arribas, 1995; Richards, 1995; Simmons, 1995; Cooke & Simmons, 2000; Jensen & Barton, 2000; Sillitoe & Hedenquist, 2003; Simmons et al., 2005) were also developed from a compilation of documented epithermal deposits around the world to show the characteristics of the geologic setting, alteration assemblages and mineralization styles, to provide the physicochemical conditions of the epithermal environments, to determine the sources of the fluids and metals, to determine the ore-forming processes, and to provide useful guides for exploration.

1.2 Epithermal deposits in the Philippines

The Philippines is one of the countries in the circum-Pacific region endowed with numerous epithermal precious and base metal deposits (Mitchell & Balce, 1990; White et al., 1995; Garwin et al., 2005; Cooke et al., 2011b; Hollings et al., 2018). Located in a trapped zone between two active subduction zones systems with opposing polarity and transected by a 1200 km left-lateral strike slip fault, the country is also considered one of the most complex and tectonically active terrains in the world (Aurelio, 2000; Yumul et al., 2008).

Epithermal deposits in the Philippines are primarily related to magmatic-hydrothermal systems associated with volcanic arc systems that have evolved since the Paleogene (Mitchell & Balce, 1990; Mines and Geosciences Bureau (MGB), 2004). Most Philippine epithermal deposits are Plio-Pleistocene in age, and the majority of auriferous deposits, including most porphyry Cu-Au deposit, are associated with Oligocene to Pleistocene dioritic intrusions (Sillitoe & Gappe, 1984; Zanoria et al., 1984; Mitchell & Balce, 1990; Arribas et al., 1995; Aurelio, 2000; Imai, 2002; Waters et al., 2011). They are found alongside other magmatic-hydrothermal deposits such as porphyry Cu-Au and skarn deposits (Mitchell & Balce, 1990; MGB, 2004; Garwin et al., 2005; Hollings et al., 2018). Most epithermal deposits are concentrated along two late Cenozoic volcanic arcs, the Western Luzon Volcanic Arc and the Eastern Philippine Volcanic Arc, which correspond to the subduction of the South China Sea Basin along the Manila Trench (Hayes & Lewis, 1984, 1985; Yang et al., 1996; Aurelio, 2000), and the subduction of the Philippine Sea Plate along the Philippine Trench, respectively (Aurelio, 2000; Ozawa et al., 2004; Yumul et al., 2008). Clustering of productive mines and numerous prospects along these two volcanic arcs led to the establishment of six major gold districts: (1) the Baguio-Mankayan Gold District along the Central Cordillera in northern Luzon; (2) the Camarines Norte Gold District in southeastern Luzon; (3) the Masbate Gold District in Masbate Island; and three gold districts in the Eastern Mindanao Gold Province which includes (4) the Surigao Gold District, (5) the Central Gold District, and (6) the Masara Gold District (MGB, 2004) (Fig. 1.1).

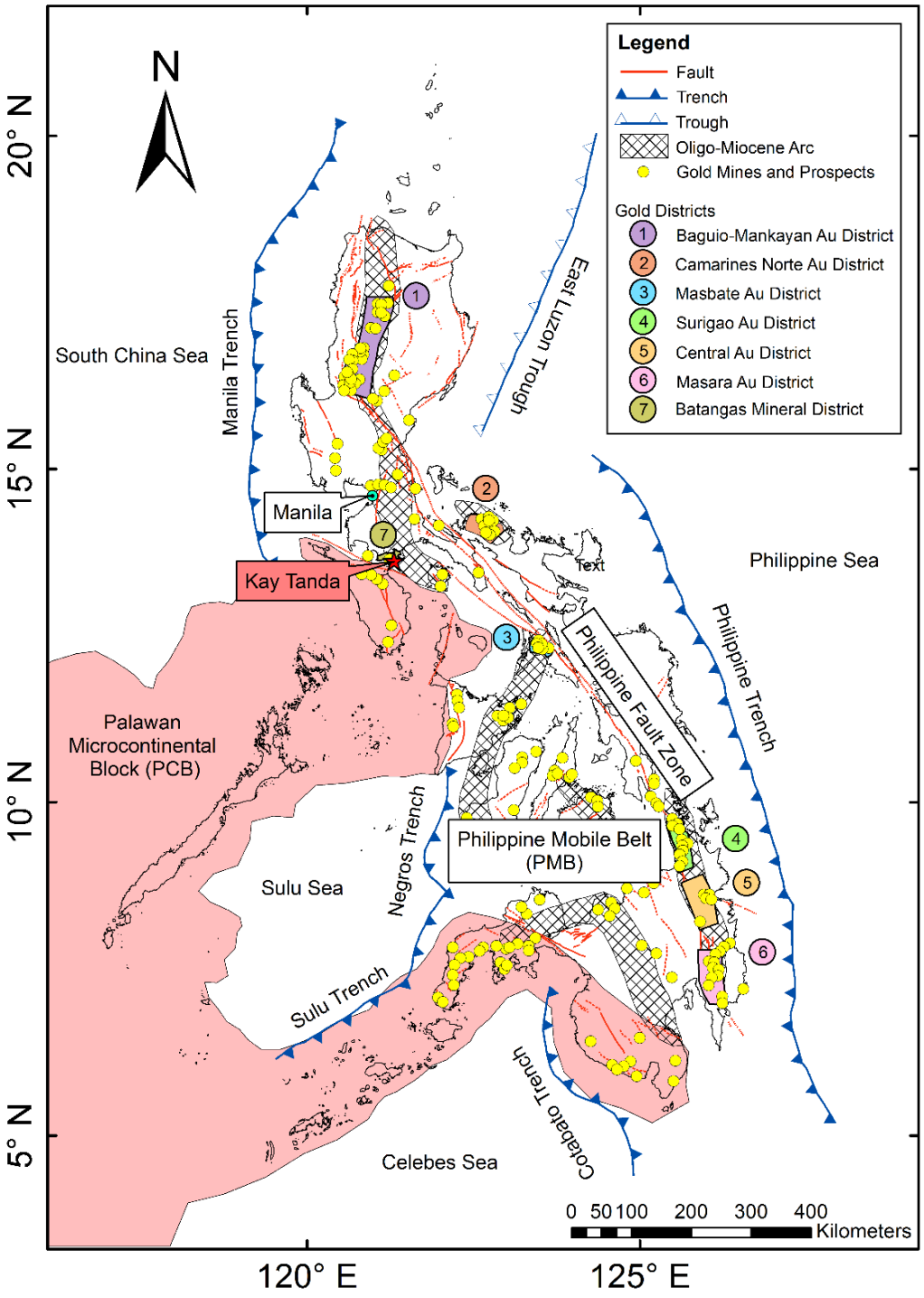

Fig. 1.1 Gold mines, prospects and districts in the Philippines. The Surigao, Central and Masara Gold Districts comprise the Eastern Mindanao Gold Province (MGB, 2004). The Kay Tanda epithermal gold deposit is located in the Batangas Mineral District in southern Luzon and is associated with Miocene volcanic arc (Aurelio, 2000). Country boundary was taken from PhilGIS (2011); outline of PCB-PMB collision zone from Manalo et al. (2016); outline of trenches and faults from PHIVOLCS (2015); Oligo-Miocene volcanic arcs from Aurelio (2000); gold mines, prospects and districts from MGB (2004).

The Western Luzon Arc is among the most productive volcanic arcs in the country (MGB, 2004; Garwin et al., 2005). The Baguio Au district and the Mankayan Au district, which lie on the northern segment of the Central Cordillera and along the splays of the northern end of the Philippine Fault, are two of the most prolific and well-studied gold districts in the Philippines (MGB, 2004; Waters et al., 2011). They house some of the world-class epithermal deposits such as the Antamok and Acupan epithermal deposits in Baguio and the Lepanto and Victoria epithermal deposits in Mankayan (Fernandez et al., 1979; Cooke & Bloom, 1990; Cooke et al, 1996; Hedenquist et al., 1998; Sajona et al., 2002). The Baguio District is considered one of the oldest and largest gold mining areas in the Philippines with a combined historic production and remaining resource of more than 35M oz Au (Sillitoe, 1993a; MGB, 2004; Waters et al., 2011). The young epithermal mineralization in Baguio District (Aoki et al., 1993) is related to the second phase of magmatism that occurred during the Pliocene and Pleistocene (Waters et al., 2011). Aside from the economic significance of these deposits, they also contributed to the development of magmatic-hydrothermal ore deposit models. The Lepanto-Victoria-Far Southeast deposits in Mankayan demonstrated the spatial and temporal association of porphyry and epithermal ore deposits, which have significant exploration implications for these types of deposits (Arribas et al., 1995; Hedenquist et al., 1998).

Smaller gold districts are also found in other regions of the archipelago (MGB, 2004). Nearest to Manila is the Batangas Mineral District in southern Luzon whose metallogenic potential is among the least studied in the Philippines (Fig. 1.1). Unlike the deposits in the northern Luzon Central Cordillera and the eastern Mindanao, only a few mineral prospects have been successfully mapped and described in this district. Located in the highlands of southern Batangas, the Batangas Mineral District hosts several porphyry Cu-Au and epithermal Au prospects which were explored and mined even before the colonial era (MGB, 2004).

1.3 Study area location, geography, accessibility and resource estimate

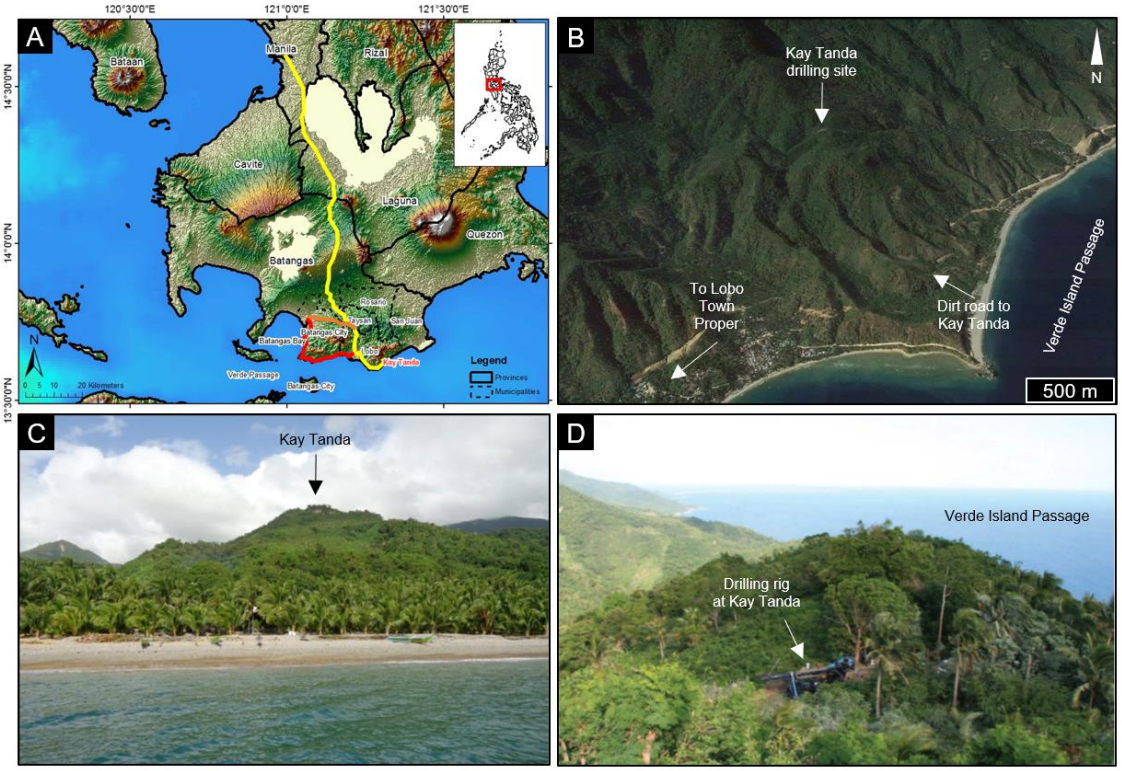

Fig. 1.2 Location of the Kay Tanda deposit. (A) Location and accessibility map showing the three routes to Kay Tanda: yellow route from Manila, orange route from Batangas City via the Gov. Antonio Carpio Road, red route from Batangas City via the Batangas-Tabangao-Lobo Road. Country, province and municipality boundaries, road network, and topography were taken from PhilGIS (2011) (B) Modified oblique Google Earth view of Kay Tanda (no vertical exaggeration). (C) View of Kay Tanda from the sea showing its rugged topography and lush vegetation cover (photo from Sosa, 2014, unpublished report). (D) Drilling activity in Kay Tanda (photo from Lab-oyan & Climie, 2010, conference presentation).

Kay Tanda is an epithermal Au deposit lying on the southeastern flank of Mt. Lobo, an inactive volcano in the highlands of the Batangas Mineral District in the Batangas Province of southern Luzon, Philippines (Fig. 1.2). It is situated in Sitio Malagundi, Barangay Balibago in the Municipality of Lobo (Fig. 1.2A). The deposit is located approximately 115 aerial km south of Metro Manila and is less than a kilometer from the coastline of southern Batangas (Fig. 1.2A). The deposit's topography is characterized by moderate to high relief with elevations varying mostly between 260 m to 430 m above sea level and is deeply incised by numerous southeast-draining creeks (Rohrlach & Fredericksen, 2008, unpublished data) (Fig. 1.2B-C). The area is covered by timberland with sporadic bushlands and the vegetation is composed of tropical fruit-

and non-fruit-bearing trees (Sosa, 2014, unpublished data) (Fig. 1.2C-D). Mountain clearings were made during drilling operations, which are visible in Google Earth images (Fig. 1.2B-D). The area experiences a tropical maritime climate with a dry season from November to April and a wet season from May to October (Sosa, 2014, unpublished data). The monthly average rainfall is about 191 mm, which peaks to about 365 mm during the maximum rain period from June to September (MSN Weather, 2019). The monthly average temperature is about 27°C and may peak to above 30°C from May to July (MSN Weather, 2019).

The deposit can be accessed from Metro Manila via the South Luzon Expressway (SLEX) continuing to the Southern Tagalog Arterial Road (STAR Tollway or CALABARZON Expressway) (approximately 100 km). From the Ibaan exit, the 19.3 km Taysan-Lobo zigzag road up the mountains to the Lobo town proper is 15.5 km away via the Taysan-Ibaan Road. From the Lobo town proper, the deposit is another 19.5 km away via the Lobo-Malabrigo-Laiya Road, a coastal road that runs through Barangay Mabilog na Bundok, Sawang, Soloc, Malabrigo to Barangay Balibago. The deposit can be accessed via a 2 km dirt road up a steep ridge from the coastal road (Fig. 1.2A, yellow route). Lobo can also be accessed from Batangas City either via the Gov. Antonio Carpio Road (approximately 16.7 km) (Fig. 1.2A, orange route) which continues to the Taysan-Lobo zigzag road or via the Batangas-Tabangao-Lobo Road (approximately 42.3 km) (Fig. 1.2A, red route) which runs along the coastline of southern Batangas. There is no existing domestic airport in Batangas City. The nearest one is the Ninoy Aquino International Airport in Pasay City, Metro Manila. A commercial pier, the Batangas International Port, is located in the southern coast of Batangas City.

The deposit belongs to Mindoro Resources Ltd.'s Archangel Property which is covered by an approved Mineral Production Sharing Agreement (MPSA) denominated as MPSA 177-2002-IV held by the Egerton Gold Philippines, Inc. (Cox, 2010, unpublished data; MGB, 2018). The Archangel Property covers 1,011.54 ha of land and is contained within geographical coordinates 13°36'30" N to 13°39'30" N and 121°17'30" E to 121°20'00" E (Rohrlach & Fredericksen, 2008, unpublished data). Based on a resource estimate by Cox in 2010, the deposit contains a total of 4.9 M metric tonnes of measured and indicated resource at 1.09 g/t Au and 2.15 g/t Ag at a 0.5

g/t Au cut-off grade (Cox, 2010, unpublished data). Assay reports bonanza-grade Au intercepts reaching values exceeding 200 g/t Au (Cox, 2010, unpublished data). It also contains appreciable amounts of Zn, Pb, and Cu (Cox, 2010, unpublished data).

1.4 Exploration history and previous works

The information in this subsection were summarized from the unpublished report of Rohrlach and Fredericksen (2008).

The earliest records of mining activity in the present-day Kay Tanda area dated back to the pre-Spanish era which consisted of Chinese small-scale mining activity on pits and adits along the present-day Ahit Ridge and Kay Tanda (Rohrlach & Fredericksen, 2008, unpublished data). These records made by the Spaniards during their colonization were preserved and archived in the 55-volume series of *The Philippine Islands, 1493-1898* which were translated and published by Emma Helen Blair and James Alexander Roberston in 1902 to 1909 (Rohrlach & Fredericksen, 2008, unpublished data). Prior to the World War II, the Japanese also explored the present-day Balibago area for base metal deposits (Rohrlach & Fredericksen, 2008, unpublished data).

In the 1970s, the Japanese company Sumitomo Mining Corporation conducted exploration in the region and drilled two diamond drill holes (Rohrlach & Fredericksen, 2008, unpublished data). In 1974 to 1975, the Bureau of Mines and Geo-Sciences conducted reconnaissance geological mapping, mineral resource evaluation and steam sediment sampling in southern Batangas that covered a total area of 110,000 ha (Avila, 1980). They reported several copper prospects as well as prospects for non-metallic resources such as gypsum, guano, phosphate, and cement raw materials (Avila, 1980). Their report served as the main reference for the most recent published map of southern Batangas.

In the late 1980s, the Western Mining Corporation conducted reconnaissance exploration in the Archangel Project which consisted of regional mapping, rock-chip sampling and surface soil sampling (Rohrlach & Fredericksen, 2008, unpublished data). The results of assay and geochemical analysis revealed geochemical signatures related to epithermal mineralization

(Rohrlach & Fredericksen, 2008, unpublished data). They also conducted ground magnetic surveys which delineated the high magnetic signatures of the Lobo Agglomerate and low magnetic signatures of the hydrothermally altered Talahib Volcanic Sequence (Rohrlach & Fredericksen, 2008, unpublished data). A total of 7 diamond drill holes with a total length of 1002 m were drilled by the company (Rohrlach & Fredericksen, 2008, unpublished data).

In the 1990s, several companies showed renewed interest on the prospect. Chase Resources of Canada, in joint venture with BHP Minerals, conducted an exploration program and an extensive reverse circulation (RC) drilling at Kay Tanda from 1995 to 1998 (Rohrlach & Fredericksen, 2008, unpublished data). BHP Minerals commissioned World Geoscience to conduct a helicopter-borne magnetic and radiometric survey with a 200 m spacing and 1000 m tie lines over Archangel (Rohrlach & Fredericksen, 2008, unpublished data). The data were interpreted and ground verified by Dr. Greg Corbett (Rohrlach & Fredericksen, 2008, unpublished data). Chase did not do any further studies on Kay Tanda and focused their work on the nearby Taysan porphyry copper-gold deposit, located 13 km north of Lobo (Rohrlach & Fredericksen, 2008, unpublished data). Egerton Gold NL of Australia entered a deal with the claim holder Apical Mining in 1997 but later withdrew from the project (Rohrlach & Fredericksen, 2008, unpublished data). The project was purchased by Egerton Gold Philippines afterwards (Rohrlach & Fredericksen, 2008, unpublished data). Billiton continued their work in Archangel in 1998 by purchasing and interpreting the aeromagnetic data from Chase (Rohrlach & Fredericksen, 2008, unpublished data).

In 2000, Mindoro Resources Ltd., through its wholly owned subsidiary MRL Gold Philippines Inc., entered into a deal with Egerton Gold Philippines and acquired 75% interest on the project (Rohrlach & Fredericksen, 2008, unpublished data). The company continued to acquire the other adjacent lands with other gold-copper prospects (Rohrlach & Fredericksen, 2008, unpublished data). Mindoro Resources Ltd. conducted reconnaissance survey in July 2002 (Rohrlach & Fredericksen, 2008, unpublished data). The Mineral Production Sharing Agreement with the Department of Environment and Natural Resources was registered on 22 January 2003 (Rohrlach & Fredericksen, 2008, unpublished data). The companies carried out more extensive and detailed

work which included metallurgical test in 2004, reverse-circulation drilling program in March 2006 to April 2007 and diamond drilling program in August 2006 to July 2007 (Rohrlach & Fredericksen, 2008, unpublished data). Mindoro acquired the remaining 25% of the shares from Egerton in 2008 (Rohrlach & Fredericksen, 2008, unpublished data). An NI 43-101 Report on the Mineral Resource Estimate Upgrade on the Kay Tanda Project was prepared for Mindoro Resource Limited in 2010 (Cox, 2010).

In 2012, a moratorium on granting new mining projects was imposed by the Philippine government through the Executive Order No. 79 (Series of 2012) which affected the company's mining application. In 2016, the Red Mountain Mining (RMM), the Australian Securities Exchange-listed company that wholly owns MRL Gold Philippines, Inc. withdrew from the project which resulted to the termination of all exploration and other related activities in Kay Tanda (Engr. Edsel Abrasaldo, 2016, personal communications).

1.5 Thesis statement and objectives

Most of the work done on the Kay Tanda deposit focused on delineating the resource area of the deposit through extensive mapping and drilling. Though company reports contain significant findings from surface mapping, drilling, petrography, geochemical analysis and geophysical surveys, little is known about the processes responsible for the formation of the deposit.

This thesis focuses on understanding and documenting the formation and the evolutionary history of the gold and base metal mineralization of the Kay Tanda epithermal deposit. This involves the establishment of the geological framework of the deposit, the characteristics, occurrence, and timing of the mineralization, the sources of the components and changes in the physicochemical conditions of the hydrothermal system, and the ore-forming processes that led to the formation of the deposit. This study aims to address the following specific objectives:

(1) to document the mineralogical and textural differences among the lithologic units to determine the pre-mineralization, syn-mineralization, and post-mineralization rocks

(2) to document the style, occurrence, characteristics, and age of the mineralization and develop a paragenetic sequence of the different mineralization stages and the associated alteration zones

(3) to elucidate the relationship between the different ore textures and their major and minor element composition to understand the characteristics of the hydrothermal fluids

(4) to determine sources of the components of the hydrothermal system and the changes in the physicochemical conditions during ore deposition throughout the development of the deposit, and

(5) to determine the mechanisms of ore deposition.

Situated in one of the least studied mineral districts in the Philippines, this study on Kay Tanda offers an impetus in establishing the poorly documented metallogenic history of southern Batangas, which could lead to more successful exploration efforts in the region, and other areas of similar tectonic setting.

1.6 Thesis organization

This thesis contains nine chapters: Chapter 1: Introduction, Chapter 2: Regional Tectonic and Geological Setting, Chapter 3: Deposit Geology, Chapter 4: Alteration and Mineralization, Chapter 5: Ore Mineral Chemistry, Chapter 6: Fluid Inclusion Studies, Chapter 7: Stable Isotope Systematics, Chapter 8: Physicochemical Conditions of Ore Deposition, and Chapter 9: Genetic Model. Chapters 3 to 7 contain an introduction, methodology, results, discussion and summary/conclusion subsections. In Chapter 8, the methodology part is omitted and the thermodynamic calculations are explained throughout the discussion. In Chapter 9, the conclusions and main findings of this thesis are incorporated in the discussion of the genetic model. It also contains implications for exploration and recommendations for future work. The results of all geochemical analysis are compiled and arranged in the Appendices.

The findings in Chapters 3 to 6 are written into a paper entitled “Geology, Alteration and Mineralization of the Kay Tanda Epithermal Gold Deposit, Lobo, Batangas, Philippines” and was

accepted for publication to the Resource Geology journal in March 2019. The primary author is Sofia Marah Pascual Frias and the co-authors are Dr. Akira Imai of Kyushu University, Dr. Ryohei Takahashi of Akita University, Dr. Ma. Ines Rosana Balangue-Tarriela and Dr. Carlo Arcilla of the University of the Philippines Diliman, and Dr. Nigel Blamey of Western University. A second paper, which contains the stable isotope studies is currently under production and will be later submitted to the Economic Geology journal for review.

CHAPTER 2

REGIONAL TECTONIC AND GEOLOGIC SETTING

2.1 Introduction

This chapter provides a review of the tectonic and geologic setting of the Philippine archipelago, the metallogenic potential of the Western Luzon Arc and the Batangas Mineral District, and the regional geology of southern Batangas. The following subsections summarize the findings of several workers which consist of studies on paleo- and modern-day tectonics, regional geologic mapping, and mineral resource exploration on several mineral prospects in southern Batangas.

2.2 Philippine tectonic and geologic setting

The Philippine archipelago is located at the triple-junction of three major tectonic plates: the Eurasian Plate, the Indo-Australian Plate, and the Pacific Plate (Aurelio, 2000). It directly interacts with the western edge of the Philippine Sea Plate on its eastern margin and the eastern edge of the Sundaland-Eurasian Plate on its western margin (Aurelio, 2000). The interaction between these tectonic plates is convergent in nature which makes it one of the most complex and tectonically active terrains in the world (Aurelio, 2000) (Fig. 2.1). As a consequence of this interaction with surrounding tectonic plates, the country is trapped between two active subduction zones systems with opposing polarity (Aurelio, 2000). It is bounded on its eastern margin by westward-verging trench systems (the Philippine Trench and the East Luzon Trough) and on its western margin by eastward-verging trench systems (the Manila Trench, the Negros Trench, the Sulu Trench, and the Cotabato Trench) (Aurelio, 2000) (Fig. 2.1).

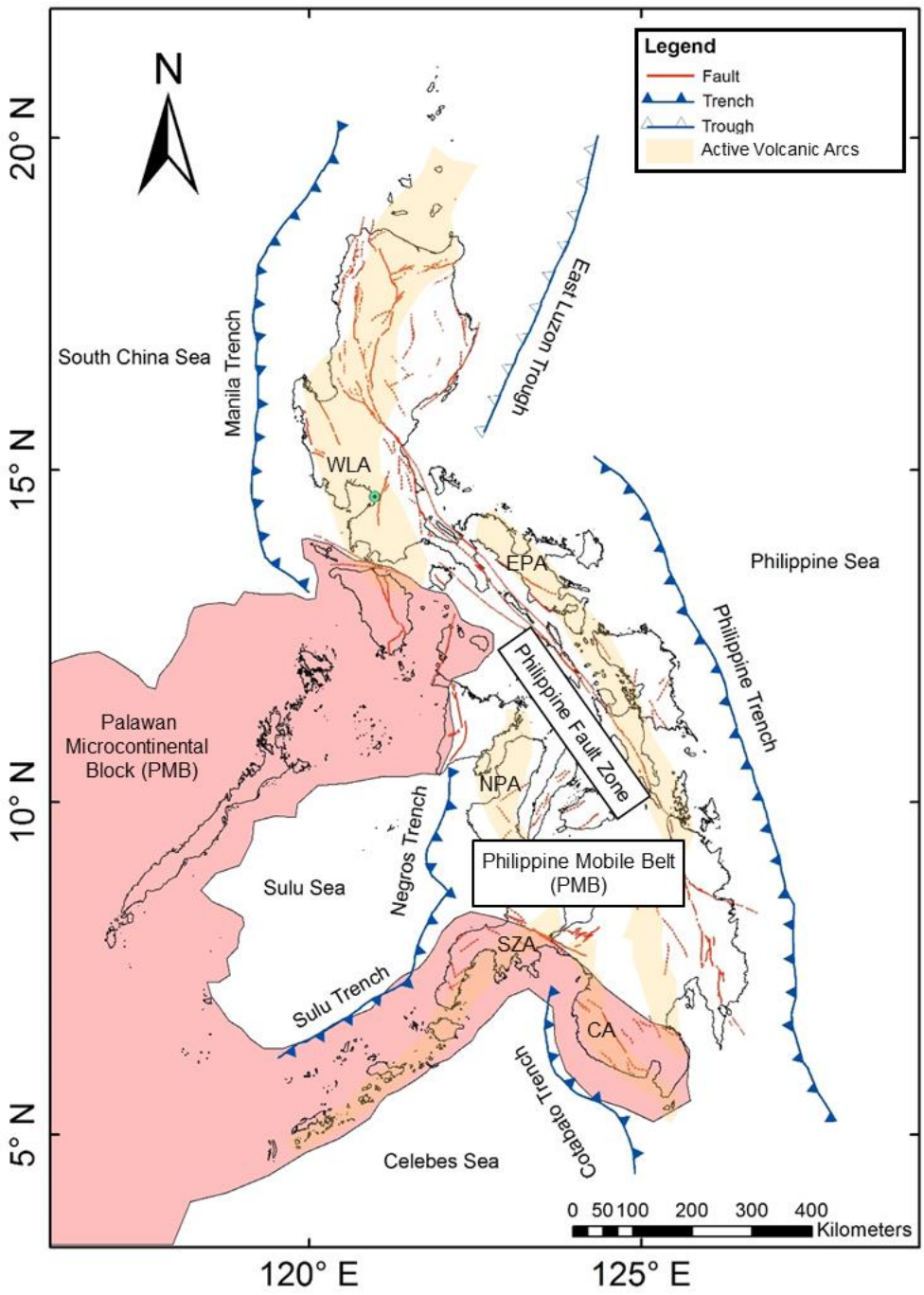

Fig. 2.1 Tectonic map of the Philippines showing major structural features such as the two major tectono-stratigraphic blocks namely the Philippine Mobile Belt (PMB) and the Palawan Microcontinental Block (PCB), the trench systems on the eastern (Philippine Trench and East Luzon Trough) and western side (Manila Trench, Negros Trench, Sulu Trench, and Cotabato Trench) of the archipelago and their corresponding volcanic arcs (WLA - Western Luzon Arc, EPA - Eastern Philippine Arc, NPA – Negros-Panay Arc, SZA – Sulu-Zamboanga Arc, CA – Cotabato Arc), the surrounding marginal sea basins, the Philippine Fault Zone and other major faults. Country boundary taken from PhilGIS (2011), outline of PCB-PMB collision zone from Manalo et al. (2016), outline of trenches and faults from PHIVOLCS (2015), Oligo-Miocene and active volcanic arcs from Aurelio (2000).

The Philippine Trench is a surface manifestation of the subduction of the Eocene Philippine Sea Plate underneath the Philippine archipelago (Fitch, 1972; Cardwell et al., 1980; Hamburger et al., 1983; Aurelio, 2000; Ozawa et al., 2004; Yumul et al., 2008) (Fig. 2.1). This resulted to the formation of the Eastern Philippine Arc which is composed of an active chain of volcanoes along the eastern Philippines from Bicol to Leyte (Aurelio, 2000) (Fig. 2.1). The continuity of the volcanic arc in Mindanao is unclear (Aurelio, 2000). Though the termination of the southern segment of the Philippine Trench is still uncertain, a geophysical study by Nichols et al. (1990) suggested that the subduction along the southern segment of the Philippine Trench is propagating southwards towards the Moluccas Sea Collision Zone (Nichols et al., 1990; Aurelio, 2000). The activity along this trench is estimated to have started around 5 Ma ago based on the estimated length of the subducted slab and the displacement rate of the Philippine Sea Plate (Aurelio, 2000). At the northeastern margin of the Philippines, however, the East Luzon Trough demonstrates an incipient subduction zone setting which propagates northwards (Lewis & Hayes, 1983; Aurelio, 2000; Milsom et al., 2006) (Fig. 2.1). The East Luzon Trough is bounded on its eastern side by the Benham Rise, an oceanic bathymetric high which inhibits the development of the subduction zone (Milsom et al., 2006).

The western margin of the country is characterized by thinned margins composed of several marginal sea basins which opened at different times within the Cenozoic (Aurelio, 2000). These marginal sea basins are the Early Oligocene to Early Miocene South China Sea Basin which is consumed along the Manila Trench, the Early to Middle Miocene Sulu Sea Basin which is consumed along the Negros and Sulu Trench, and the Eocene Celebes Sea basin which is consumed along the Cotabato Trench (Hayes & Lewis, 1984, 1985; Mitchell et al., 1986; Aurelio, 2000; Solidum et al., 2003; Castillo et al., 2007; Yumul et al., 2008) (Fig. 2.1). The volcanic arcs corresponding to these subduction zones are the Western Luzon Arc, the Negros-Panay Arc, the Sulu-Zamboanga Arc and the Cotabato Arc, respectively (Aurelio, 2000) (Fig. 2.1). The interaction also produced different collision zones on the northern, west-central and southern parts of the archipelago (Aurelio, 2000).

The Philippines is made up of two major tectonostratigraphic blocks which are distinct in terms of composition, seismicity and age: (1) the Philippine Mobile Belt (PMB) (Gervasio, 1966) and (2) the Palawan Microcontinental Block (PCB) (Aurelio, 2000) (Fig. 2.1). The Palawan Microcontinental Block was formerly a part of mainland Asia which drifted away consequent to the opening of the South China Sea and later on collided with the western edge of the Philippine Mobile Belt during the Miocene (Taylor & Hayes, 1980; Holloway, 1982; Aurelio, 2000). This collision transformed the southern tip of the Manila Trench from a subduction zone into an arc-continent collision zone (Marchardier & Rangin, 1990; Aurelio, 2000) (Fig. 2.1). The Palawan Microcontinental Block, which is composed of the Palawan Island, the Mindoro Island, the Romblon Island Group, and the Buruanga Peninsula, and Western Mindanao, is an aseismic block of continental affinity (Hamilton, 1979; Dimalanta et al., 2009; Concepcion et al., 2012; Aurelio, 2013; Manalo et al., 2016) (Fig. 2.1). The oldest rocks are composed of Paleozoic sedimentary rocks mapped in Palawan and the metamorphic rocks mapped in the Mindoro Island and Romblon Island Group (Aurelio, 2013). The Philippine Mobile Belt is an amalgamation of different accreted terrains which formed and originated from subequatorial regions and travelled to its present location consequent to the movement and the rotation of the Philippine Sea Plate since 50 Ma (Hall, 2002). It is mainly an island arc system composed of pre-Tertiary metamorphic basement rocks, Cretaceous to Oligocene ophiolites and ophiolitic basement rocks, Cretaceous-Paleogene and Oligo-Miocene magmatic arcs, Plio-Quaternary volcanic arcs, and several sedimentary basins (Aurelio, 2000; Aurelio, 2013). This is an actively deforming zone characterized by several fault systems. The most prominent among them is the Philippine Fault Zone, a 1200 km left-lateral strike slip fault, straddling the archipelago from Luzon to Mindanao (Allen, 1962; Barrier et al., 1991; Aurelio, 2000) (Fig. 2.1). The formation and activity of this fault are attributed to the shear partitioning of the oblique convergence between the Philippine Mobile Belt and the Philippine Sea Plate (Fitch, 1972; Aurelio, 2000).

2.3 Western Luzon Arc and its metallogenic potential

The Western Luzon Volcanic Arc, also called the Bataan-Mindoro Arc in several literature, is a series of northwest-trending volcanic centers with ages dated Miocene to Recent and extending from Babuyan Islands to Central Mindoro along the western Luzon Island (De Boer et al., 1980; Defant et al., 1988; Defant et al., 1991; Aurelio, 2000; MGB, 2004) (Fig. 2.2). It was formed due to the subduction of the South China Sea Basin underneath the western edge of Luzon Island along the Manila Trench (Cardwell et al., 1980; Aurelio, 2000). Based on Cardwell et al. (1980), the main volcanic arc that was formed directly due to the subduction occurs at about 100 km above the Wadati-Benoiff zone (Cardwell et al., 1980; Arpa et al., 2008). Among these volcanic centers, there is only one active volcano (Mt. Pinatubo) and three potentially active volcanoes (Mt. Natib, Mt. Mariveles and Corregidor) (PHIVOLCS, 2008). The rest are inactive volcanoes (PHIVOLCS, 2008). The other volcanic centers, such as calderas (Laguna de Bai and Taal Caldera), stratovolcanoes (Mt. Taal, Mt. Banahaw, Mt. San Cristobal) and domes, in the southern Luzon region which are located east of the Western Luzon Arc and more than 100 km above the subducted slab (e.g. Taal occurs at around 200 km above the subducted slab) belong to the Macolod Corridor (Fig. 2.2) (Arpa et al, 2008). The Macolod Corridor is a 40 km-wide northeast-southwest-trending topographic depression oriented perpendicular with respect to the Western Luzon Arc which features intensely active Late Pliocene to Recent volcanism (Defant et al., 1988; Förster et al., 1990; Sudo et al., 2000; Arpa et al., 2008). Unlike the volcanoes in the Western Luzon Arc, the origin of the volcanism in the Macolod Corridor is still a matter of discussion (Sudo et al., 2000; Vogel et al., 2006). Several hypotheses have been proposed by several workers which include: (1) a pull-apart rift zone (Defant et al., 1988), (2) a pull-apart structure formed by NW-SE-trending shear systems (Förster et al., 1990), and (3) rifting due to transtensional motion (Pubellier et al., 2000; Aquino, 2004; Vogel et al., 2006). On the other hand, other workers found slab-derived components in Taal lavas based on geochemical analysis (Knittel & Oles, 1995; Castillo & Newhall, 2004).

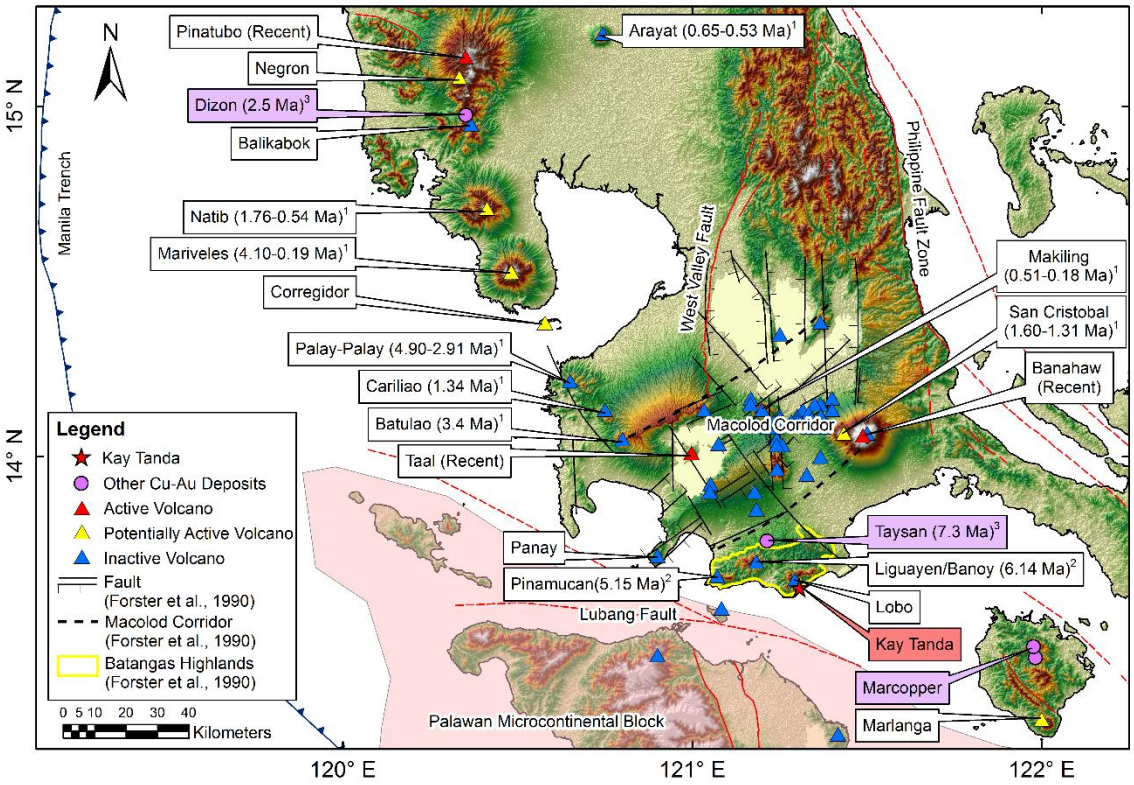

Fig. 2.2 Regional tectonic map of southern Luzon and the immediate vicinity showing the major structures and the location of Kay Tanda. Kay Tanda is situated on Mt. Lobo, an eroded volcanic center at the southern tip of the Western Luzon Arc. Also shown are the other volcanoes in the Western Luzon Arc and Macolod Corridor and three porphyry copper deposits. Location of porphyry copper deposits was taken from Loudon (1976), Wolfe et al. (1978), Imai (2002), and Imai (2005), location of volcanoes in Western Luzon Arc from PHIVOLCS (2008), location of volcanoes in Macolod Corridor from Wolfe and Self (1983), Defant et al. (1988), Förster et al. (1990), and Sudo et al. (2000). K-Ar age dates of the volcanoes from [1]De Boer et al. (1980) and [2]Sudo et al. (2000). K-Ar age dates of porphyry copper-gold deposits from [3]Imai (2002).

The subduction along the southern segment of Manila Trench was terminated during the Miocene collision of the Palawan Microcontinental Block (PCB) to the Philippine Mobile Belt (PMB) (Rangin et al., 1985; Aurelio, 2000). This led to the transformation from a subduction zone to an arc-collision zone causing the decline in volcanic activity at the southern tip of Western Luzon Volcanic Arc (Stephan et al., 1986; Faure et al., 1989; Marchadier & Rangin, 1990). This waning of the volcanism in the southern segment of the arc is reflected in the older reported ages of the volcanic centers in southern Batangas than those in the central to northern part of the Western Luzon Arc (De Boer et al., 1980; Wolfe, 1981; Sudo et al., 2000) (Fig. 2.2). In this discussion, focus will be given to the central to southern tip of the Western Luzon Arc.

The metallogenic productivity of the Western Luzon Arc has been well exemplified by the abundance of successful mines and mapped prospects on its northern segment in the Baguio and Mankayan Au Districts. Though a few mineral prospects have been successfully mapped and exploited along the southern segment of the Western Luzon Arc, its metallogenic potential can still be observed as evidenced by the high SO_3 contents in microphenocrystic apatite in the intrusive rocks associated to known porphyry Cu deposits and the presence of microphenocrystic anhydrite and sulfur-rich dacitic pumices in pyroclastic-flow and tephra fall deposits of Mt. Pinatubo (Imai et al., 1996; Imai, 2002). These are related to oxidizing hydrous magmatism which generates porphyry Cu mineralization (Imai et al., 1996; Imai, 2002). Among the known ore deposits in the southern segment of the Western Luzon Arc are three porphyry copper deposits namely the Dizon porphyry Cu deposit in Zambales, the Taysan porphyry Cu deposit in Batangas, and the Marcopper porphyry Cu deposit in Marinduque Island (Fig. 2.2) (Loudon, 1976; Wolfe et al., 1978; Imai, 2005).

2.4 Batangas Mineral District

The Batangas Mineral District is located in the highlands of southern Batangas which is a part of the southern tip of the Western Luzon Volcanic Arc (Fig. 2.2-2.3). It is bounded to the north by the Macolod Corridor and to the south by the Lubang Fault, a left-lateral strike-slip fault whose western end cuts through the southern section of the Manila Trench accretionary prism (Rangin et al., 1988; MGB, 2010). The Kay Tanda deposit lies on the southeastern flank of Mt. Lobo, an eroded inactive volcano of Late Cenozoic age.

The report by Avila (1980) documented several mineralized areas in the district which were subjected to mineral verification and geological investigation (Avila, 1980). Stream sediment samples were analyzed for copper content using atomic absorption analysis (Avila, 1980). These mineralized areas include (1) the Taysan Cu prospect in Taysan, Batangas which was owned by Lobo Mines, Inc. and was being explored by Benguet Consolidated Inc. during that time, (2) the Biga Cu prospect along the upper reaches of Biga River in Mt. Banoy, (3) the Talahib Cu prospect

along the upper tributaries of the Talahib River, (4) the Hebanga Cu prospect in Rosario, (5) the Palacpac Cu prospect along the upper tributaries of the Lobo River which was being explored by Sumitomo Metal Mining Corporation during that time, and (6) an unnamed Cu-Ag-barite mine in Mataas na Bundok (4 km from Lobo town proper) which was previously operated by Pan Philippines in 1956 and by Frontino Incorporated in 1966 (Avila, 1980). Gypsum, guano, phosphate prospects and raw materials for cement were also mapped in the region (Avila, 1980). The more recent literature on the mineral deposits in Batangas is limited to the mineral exploration reports conducted by several private mining companies which hold exploration permits in the area.

2.5 Regional geology of southern Batangas

Over the years, the regional geologic mapping conducted in the Philippines is primarily driven by mineral and petroleum exploration which led to a variation in the degree of quality and accuracy of the mapping over the archipelago (Hall, 2002). The most recent geologic map of the southern Batangas was based on the report by Avila (1980) which involved a reconnaissance geological survey to evaluate the economic mineral potential of the region. The geology of southern Batangas belongs to the Southwest Luzon Uplands Stratigraphic Group (SG7) defined by MGB (2010) (Fig. 2.3).

The oldest rocks are composed of Oligocene arc-basement sequences of the San Juan Formation which was referred to as the San Juan Metavolcanics and Metasediments in earlier literatures (Avila, 1980). The metavolcanic rocks are composed of metamorphosed fine- to medium-grained basalts and andesites while the metasedimentary rocks are composed of metamorphosed greywacke, shale and chert (Avila, 1980; MGB, 2010). There are also occurrences of slates, paraschists, marble and hornfels in the contact metamorphic aureoles around the quartz diorite body (Avila, 1980; MGB, 2010). It is not exposed in the deposit nor encountered in the drill holes but it outcrops on the northern side of Mt. Lobo, around the margins of the Tolos Quartz Diorite (Avila, 1980; MGB, 2010).

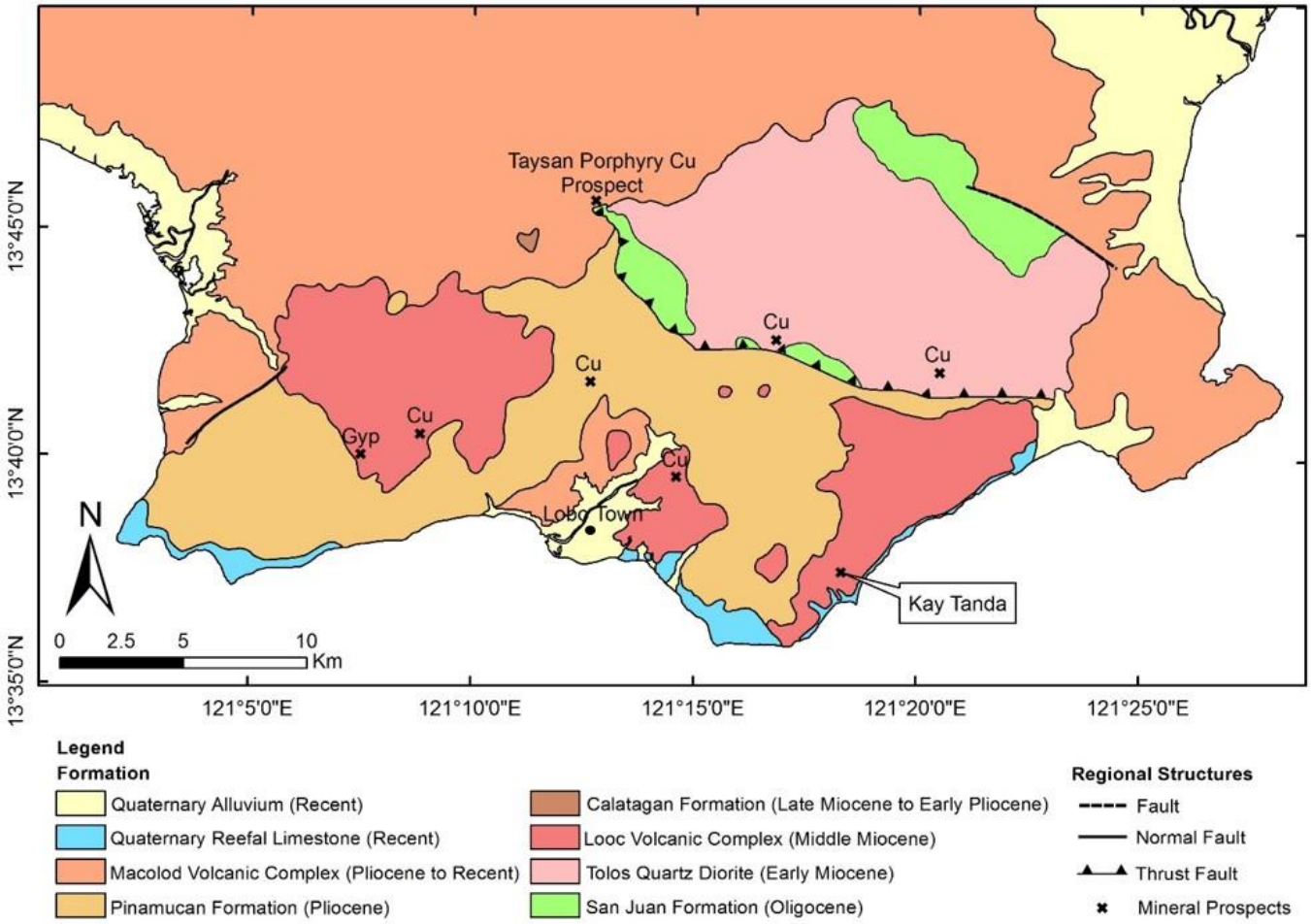

Fig. 2.3 Consolidated geologic map of southern Batangas. The maps included are Batangas (Sheet 3261 III), Lobo (Sheet 3260 IV), Malabrigo (Sheet 3260 I), and San Juan (Sheet 3261 II) Quadrangles based on Avila (1980) prepared and published by the Bureau of Mines and Geo-Sciences, Ministry of Natural Resources (1985a, b, c, d).

The San Juan Formation was intruded by the Early Miocene Tolos Quartz Diorite which was previously named as the Tolos Batholith by Wolfe et al. (1978) and as the San Juan Quartz Diorite by Avila (1980) (MGB, 2010). This batholith is composed of quartz diorite, hornblende quartz diorite, hornblende diorite, quartz monzonite and dacite porphyry, and it occurs along the northern side of the Laiya Fault Zone (MGB, 2010). The Taysan porphyry Cu deposit lies near the northwest margin of the Tolos Quartz Diorite. It is also reported that these intrusive rocks are similar to those associated with the porphyry Cu mineralization in the Baguio Au District in northern Luzon and in Marinduque Island south of Luzon (Wolfe et al., 1978).

The volcanic centers in southern Batangas, which include Mt. Liguayen/Banoy and Mt. Lobo (Fig. 2.2), are comprised mainly of the Middle Miocene andesitic to dacitic volcaniclastic sequences of the Looc Volcanic Complex (Avila, 1980). It unconformably overlies the San Juan Formation (MGB, 2010). It is equivalent to the Batangas Volcanics by Corby et al. (1951), the Banoy Volcanics by Wolfe et al. (1978) and the Talahib Andesite by Avila (1980) (MGB, 2010). It was previously named as the Batangas Extrusives and Pyroclastics by Malicdem et al. (1963) for the andesitic to dacitic volcanic rocks exposed around the Looc Pb-Ag-Sb mine at Looc, Nasugbu, Batangas (MGB, 2010). Locally, it is referred to as the Talahib Volcanic Sequence and is mainly characterized as thick volcanic sequences of agglomerates, andesitic and dacitic tuffs and flows (Rohrlach & Fredericksen, 2008, unpublished data). This formation hosts the majority of the Au mineralization at Kay Tanda (Rohrlach & Fredericksen, 2008, unpublished data).

Another formation, the Dagatan Wacke of Middle Miocene age, unconformably overlies the San Juan Formation and is exposed in the Taysan porphyry Cu mine and along the road cuts between Dagatan and Lobo (Wolfe et al., 1978; MGB, 2010). It is composed of feldspathic and volcanic wacke and conglomerate sequences (Wolfe et al., 1978; MGB, 2010).

Overlying the Looc Volcanic Complex is the Late Miocene to Early Pliocene Calatagan Formation which is composed of soft tuffaceous marine siltstones, coralline limestones and marl (MGB, 2010). It was previously named as the Calatagan Marl by Corby et al. (1951) and is equivalent to the Dingle Limestone by Wolfe et al. (1978) and the Mapulo Limestone by Avila (1980) (MGB, 2010).

The Pinamucan Formation named by Avila (1980) is comprised of Pliocene age interbedded sedimentary sequences of conglomerate, sandstone, shale and agglomerate that unconformably overlie the Tolos Quartz Diorite and San Juan Formation (MGB, 2010). It differs from the Calatagan Formation due to the absence of a limestone member (MGB, 2010). The lower member of this formation is rarely exposed in Kay Tanda but the upper member named the Lobo Agglomerate by Avila (1980) is extensively distributed in the northwestern portion of the Kay Tanda deposit (Rohrlach & Fredericksen, 2008, unpublished data). The Lobo Agglomerate has intercalated pyroclastic rocks within the sedimentary sequences (Avila, 1980; MGB, 2010).

A Pleistocene sub-aerial ash-fall vitric tuff overlies the older volcano-sedimentary sequences in the area and is locally called the Taysan Tuff (Avila, 1980). It is equivalent to the Taal Tuff of Wolfe et al. (1978) and the Macolod Volcanic Complex of MGB (2010) which is found in various areas of Batangas, Laguna, Rizal and Quezon (MGB, 2010). Sequences of Quaternary reefal limestone with a conglomerate base cap the previous units and are found outcropped along the coast of the study area (Avila, 1980; Rohrlach & Fredericksen, 2008, unpublished data).

CHAPTER 3

DEPOSIT GEOLOGY

3.1 Introduction

The geology of Kay Tanda was established from extensive field mapping and systematic drilling campaigns and core logging conducted by the geologists of MRL Gold Philippines, Inc. and other companies which previously worked on the deposit. Formed at the southeastern flank of an inactive volcano less than a kilometer from the coastline of southern Batangas, the geology of the Kay Tanda deposit is mainly composed of thick sequences of intercalated dacitic and andesitic volcaniclastic rocks (the Talahib Volcanic Sequence) which were intruded by two intrusive bodies (the Balibago Diorite Complex and the Dacite Porphyry Intrusives) that are distinct in terms of composition, texture, configuration and age of intrusion. Several younger volcaniclastic rocks intertonguing with sedimentary sequences composed of clastic rocks with limestone lenses (the Calatagan Formation) were also mapped overlying the older volcaniclastic rocks. These volcaniclastic and sedimentary sequences host the epithermal mineralization at Kay Tanda. Hydrothermal alteration is pervasive in these host rocks which are covered by a post-mineralization andesitic volcaniclastic unit (the Balibago Andesite). Erosion exposed the altered host rocks at the eastern and southwestern parts of the deposit but they remain covered by post-mineralization rocks at the northwestern side.

The geology of Kay Tanda has been shaped by several episodes of subaerial volcanism, magmatism and reworking by surface processes. It is of great significance to determine the mineralogical and textural differences among the lithologic units to determine the pre-mineralization, syn-mineralization, and post-mineralization rocks. This chapter aims to present a comprehensive documentation of the lithologic units related to the epithermal Au and base metal mineralization of the Kay Tanda deposit to provide a geologic framework of the deposit through

detailed petrography of the rock samples collected from the representative drill holes selected for this study. Due to the altered nature of the host rocks, this chapter also aims to introduce the associated alteration assemblages which will be later discussed in detail alongside with mineralization in Chapter 4.

3.2 Methodology

Due to restrictions in the access of the property, independent surface mapping was not conducted in this study. Instead, detailed core logging and sampling were conducted in January 2017 to delineate the extent of the lithologic units at depth and to collect representative host rocks for petrography. There are 162 drill holes in the Kay Tanda which include 46 diamond drill holes and 116 reverse circulation drill holes. In this study, 13 representative diamond drill holes, totaling 2,800 m, were selected, logged and sampled based on their location in the deposit, the intersected lithologies, and the assay data (Fig. 3.1). A total of 85 thin sections of host rocks underwent transmitted light microscopy using a Nikon ECLIPSE LV100NPOL petrographic microscope at Akita University. Radiometric age dating of the lithologic units was not conducted due to the pervasive alteration. The ages of the lithologic units were approximated using correlation to regionally mapped formations and stratigraphic relations among lithologic units. The collar coordinates, length, depth, azimuth, and dip of the drill holes examined in this study are listed in Appendix A. A drill hole location map is also provided in Appendix A.

3.3 Lithologic units

The succeeding subsections contain the petrographic descriptions of each lithologic unit, as well as the general description of their occurrences and distribution based on the mapping and drilling results of the company. A local geologic map generated from the surface mapping of the company is shown in Figure 3.1. A composite cross section is also shown in Figure 3.1 which was modified based on the results of the petrography conducted in this study.

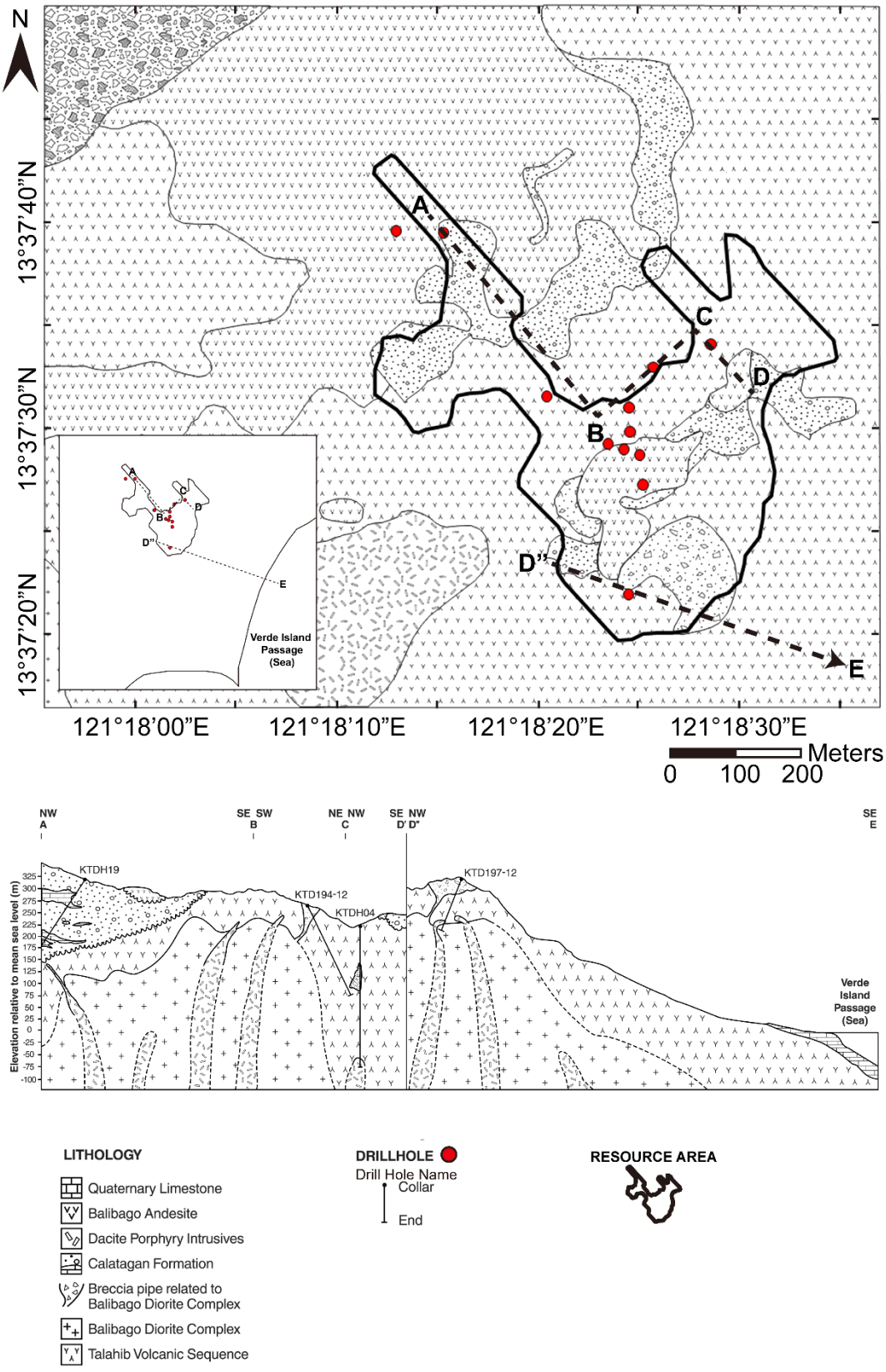

Fig. 3.1 Lithologic map and representative composite cross section of Kay Tanda showing the distribution and relationships among lithologic units. The composite cross section traverses through points A-B-C-D and D"-E. Inset shows the location of Kay Tanda with respect to the coastline and Verde Island Passage and the extent of a composite cross section towards the sea. Map and cross section were modified from MRL Gold Philippines, Inc. (unpublished).

3.3.1 Talahib Volcanic Sequence

The Talahib Volcanic Sequence is composed of a thick sequence of intercalated pyroclastic rocks and lava flow deposits of dacitic to andesitic composition. This formation is widely exposed in Kay Tanda and extends further to the northwest and northeast of the Archangel MPSA (Rohrlach & Fredericksen, 2008, unpublished data). The thickness of this formation reaches up to 365 m, but in the majority of the drill holes the thickness is between 100 m to 200 m before encountering the cogenetic dioritic intrusions of the Balibago Diorite Complex and the younger Dacite Porphyry Intrusives at depth (Rohrlach & Fredericksen, 2008, unpublished data). The dacitic rocks are composed of porphyritic dacite flows (Fig. 3.2A-C), dacitic crystal tuffs (Fig. 3.2D-F), and dacitic lapilli tuffs (Fig. 3.2G-I) while the andesitic rocks are composed of porphyritic andesite flows (Fig. 3.3A-C), porphyritic hornblende andesite flows (Fig. 3.3D-F), and andesitic lapilli tuffs (Fig. 3.3G-I). This formation is correlated to the Middle Miocene Looc Volcanic Complex of MGB (2010). It hosts the bulk of the mineralization of the Kay Tanda deposit and exhibits pervasive hydrothermal alteration. Oxidation is widespread in the shallower levels.

The dacitic rocks are mainly characterized by the occurrence and abundance of unaltered quartz phenocrysts. Porphyritic dacite flows have rounded, resorbed or embayed quartz phenocrysts and clay-altered euhedral plagioclase phenocrysts surrounded by clay-silica-altered groundmass (Fig. 3.2B-C). The dacitic crystal tuffs are dominantly composed of crystal fragments of unaltered quartz and clay-altered feldspars set in silica-altered tuffaceous matrix (Fig. 3.2E-F). The dacitic lapilli tuffs are polymictic and are composed dominantly of porphyritic dacite fragments with minor andesitic fragments set in crystal fragment-rich tuffaceous matrix (Fig. 3.2H-I).

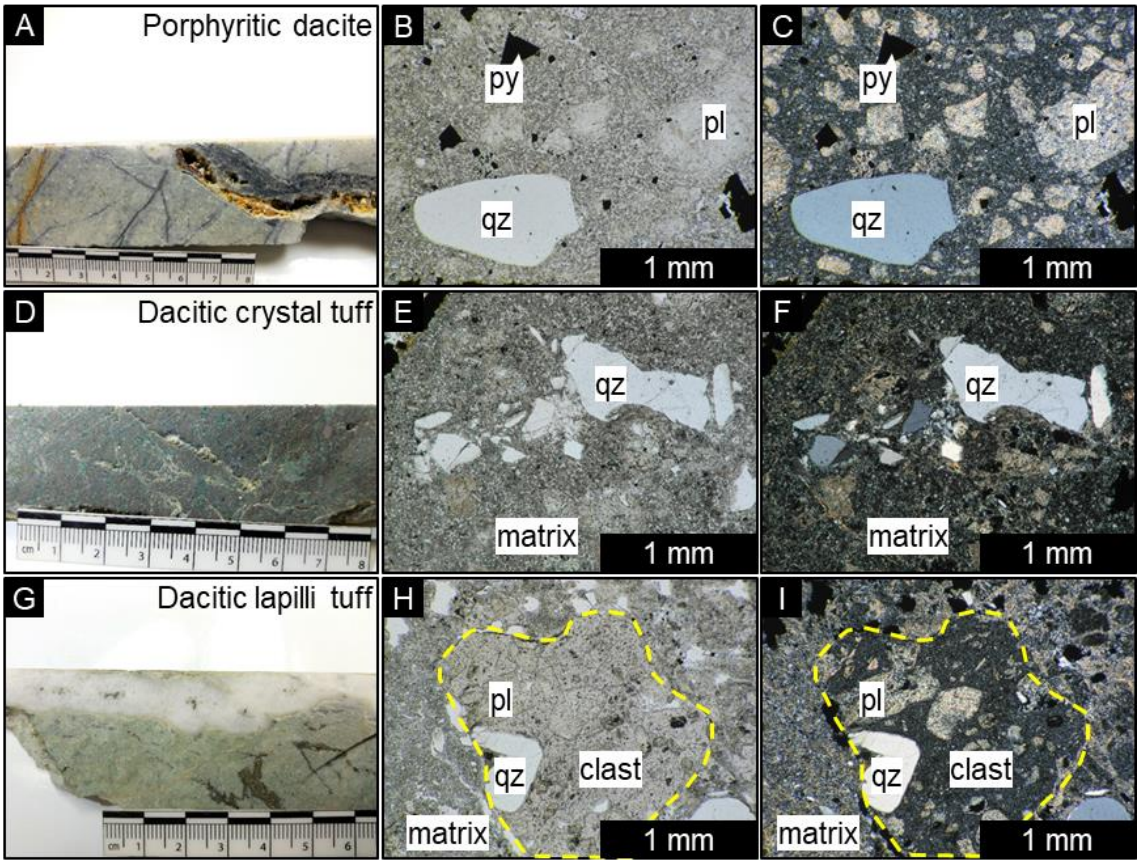

Fig. 3.2 Representative samples and corresponding photomicrographs of representative samples of the dacitic members of the Talahib Volcanic Sequence. (A-C) Porphyritic dacite showing rounded quartz phenocryst and clay-altered plagioclase phenocrysts set in fine-grained groundmass (Sample: KTD197-12 121.60m, B18). (D-F) Dacitic crystal tuff showing quartz crystal fragments set in clay-altered matrix (Sample: KTD197-12 90.30m, B13). (G-I) Dacitic lapilli tuff showing porphyritic dacite fragment set in clay-altered matrix. (Sample: KTD197-12 93.10m, B14). Abbreviations: pl – clay-altered plagioclase, py – pyrite, qz – quartz.

The porphyritic andesites and porphyritic hornblende andesites have different plagioclase-amphibole phenocryst ratio: porphyritic andesites have more plagioclase phenocrysts (Fig. 3.3B-C) while hornblende andesites have more hornblende phenocrysts (Fig. 3.3E-F). Andesitic lapilli tuffs are mainly composed of porphyritic andesite fragments surrounded by crystal fragment-rich tuffaceous matrix (Fig. 3.3H-I). Some rocks also show trachytic texture which represents flow direction.

At shallower levels, the rocks were mainly altered by quartz ± pyrophyllite ± dickite/kaolinite ± diaspore alteration and illite ± quartz ± smectite ± kaolinite alteration. Chlorite-illite-quartz alteration is more common at deeper levels.

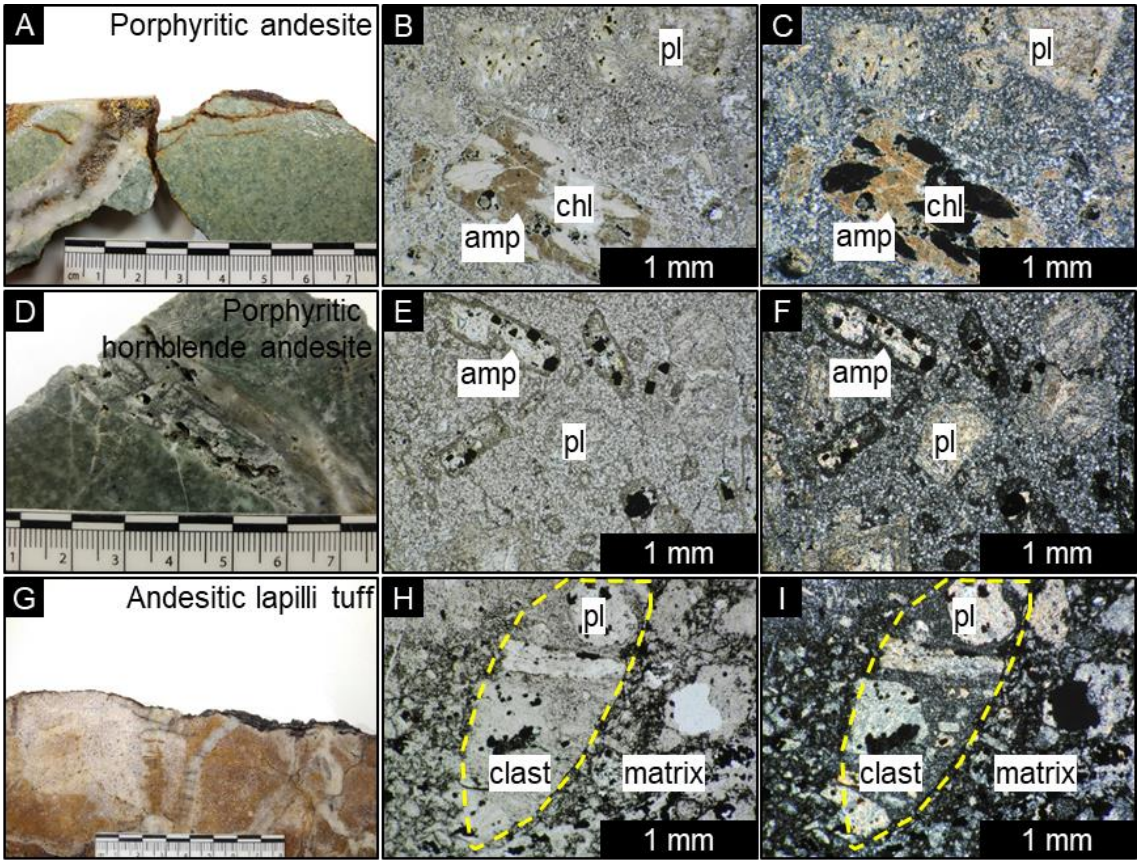

Fig. 3.3 Representative samples and corresponding photomicrographs of representative samples of the andesitic members of the Talahib Volcanic Sequence. (A-C) Porphyritic andesite showing clay-altered plagioclase phenocrysts and chlorite-altered amphibole phenocrysts set in fine-grained groundmass (Sample: KTD197-12 115.80m, B16). (D-F) Porphyritic hornblende andesite showing chlorite-altered amphibole phenocrysts set in fine-grained groundmass (Sample: KTD194-12 122.30m, A14). (G-I) Andesitic lapilli tuff showing porphyritic andesite fragments set in fine-grained matrix (Sample: KTD198-12 35.00m, I07). Abbreviations: amp – amphibole, chl – chlorite, pl – clay-altered plagioclase.

3.3.2 Balibago Diorite Complex

The Balibago Diorite Complex, also called Balibago Intrusive Complex, is a local intrusive body of intermediate composition that has been intersected at the deeper portions of various drill holes and also outcrops at other prospects surrounding Kay Tanda. According to the company reports (Rohrlach & Fredericksen, 2008, unpublished data), it is composed of equigranular diorite, diorite porphyry and quartz diorite which forms a broad and crudely domal intrusive complex intruding the dacitic and andesitic volcaniclastic sequences of the Talahib Volcanic Sequence. Due to this intrusive relationship with the Talahib Volcanic Sequence, the age of this complex is assigned as Middle Miocene to Late Miocene (Rohrlach & Fredericksen, 2008, unpublished data).

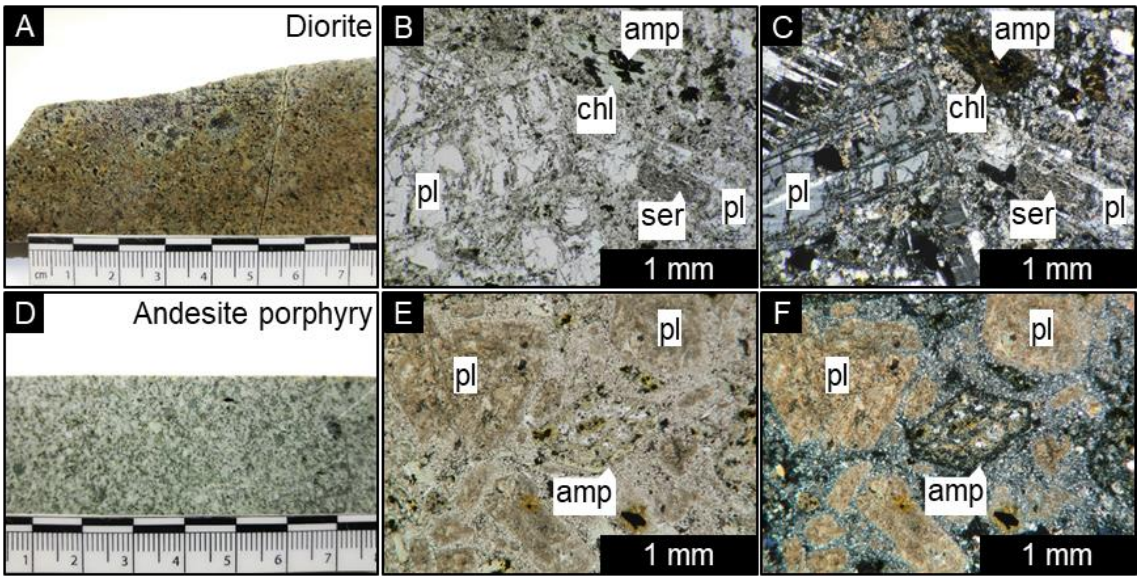

Fig. 3.4 Representative samples and corresponding photomicrographs of representative samples of the Balibago Diorite Complex. (A-C) Diorite composed of interlocking sericite-altered plagioclase and chlorite-altered amphibole (Sample: KTD197-12 149.50m, B23). (D-F) Andesite porphyry showing chlorite-altered amphibole phenocrysts and clay-altered plagioclase phenocrysts set in fine-grained groundmass (Sample: KTDH10 278.35m, D09). Abbreviations: amp – amphibole, chl – chlorite, pl – plagioclase, ser- sericite.

In this study, diorite (Fig. 3.4A-C), quartz diorite and andesite porphyries (Fig. 3.4D-F) were identified. The intrusive contact with the volcanic sequences were encountered during core logging. The diorite and quartz diorite consist mainly of interlocking medium-grained plagioclase, quartz and amphibole crystals. Plagioclase crystals were moderately altered to sericite, amphiboles were moderately to strongly altered to chlorite and calcite, while quartz remained unaltered (Fig. 3.4B-C). Andesite porphyries show porphyritic texture with more phenocryst-crowded appearance. The phenocrysts in the andesite porphyries are larger than those of the porphyritic andesites of the Talahib Volcanic Sequence. The groundmass was also altered to secondary microcrystalline quartz (Fig. 3.4E-F).

Steep breccia pipes were also emplaced into the Talahib Volcanic Sequence synchronous with the intrusion of the Balibago Diorite Complex (Rohrlach & Fredericksen, 2008, unpublished data). These are exposed on the surface in the southern portion of Kay Tanda and were developed above the Balibago Diorite Complex (Rohrlach & Fredericksen, 2008, unpublished data). These breccias show coarse mosaic to rotational textures from the margins toward the interior of the breccia body (Rohrlach & Fredericksen, 2008, unpublished data). At the shallow levels, the breccias were

silicified and were overprinted by epithermal veins associated with quartz ± pyrophyllite ± dickite/kaolinite ± diaspore and illite ± quartz ± smectite ± kaolinite alteration. Chlorite-illite-quartz alteration is pervasive at deeper levels (Rohrlach & Fredericksen, 2008, unpublished data).

3.3.3 Calatagan Formation

Volcano-sedimentary sequences of interbedded conglomerates, sandstones, siltstones (Fig. 3.5A-C), shales, limestones (Fig. 3.5D-F), andesitic (Fig. 3.5G-I) and dacitic flows (Fig. 3.5J-L) and tuffs (Fig. 3.5M-O) unconformably overlie the Talahib Volcanic Sequence. They are mainly distributed in the northwestern and southeastern portions of the deposit. The conglomerate beds are volumetrically dominant over the sandstone and siltstone beds. The limestone lenses are found within both the clastic sedimentary layers and the volcaniclastic layers. Since limestones were not recorded in the Dagatan Wacke nor the Pinamucan Formation (MGB, 2010), these sedimentary units were classified as members of Late Miocene to Early Pliocene Calatagan Formation (Rohrlach & Fredericksen, 2008, unpublished data).

Conglomerates, sandstones, siltstones and shales are composed of volcanic fragments and tuffaceous components. Patches of epidote crystals were observed in altered siltstones and sandstones (Fig. 3.5B-C). Some beds were encountered during core logging which was recognized due to the grading of the sediments. The thicknesses of the beds vary from a few meters to a few tens of meters.

The limestones lenses were dolomitized and partly silicified (Fig. 3.5E). Some contain abundant fossils such as coral fragments, benthic foraminifera, red algae, echinoid spines, gastropods and other bivalves (Fig. 3.5F). Minor mineralization is encountered in the lower members of the formation. Silicified limestones contain pyrite and minor amounts of base metal sulfides. The thickness of the lenses also varies from a few meters to a few tens of meters.

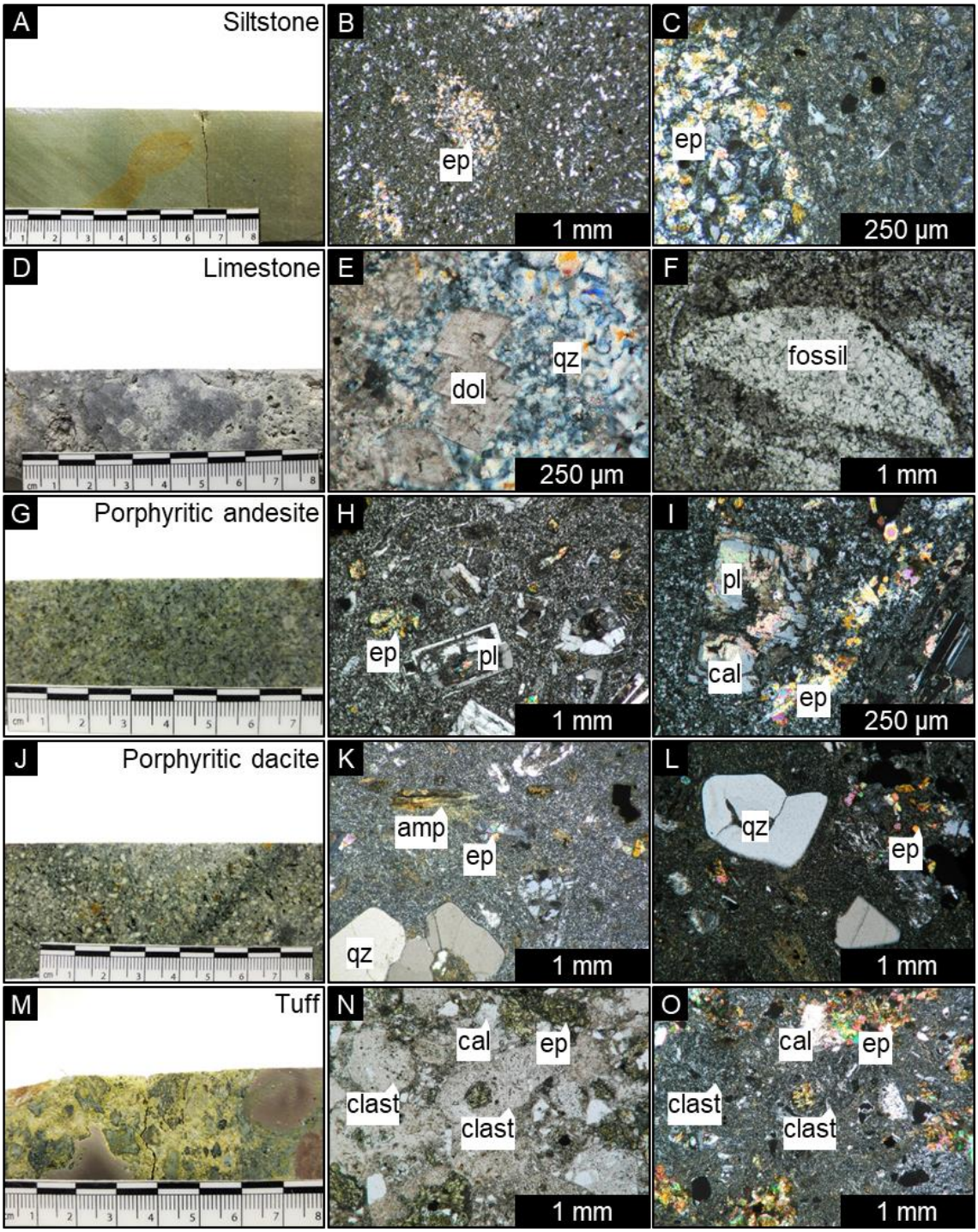

Fig. 3.5 Representative samples and corresponding photomicrographs of representative samples of the volcano-sedimentary rocks of the Calatagan Formation. (A-C) Siltstone with patches of epidote (Sample: KTDH19 81.90m, E17). (D-E) Silicified and dolomitized limestone (Sample: KTDH19 142.60m, E31). (F) Benthic foraminifera in limestone (Sample: KTDH19 62.30m, E14). (G-I) Porphyritic andesite showing calcite- and epidote-altered plagioclase phenocrysts (Sample: KTDH19 34.60m, E04). (J-L) Porphyritic dacite showing rounded quartz phenocrysts and epidote-altered amphibole and plagioclase phenocrysts (Sample: KTDH19 69.10m, E16). (M-O) Tuff showing calcite- and epidote-altered clasts set in tuffaceous matrix (Sample: KTDH19 83.00m, E19). Abbreviations: amp – amphibole, cal – calcite, dol – dolomite, ep – epidote, pl – plagioclase, qz – quartz.

The andesitic and dacitic flows and tuffs show the same textures and mineral assemblages as their counterparts in Talahib Volcanic Sequence but they were affected by weak epidote-calcite-chlorite alteration. Plagioclase phenocrysts were commonly altered to calcite and epidote while hornblende crystals were altered to epidote, chlorite and calcite (Fig. 3.5H-I, K-L, N-O).

3.3.4 Dacite Porphyry Intrusives

Younger Dacite Porphyry Intrusives intruded the members of the Balibago Diorite Complex. In the company reports (Rohrlach & Fredericksen, 2008, unpublished data), they were described as dike-like bodies of variable widths which intruded the Talahib Volcanic Sequence and the overlying Calatagan Formation in some drill holes. There was no record of its intrusion in the post-mineralization Balibago Andesite (Rohrlach & Fredericksen, 2008, unpublished data). Some of these intrusions are exposed on the surface southeast of Pulang Lupa, another prospect west of Kay Tanda (Rohrlach & Fredericksen, 2008, unpublished data). Due to this crosscutting relationships, the age of these intrusions is approximated to be syn- to post-Calatagan Formation (Late Miocene to Early Pliocene) but pre-Balibago Andesite (approximated to be Pliocene) (Rohrlach & Fredericksen, 2008, unpublished data).

The Dacite Porphyry Intrusives have a distinct texture compared to the other dioritic intrusive rocks. These porphyritic rocks are less phenocryst-crowded and have coarser quartz phenocrysts (Fig. 3.6B-C, E-F). Coarse quartz-eye phenocrysts are recognizable in the hand samples with sizes that may range from 0.5 to 3 mm. These quartz phenocrysts are rounded, resorbed or embayed. Other phenocrysts include coarse-grained euhedral plagioclase and amphibole crystals that were typically altered to illite, epidote, calcite, and chlorite (Fig. 3.6B-C, E-F). These phenocrysts are surrounded by silica-altered groundmass.

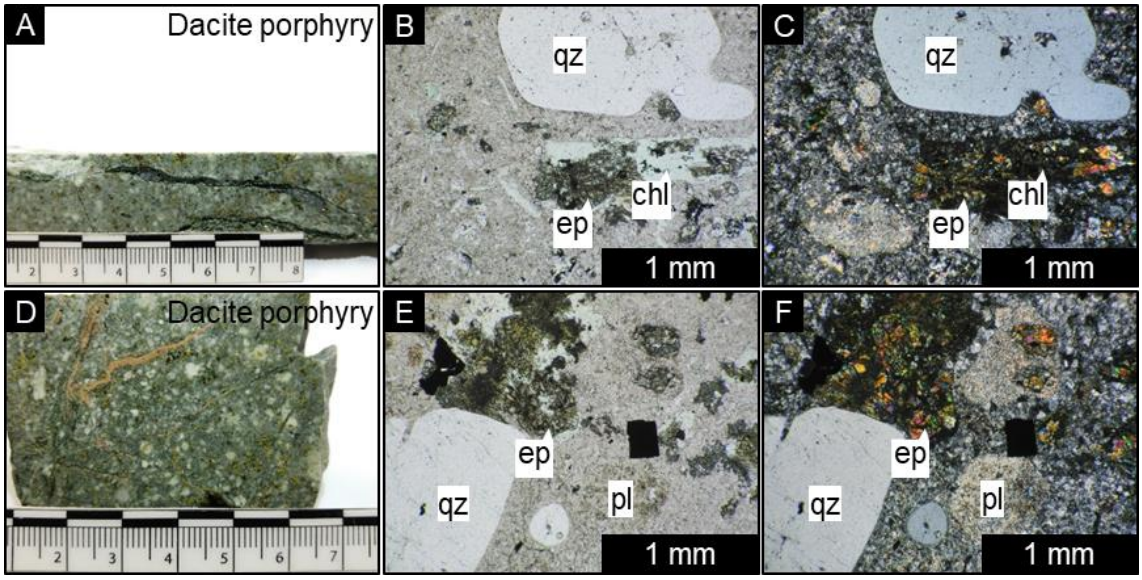

Fig. 3.6 Representative samples and corresponding photomicrographs of representative samples of the Dacite Porphyry Intrusives. (A-C) Dacite porphyry showing rounded quartz phenocrysts and chlorite- and epidote-altered amphibole phenocrysts and clay-altered plagioclase phenocrysts (Sample: KTDH04 299.65m, C53). (D-F) Dacite porphyry showing rounded quartz phenocrysts and chlorite- and epidote-altered amphibole phenocrysts and clay-altered plagioclase phenocrysts (Sample: KTDH04 300.60m, C54). Abbreviations: chl – chlorite, ep – epidote, pl – clay-altered plagioclase, qz –quartz.

3.3.5 Balibago Andesite

A local andesitic volcaniclastic unit, the Balibago Andesite, unconformably overlies the Talahib Volcanic Sequence and Calatagan Formation. This is believed to be coeval to the other volcanic rocks that are of similar age to the Mataas na Gulod Volcanic Complex which is exposed in western Cavite (Rohrlach & Fredericksen, 2008, unpublished data; MGB, 2010). This relationship assigns its age to Pliocene (Rohrlach & Fredericksen, 2008, unpublished data). The drill holes intersected this formation at the northwestern and southeastern parts of the deposit with intercept thickness ranging from 5 to 50 meters (Rohrlach & Fredericksen, 2008, unpublished data). It is composed of partially weathered brown to greenish brown porphyritic andesite flows (Fig. 3.7A-C) and andesitic lapilli tuffs (Fig. 3.7D-F). This is a post-mineralization volcanic sequence and was not affected by hydrothermal alteration.

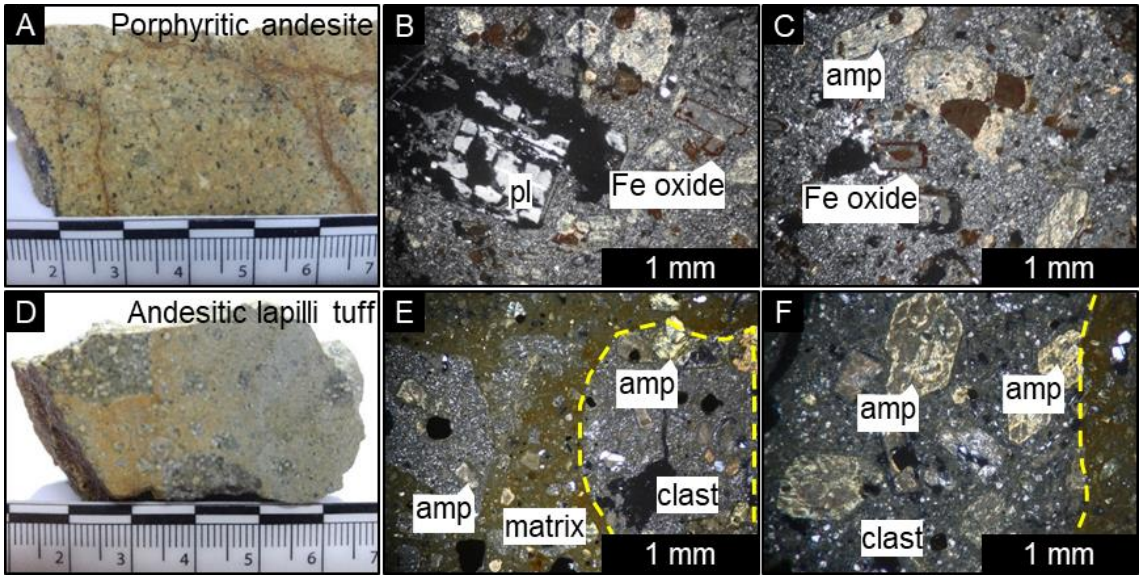

Fig. 3.7 Representative samples and corresponding photomicrographs of representative samples of the Balibago Andesite. (A-C) Porphyritic andesite showing plagioclase phenocrysts and altered amphibole phenocrysts (Sample: KTD183 20.00m) (D-F) Andesitic lapilli tuff with altered porphyritic andesite clasts (Sample: KTD191-12 8.60m). Abbreviations: amp – amphibole, pl –plagioclase.

The porphyritic andesite flows contain subhedral to euhedral amphibole phenocrysts and laths of plagioclase phenocrysts which are partly surrounded by brownish red iron oxide staining. Some of the plagioclase crystals still have preserved zoning or polysynthetic twinning but others were clay-altered and are only recognizable by its relict lath-like shape. The groundmass which is composed of microlaths of plagioclase was also altered to clay and microcrystalline quartz (Fig. 3.7B-C).

Andesitic lapilli tuffs are also found overlying the andesite flows. They are composed of porphyritic andesite fragments identical to the andesitic flows described above. The matrix is composed of smaller lithic and crystal fragments such as amphibole, plagioclase and quartz (Fig. 3.7E-F).

3.4 Geologic setting and depositional environment

Although there is no available radiometric age date on the host rocks of Kay Tanda because of the pervasive hydrothermal alteration, the thick andesitic and dacitic volcaniclastic sequences of the Talahib Volcanic Sequence which mantle Kay Tanda and the rest of Mt. Lobo can be

correlated to the regionally mapped Middle Miocene Looc Volcanic Complex (MGB, 2010). The production of thick sequences of volcaniclastic rocks in southern Batangas is attributed to the Neogene volcanism at the southern tip of the Western Luzon Arc corresponding to the eastward subduction of the South China Sea Basin underneath the western edge of the Luzon Island along the Manila Trench (Hayes & Lewis, 1985; Defant et al., 1991; Aurelio, 2000). The Balibago Diorite Complex which is also of intermediate composition is likely to be a coeval intrusive unit which is supported by the intrusive relationship and the absence of unconformity between the intrusive rocks and the Talahib Volcanic Sequence. Both the Talahib Volcanic Sequence and Balibago Diorite Complex may be products of the volcanic and magmatic activity of Mt. Lobo when it was still on its active state.

The Middle Miocene collision of the Palawan-Mindoro Microcontinental Block and the western portion of the Philippine Mobile Belt (estimated between 15 Ma to 12 Ma) affected southern Batangas as well as the Mindoro-Panay areas (Rangin et al., 1985; Stephan et al., 1986; Rangin et al., 1988; Aurelio et al., 2013). As the collision advanced, the southern tip of the Manila Trench transformed from a subduction zone into a collision zone (Stephan et al., 1986; Rangin et al., 1988; Marchadier & Rangin, 1990) which eventually led to the decline in volcanic activity on its southern tip. The activity in the volcanic centers of southern Batangas can be inferred from the radiometric ages dates of volcanic centers such as Mt. Liguayen or Mt. Banoy (6.14 Ma) and Mt. Pinamucan (5.15 Ma) (Sudo et al., 2000).

During the Late Miocene when the volcanic activity in the region became less frequent, the volcaniclastic sequences became more susceptible to surface processes such as weathering, erosion and reworking. The clastic sedimentary sequences of the Calatagan Formation, which are mainly composed of reworked volcanic sediments, were deposited especially at low elevation areas. The abundance of texturally immature clastic rocks (conglomerates) over the texturally mature clastic rocks (siltstones and shales) and their compositional similarity to the older volcaniclastic rocks indicate local derivation (Tucker, 2001). The presence of graded beddings in the sedimentary layers also indicate sub-aqueous deposition (Tucker, 2001). Minor volcaniclastic sequences were found intercalated and intertonguing with the sedimentary sequences which

indicates intermittent pulses of volcanic activity within a prolonged period of quiescence and sedimentation. The presence of fossiliferous limestone lenses within the clastic sedimentary rocks and volcaniclastic rocks also points to a volcanic environment transitioning to a shallow marine environment (Tucker, 2001). The abundance of corals and presence of benthic foraminifera are evidence of a marine setting (Tucker, 2001).

Towards the end of the Late Miocene, an extensional tectonic regime dominated southern Batangas which propagated northwards during the Pliocene. The extensional structures formed in the region focused renewed magmatism which emplaced the Dacite Porphyry Intrusives. This generated a hydrothermal system which would later form the epithermal deposit.

3.5 Conclusions

The geology of Kay Tanda is mainly composed of volcanic pre-mineralization rocks of the Talahib Volcanic Complex and the cogenetic intrusive rocks of the Balibago Diorite Complex. These lithologic units were formed as products of volcanic and magmatic activity at the southern tip of the Western Luzon Arc during the Miocene. During the Middle Miocene collision of the Palawan Microcontinental Block with the Philippine Mobile Belt, volcanism decreased in southern Batangas as a consequence of the transformation of the southern tip of the Manila Trench from a subduction zone setting into a collision zone setting. This was observed in Kay Tanda with the deposition of the volcano-sedimentary sequences of the Calatagan Formation which indicates periods of quiescence leading to the deposition of intercalated sedimentary rocks within volcaniclastic rocks. Lenses of limestones within the Calatagan Formation also indicate that the rocks were deposited in a volcanic environment transitioning to a shallow marine environment. Magmatism was still active in Kay Tanda from Late Miocene to Early Pliocene as evidenced by the emplacement of the shallow Dacite Porphyry Intrusives. In the later chapters, the importance of this lithologic unit to the formation of the Kay Tanda epithermal deposit will be discussed. The post-mineralization lithologic unit is represented by the Balibago Andesite, an andesitic volcaniclastic unit which unconformably overlies the older lithologic units in Kay Tanda.

CHAPTER 4

ALTERATION AND MINERALIZATION

4.1 Introduction

The epithermal mineralization in Kay Tanda occurs at the higher elevations of a partially eroded hill at the southeastern flank of Mt. Lobo in southern Batangas, Philippines. The mineralization is hosted by the hydrothermally altered volcaniclastic rocks of the Talahib Volcanic Sequence and the volcano-sedimentary package of the overlying Calatagan Formation. Two main styles of epithermal mineralization were identified in Kay Tanda, each characterized by mineralized veins and hydrothermal breccias of distinct mineral assemblages. This chapter aims to document the style, occurrence, and characteristics of the Kay Tanda epithermal deposit. It also aims to develop a paragenetic sequence of the different mineralization stages and the associated hydrothermal alteration zones through core logging and detailed examination of the collected veins, hydrothermal breccias, and altered wall rocks, with emphasis on ore and alteration mineral assemblages, textures and crosscutting relationships. This chapter also aims to present the first radiometric age for the epithermal mineralization obtained from K-Ar dating method.

4.2 Methodology

Veins and hydrothermal breccia samples were collected following the detailed core logging of the 13 representative drill holes used in this study. A total of 66 polished thin sections and 55 polished sections of veins and hydrothermal breccias were examined. Mineral identification and texture observation were conducted through transmitted and reflected light (ore) microscopy using a Nikon ECLIPSE LV100NPOL petrographic microscope, coupled with scanning electron microscopy (SEM), including secondary electron imaging (SEI) and backscattered electron imaging (BEI) using a JEOL JSM-6610LV scanning electron microscope with an Oxford

Instruments INCA X-act energy dispersive spectrometer detector (SEM-EDS) at Akita University. Several vein samples were also subjected to etching using hydrofluoric acid vapor and staining using sodium hexanitrocobaltate for K-feldspar (adularia) identification.

Wallrock alteration was also examined in several samples. Detailed alteration mineral identification through petrography was coupled with powder X-ray diffraction using a Rigaku Multiflex X-ray diffractometer (XRD) with CuKα tube (voltage = 30 kV, current = 16 mA, receiving slit = 0.3 mm, step = 0.01). The X-ray diffraction studies involved several sample preparations to determine the bulk mineral composition and detailed clay mineral composition of the samples. A total of 51 samples were analyzed. Randomly oriented powdered samples were scanned from 2° to 70° 2θ at 2° per minute. Hydraulic elutriation was conducted to separate the clay fraction (≤2 μm) in the samples. Air dried, ethylene glycol-treated, and HCl-treated oriented samples were scanned from 2° to 40° at 2° per minute.

To determine the age of the mineralization at Kay Tanda, illite samples were separated from haloes surrounding selected mineralized quartz veins. Hydraulic elutriation was conducted to separate the clay mineral fraction from the non-clay minerals. Approximately 50 g of lightly crushed samples was poured into 300 mL distilled water and ultrasonicated for 15 minutes to avoid flocculation. The sample was left for 3 hours and 54 minutes at 20 °C before the suspension was extracted at a settling distance of 5 cm from the water surface. The extracted suspension was centrifuged at 2000 rpm for 5 minutes and the supernatant was disposed. The sample was collected and smeared over a slide glass for air-drying. The presence of illite in the sample was confirmed by XRD at Akita University. Two illite samples (500 mg each) were sent to GeochronEx Analytical Services & Consulting in Canada for K-Ar dating.

The company conducted an extensive work in describing the alteration and mineralization framework of Kay Tanda. In conjunction to extensive surface mapping, drilling and core logging, the company also conducted petrography and PIMA work to determine alteration assemblages and a systematic (per meter) elemental assay (involving Au, Ag, Pb, Cu, and Zn) to determine mineralized zones.

4.3 Alteration and mineralization style and characteristics

A geologic map and a composite cross section showing the relationship among lithologic units, alteration, and mineralized zones were generated from the company's data with modifications based on the work conducted in this study (Fig. 4.1). Two styles of epithermal mineralization have been identified in Kay Tanda. The first style is an early-stage extensive epithermal mineralization characterized by Au-Ag-bearing quartz stockworks consisting of crustiform to colloform quartz veins, quartz-pyrite veins, pyrite stringers and silicified hydrothermal breccias hosted at the shallower levels of the Talahib Volcanic Sequence (Fig. 4.1). They are commonly oxidized and are associated with the pervasive illite ± quartz ± smectite ± kaolinite alteration but are sometimes found crosscutting zones of localized quartz ± pyrophyllite ± dickite/kaolinite ± diaspore alteration (Fig. 4.1). The thickness of the stockwork zones ranges from a couple of tens of meters to more than a hundred meters in some sections and are strongly influenced by NE- to ENE-trending structures (Rohrlach & Fredericksen, 2008, unpublished data). Chalcopyrite, bornite and galena are the only base metal sulfides found in this stage and occur in trace amounts. The Au grades are generally low (less than 1 ppm Au) but increase significantly in areas cut by veins and stockworks (may reach up to 10 ppm Au) (Rohrlach & Fredericksen, 2008, unpublished data). The second style is a late-stage base metal (Zn, Pb, and Cu) epithermal mineralization with local bonanza-grade Au mineralization hosted in quartz ± adularia ± calcite veins, anhydrite-gypsum veins, and hydrothermal breccias which are intersected at deeper levels of the Talahib Volcanic Sequence and the shallower levels of the Balibago Intrusive Complex (Fig. 4.1). They are associated with chlorite-illite-quartz alteration (Fig. 4.1). Unlike the quartz veins from the first style of mineralization, the base metal-rich veins have a wide range of orientations (Rohrlach & Fredericksen, 2008, unpublished data). The thickness of the mineralized zones are only a few meters to a few tens of meters thick. Bonanza Au grades peak at 240 ppm Au and 12% Zn (Rohrlach & Fredericksen, 2008, unpublished data).

Hydrothermal alteration is pervasive in the host rocks at Kay Tanda especially in the mineralized zones. Surface alteration is widespread and extends to the northeast and southwest of the deposit. Alteration is also continuous towards the northwest and is covered by younger post-mineralization rocks (Fig. 4.1). The rocks at the surface of the deposit are primarily altered by illite ± quartz ± smectite ± kaolinite alteration, with small areas affected by quartz ± pyrophyllite ± dickite/kaolinite ± diaspore alteration associated with silicification (Fig. 4.1). At deeper levels, chlorite-illite-quartz alteration is more common (Fig. 4.1). Epidote-calcite-chlorite alteration is prevalent in areas proximal to the Dacite Porphyry Intrusives and around the periphery of the deposit (Fig. 4.1).

4.4 Alteration and mineralization stages

Rohrlach and Fredericksen (2008) compiled a database of the number of crosscutting occurrences among veins and breccias from different mineralization stages. Crosscutting relationships were also observed among some of the stages during the core logging conducted in this study. This paragenetic study which was based on the documented number of crosscutting relationships resulted into six identified mineralization stages in Kay Tanda. The Stages 1 and 2 characterize the shallow Au-Ag epithermal mineralization while the Stages 3 to 6 comprise the deep base metal (Zn, Pb, Cu) with bonanza-grade Au mineralization. Because of the limited structural data of the veins and hydrothermal breccias observed in this study, the extent and continuity of the veins and hydrothermal breccias per mineralization stage cannot be projected to the surface. Instead, a sample location map is provided to show the spatial distribution of the observed veins and hydrothermal breccias per mineralization stage (Fig. 4.2A-F). The collar coordinates, length, depth, azimuth, and dip of the drill holes examined in this study are listed in Appendix A. A drill hole location map is also provided in Appendix A.

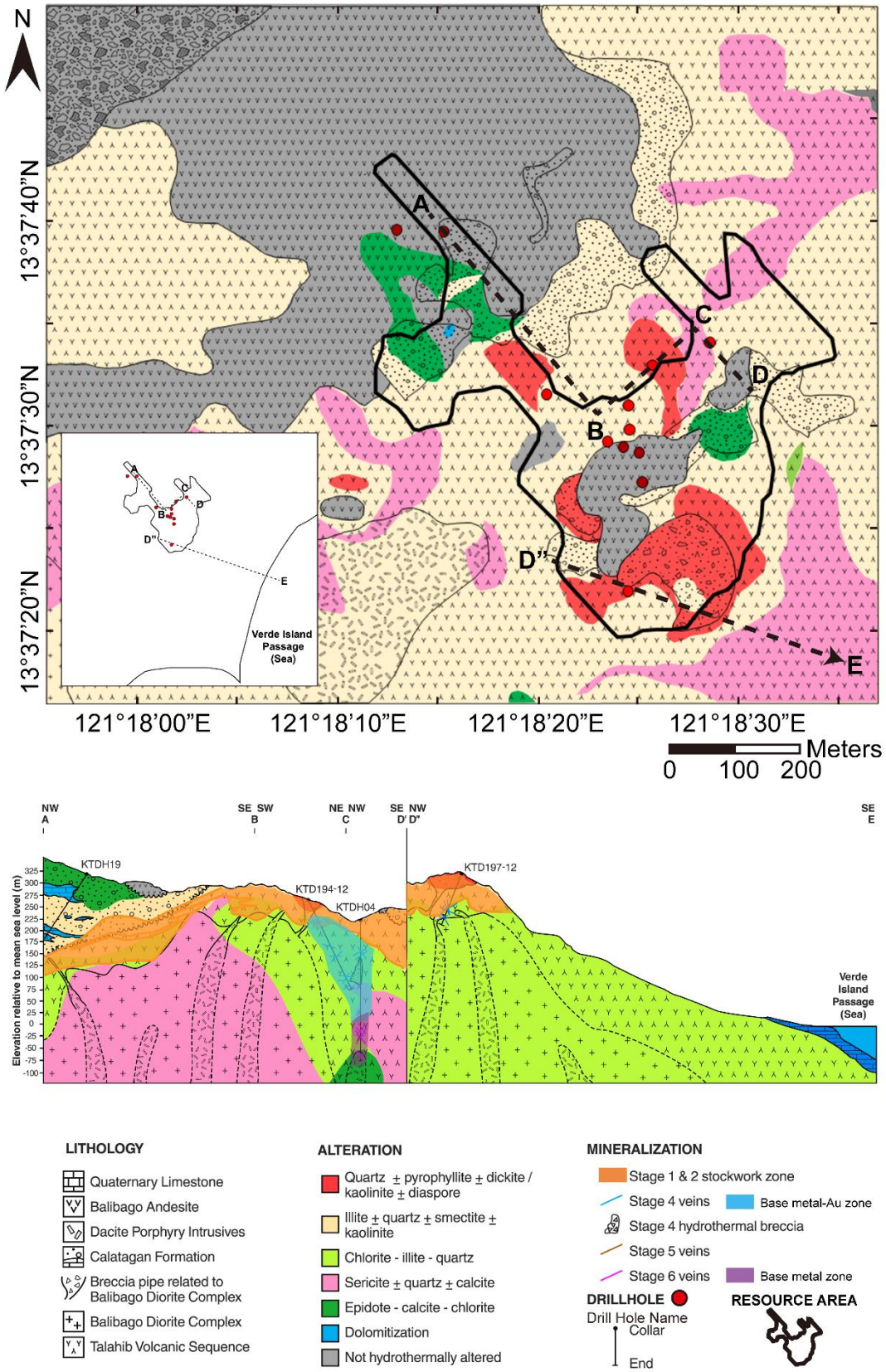

Fig. 4.1 Geologic map and representative composite cross section of Kay Tanda showing the relationships among lithologic units, alteration, and mineralized areas. The composite cross section traverses through points A-B-C-D and D"-E. Inset shows the location of Kay Tanda with respect to the Verde Island Passage and the extent of a composite cross section towards the sea. Map and cross section were modified from MRL Gold Philippines, Inc. (unpublished).

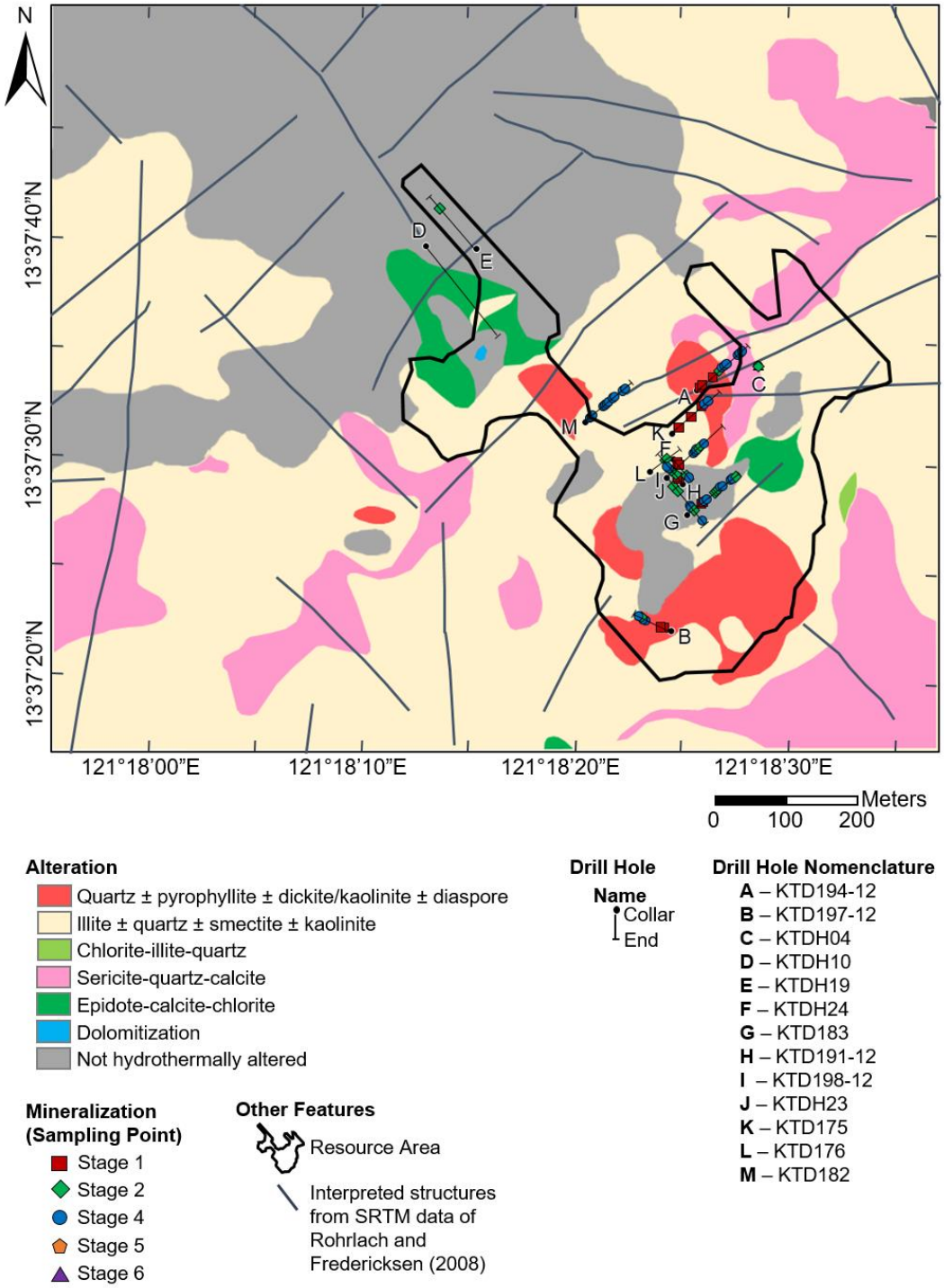

Fig. 4.2 (A) Sample location map of all mineralized samples (veins and hydrothermal breccias per mineralization stage) collected from the selected drill holes in Kay Tanda. The map aims to show the spatial distribution of the observed mineralized samples per mineralization stage. Drill hole KTDH04 is a vertical drill hole so the observed veins and hydrothermal breccias from Stages 2, 4, 5 and 6 coincide in a single point. Map was modified from MRL Gold Philippines, Inc. (unpublished).

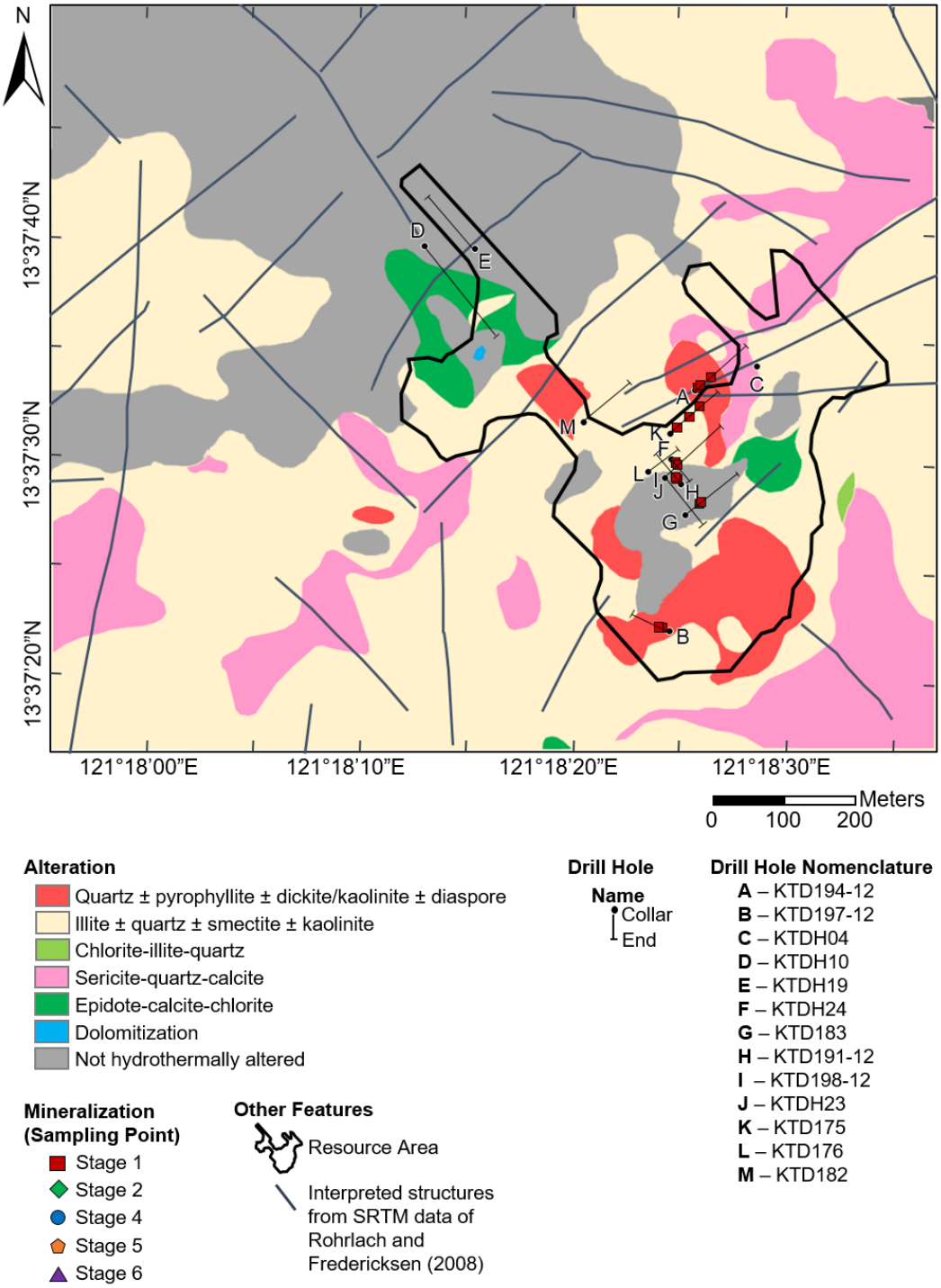

Fig. 4.2 (B) Sample location map of all Stage 1 samples collected from the selected drill holes in Kay Tanda. Most of the Stage 1 samples were observed at the shallower levels of the drill holes. Map was modified from MRL Gold Philippines, Inc. (unpublished).

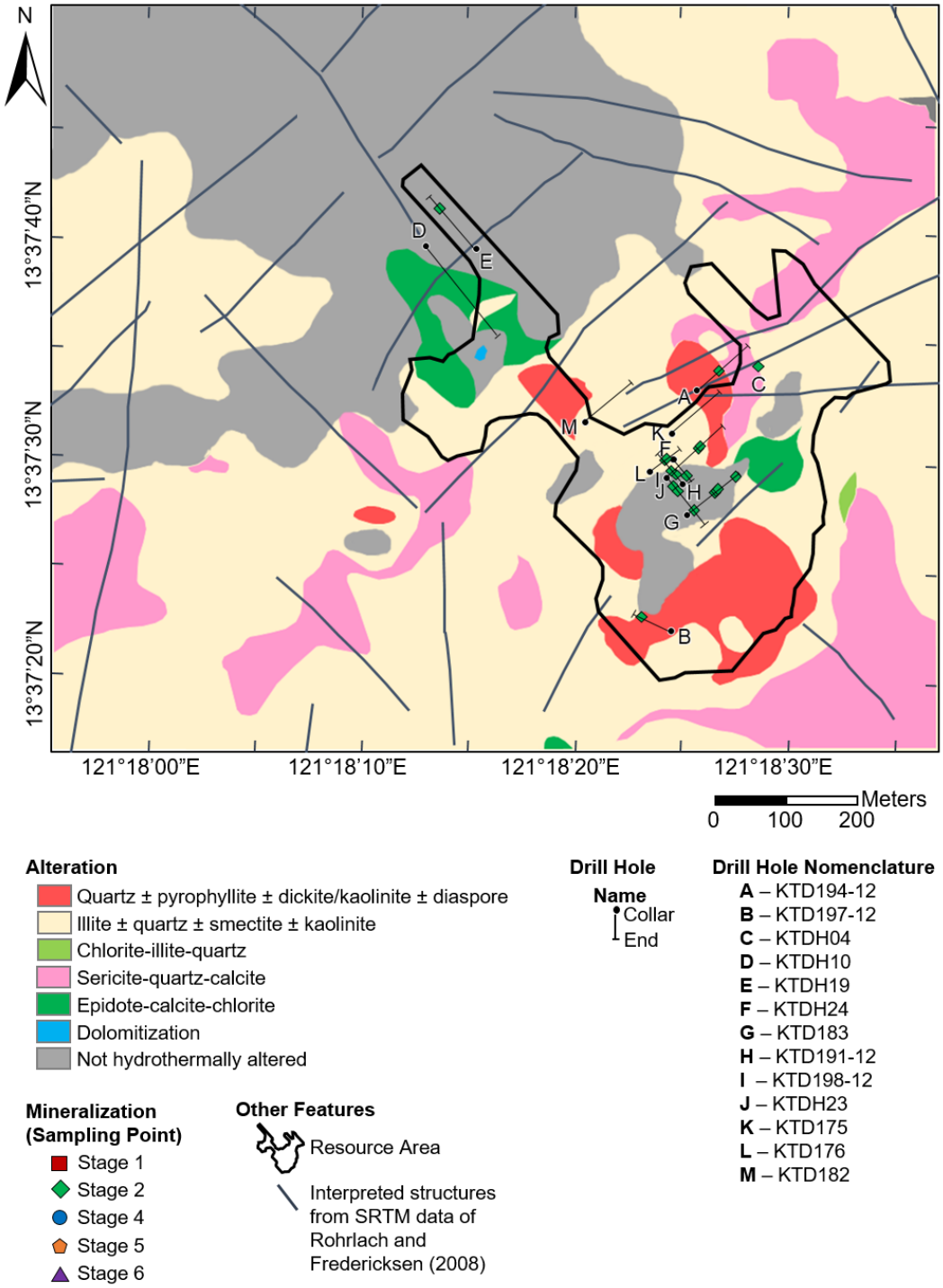

Fig. 4.2 (C) Sample location map of all Stage 2 samples collected from the selected drill holes in Kay Tanda. Most of the Stage 2 samples were observed at the shallower levels of the drill holes, though there were some samples collected from deeper levels. Map was modified from MRL Gold Philippines, Inc. (unpublished).

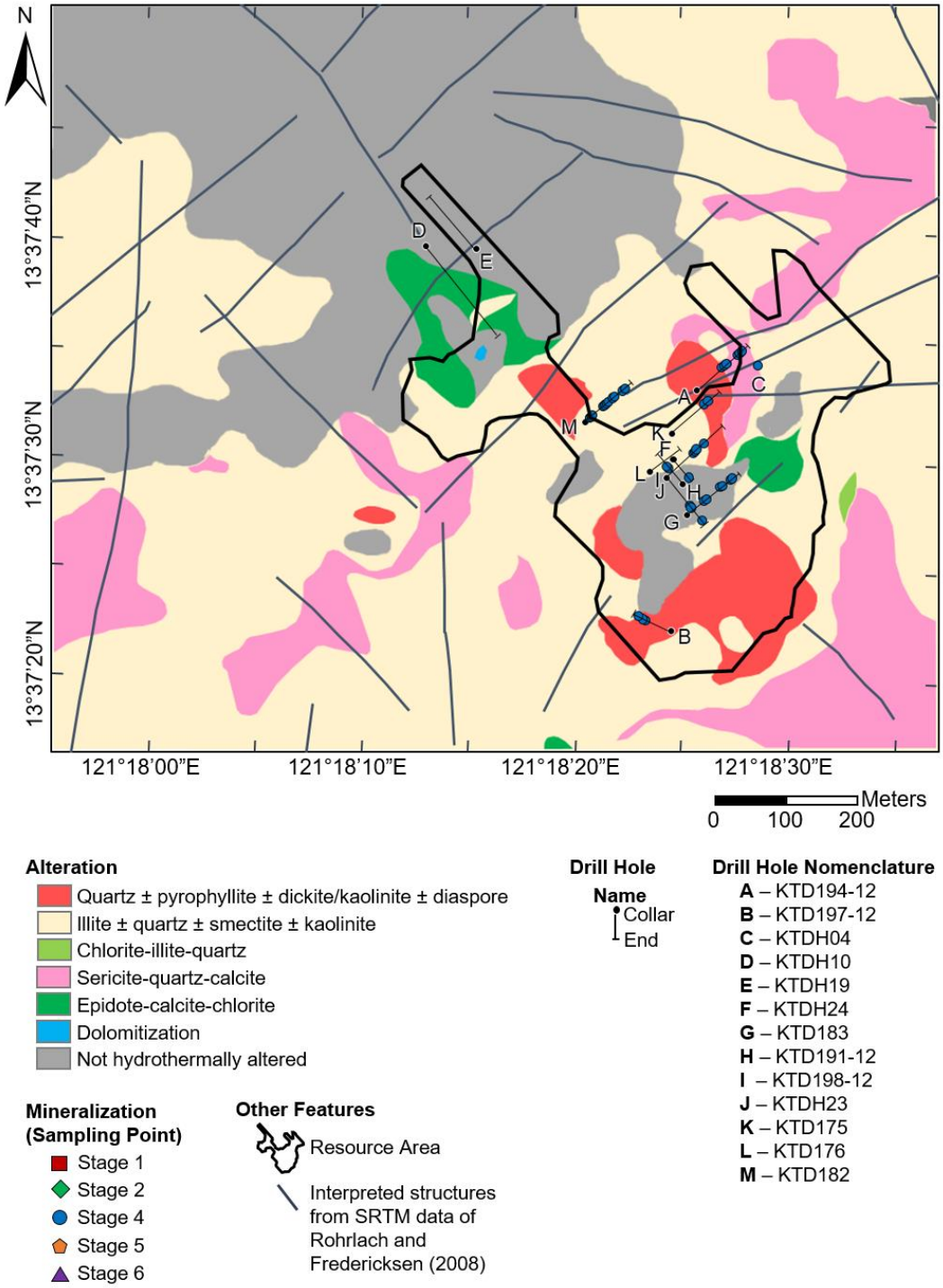

Fig. 4.2 (D) Sample location map of all Stage 4 samples collected from the selected drill holes in Kay Tanda. Most of the Stage 4 samples were observed at the deeper levels of the drill holes though some were found crosscutting shallow Stage 2 veins. Map was modified from MRL Gold Philippines, Inc. (unpublished).

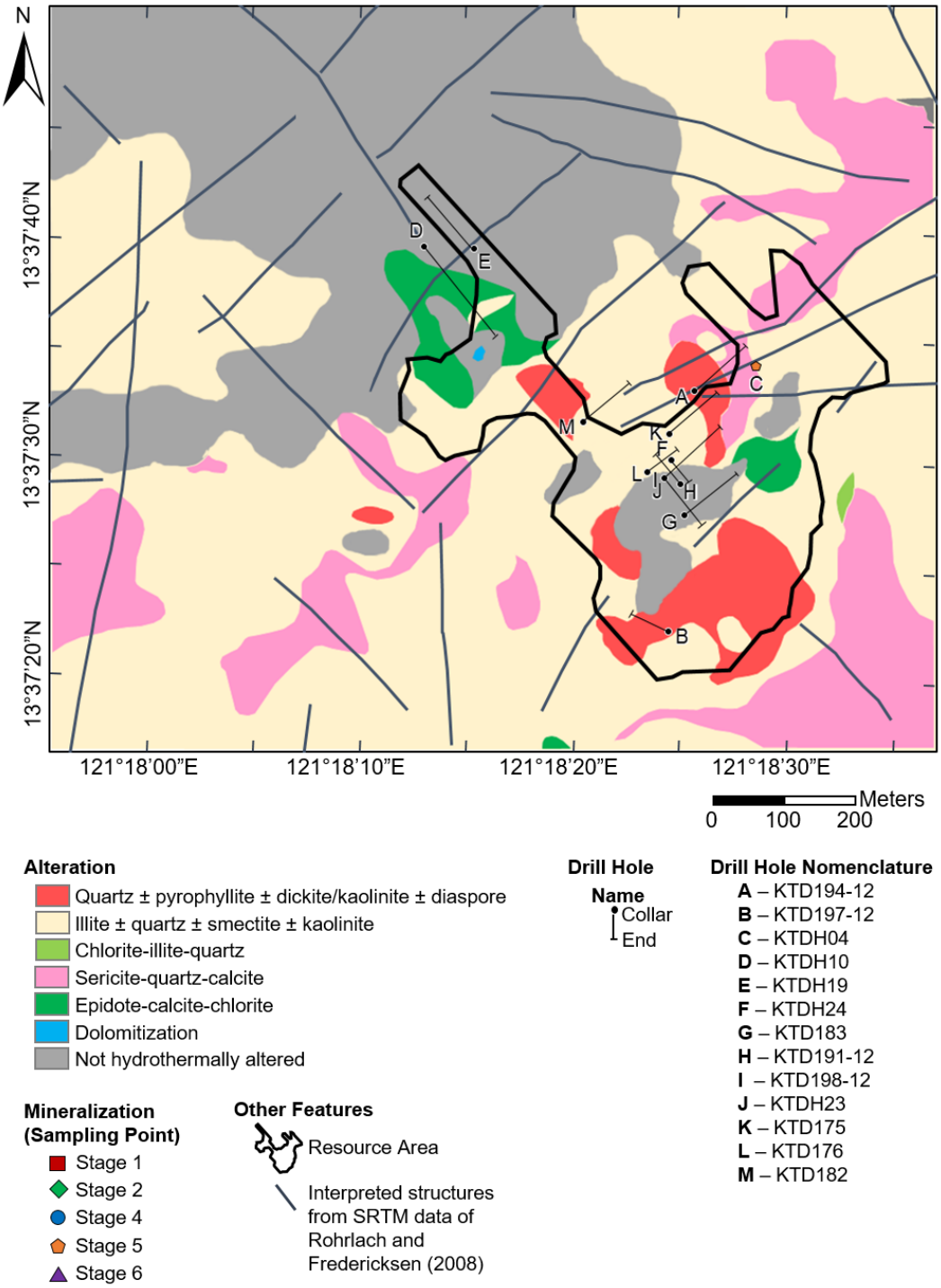

Fig. 4.2 (E) Sample location map of all Stage 5 samples collected from the selected drill holes in Kay Tanda. Stage 5 samples were observed at the deeper levels of KTDH04. Map was modified from MRL Gold Philippines, Inc. (unpublished).

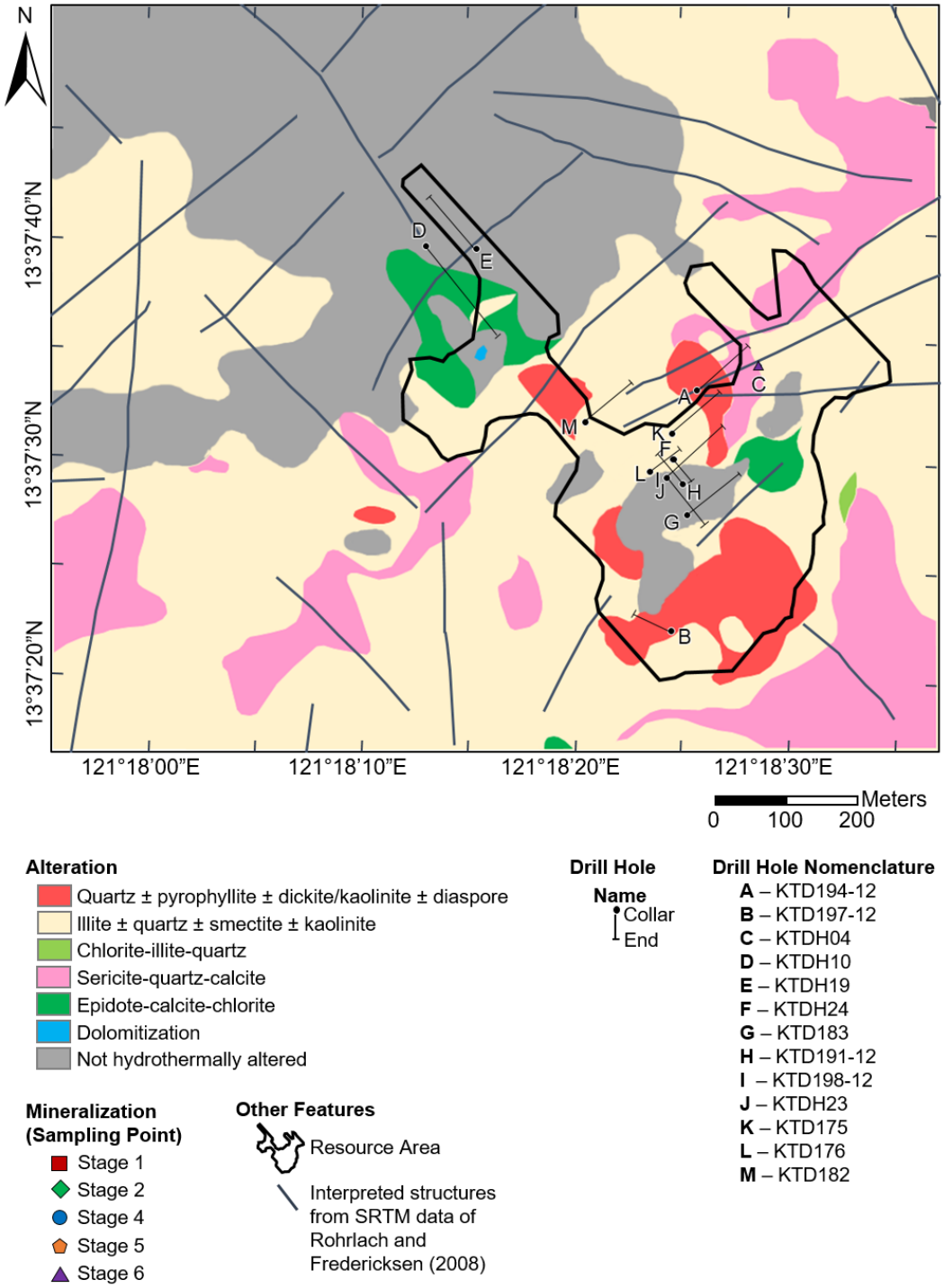

Fig. 4.2 (F) Sample location map of all Stage 6 samples collected from the selected drill holes in Kay Tanda. Stage 6 samples were observed at the deeper levels of KTDH04. Map was modified from MRL Gold Philippines, Inc. (unpublished).

4.4.1 Stage 1

The first epithermal event documented in Kay Tanda is the quartz ± pyrophyllite ± dickite/kaolinite ± diaspore alteration affecting discrete patches of volcanic rocks on the surface of the deposit and the breccias associated with the emplacement of the Balibago Intrusive Complex (Fig. 4.1, 4.2B, 4.3A-C). These altered areas are approximately a few tens of meters across and may penetrate up to a few tens of meters below the present-day surface (Fig. 4.1). Rock textures are often obliterated (Fig. 4.3A) although some host rocks show relict porphyritic texture where vugs after leached original phenocrysts were filled by diaspore and acicular pyrophyllite crystals (Fig. 4.3B-C). XRD analysis of altered host rocks confirmed the presence of pyrophyllite, kaolinite/dickite, and diaspore.

Au-Ag-bearing crustiform and colloform quartz veins were found cutting rocks affected by quartz ± pyrophyllite ± dickite/kaolinite ± diaspore alteration (Fig. 4.3D-I). Quartz crystals observed in quartz veins exhibit mosaic, flamboyant and feathery textures which were formed from the recrystallization of quartz (Fig. 4.3E, H). The timing of the formation of these veins with respect to the alteration is still uncertain but the occurrence of trace amounts of diaspore, pyrophyllite and illite crystals in the interstices between quartz crystals (Fig. 4.3F) may indicate that these veins are associated with the quartz ± pyrophyllite ± dickite/kaolinite ± diaspore alteration. These veins also contain trace amounts of euhedral to anhedral pyrite and chalcopyrite partially altered to covellite. (Fig. 4.3I). The Au grades are typically less than 1 to about 5 ppm with some sections reaching more than 100 ppm Au due to supergene enrichment (Rohrlach & Fredericksen, 2008, unpublished data). Native gold/electrum crystals were not observed in the collected quartz veins. Oxidation is also prevalent in this stage and some rocks are also cut by jarosite veins.

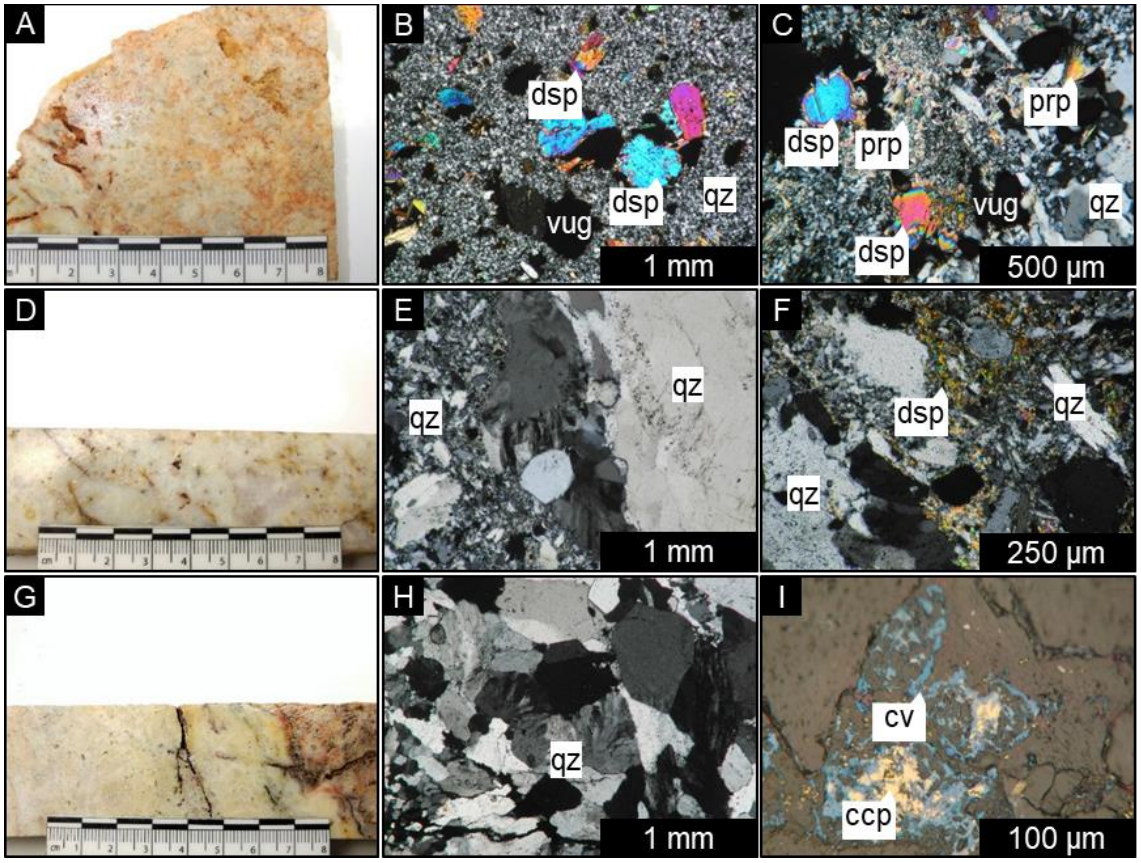

Fig. 4.3 Representative samples and corresponding photomicrographs of Stage 1 mineralization. (A-C) Quartz ± pyrophyllite ± dickite/kaolinite ± diaspore – altered rock showing vug-filling pyrophyllite and diaspore (Sample: KTD194-12 15.55m, A02). (D-F) Stage 1 quartz vein showing flamboyant to feathery quartz and diaspore in between quartz interstices (Sample: KTDH24 42.80m, F11). (G-I) Stage 2 vein showing flamboyant quartz and chalcopyrite altering to covellite (Sample: KTDH24 9.20m, F02). Abbreviations: ccp – chalcopyrite, cv – covellite, dsp – diaspore, prp – pyrophyllite, qz – quartz.

4.4.2 Stage 2

The development of Au-Ag-bearing quartz stockworks continued and became more extensive in Kay Tanda. The Stage 2 mineralization represents the majority of the Au-Ag epithermal mineralization. It is characterized by extensive Au-Ag-bearing quartz stockworks consisting of banded crustiform to colloform quartz veins, quartz-pyrite veins, pyrite stringers and silicified hydrothermal breccias associated with pervasive illite ± quartz ± smectite ± kaolinite alteration (Fig. 4.4A-L). According to the crosscutting database by Rohrlach and Fredericksen (2008), there were more than 160 documented crosscutting cases among the mentioned veins in the stockwork zone and some of them were observed during the core logging conducted in this study.

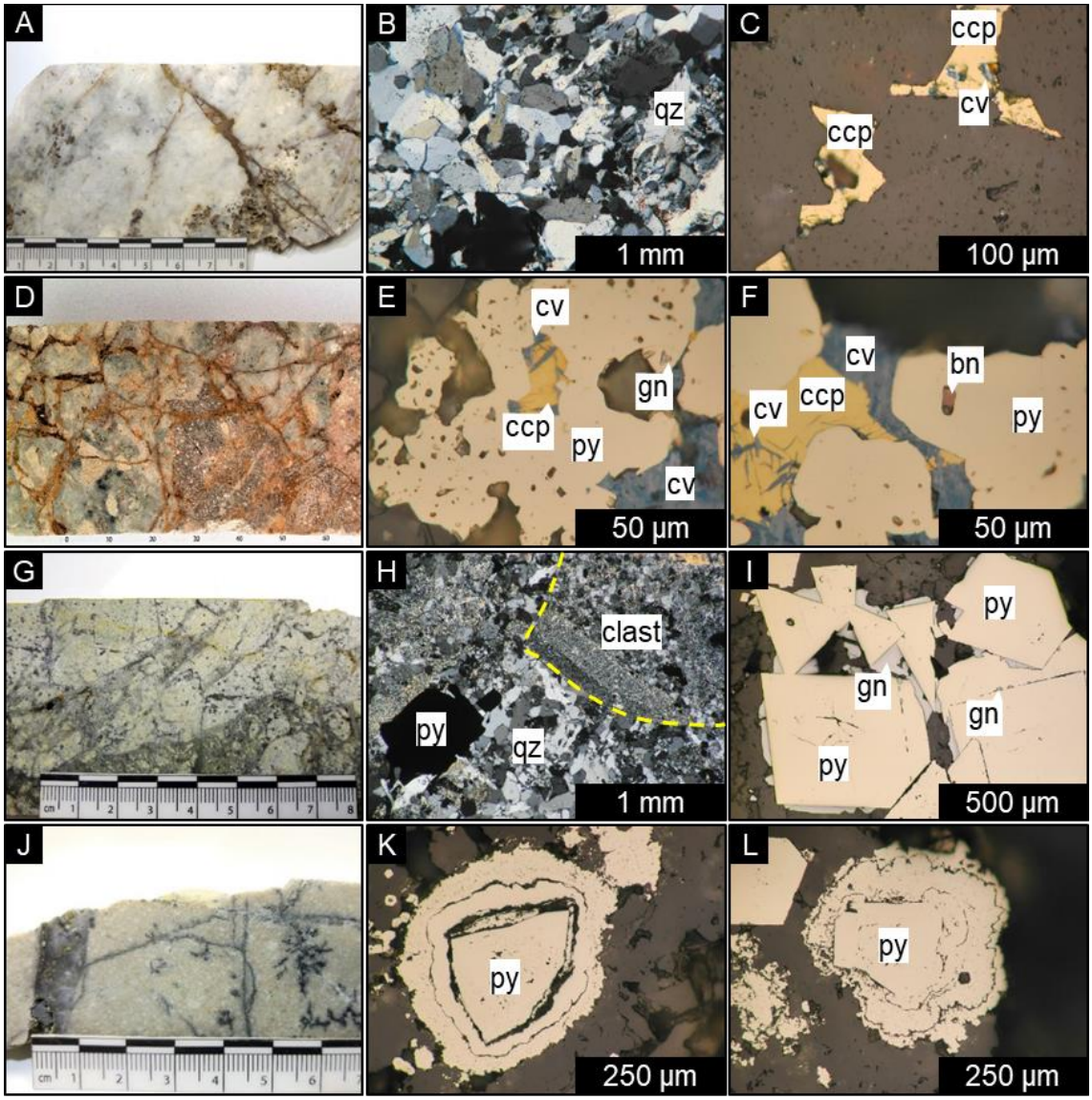

Fig. 4.4 Representative samples and corresponding photomicrographs of Stage 2 mineralization. (A-C) Stage 2 vein showing mosaic quartz and chalcopyrite altering to covellite (Sample: KTDH23 53.50m, J05). (D-F) Stage 2 hydrothermal breccia containing chalcopyrite altering to covellite and pyrite containing inclusions of galena and bornite (Sample: KTDH23 54.20m, J07). (G-I) Stage 2 hydrothermal breccia showing illite-altered clasts, quartz-rich matrix and euhedral pyrite crystals overgrown by galena (Sample: KTD194-12 86.55m, A09). (J-L) Stage 2 quartz-pyrite vein and pyrite stringers showing multiple growth zones in pyrite crystals (KTDH04 16.30m, C01). Abbreviations: bn – bornite, ccp – chalcopyrite, cv – covellite, gn – galena, py – pyrite, qz – quartz.

The thickness of Stage 2 quartz veins varies from a few cm to almost a meter. Chalcedonic quartz veins are common at shallower levels and become progressively coarse-grained at deeper levels (Fig. 4.4A). Common quartz textures include mosaic, flamboyant and feathery textures (Fig. 4.4B). The hydrothermal breccias contain altered and angular clasts surrounded by fracture-filling quartz and sulfides. Clast-matrix proportions vary (Fig. 4.4D, G). The Stage 2 veins and

hydrothermal breccias also contain slightly higher sulfide content than that of the Stage 1. Pyrite and chalcopyrite occur as infill between quartz crystals (Fig. 4.4C, E, F, I, K, L). Chalcopyrite is usually partly altered to covellite (Fig. 4.4C, E, F). Galena and bornite may also occur as inclusions in pyrite (Fig. 4.4E-F). Galena also occurs as overgrowths around euhedral pyrite (Fig. 4.4I). Some pyrite crystals show growth zones with slightly elevated As content along the outer rims (Fig. 4.4K-L). The Au grades are typically around less than 1 to 10 ppm (Rohrlach & Fredericksen, 2008, unpublished data) and Ag grades are usually elevated in samples with galena. The veins are typically oxidized and are cut by jarosite veins especially at shallower levels.

Illite ± quartz ± smectite ± kaolinite alteration is the most dominant alteration exposed in Kay Tanda. The mineral assemblage is dominated by illite with subordinate amounts of kaolinite and/or smectite. Plagioclase phenocrysts of volcanic rocks were altered to illite while the groundmass was altered to illite and secondary quartz (Fig. 4.4H).

4.4.3 Stage 3

The late-stage base metal mineralization in Kay Tanda commenced with the emplacement of the Stage 3 carbonate-base metal sulfide veins. Though these veins were not observed during this study, this stage of mineralization was documented in company reports (Rohrlach & Fredericksen, 2008, unpublished data). There were nine documented crosscutting cases of Stage 3 carbonate veins on the Stage 2 quartz veins (Rohrlach & Fredericksen, 2008, unpublished data). This stage contains minor base metal mineralization composed of small amounts of sphalerite, galena, chalcopyrite and pyrite in carbonate veins.

4.4.4 Stage 4

The main base metal mineralization in Kay Tanda is hosted by the Stage 4 veins (Fig. 4.5A-F) and hydrothermal breccias (Fig. 4.5G-L) associated with chlorite-illite-quartz alteration.

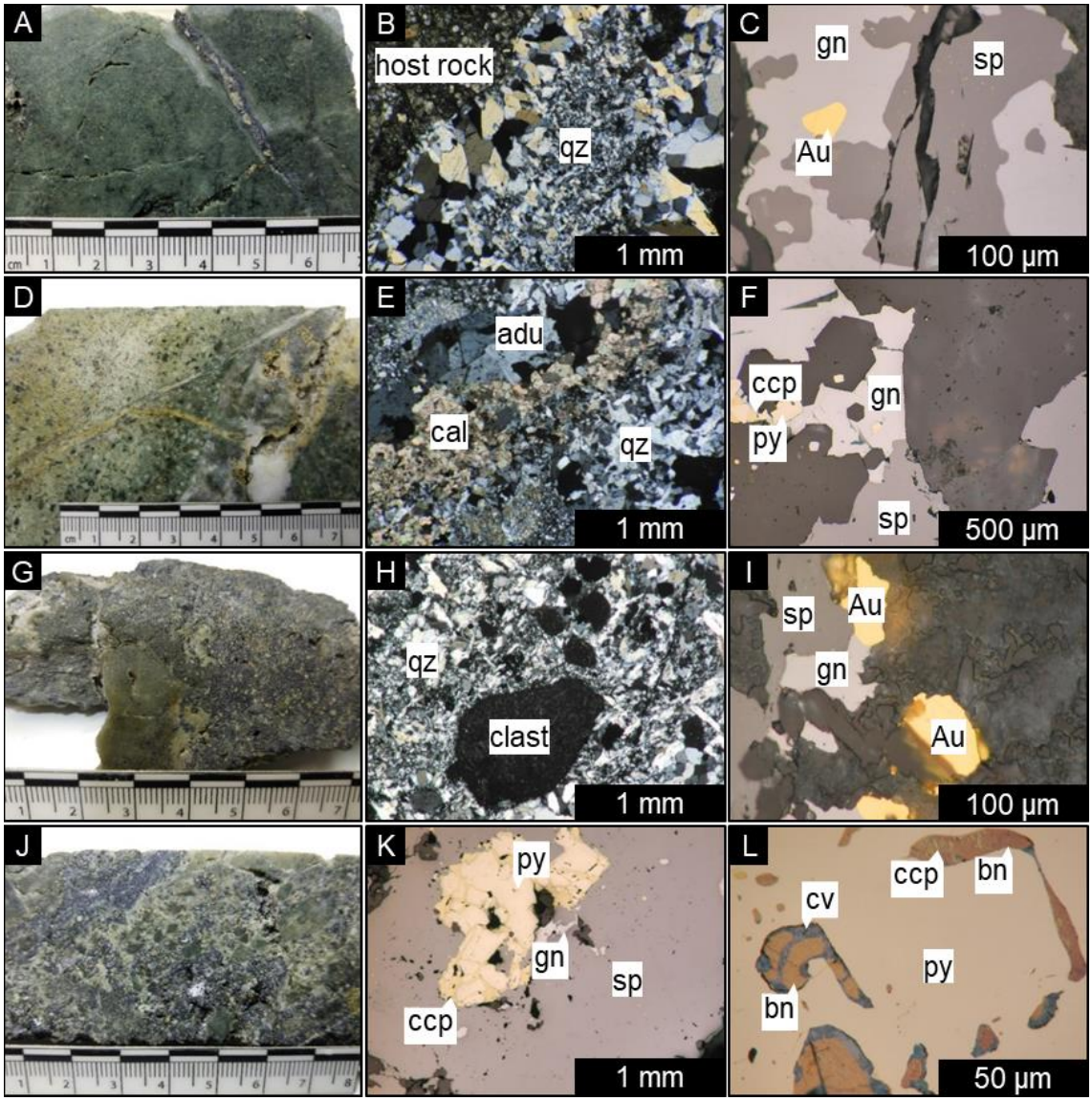

Fig. 4.5 Representative samples and corresponding photomicrographs of Stage 4 mineralization. (A-C) Quartz-base metal sulfide vein cutting chlorite-quartz-altered host rock, native Au intergrown with the sulfides (Sample: KTDH04 85.30m, C11). (D-F) Quartz ± adularia ± calcite vein showing rhombic adularia and base metal sulfides (Sample: KTD194-12 110.45m, A13). (G-I) Hydrothermal breccia showing chlorite-altered clasts surrounded by mosaic to saccharoidal quartz, base metal sulfides and native gold (Sample: KTDH04 101.40m, C20). (J-K) Hydrothermal breccia sample containing fractured pyrite with interstices filled and replaced by chalcopyrite (Sample: KTDH04 93.50m, C16). (L) Pyrite crystal with chalcopyrite inclusion and bornite inclusions with chalcopyrite exsolution, both altering to covellite (Sample: KTDH04 68.30m, C06). Abbreviations: adu – adularia, Au – native gold, bn – bornite, cal – calcite, ccp – chalcopyrite, cv – covellite, gn – galena, hbx – hydrothermal breccia, py – pyrite, qz – quartz, sp – sphalerite.

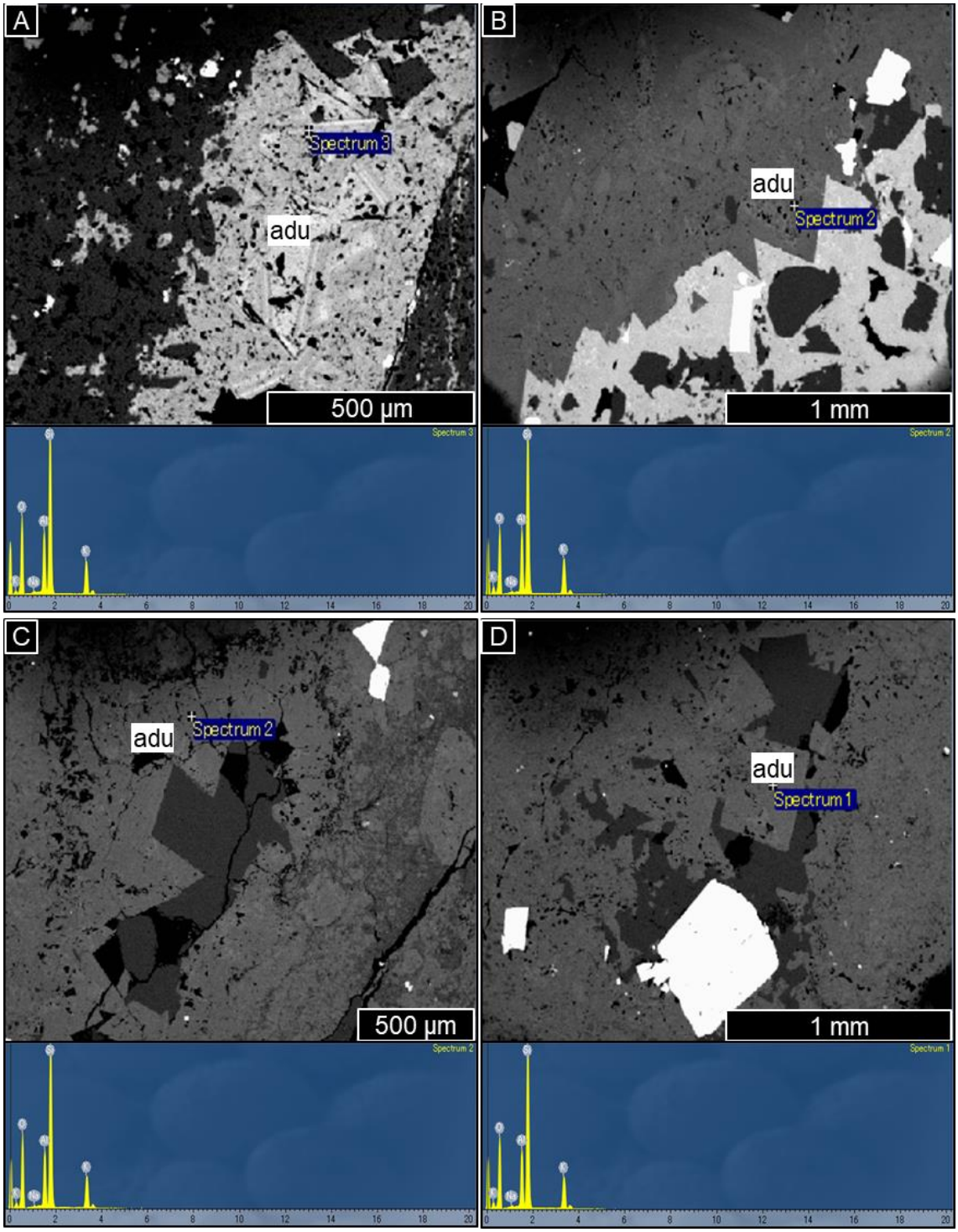

Fig. 4.6 Backscattered electron image (BEI) of rhombic adularia (adu) found in Stage 4 veins. (A) Sample: KTD194-12 122.30m, A14. (B) Sample: KTD194-12 179.25m, A21. (C) Sample: KTD194-12 204.90m, A25.

Company reports (Rohrlach & Fredericksen, 2008, unpublished data) documented 60 crosscutting cases of Stage 4 veins on Stage 2 quartz veins and 2 cases on Stage 3 carbonate veins. Some were also observed during the core logging conducted in this study. The Stage 4 veins and hydrothermal breccias are dominated by quartz and contain base metal sulfides such as sphalerite, galena, and chalcopyrite in decreasing order of abundance. Pyrite is also a major sulfide. Bonanza-grade Au intercepts are found in a hydrothermal breccia zone intercepted at drill hole KTDH04 (Fig. 4.1, 4.2D) (Rohrlach & Fredericksen, 2008, unpublished data).

The Stage 4 veins are primarily composed of quartz (Fig. 4.5B, E). Adularia and calcite sometimes occur along the margins of the quartz veins (Fig. 4.5E). Some adularia and calcite veins crosscut the Stage 4 quartz veins. Quartz crystals are typically coarse-grained and exhibit mosaic (Fig. 4.5B, E), feathery and flamboyant textures while adularia crystals are usually rhombic (Fig. 4.5E). The rhombic shape of adularia was observed to be more pronounced in backscattered electron images (Fig. 4.6). Ore minerals either occur scattered in quartz veins or as centerlines (Fig. 4.5A, D). Based on the ore mineral assemblage and their abundances, the Stage 4 veins are classified into 3 different types: (1) quartz ± adularia ± calcite veins with sphalerite + galena + pyrite > chalcopyrite ± native gold, (2) quartz ± adularia veins with chalcopyrite > sphalerite + galena + pyrite and (3) quartz veins with pyrite > chalcopyrite ± sphalerite ± galena.

The Stage 4 hydrothermal breccias are best documented in a hydrothermal breccia zone intercepted by KTDH04 (Fig. 4.1), a vertical drill hole located at the eastern part of the deposit. This zone was intersected around 90 m deep from the present-day surface. The breccia zone is discontinuous but the base metal sulfide-rich zone is approximately 50 m thick. Drillings around the KTDH04 hole were done to delineate the continuity and lateral extent of the hydrothermal breccia zone but was not intersected (Mr. Jun Marius Aguirre, January 2017, personal communication). Because of this, the hydrothermal breccia zone was interpreted as a steep breccia pipe (Rohrlach & Fredericksen, 2008, unpublished data; Mr. Jun Marius Aguirre, January 2017, personal communication). Multiple episodes of overprinting hydrothermal breccias were found in some intervals. Different hydrothermal breccias were observed based on clast-matrix proportions and gangue-ore mineral proportions. The clasts of the hydrothermal breccias are the

volcaniclastic host rocks that were extremely altered to chlorite and secondary quartz (Fig. 4.5H). Textures are usually completely obliterated although some clasts still show relict porphyritic or fragmented textures. These clasts often contain disseminated euhedral pyrite crystals. The matrix is composed of hydrothermal minerals such as quartz and sulfide minerals. Quartz is the dominant gangue mineral in the matrix. It usually exhibits mosaic and saccharoidal textures (Fig. 4.5H). Drusy prismatic quartz crystals also occur around altered clasts. Sphalerite is the dominant base metal sulfide. It typically exhibits chalcopyrite disease and is sometimes rimmed by chalcopyrite. It also commonly hosts fractured pyrite crystals (Fig. 4.5K). Galena is often intergrown with sphalerite (Fig. 4.5I). The Stage 4 pyrites in hydrothermal breccias are distinctly fractured. The edges are usually rounded and the interstices were filled by chalcopyrite which may indicate replacement of pyrite by chalcopyrite (Fig. 4.5K). The fractured pyrite crystals also show abundant chalcopyrite and bornite inclusions with exsolution lamellae of chalcopyrite. Both the inclusions and the exsolution lamellae were partially altered to covellite (Fig. 4.5L). Native gold is associated with the base metal sulfides and also occurs as free native gold crystals filling interstices between quartz crystals (Fig. 4.5I) or as inclusions in the sulfides.

4.4.5 Stage 5

The Stage 5 veins are composed of epidote and carbonate (Fig. 4.7A-E). Crosscutting relationships with the earlier Stage 4 veins and the later Stage 6 anhydrite-gypsum veins were observed in some intervals in drill hole KTDH04. These veins are commonly found at deeper levels (approximately 200 m below the surface) crosscutting the top portions of Dacite Porphyry Intrusives. These veins a few millimeters thick and are commonly pinkish tan in color. XRD results show the presence of both calcite and dolomite in the veins.

These veins are mainly associated with epidote-calcite-chlorite alteration. Plagioclase phenocrysts were commonly altered to calcite and epidote while hornblende crystals were altered to epidote and chlorite. Quartz phenocrysts remained unaltered. The groundmass was also altered to calcite, epidote and secondary quartz (Fig. 4.7F).

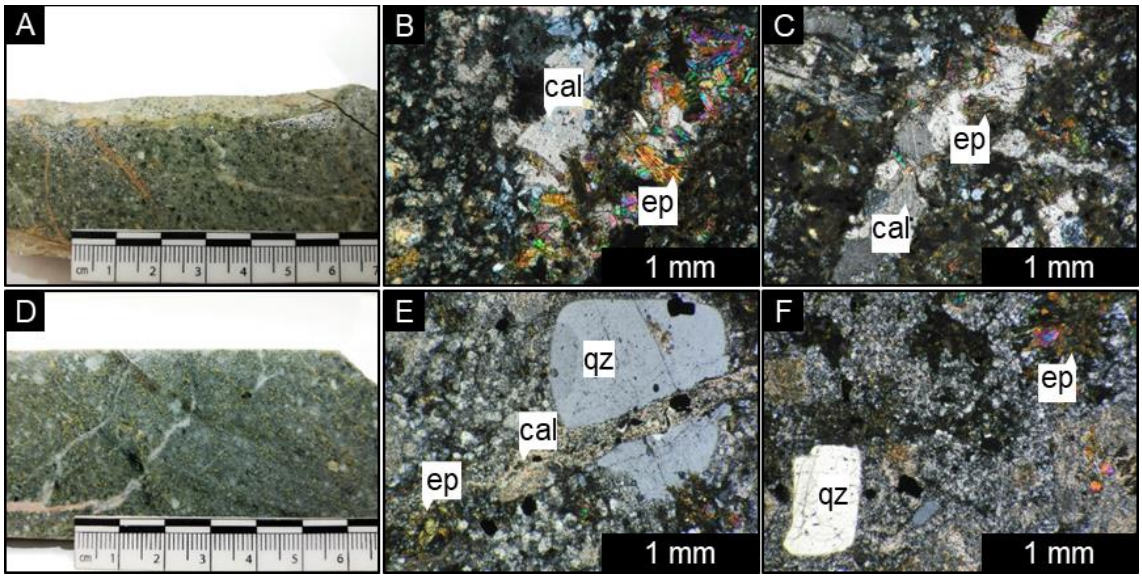

Fig. 4.7 Representative samples and corresponding photomicrographs of Stage 5 mineralization. (A-C) Stage 5 epidote-calcite vein cut by Stage 6 anhydrite-gypsum vein (Sample: KTDH04 263.64m, C49). (D-F) Stage 5 epidote-calcite vein in propylitic-altered dacite porphyry (KTDH04 302.90m, C55). Abbreviations: cal – calcite, ep – epidote, qz – quartz.

4.4.6 Stage 6

The last stage of base metal mineralization is hosted in the Stage 6 anhydrite-gypsum veins (Fig. 4.8A-C) and hydrothermal breccias (Fig. 4.8D-F). These veins are commonly found at deeper levels of the deposit. Rohrlach and Fredericksen (2008) documented 20 crosscutting cases of Stage 6 anhydrite-gypsum veins on Stage 2 quartz veins, 1 on Stage 3 carbonate veins and 3 on Stage 4 quartz-base metal veins, while 2 crosscutting cases on Stage 5 epidote-carbonate veins were observed in the core logging conducted in this study.

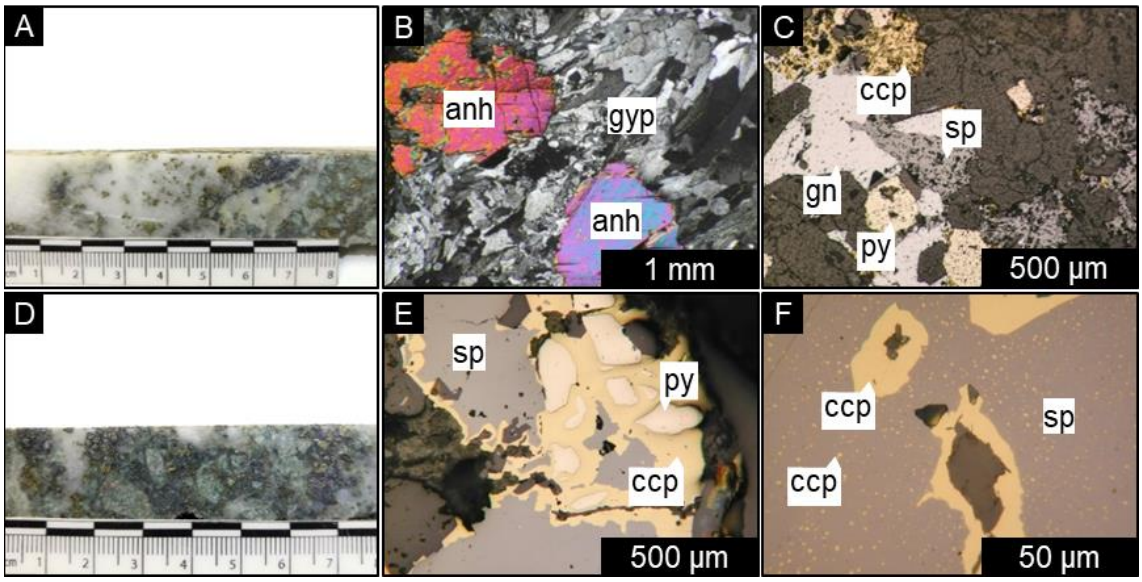

Fig 4.8 Representative samples and corresponding photomicrographs of Stage 6 mineralization. (A-C) Stage 6 vein composed of anhydrite being hydrated to gypsum and also contains base metal sulfides (Sample: KTDH04 228.60m, C42). (D-F) Stage 6 hydrothermal breccia showing fractured pyrite being replaced by chalcopyrite and sphalerite being replaced by chalcopyrite (Sample: KTDH04 229.80m, C43). Abbreviations: anh – anhydrite, ccp – chalcopyrite, gn – galena, gp – gypsum, py – pyrite, sp – sphalerite.

Coarse-grained anhydrite crystals show jagged outlines and are surrounded by finer gypsum blades. Anhydrite crystals were replaced by gypsum indicating transformation to gypsum by hydration (Fig. 4.8B). Some gypsum crystals recrystallized to form coarser crystals. The base metal sulfides are sphalerite, galena and chalcopyrite in decreasing order of abundance (Fig. 4.8C, E, F). They occur as infill between anhydrite and gypsum. Chalcopyrite typically surrounds sphalerite and galena crystals and also occurs as chalcopyrite disease in sphalerite (Fig. 4.8E, F). Pyrite is also a major sulfide in this stage. Pyrite crystals were fractured and the interstices were filled with chalcopyrite (Fig. 4.8E). Unlike the Stage 4 veins and hydrothermal breccias, the Stage 6 veins and hydrothermal breccias do not contain significant amounts of Au and Ag. These veins are associated with chlorite-illite-quartz-altered and epidote-calcite-chlorite-altered rocks but company reports described that the Stage 6 veins were surrounded by sericitic halos (Rohrlach & Fredericksen, 2008, unpublished data).

4.5 Mineralization age from K-Ar dating

Two illite samples (Fig. 4.9) from halos surrounding mineralized Stage 2 quartz veins cutting through argillic-altered volcanic rocks from Talahib Volcanic Sequence were collected for K-Ar dating. The K-Ar age determined for the samples representing the mineralization of Kay Tanda yielded 5.9 ± 0.2 and 5.5 ± 0.2 Ma corresponding to Late Miocene (Table 4.1). The acquired age of the mineralization of the Kay Tanda deposit (Late Miocene) is well-constrained by the timing of the deposition of pre-mineralization host rocks, the Middle Miocene Talahib Volcanic Sequence and the lower members of the Late Miocene Calatagan Formation, and of the deposition of the post-mineralization Balibago Andesite, which is equivalent to the Pliocene Mataas na Gulod Volcanic Complex (Rohrlach & Fredericksen, 2008, unpublished data; MGB, 2010).

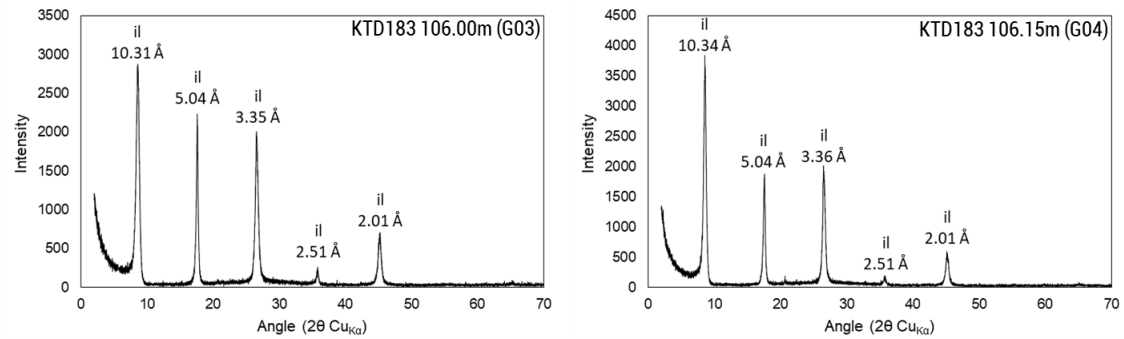

Fig. 4.9 XRD diffractograms of illite samples collected for K-Ar dating.

Table 4.1 K-Ar age determined for the samples representing the mineralization of Kay Tanda.

Sample ID	Sample description	Mineral	% K	^{40}Ar rad (nl/g)	% ^{40}Ar air	Age (Ma)	Error (1σ)
KTD183 106.00m (G03)	Stage 2 quartz vein with illite halo and cutting through volcanic rock	illite	6.80 6.78 6.79	1.421 1.423 1.422	48.9 41.8	5.5	0.2
KTD183 106.15m (G04)	Stage 2 quartz vein with illite halo and cutting through volcanic rock	illite	6.64 6.66 6.65	1.490 1.503 1.496	35.5 42.4	5.9	0.2

4.6 Discussion and conclusions

Based on the crosscutting database of Rohrlach & Fredericksen (2008) and some of the observed crosscutting relationships encountered during the core logging conducted in this study, there are two distinct styles of mineralization in Kay Tanda: (1) an early-stage extensive epithermal mineralization characterized by Au-Ag-bearing quartz stockworks consisting of crustiform to colloform quartz veins, quartz-pyrite veins, pyrite stringers and silicified hydrothermal breccias, and (2) a late-stage base metal (Zn, Pb, and Cu) epithermal mineralization with local bonanza-grade Au mineralization hosted in quartz ± adularia ± calcite veins, anhydrite-gypsum veins, and hydrothermal breccias. A summary of the paragenetic sequence of Kay Tanda is shown in Figure 4.10. The first stages of epithermal vein formation contain the bulk Au-Ag mineralization of the deposit despite its lower grade compared to the bonanza Au-grade encountered in the base-metal sulfide rich hydrothermal breccias because the vein formation was mapped over a wider area and volume of rock while the hydrothermal brecciation is localized and encountered only in one drill hole (KTDH04).

Based on the mineral assemblages and textures observed using microscopy, several interpretations about the mineralization of Kay Tanda can be made:

1. The precipitation of pyrophyllite and diaspore in the vugs of advanced argillic-altered rocks in Stage 1 indicates the passage of strongly acidic and silica undersaturated fluids. This is attributed to the emplacement of the Balibago Diorite Complex and its associated steep breccia pipes. Magmatic volatiles released from the intrusion passed through the permeable breccia pipes and condensed into the groundwater which formed highly acidic fluids (Arribas, 1995). This leached the host rocks, primarily the steep breccia pipes and the surrounding periphery.
2. Stage 1 quartz veining can be attributed to the passage of silica saturated fluids. This may explain the coexistence of diaspore and quartz in the vein especially along the contact of the Stage 1 quartz veins and the altered host rock.

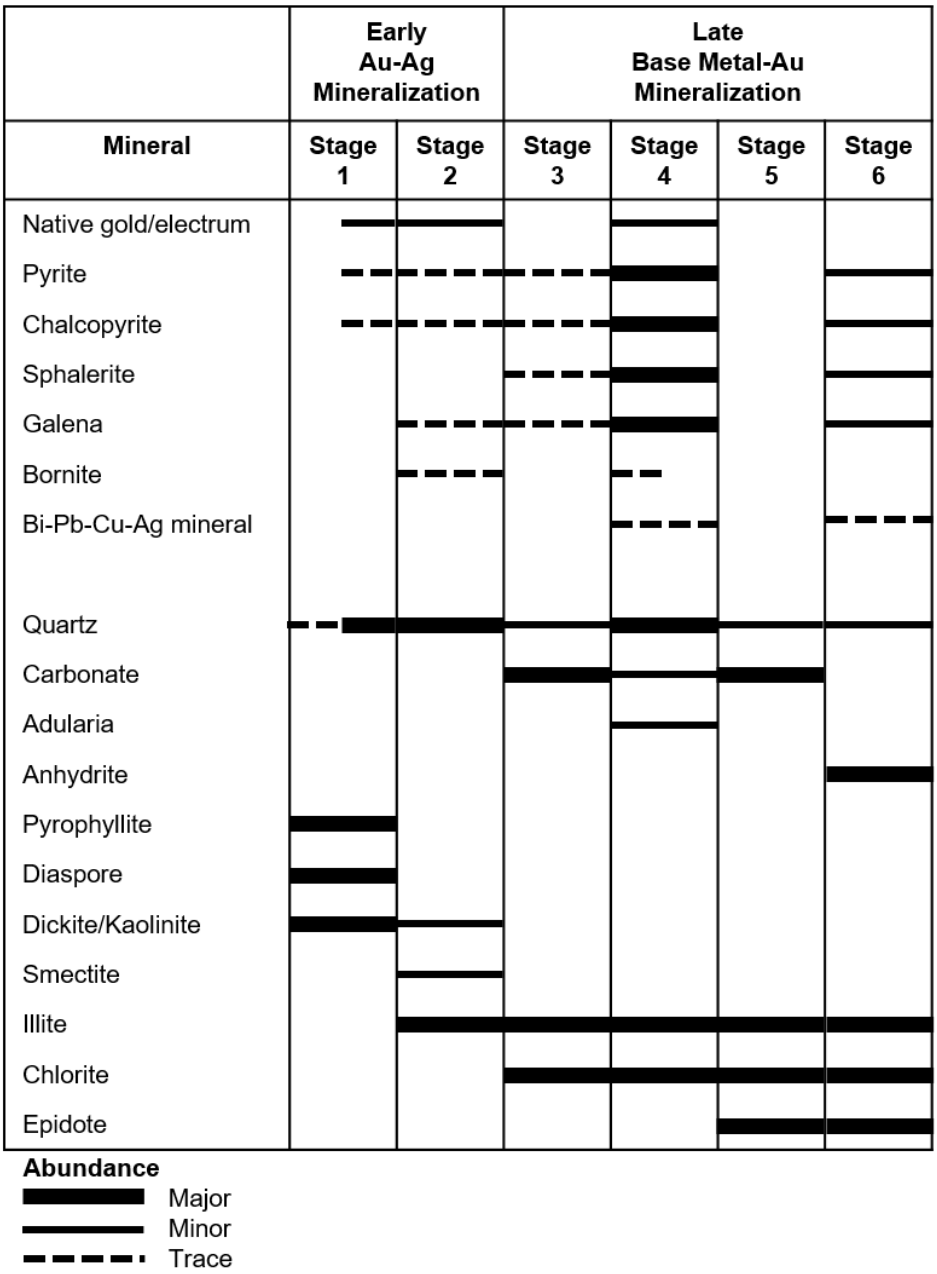

Fig. 4.10 Paragenesis of the mineralization and alteration in Kay Tanda. Stage 3 was not observed in the study but was documented in the company report (Rohrlach & Fredericksen, 2008, unpublished data).

3. The occurrence of pyrite with distinct growth zones with slightly different composition as the core in Stage 2 may indicate changes in the hydrothermal fluid composition and condition as the mineralization progressed.
4. Stage 2 veins containing trace amounts of galena (either as overgrowth around pyrite or inclusion in pyrite) correlates with elevations in Ag. This may indicate the presence of Ag in galena which will be confirmed in the succeeding chapter.

5. The presence of rhombic adularia in some Stage 4 veins indicate boiling conditions (Dong & Morrison, 1995). This may be the mechanism for the precipitation of gold and the base metal sulfides in this stage.
6. Stage 4 pyrite crystals often contain unaltered chalcopyrite inclusions, covellite-altered bornite inclusions and bornite with exsolution lamellae of chalcopyrite. The exsolution of chalcopyrite from bornite inclusions formed from the reaction of the host pyrite crystal and bornite solid solution occurring as inclusions as the temperature decreased (Craig & Scott, 1974). The latter is a texture indicative of high sulfidation conditions.
7. Stage 4 pyrite crystals are also fractured with interstices filled by chalcopyrite. The rounded edges of pyrite indicate replacement by chalcopyrite.
8. Stage 4 sphalerite crystals usually hosts smaller crystals of galena, and fractured pyrite replaced by chalcopyrite. This may indicate that sphalerite precipitated in a later time during this stage.
9. Gypsum is unlikely to form in a hydrothermal environment at temperatures above 70°C (Hardie, 1967). The Stage 6 gypsum-anhydrite veins clearly show hydration textures. The original anhydrite veins must have been transformed to gypsum during the circulation of meteoric fluids in the deeper levels of the deposit.
10. The changes in the alteration assemblages associated to each mineralization stage indicates that the pH of the hydrothermal fluids evolved from an acidic (Stage 1), to a slightly acidic (Stage 2), to a neutral pH fluid (Stages 3-6).

Based on the K-Ar dating of the illite samples collected from hydrothermally altered host rocks cut by quartz veins, the age of the mineralization is around 5.9 ± 0.2 Ma to 5.2 Ma ± 0.2 Ma (end of Late Miocene to start of Early Pliocene). This age fits well with the emplacement of the late Dacite Porphyry Intrusives which is estimated to be syn- to post-Calatagan Formation but pre-Balibago Andesite (Pliocene), a post mineralization lithologic unit.

CHAPTER 5

ORE MINERAL CHEMISTRY

5.1 Introduction

The extensive ore microscopy study conducted on representative samples from different mineralization stages in Kay Tanda revealed interesting ore textures that warrant further investigation. Some ore textures were found uniquely in certain mineralization stages, which raised questions about the changes in the conditions and the composition of the hydrothermal fluids throughout the evolution of the deposit. This chapter aims to elucidate the relationship between the ore mineral's major and minor element composition and their different ore textures to understand the characteristics of the hydrothermal fluids responsible for the formation of the deposit. The ore minerals analyzed were: (1) native gold and electrum, (2) sphalerite, which is the most common base metal sulfide in the deposit, (3) galena, whose occurrence is correlated to the elevations in Ag content in the company's assay data, and (4) pyrite, which is a ubiquitous sulfide in the deposit.

5.2 Methodology

The chemical composition of the ore minerals, specifically native gold and electrum, sphalerite, galena, and pyrite, were determined using a JEOL JXA-8800R electron probe microanalyzer (EPMA) at Akita University. Multiple points were analyzed in each target mineral in each sample and the results were summarized in the succeeding tables. The detection limits of the elements in each analysis are also shown in each table. A more detailed list of all measured points per sample per target mineral is shown in Appendices B (for native gold and electrum), C (for sphalerite), and D (for galena).

The Au and Ag contents of native gold and electrum identified in 7 samples were quantitatively analyzed under the following parameters: 20 kV acceleration voltage and 20 nA current. The standard materials used were pure metals (Au and Ag). The data were corrected using the Bence-Albee method (Taguchi & Hirowatari, 1976; Hirowatari & Taguchi, 1978).

The S, Zn, Fe, Cd, Ga, Mn, Cu, Ag, Sn, and In contents of sphalerite crystals were quantitatively analyzed under the following parameters: 15 kV acceleration voltage and 20 nA current. Caution was observed during the point analysis to avoid the analysis of chalcopyrite disease. Compositional mapping of the aforementioned elements in sphalerite was also conducted. The standard materials used were synthesized compounds (ZnS, GaAs, FeS_2, CdS, and InP) and pure metals (Ag, Mn, Cu, and Sn).

Galena's major and minor element composition were quantitatively analyzed under the following parameters: 25 kV acceleration voltage and 15 nA current. The elements analyzed were S, Pb, Bi, Ag, Sb, Cu, As, Se, and Sn. Other Bi-Pb-Cu-Ag minerals were also identified during the analysis. The standard materials used were synthesized compounds (PbS, Bi_2S_3, GaAs, and SnSe) and pure metals (Ag, Sb, Cu, and Sn).

Several textures of pyrite, as well as inclusions in pyrite, were observed during petrography. Representative samples underwent compositional mapping for the following elements: S, Fe, As, Co, Ni, Cu, Pb, Zn, Au and Ag. The analysis was carried out under the following parameters: 20 kV acceleration voltage and 20 nA current. The standard materials used were synthesized compounds (FeS_2, GaAs, PbS, and ZnS) and pure metals (Co, Ni, Cu, Au, Ag).

5.3 Ore mineral occurrence, textures and chemistry

5.3.1 Native gold and electrum

The Au grades in the Stage 1 and Stage 2 veins and hydrothermal breccias are generally low and highly variable. The per meter assay of drill holes report less than 1 ppm Au to 10 ppm Au (Rohrlach & Fredericksen, 2008, unpublished data). No visible native gold or electrum was observed from the collected samples of the Stage 1 and Stage 2 veins and hydrothermal breccias.

The Stage 4 veins and hydrothermal breccias, however, contain abundant native gold and electrum crystals. A total of 176 individual native gold and electrum grains were observed in six polished sections and four polished thin sections. Native gold and electrum occur as anhedral crystals with sizes ranging from less than 10 µm up to 180 µm with an average of around 35 µm. The crystals occur within the sulfides or along the crystal boundaries of sphalerite, galena, chalcopyrite and pyrite (Fig. 5.1A-E). They also occur as infill between quartz crystals (Fig. 5.1F).

Electron probe microanalysis of native gold and electrum showed that the dominant Au-bearing mineral (around 98.4% of all analyzed points) is native gold with Au content ranging from 81.2 to 94.2 atomic % with an average Au content of 92.4 atomic %. Electrum, on the other hand, has Au content ranging from 78.4 to 79.0 atomic % with an average Au content of 78.7 atomic % (Table 5.1). EPMA mapping showed no prominent zoning in the concentration of Au and Ag in the crystals (Fig. 5.2).

No native gold/electrum was observed in Stages 5 and 6.

Table 5.1 Au and Ag contents of native gold and electrum in Stage 4 mineralization.

Sample	Number of points	Sample type	Au content range (atomic %)	Au content average (atomic %)	Ag content range (atomic %)	Ag content average (atomic %)	Mineral ID
KTD194-12 186.60m (A23)	4	vein	91.5-92.6	92.1	7.5-8.5	7.9	native gold
KTDH04 85.30m (C11)	15	vein	88.5-91.8	90.7	8.2-11.5	9.3	native gold
KTDH04 101.40m (C20)	114	hbx	91.9-93.6	92.9	6.4-8.1	7.1	native gold
KTDH04 102.95m (C21)	11	hbx	92.0-92.5	92.3	7.5-8.0	7.7	native gold
KTDH04 105.50m (C23)	10	vein	81.2-94.2	91.4	5.8-18.8	8.6	native gold
KTDH04 105.50m (C23)	3	vein	78.4-79.0	78.7	21.0-21.6	21.3	electrum
KTDH04 119.10m (C30)	24	hbx	92.0-93.2	92.6	6.8-8.0	7.4	native gold
KTDH04 169.20m (C33)	3	vein	86.2-94.1	88.9	5-9-13.9	11.1	native gold

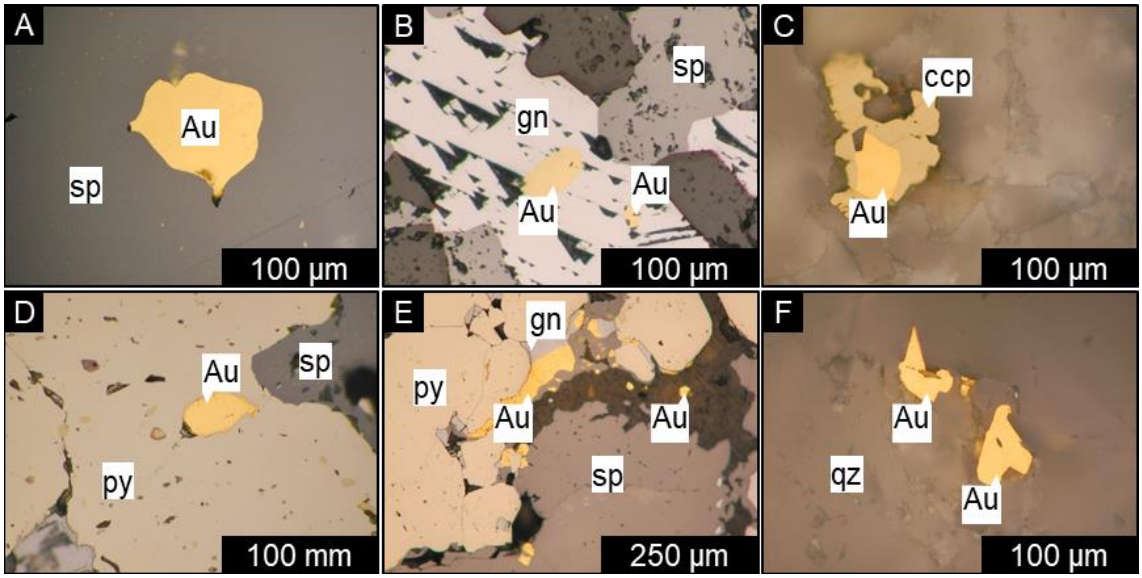

Fig. 5.1 Occurrence of native gold/electrum in Kay Tanda. (A) Native gold in sphalerite (Sample: KTDH04 101.40m, C20). (B) Native gold in galena (Sample: KTDH04 105.50m, C23). (C) Native gold in chalcopyrite (Sample: KTDH04 102.95m, C21). (D) Native gold in pyrite (Sample: KTDH04 101.40m, C20). (E) Native gold intergrown with sulfides (Sample: KTDH04 119.10m, C30). (F) Native gold as infill between quartz crystals (Sample: KTDH04 169.20m, C33). Abbreviations: Au – native gold/electrum, ccp – chalcopyrite, gn – galena, py – pyrite, qz – quartz, sp – sphalerite.

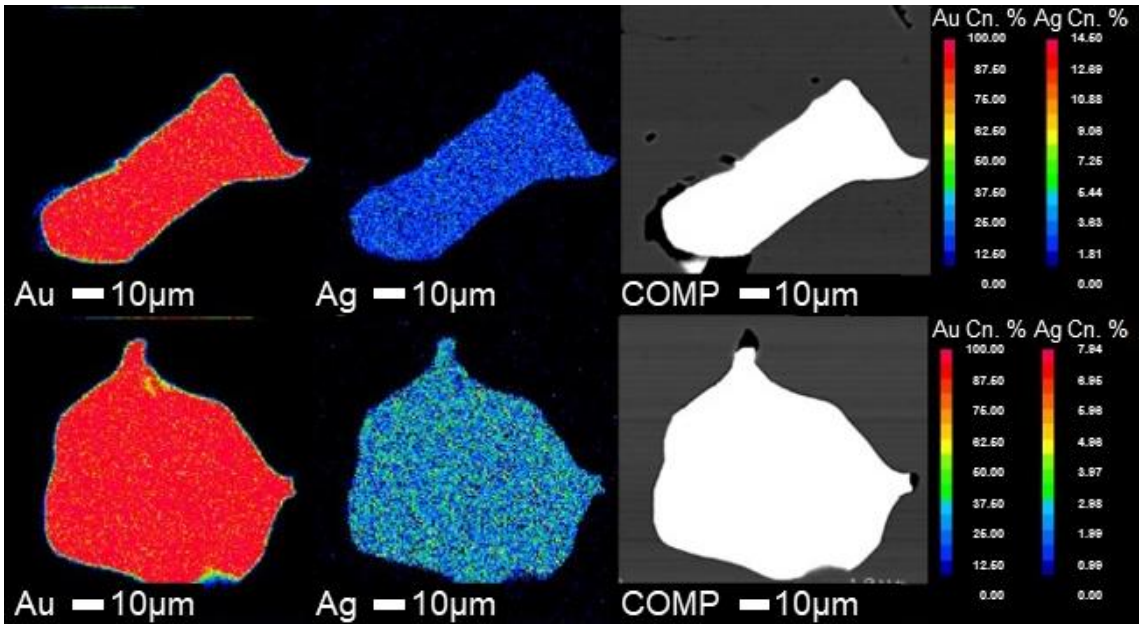

Fig. 5.2 Element mapping on native gold crystals from Stage 4 hydrothermal breccia shows homogenous distribution of Au and Ag in the crystal (Sample: KTDH04 101.40m, C20).

5.3.2 Sphalerite

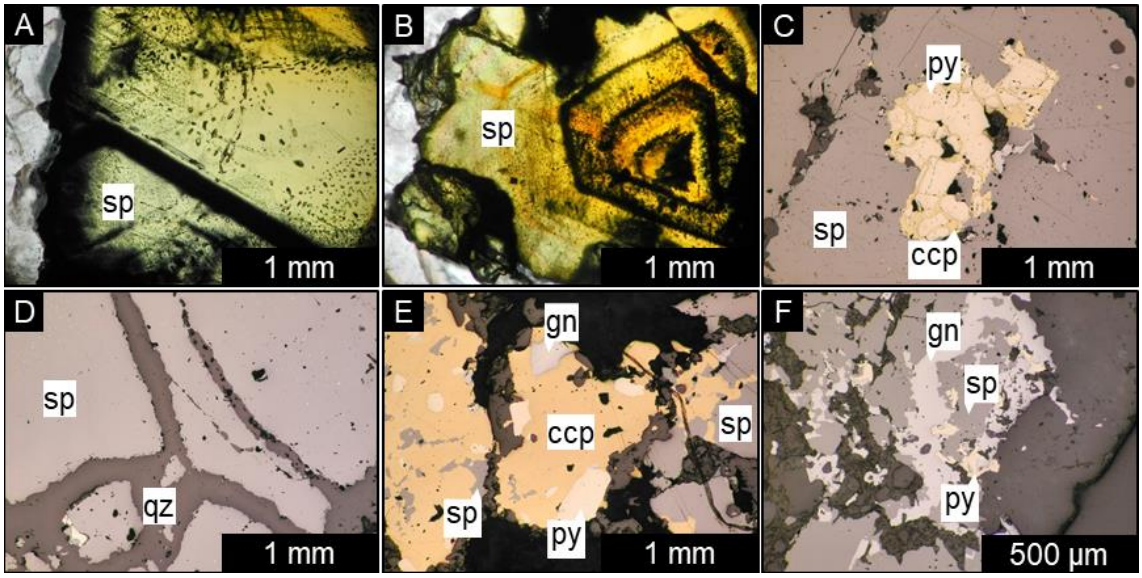

Fig. 5.3 Occurrence and common textures of sphalerite in Kay Tanda observed under plane polarized light (PPL) (A-B) and under crossed polarized light (XPL) (C-F). (A) Unzoned sphalerite crystal with dark crystal outlines and abundant fluid inclusions (Sample: KTDH04 114.80m, C28). (B) Zoned sphalerite crystal (Sample: KTD194-12 110.45m, A13). (C) Fractured pyrite replaced by chalcopyrite, hosted in coarse-grained sphalerite (Sample: KTDH04 93.50m, C16). (D) Fractured sphalerite (Sample: KTDH04 114.80m, C28). (E) Sphalerite almost completely replaced by chalcopyrite (Sample: KTDH04 232.30m, C44). (F) Sphalerite partially replaced by galena (Sample: KTDH04 83.90m, C09). Abbreviations: ccp – chalcopyrite, gn – galena, py – pyrite, qz – quartz, sp – sphalerite.

Sphalerite is the dominant base metal sulfide in Kay Tanda commonly occurring in the Stage 4 quartz ± adularia ± calcite veins and hydrothermal breccias and the Stage 6 anhydrite-gypsum veins and hydrothermal breccias. The crystal size of subhedral to anhedral sphalerite crystals ranges from less than 50 µm up to 5 mm but commonly less than 2 mm. In hand specimens, sphalerite crystals are resinous and dark brown to black in color. Under plane polarized light, the crystals are transparent to translucent, light yellow to light green in color with thick and dark crystal outlines (Fig. 5.3A). Some sphalerite crystals show prominent growth zones (Fig. 5.3B). Under reflected light, most sphalerite crystals exhibit chalcopyrite disease. Sphalerite commonly occurs as solitary minerals or as intergrowths with galena, chalcopyrite, pyrite, and native gold and electrum. Some coarse-grained sphalerite crystals host smaller crystals of pyrite, chalcopyrite and galena (Fig. 5.3C). Fractured sphalerite is common in hydrothermal breccias (Fig. 5.3D). Replacement textures such as chalcopyrite (Fig. 5.3E) and galena (Fig. 5.3F) replacing sphalerite

along the rim, fractures or cleavage planes were also observed. These textures were observed in both Stage 4 and Stage 6 sphalerite.

The concentrations of several elements of sphalerite, such as S, Zn, Fe, Mn, Cd, Cu, Sn, In, Ag, and Ga in the Stage 4 and Stage 6 sphalerite were determined. Tables 5.2A and 5.2B show the summary of the analyses conducted in two different dates of analyses, hence the different sets of detection limit. The FeS contents of the Stage 4 and Stage 6 sphalerite are both low, however, the FeS content of Stage 6 sphalerite is slightly higher than that of Stage 4 sphalerite. Stage 4 sphalerite contains 0.6 to 2.9 mol% FeS with an average of 1.1 mol% FeS while the Stage 6 sphalerite contains 1.0 to 2.1 mol% FeS with an average of 1.5 mol% FeS. The histograms of the FeS content of Stage 4 sphalerite show a normal distribution with a mode at 1.0 to 1.05 mol% (Fig. 5.4A) but the histogram of the FeS content of Stage 6 sphalerite show a bimodal distribution with mode at 1.4 to 1.45 mol% and at 1.6 to 1.65 mol% (Fig. 5.4B). Moreover, the samples in the histograms are arranged according to decreasing elevation, which shows increasing FeS content from the shallow to deeper levels. The Cd concentration ranks second next to Fe which is around 0.22 to 0.39 wt% with an average of 0.32 wt% for Stage 4 sphalerite and around 0.30 to 0.35 wt% with an average of 0.32 wt% for Stage 6 sphalerite. The Mn and Ga concentrations are both lower than Cd concentration. The Mn concentration of Stage 4 sphalerite is around 0.05 to 0.24 wt% with an average of 0.12 wt% while that of the Stage 6 sphalerite is around 0.11 to 0.19 wt% with an average of 0.14 wt%. The Ga concentration of the Stage 4 sphalerite is around 0.09 to 0.13 wt% with an average of 0.12 wt% while that of the Stage 6 sphalerite is around 0.11 to 0.14 wt% with an average of 0.13 wt%. The average Cu content of the Stage 4 and Stage 6 sphalerite is around 0.13 wt% and 0.23 wt%, respectively. The maximum CuS content in all analyzed samples is 1.5 mol% which below the determined solubility of CuS in sphalerite (~2.4 mol%) (Kojima & Sugaki, 1985). The Ag, Sn and In concentrations are below the detection limit. Elemental mapping of these trace elements in sphalerite crystals was also done. Sphalerite crystals that do not exhibit growth zones do not show any variation in the concentration and distribution in any of the analyzed trace elements (Fig. 5.5A). On the other hand, sphalerite crystals which exhibit

growth zones show slight elevation in Cu concentration along growth zones which corresponds to the distribution of chalcopyrite disease along the crystallographic growth planes (Fig. 5.5B).

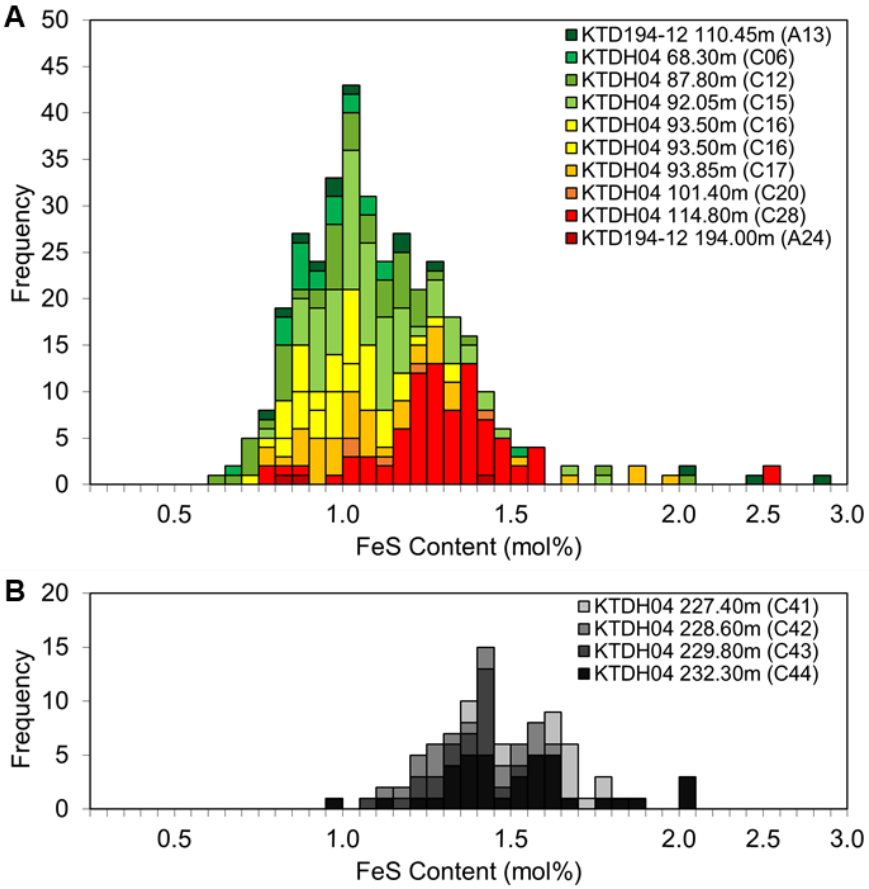

Fig. 5.4 FeS content of Stage 4 and Stage 6 sphalerite. (A) Stage 4 sphalerite FeS histogram shows normal distribution. (B) Stage 6 sphalerite FeS histogram shows bimodal distribution. Stage 6 sphalerite has generally higher FeS content than Stage 4 sphalerite. The samples are arranged according to decreasing elevation with respect to mean sea level.

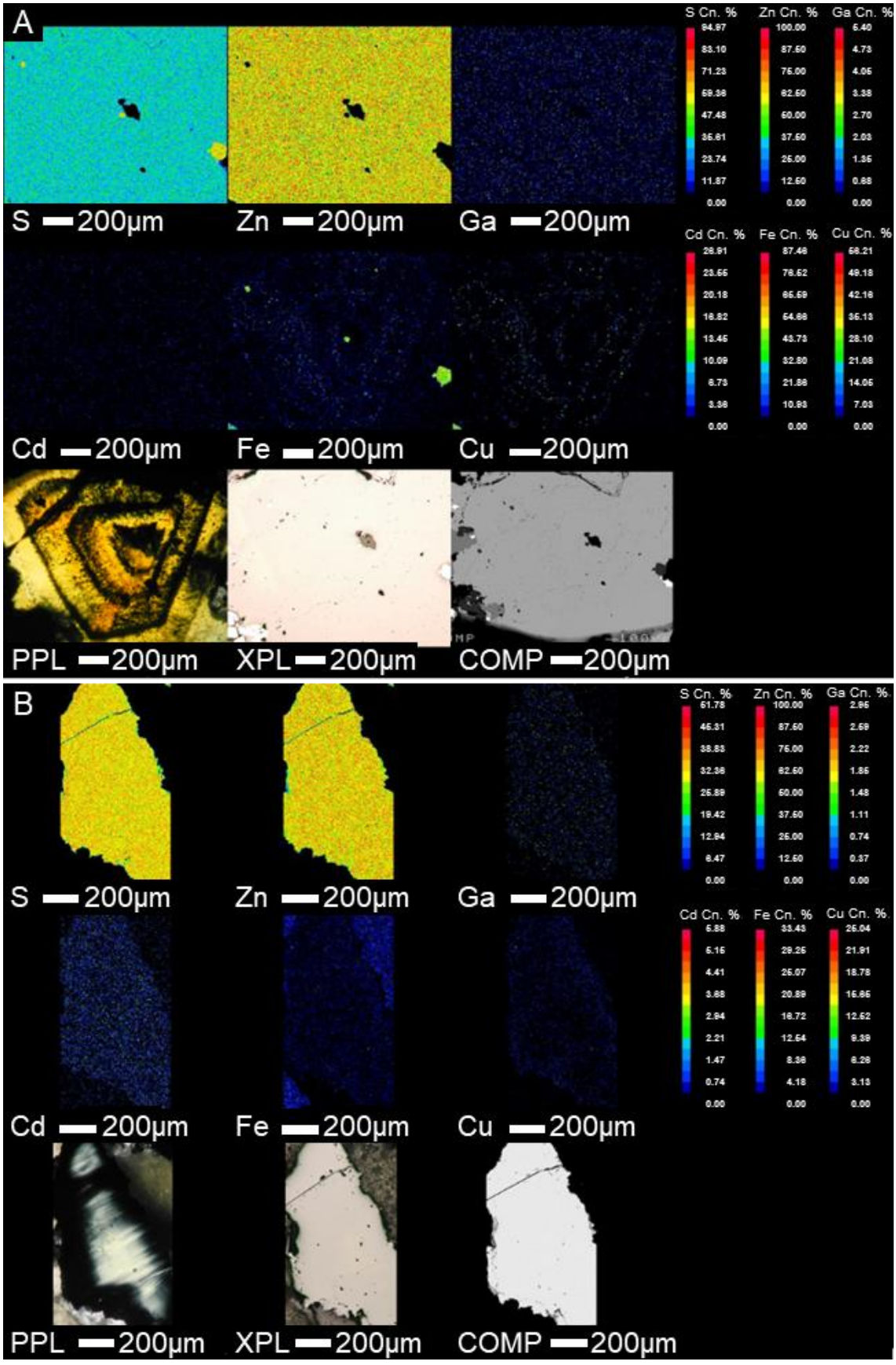

Fig. 5.5 Element mapping on (A) zoned sphalerite from Stage 4 quartz ± adularia ± calcite vein (Sample: KTD194-12 110.45m, A13) and (B) unzoned sphalerite from Stage 4 hydrothermal breccia (Sample: KTDH04 92.05 m, C15).

The MnS and CdS content of the Stage 4 and Stage 6 sphalerite were also calculated and were plotted against FeS in the FeS-MnS-CdS ternary diagram (Fig. 5.6). The MnS content of Stage 4 sphalerite is from 0.03 to 0.58 mol% with an average of 0.22 mol% while that of the Stage 6 sphalerite is from 0.04 to 0.70 mol% with an average of 0.26 mol%. The CdS content of Stage 4 sphalerite is from 0.11 to 0.50 mol% with an average of 0.28 mol% while that of the Stage 6 sphalerite is from 0.19 to 0.39 mol% with an average of 0.28 mol%. Generally, the minor element concentrations in FeS, MnS and CdS of Stage 4 and Stage 6 sphalerite are within the same range (Fig. 5.6A-C). On closer inspection, however, the Stage 4 sphalerite show decreasing Cd concentration from shallower to deeper levels. This is also shown in the binary plots of the minor element concentrations against Cd concentration (Fig. 5.7).

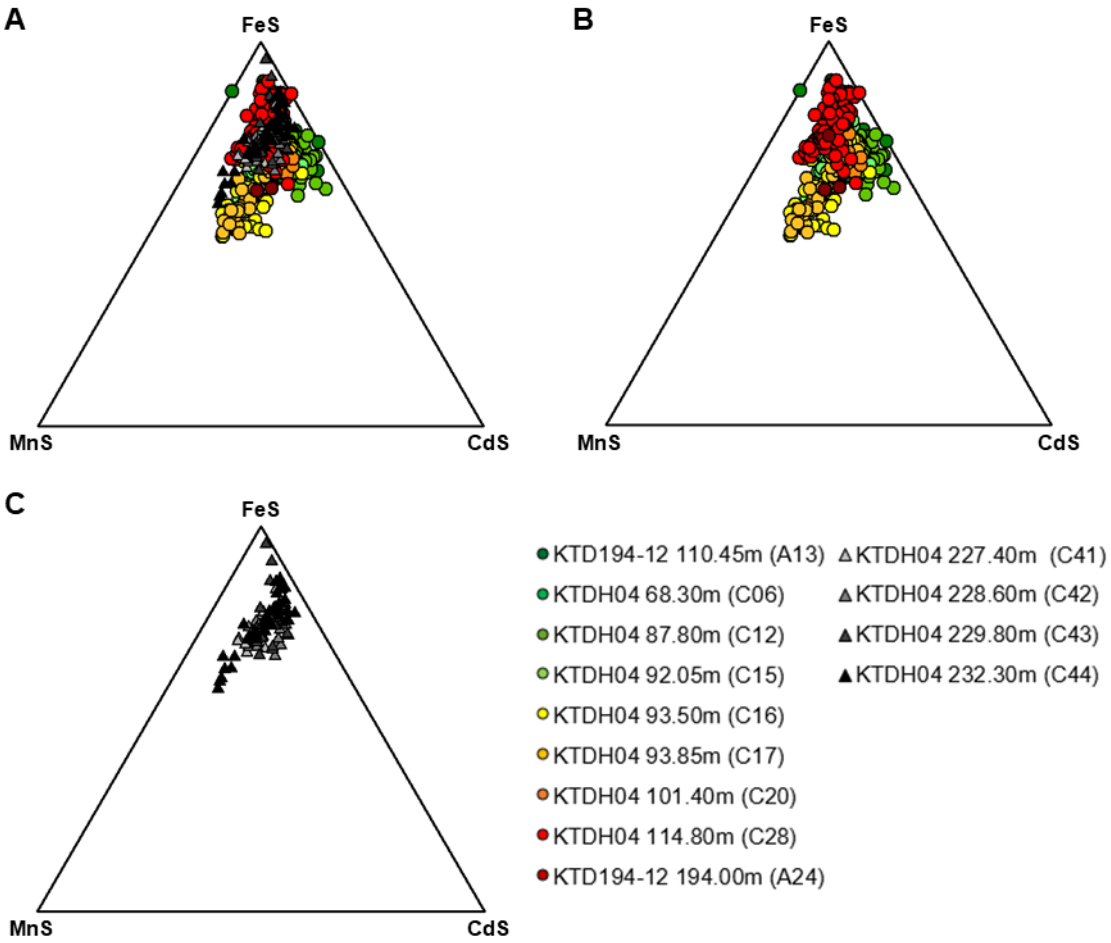

Fig. 5.6 FeS-MnS-CdS ternary diagram of Stage 4 and Stage 6 sphalerite. (A) All analyzed sphalerite crystals. (B) All Stage 4 sphalerite. (C) All Stage 6 sphalerite.

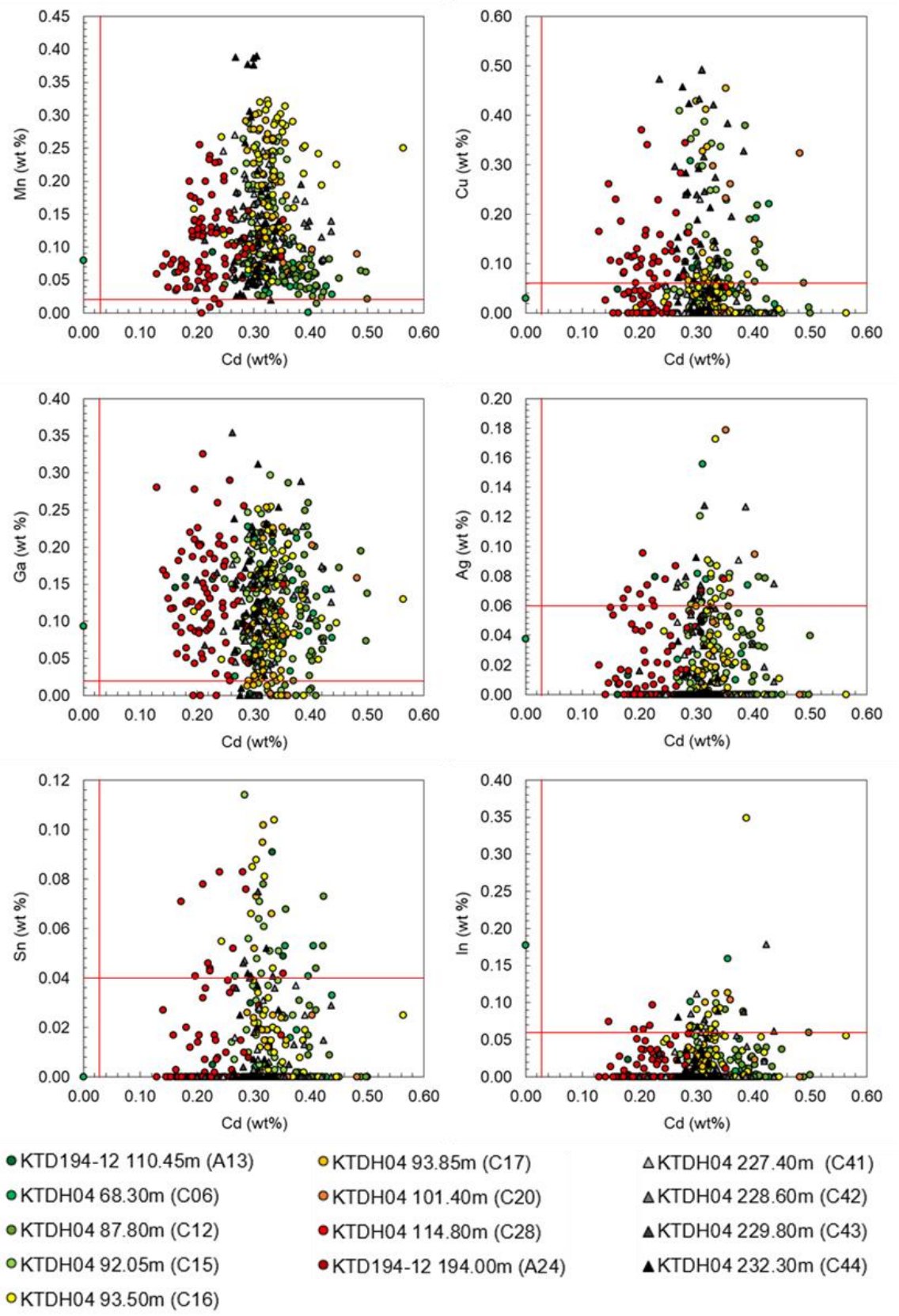

Fig. 5.7 Binary plots of minor elements vs Cd. The concentration of minor elements in Stage 4 and Stage 6 sphalerite are within the same range. Stage 4 sphalerite, however, show decreasing Cd concentration with decreasing elevation from mean sea level. Red lines represent the detection limit of the element in the analysis.

Table 5.2A Major and minor element composition of sphalerite from Stage 4 and Stage 6 mineralization.

Sample		**KTD194-12 110.45m (A13)**	**KTDH04 87.80m (C12)**	**KTDH04 92.05m (C15)**	**KTDH04 93.50m (C16)**	**KTDH04 93.85m (C17)**	**KTDH04 114.80m (C28)**	**KTD194-12 194.00m (A24)**	**KTDH04 232.30m (C44)**
Elevation from mean sea level (m)		165.9	137.7	133.5	132.0	131.7	110.7	90.4	-6.8
Mineralization stage		4	4	4	4	4	4	4	6
Number of points		13	48	82	43	44	84	3	39
Average Weight %	L.L.D. %								
Zn	0.08	64.78	65.52	65.31	65.56	64.73	65.63	64.09	64.80
Fe	0.04	0.76	0.59	0.63	0.58	0.64	0.75	0.57	0.86
Mn	0.02	0.08	0.06	0.16	0.18	0.17	0.10	0.13	0.14
Cd	0.02	0.29	0.39	0.31	0.33	0.32	0.22	0.29	0.30
Cu	0.06	<0.06	<0.06	0.09	<0.06	0.09	0.10	<0.06	0.13
Sn	0.04	<0.04	<0.04	<0.04	<0.04	<0.04	<0.04	<0.04	<0.04
In	0.04	<0.04	<0.04	<0.04	<0.04	<0.04	<0.04	<0.04	<0.04
Ag	0.03	<0.03	<0.03	<0.03	<0.03	<0.03	<0.03	0.05	<0.03
Ga	0.02	0.13	0.12	0.11	0.11	0.11	0.13	0.11	0.14
S	0.02	32.35	33.42	33.64	32.25	32.94	33.00	32.16	32.93
Total		98.38	100.09	100.26	99.02	99.00	99.93	97.41	99.30
Average Atomic %									
Zn		49.07	48.62	48.31	49.48	48.59	48.88	49.00	48.52
Fe		0.67	0.51	0.54	0.51	0.56	0.65	0.51	0.76
Mn		0.07	0.05	0.14	0.17	0.15	0.09	0.12	0.13
Cd		0.13	0.17	0.14	0.14	0.14	0.09	0.13	0.13
Cu		-	-	0.07	-	0.07	0.07	-	0.10
Sn		-	-	-	-	-	-	-	-
In		-	-	-	-	-	-	-	-
Ag		-	-	-	-	-	-	0.02	-
Ga		0.09	0.09	0.08	0.08	0.08	0.09	0.08	0.10
S		49.97	50.56	50.73	49.62	50.41	50.11	50.13	50.27
Total		100.00	100.00	100.00	100.00	100.00	100.00	100.00	100.00

Sample		KTD194-12 110.45m (A13)	KTDH04 87.80m (C12)	KTDH04 92.05m (C15)	KTDH04 93.50m (C16)	KTDH04 93.85m (C17)	KTDH04 114.80m (C28)	KTD194-12 194.00m (A24)	KTDH04 232.30m (C44)
Elevation from mean sea level (m)		165.9	137.7	133.5	132.0	131.7	110.7	90.4	-6.8
Mineralization stage		4	4	4	4	4	4	4	6
Number of points		13	48	82	43	44	84	3	39
FeS	Minimum	0.80	0.64	0.77	0.72	0.79	0.77	0.80	0.97
	Maximum	2.87	2.06	1.77	1.32	1.96	2.59	1.41	2.08
	Average	1.34	1.03	1.10	1.02	1.13	1.31	1.02	1.52
MnS	Minimum	0.10	0.03	0.08	0.09	0.12	0.00	0.22	0.04
	Maximum	0.19	0.18	0.52	0.58	0.53	0.45	0.28	0.70
	Average	0.14	0.10	0.28	0.33	0.31	0.18	0.24	0.25
CdS	Minimum	0.14	0.22	0.23	0.25	0.25	0.11	0.23	0.23
	Maximum	0.32	0.44	0.32	0.34	0.34	0.31	0.28	0.30
	Average	0.26	0.34	0.27	0.29	0.29	0.19	0.25	0.27

Table 5.2B Major and minor element composition of sphalerite from Stage 4 and Stage 6 mineralization.

Sample		**KTDH04 68.30m (C06)**	**KTDH04 93.50m (C16)**	**KTDH04 101.40m (C20)**	**KTDH04 227.40m (C41)**	**KTDH04 228.60m (C42)**	**KTDH04 229.80m (C43)**
Elevation from mean sea level (m)		157.2	132.0	124.1	-1.9	-3.1	-4.3
Mineralization stage		4	4	4	6	6	6
Number of points		21	17	5	15	19	20
Average Weight %	L.L.D. %						
Zn	0.07	64.90	64.58	63.57	63.58	64.87	64.79
Fe	0.03	0.54	0.53	0.65	0.90	0.79	0.77
Mn	0.02	0.05	0.24	0.08	0.19	0.13	0.11
Cd	0.03	0.34	0.35	0.39	0.31	0.35	0.31
Cu	0.06	<0.06	<0.06	0.25	0.11	<0.06	0.45
Sn	0.03	<0.03	<0.03	<0.03	<0.03	<0.03	<0.03
In	0.06	<0.06	<0.06	<0.06	<0.06	<0.06	<0.06
Ag	0.06	<0.06	<0.06	0.08	<0.06	<0.06	<0.06
Ga	0.02	0.12	0.11	0.09	0.11	0.12	0.14
S	0.03	32.65	32.82	33.22	33.46	33.61	32.60
Total		98.60	98.63	98.32	98.65	99.88	99.17
Average Atomic %							
Zn		48.99	48.66	47.88	47.63	48.12	48.69
Fe		0.48	0.47	0.57	0.79	0.68	0.67
Mn		0.04	0.21	0.07	0.17	0.12	0.10
Cd		0.15	0.15	0.17	0.13	0.15	0.14
Cu		-	-	0.20	0.09	-	0.35
Sn		-	-	-	-	-	-
In		-	-	-	-	-	-
Ag		-	-	0.04	-	-	-
Ga		0.09	0.08	0.06	0.08	0.08	0.10
S		50.25	50.43	51.01	51.11	50.84	49.96
Total		100.00	100.00	100.00	100.00	100.00	100.00

Sample		KTDH04 68.30m (C06)	KTDH04 93.50m (C16)	KTDH04 101.40m (C20)	KTDH04 227.40m (C41)	KTDH04 228.60m (C42)	KTDH04 229.80m (C43)
Elevation from mean sea level (m)		157.2	132.0	124.1	-1.9	-3.1	-4.3
Mineralization stage		4	4	4	6	6	6
Number of points		21	17	5	15	19	20
FeS	Minimum	0.67	0.84	1.01	1.40	1.13	1.05
	Maximum	1.51	1.05	1.42	1.79	1.61	1.51
	Average	0.96	0.94	1.16	1.62	1.39	1.35
MnS	Minimum	0.00	0.21	0.12	0.10	0.11	0.08
	Maximum	0.15	0.54	0.18	0.49	0.36	0.35
	Average	0.09	0.43	0.15	0.34	0.24	0.19
CdS	Minimum	0.00	0.17	0.29	0.22	0.23	0.19
	Maximum	0.39	0.50	0.43	0.35	0.39	0.35
	Average	0.30	0.31	0.34	0.27	0.30	0.27

5.3.3 Galena

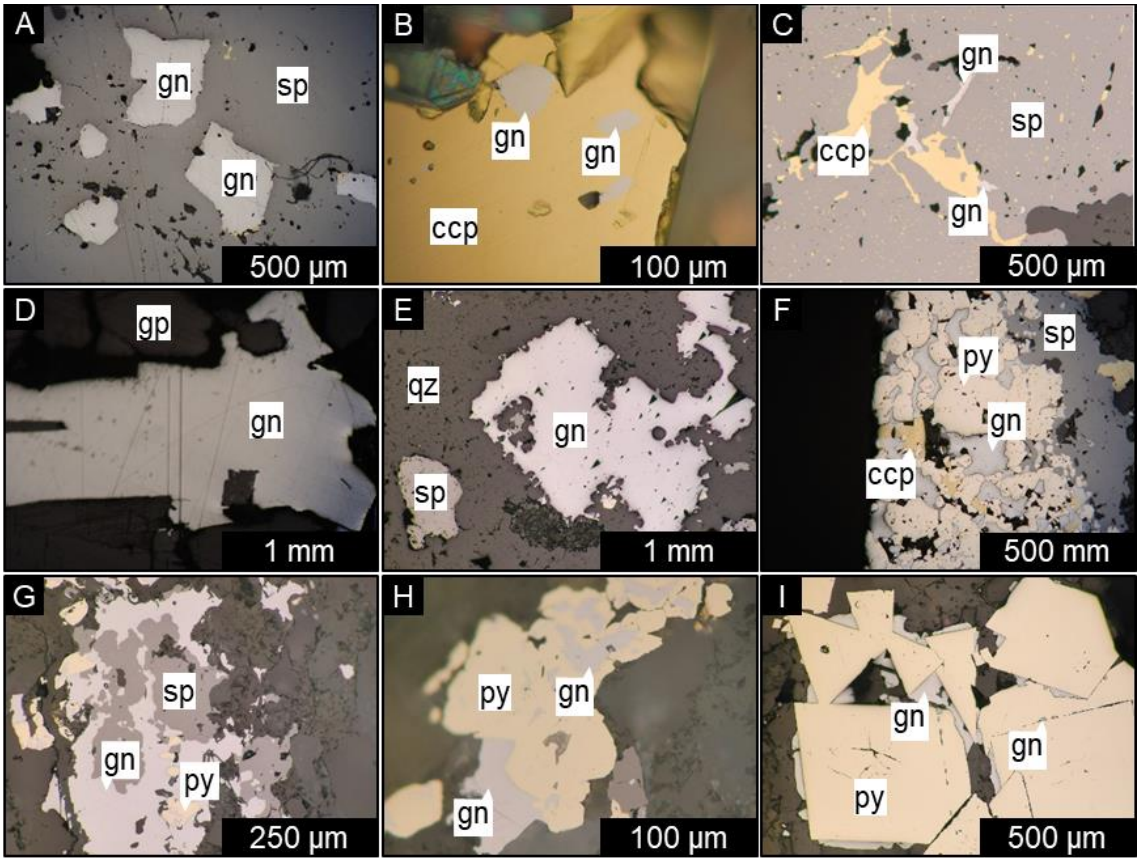

Fig. 5.8 Occurrence and common textures of galena in Kay Tanda. (A) Galena intergrown and hosted inside coarse sphalerite crystals (Sample: KTDH04 229.80m, C43). (B) Galena inclusions in chalcopyrite (Sample: KTDH04 229.80m, C43). (C) Galena inclusions in sphalerite (Sample: KTD194-12 135.60m, A16). (D) Infill between Stage 6 anhydrite and gypsum crystals (Sample: KTDH04 232.30m, C44). (E) Infill between Stage 4 quartz crystals (Sample: KTD194-12 109.35m, A11) (F) Galena replaced by chalcopyrite (Sample: KTDH04 93.50m, C16). (G) Galena replacing sphalerite (Sample: KTDH04 85.30m, C11). (H) Galena replacing pyrite (Sample: KTDH04 85.30m, C11). (I) Galena overgrowths around Stage 2 euhedral pyrite (Sample: KTD194-12 86.55m, A09). Abbreviations: ccp – chalcopyrite, gn – galena, gp – gypsum, py – pyrite, qz – quartz, sp – sphalerite.

The occurrences of galena have been observed to be correlated with elevations in Ag in drill core assay data. Different textures of galena were observed which include (1) galena intergrown or hosted in sphalerite (Fig. 5.8A), (2) galena inclusions in chalcopyrite (Fig. 5.8B), pyrite, and sphalerite (Fig. 5.8C), (3) infill between gypsum/anhydrite crystals (Fig. 5.8D) and quartz crystals (Fig. 5.8E), (4) galena being replaced by chalcopyrite (Fig. 5.8F), (5) galena replacing sphalerite (Fig. 5.8G) and pyrite (Fig. 5.8H), and (6) galena overgrowths around euhedral pyrite (Fig. 5.8I).

Of these occurrences, elevations in Ag concentrations were detected in galena inclusions in sphalerite and chalcopyrite and galena overgrowths around euhedral pyrite (Table 5.3).

Galena inclusions in sphalerite contains around 0.12 to 0.20 atomic % Ag with an average of 0.15 atomic % Ag. Galena inclusions in chalcopyrite contains 0.48 to 0.58 atomic % Ag with an average of 0.52 atomic % Ag. Galena overgrowths around euhedral pyrite contains 0.05 to 0.25 atomic % Ag with an average of 0.15 atomic % Ag. The other textures do not contain detectable amounts of Ag. However, all textures showed elevations in Bi concentrations. Bi concentrations ranges from 0.05 to 0.76 atomic % Bi with an average of 0.14 atomic % Bi. Ag concentrations were plotted against Bi concentrations (Fig. 5.9) and the plot shows a positive correlation (Ag = 0.74Bi). Cu concentrations are elevated in samples which are partially replaced by chalcopyrite, though caution was observed during the analysis to avoid the analysis of chalcopyrite. Cu concentrations ranges from 0.7 to 0.27 atomic % with an average of 0.13 atomic % Cu. Se, Sn, Sb and As concentrations are generally below detection limits.

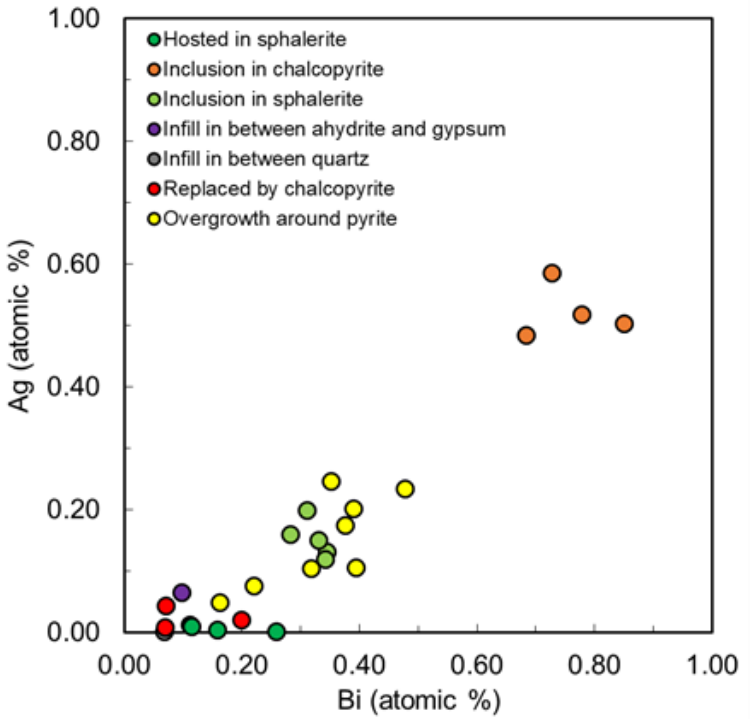

Fig. 5.9 Ag and Bi concentrations of galena and Bi-Pb-Cu-Ag minerals.

Table 5.3 Major and minor element composition of galena per occurrence.

Sample		**KTDH04 92.05m (C15)**	**KTDH04 93.50m (C16)**	**KTDH04 93.85m (C17)**	**KTDH04 101.40m (C20)**	**KTDH04 227.40m (C41)**	**KTDH04 229.80m (C43)**	**KTDH04 229.80m (C43)**	**KTDH04 232.30m (C44)**
Elevation from mean sea level (m)		133.5	132.0	131.7	124.1	-1.9	-4.3	-4.3	-6.8
Mineralization stage		4	4	4	4	6	6	6	6
Number of points		14	13	7	4	21	17	4	6
Occurrence		hosted in sphalerite	hosted in sphalerite	hosted in sphalerite	hosted in sphalerite	hosted in sphalerite	hosted in sphalerite	inclusion in chalcopyrite	inclusion in chalcopyrite
Average Weight %	L.L.D. %								
Pb	0.08	86.29	86.54	85.64	85.59	87.07	85.89	80.49	86.36
Bi	0.07	0.14	0.19	0.13	0.11	0.20	0.16	1.39	0.18
Cu	0.02	<0.02	<0.02	<0.02	<0.02	<0.02	<0.02	2.73	0.64
Ag	0.02	<0.02	<0.02	<0.02	<0.02	<0.02	<0.02	0.50	<0.02
Se	0.03	<0.03	<0.03	0.06	<0.03	<0.03	<0.03	0.49	<0.03
Sn	0.01	0.03	<0.01	0.01	<0.01	<0.01	<0.01	<0.01	<0.01
Sb	0.02	<0.02	<0.02	0.04	<0.02	<0.02	<0.02	<0.02	<0.02
As	0.05	<0.05	<0.05	<0.05	<0.05	<0.05	<0.05	<0.05	<0.05
S	0.01	13.28	13.27	13.27	13.28	13.31	13.09	13.80	13.48
Total		99.74	100.00	99.15	98.98	100.58	99.14	99.39	100.66
Average Atomic %									
Pb		50.09	50.18	49.86	49.91	50.26	50.33	44.19	49.14
Bi		0.08	0.11	0.08	0.06	0.11	0.09	0.76	0.10
Cu		-	-	-	-	-	-	4.88	1.18
Ag		-	-	-	-	-	-	0.52	-
Se		-	-	0.09	-	-	-	0.70	-
Sn		0.03	-	0.01	-	-	-	-	-
Sb		-	-	0.04	-	-	-	-	-
As		-	-	-	-	-	-	-	-
S		49.80	49.71	49.92	50.03	49.63	49.58	48.94	49.58
Total		100.00	100.00	100.00	100.00	100.00	100.00	100.00	100.00

Sample		**KTDH04 101.40m (C20)**	**KTD194-12 135.60m (A16)**	**KTDH04 232.30m (C44)**	**KTD194-12 109.35m (A11)**	**KTDH04 101.40m (C20)**	**KTD194-12 135.60m (A16)**	**KTDH04 93.50m (C16)**	**KTDH04 93.85m (C17)**
Elevation from mean sea level (m)		124.1	143.2	-6.8	166.9	124.1	143.2	132.0	131.7
Mineralization stage		4	4	6	4	4	4	4	4
Number of points		1	5	23	13	3	3	6	1
Occurrence		inclusion in pyrite	inclusion in sphalerite	infill between anhydrite and gypsum	infill between quartz	infill between quartz	replaced by chalcopyrite	replaced by chalcopyrite	replaced by chalcopyrite
Average Weight %	L.L.D. %								
Pb	0.08	85.20	84.73	86.23	85.60	85.33	85.55	86.62	85.16
Bi	0.07	0.17	0.56	0.13	0.15	0.23	0.11	0.16	0.14
Cu	0.02	<0.02	0.12	<0.02	<0.02	<0.02	0.05	0.04	0.05
Ag	0.02	<0.02	0.14	<0.02	<0.02	<0.02	<0.02	<0.02	<0.02
Se	0.03	<0.03	<0.03	<0.03	<0.03	<0.03	<0.03	<0.03	<0.03
Sn	0.01	<0.01	<0.01	<0.01	<0.01	<0.01	0.01	<0.01	<0.01
Sb	0.02	<0.02	<0.02	<0.02	<0.02	<0.02	<0.02	<0.02	<0.02
As	0.05	<0.05	<0.05	<0.05	<0.05	<0.05	<0.05	<0.05	<0.05
S	0.01	13.20	13.36	13.36	13.33	13.33	13.33	13.27	13.25
Total		98.57	98.91	99.73	99.08	98.89	99.05	100.09	98.58
Average Atomic %									
Pb		49.93	49.20	49.93	49.81	49.70	49.75	50.18	49.79
Bi		0.10	0.32	0.08	0.09	0.13	0.06	0.09	0.08
Cu		-	0.23	-	-	-	0.10	0.07	0.09
Ag		-	0.15	-	-	-	-	-	-
Se		-	-	-	-	-	-	-	-
Sn		-	-	-	-	-	0.01	-	-
Sb		-	-	-	-	-	-	-	-
As		-	-	-	-	-	-	-	-
S		49.97	50.10	49.99	50.10	50.16	50.07	49.66	50.04
Total		100.00	100.00	100.00	100.00	100.00	100.00	100.00	100.00

Sample		KTDH04 101.40m (C20)	KTDH04 199.30m (C37)	KTDH04 227.40m (C41)	KTDH04 229.80m (C43)	KTDH04 232.30m (C44)	KTDH04 85.30m (C11)	KTDH04 85.30m (C11)	KTD194-12 86.55m (A09)
Elevation from mean sea level (m)		124.1	26.2	-1.9	-4.3	-6.8	140.2	140.2	187.4
Mineralization stage		4	4	6	6	6	4	4	2
Number of points		13	9	12	4	11	11	6	9
Occurrence		replaced by chalcopyrite	replaced by chalcopyrite	replaced by chalcopyrite	replaced by chalcopyrite	replaced by chalcopyrite	replacing pyrite	replacing sphalerite	overgrowth around pyrite
Average Weight %	L.L.D. %								
Pb	0.08	85.47	85.60	86.40	86.15	86.54	85.30	85.07	85.41
Bi	0.07	0.15	0.19	0.17	0.25	0.16	0.13	0.09	0.55
Cu	0.02	0.14	0.08	0.07	0.05	<0.02	<0.02	<0.02	<0.02
Ag	0.02	<0.02	<0.02	<0.02	<0.02	<0.02	<0.02	<0.02	0.12
Se	0.03	<0.03	0.03	<0.03	0.10	<0.03	<0.03	<0.03	0.05
Sn	0.01	<0.01	<0.01	<0.01	<0.01	<0.01	<0.01	<0.01	<0.01
Sb	0.02	<0.02	<0.02	<0.02	<0.02	<0.02	<0.02	<0.02	<0.02
As	0.05	<0.05	<0.05	<0.05	<0.05	<0.05	<0.05	<0.05	<0.05
S	0.01	13.28	13.24	13.24	13.13	13.46	13.24	13.22	13.33
Total		99.05	99.13	99.89	99.68	100.15	98.67	98.38	99.46
Average Atomic %									
Pb		49.72	49.86	50.12	50.19	49.83	49.89	49.87	49.53
Bi		0.09	0.11	0.10	0.15	0.09	0.07	0.05	0.31
Cu		0.27	0.15	0.14	0.10	-	-	-	-
Ag		-	-	-	-	-	-	-	0.13
Se		-	0.05	-	0.15	-	-	-	0.08
Sn		-	-	-	-	-	-	-	-
Sb		-	-	-	-	-	-	-	-
As		-	-	-	-	-	-	-	-
S		49.93	49.83	49.64	49.42	50.08	50.04	50.08	49.94
Total		100.00	100.00	100.00	100.00	100.00	100.00	100.00	100.00

5.3.4 Bi-Pb-Cu-Ag minerals

Bi-Pb-Cu-Ag-bearing minerals were also identified during the analysis. They were initially identified as galena during ore microscopy due to similar optical properties. These minerals were found as inclusions in chalcopyrite and in sphalerite (Fig. 5.10). The size of these inclusions ranges from 10 to 100 µm and appear to be slightly bluish (compared to galena which is bright white) under reflected light. Plotted in the (Bi+Sb)-(Ag+Cu)-Pb ternary diagram, the chemical compositions of the inclusions approach the chemical composition of berryite ($Cu_3Ag_2Pb_3Bi_7S_{16}$), vikingite ($Ag_5Pb_8Bi_{13}S_{30}$) and eskimoite ($Ag_7Pb_{10}Bi_{15}S_{36}$) (Fig. 5.11).

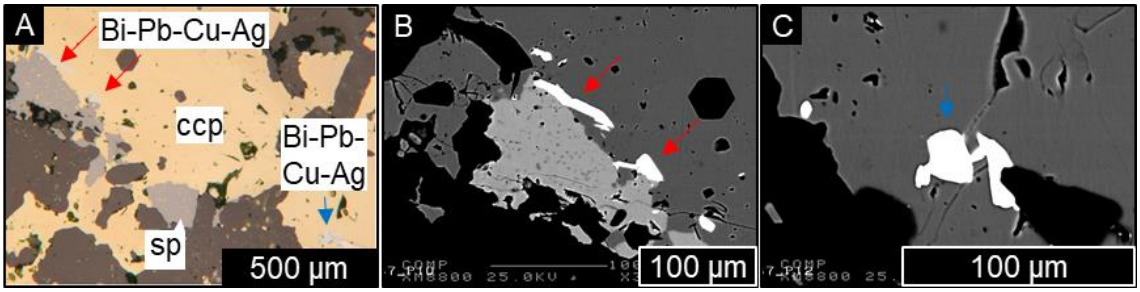

Fig. 5.10 Bi-Pb-Cu-Ag minerals found in Kay Tanda. (A) Bi-Pb-Cu-Ag mineral inclusions in chalcopyrite observed under reflected light. (B-C) Compositional image of Bi-Pb-Cu-Ag mineral inclusions. (Sample: KTD194-12 135.60m, A16)

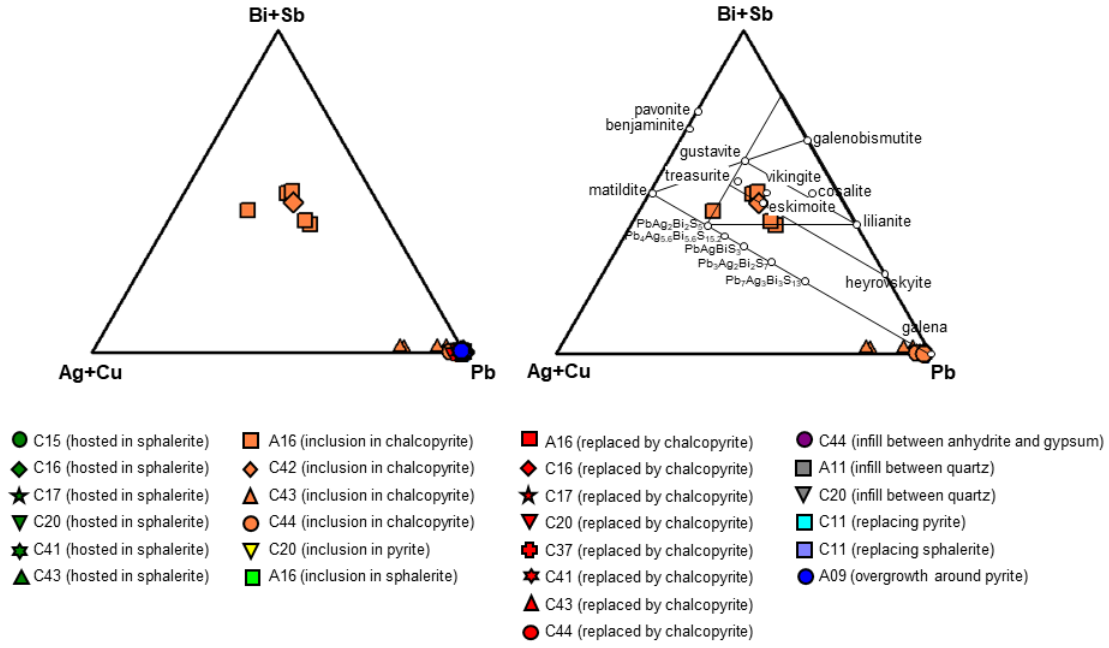

Fig. 5.11 Chemical composition of Bi-Pb-Cu-Ag mineral inclusions in chalcopyrite plotted on Bi+Sb – Ag+Cu – Pb ternary diagram (modified from Zhou et al., 2016). The chemical composition approaches the chemical composition of vikingite and eskimoite.

Table 5.4 Major and minor element composition of Pb-Bi-Cu-Ag mineral.

Sample		**KTD194-12 135.60m (A16)**	**KTD194-12 135.60m (A16)**	**KTD194-12 135.60m (A16)**	**KTD194-12 135.60m (A16)**	**KTD194-12 135.60m (A16)**	**KTDH04 228.60m (C42)**
Elevation from mean sea level (m)		143.2	143.2	143.2	143.2	143.2	-3.1
Mineralization stage		4	4	4	4	4	6
Sample point		A16-C1-8	A16-C1-9	A16-C1-10	A16-C1-11	A16-C1-12	C42-C2-5
Occurrence		inclusion in chalcopyrite	inclusion in chalcopyrite	inclusion in chalcopyrite	inclusion in chalcopyrite	inclusion in chalcopyrite	inclusion in chalcopyrite
Weight %	L.L.D. %						
Pb	0.08	20.89	26.91	27.29	36.77	34.45	28.85
Bi	0.07	46.48	48.35	47.77	37.58	38.59	44.06
Cu	0.02	7.49	5.63	4.79	1.83	1.99	5.63
Ag	0.02	7.03	2.10	2.22	7.42	7.46	1.43
Se	0.03	0.75	0.70	0.88	0.95	0.97	1.41
Sn	0.01	<0.01	<0.01	<0.01	<0.01	<0.01	<0.01
Sb	0.02	<0.02	<0.02	<0.02	<0.02	<0.02	<0.02
As	0.05	<0.05	<0.05	<0.05	<0.05	<0.05	<0.05
S	0.01	16.49	16.59	16.26	15.10	14.86	17.07
Total		99.11	100.27	99.21	99.65	98.32	98.44
Atomic %							
Pb		9.78	13.05	13.51	18.92	17.92	13.90
Bi		21.59	23.24	23.46	19.17	19.91	21.04
Cu		11.43	8.90	7.73	3.06	3.37	8.85
Ag		6.32	1.96	2.12	7.34	7.46	1.32
Se		0.92	0.89	1.14	1.29	1.32	1.78
Sn							0.00
Sb				0.01	0.01		
As		0.05				0.03	0.01
S		49.90	51.96	52.03	50.21	49.97	53.10
Total		100.00	100.00	100.00	100.00	100.00	100.00

5.3.5 Pyrite

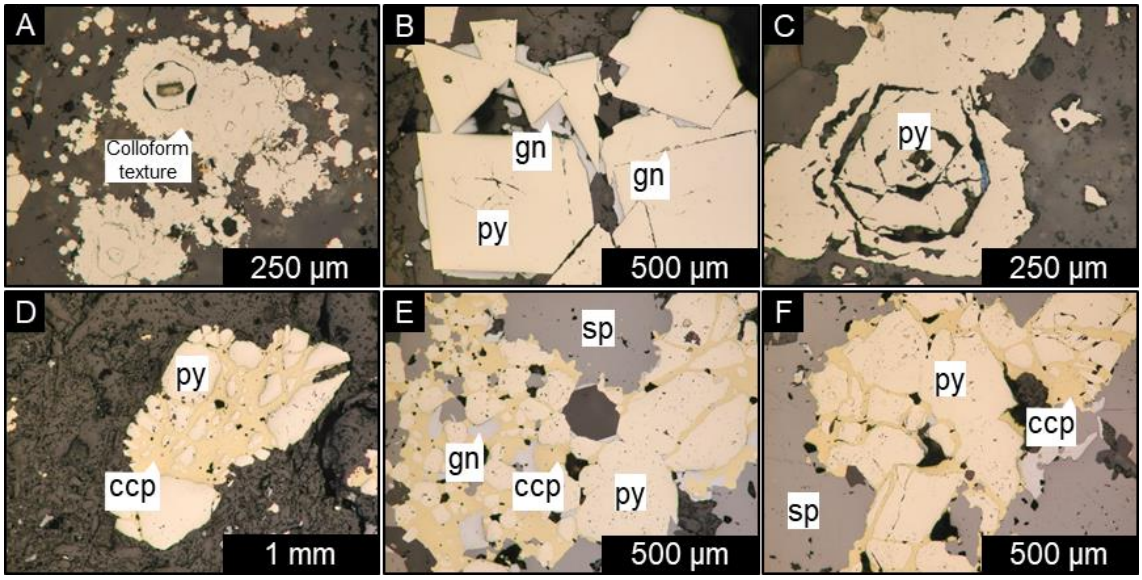

Fig. 5.12 Occurrence and common textures of pyrite in Kay Tanda. (A) Stage 2 pyrite with multiple layers of colloform growth zones (Sample: KTDH04 16.30m, C01) (B) Stage 2 euhedral pyrite overgrown by galena and pyrite (Sample: KTD194-12 86.55m, A09) (C) Stage 2 pyrite with recognizable growth zones (Sample: KTDH23 54.55m, J08) (D) Stage 6 fractured pyrite replaced by chalcopyrite (Sample: KTDH04 222.20m, C40) (E) Stage 4 fractured pyrite replaced by chalcopyrite and galena (Sample: KTDH04 92.05m, C15) (F) Stage 4 fractured pyrite replaced by chalcopyrite, hosted in coarse-grained sphalerite (Sample: KTDH04 93.50m, C16).

Pyrite is a ubiquitous sulfide mineral in the deposit and is found in all stages of mineralization. Different textures of pyrite were documented with respect to mineralization stage. The Stage 1 pyrite is commonly anhedral and is scattered in the veins filling interstices between quartz crystals. The Stage 2 pyrite shows a variety of textures. Anhedral crystals are common but zoned pyrite is characteristic (Fig. 5.12). Subhedral to euhedral pyrite crystals are found in the core and is overgrown by pyrite with colloform texture (Fig. 5.12A). EPMA mapping of zoned pyrite shows slightly elevated As content along the outer rims of the crystal (Fig. 15.13A). Some euhedral pyrite are overgrown by Bi- and Ag-bearing galena as shown in the previous subsection (Fig. 5.12B). Some pyrite crystals were also replaced by chalcopyrite and later covellite (Fig. 5.12C). The Stage 4 and Stage 6 pyrite were commonly fractured with their interstices filled by chalcopyrite (Fig. 5.12D-F). Rounded edges of fractured pyrite may indicate partial replacement of pyrite by chalcopyrite (Fig. 15.13B). The Stage 4 and Stage 6 pyrite also commonly contain

inclusions of chalcopyrite and bornite. Bornite inclusions usually contain chalcopyrite exsolutions and are both commonly altered to covellite.

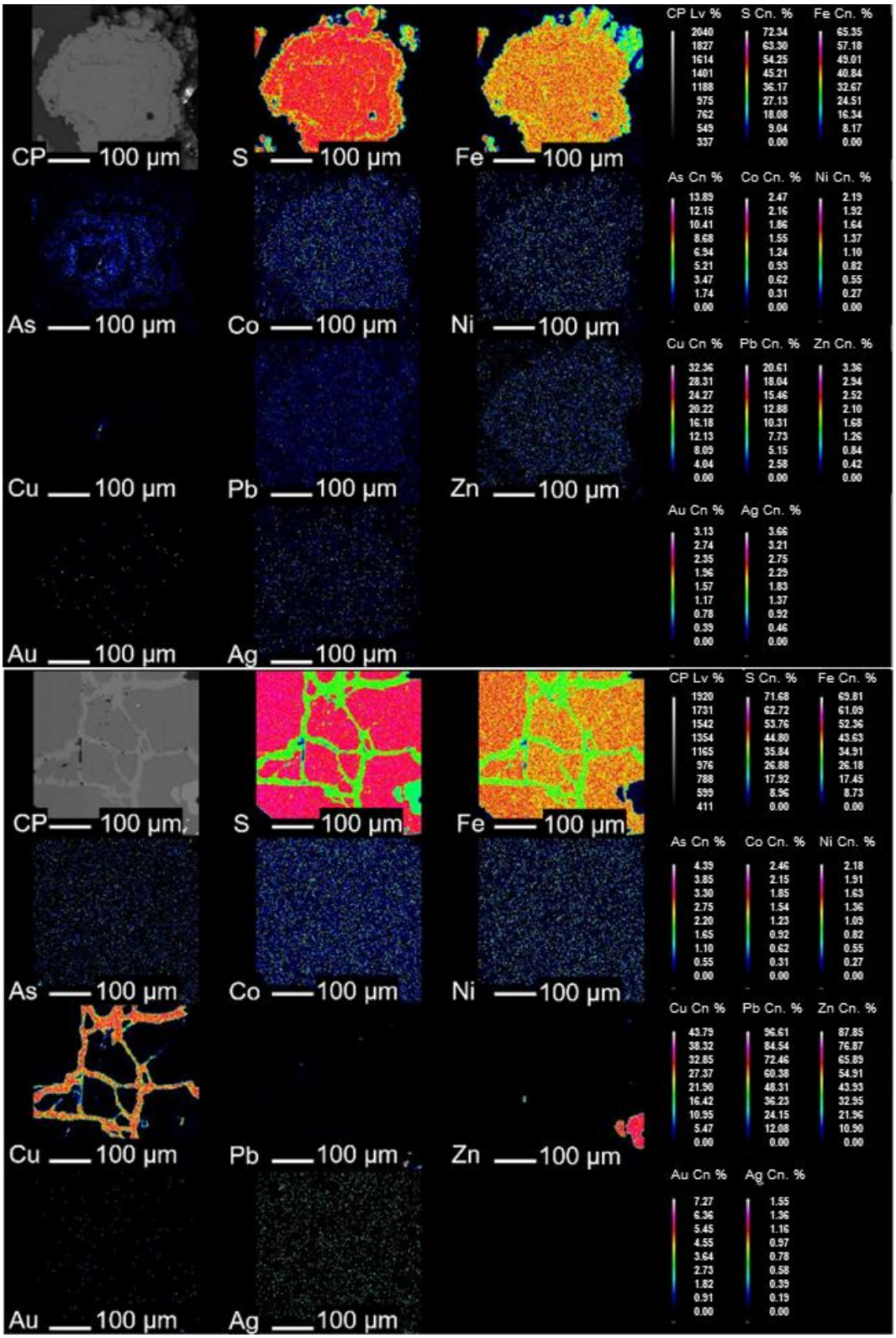

Fig. 5.13 Element mapping on (A) zoned pyrite from Stage 2 quartz-pyrite vein (Sample: KTDH04 16.30m, C01) and (B) fractured pyrite from Stage 4 hydrothermal breccia (Sample: KTDH04 93.50m, C16).

5.4 Discussion

The concentration of FeS in sphalerite is controlled by several factors, such as temperature, pressure and $a_{FeS,}$ and the variations in its concentration during crystal growth or over the span of the mineralization stages may suggest changes in the conditions during ore deposition (Zaw & Large, 1996). In the case of the sphalerite in Kay Tanda, there was no significant trend in the distribution of the FeS concentration in both zoned and unzoned sphalerite crystals. The changes in the FeS concentration were observed between Stage 4 sphalerite and Stage 6 sphalerite which showed a slight increase in FeS content towards the later mineralization stage. This may be caused by a slight decrease in the sulfur fugacity of the system (Scott & Barnes, 1971; Czamanske, 1974; Einaudi et al., 2003). This will be confirmed in Chapter 8 where the FeS content of Stage 4 and Stage 6 sphalerite will be used to determine the variations in sulfur fugacity in Kay Tanda by incorporating fluid inclusion microthermometry data collected from fluid inclusions in sphalerite. A bimodal distribution in the FeS content in Stage 6 was observed and the difference in the mode of the Stage 6 FeS concentration is small (0.2 mol%). It is difficult to determine with certainty if this variation is caused by significant changes in the ore forming conditions during Stage 6 ore formation, by a post-deposition re-equilibration event (Zaw & Large, 1996), or by the smaller number of analyzed samples compared to Stage 4.

Studies on the minor and trace element composition of sphalerite from several deposits have been done with the aim of correlating certain elemental concentrations or ratios to certain ore deposit types, or of deciphering which elements occur in solid solution or as micro-inclusions of minerals in sphalerite (Rai, 1978; Zaw & Large, 1996; Lin & Tiegeng, 1999; Cook et al., 2009; Ye et al., 2011). In Kay Tanda, Cd, Mn, Ga and Cu were detected in both Stage 4 and Stage 6 sphalerite. Cd solubility in sphalerite is extensive and forms a solid solution at high temperatures (Chen et al., 1988; Yang et al., 2015; Wen et al., 2016). The Cd content in Stage 4 sphalerite increases from deeper levels to shallower levels because of the higher fractionation of Cd at lower temperatures (Lin & Tiegeng, 1999; Yang et al., 2015; Wen et al., 2016). Ga in the form of Ga_2S_3 also exists in solid solution (Kramer et al., 1987). Mn is incorporated in the sphalerite crystal

structure by simple cation exchange ($Zn^{2+} \leftrightarrow Mn^{2+}$) (Cook et al., 2009). However, Cu exists in a limited solid solution and is hardly incorporated in the sphalerite crystal structure in significant quantities (Craig, 1973; Sugaki et al., 1987). As a result, chalcopyrite disease is formed (Barton & Bethke, 1987). In Kay Tanda, elevations in Cu content along the growth zones of sphalerite is attributed to chalcopyrite disease which developed along these crystallographic boundaries. Generally, there is no significant variation in the concentration of these minor elements in both Stage 4 and Stage 6 sphalerite (i.e. similar range of concentration and average concentration).

Bi, Ag and Cu are the minor elements that were detected in significant amounts in galena. Bi was detected in all analyzed samples while elevated Ag concentration was detected in certain galena occurrences such as (1) as inclusions in sphalerite and chalcopyrite and (2) as overgrowths around euhedral pyrite. Ag can be incorporated in significant amounts in the crystal structure of galena with the help of Bi^{3+} and/or Sb^{3+} via coupled substitution $Ag^{+} + (Bi, Sb)^{3+} \leftrightarrow 2Pb^{2+}$ (Chutas et al., 2008; Renock & Becker, 2011; George et al., 2015). In the analyzed samples, those with Bi concentrations exceeding 0.2 atomic % Bi contained detectable amounts of Ag which indicates that higher amounts of Bi aid the incorporation of Ag into the galena crystal structure. Moreover, the mol% Ag did not exceed mol % (Bi+Sb) which is consistent to the absence of submicrometer-scale inclusions of Ag-minerals (such as native Ag, acanthite, Ag-Cu-Sb- or Ag-Cu-As-sulfosalts and Ag-tellurides) in galena (George et al., 2015). Elevated Cu concentrations were observed in galena undergoing replacement by chalcopyrite. The LA-ICP-MS study by George et al. (2015) on galena suggested that Cu is incorporated in the galena crystal structure by solid solution.

Native gold is the dominant Au-bearing mineral in Kay Tanda, specifically in the Stage 4 base metal-bonanza Au mineralization. Since there was no observed Au mineral in the collected Stage 1 and Stage 2 veins despite elevated Au content based on the company's assay data, pyrite samples were analyzed for invisible Au hosted in pyrite. As-bearing pyrite can contain Au through absorption from hydrothermal fluids and this has been observed in several ore deposits, especially the Carlin-type and orogenic Au deposits (Large et al., 2009; Zhu et al., 2011). Elevations in As content are found in the rim of some of the analyzed Stage 2 zoned pyrite. However, elevations in Au content were not observed in these samples.

5.5 Conclusions

Native gold is the dominant Au-bearing mineral in Kay Tanda with Au content ranging from 81.2 to 94.2 atomic %. The analyzed crystals were mainly collected from Stage 4 veins and hydrothermal breccias which host the bonanza Au mineralization. The Au and Ag concentration and distribution in the analyzed native gold and electrum samples were homogenous based on element mapping. Au-bearing minerals were not observed in Stage 1 and 2 veins and hydrothermal breccia despite the elevated Au grades based on company assay. Stage 1 and 2 pyrite were analyzed for invisible gold but was not observed.

Elevated Ag contents correlated with elevated Au contents in assay data is attributed to the occurrence of Ag in native gold (up to 18.8 atomic % Ag) and electrum (up to 21.6 atomic % Ag). Elevated Ag contents correlated with elevated Pb contents in assay data were confirmed to be hosted (1) in Ag-bearing galena (up to 0.58 atomic % Ag) which may occur as sphalerite and chalcopyrite inclusions and as overgrowths around euhedral pyrite, and (2) in Bi-Pb-Cu-Ag minerals (up to 7.5 atomic % Ag) which occurs typically as chalcopyrite inclusions. Increasing Bi content in galena is directly correlated with increasing Ag content which is attributed to the coupled substitution $Ag^{+} + (Bi, Sb)^{3+} \leftrightarrow 2Pb^{2+}$. Samples containing more than 0.20 mol% Bi contained detectable amounts of Ag.

The base metal mineralization at Kay Tanda contains Fe-poor sphalerite. The FeS content of sphalerite increases from Stage 4 to Stage 6, which may be a consequence of decreasing sulfur fugacity from Stage 4 to Stage 6. It also contains detectable amounts of Mn, Cd, and Ga. Mn and Ga concentrations are relatively uniform throughout the Stage 4 and Stage 6 mineralization. Cd concentrations, however, appears to be inversely correlated with respect to depth. This is attributed to the increasing incorporation of Cd in sphalerite at lower temperatures. In the succeeding chapters, the FeS content of sphalerite will be used to determine sulfur fugacity conditions in Kay Tanda.

CHAPTER 6

FLUID INCLUSION STUDIES

6.1 Introduction

This chapter presents the results of the extensive fluid inclusion study conducted on Kay Tanda which involves fluid inclusion petrography, fluid inclusion microthermometry and fluid inclusion gas analysis. These techniques were conducted on every stage of the mineralization with workable fluid inclusion assemblages. The purposes of these studies are: (1) to determine the formation temperature throughout the mineralization stages by measuring the homogenization temperature, (2) to determine the salinity of the hydrothermal fluids derived from freezing and ice melting temperatures, (3) to determine the source of the hydrothermal fluids through the ratios of the gas compositions analyzed from the fluid inclusions, (4) to determine the mechanisms of ore deposition from the changes and trends of homogenization temperature and salinity, and (5) to estimate the boiling depth below the paleowater table and the minimum amount of erosion.

6.2 Methodology

Doubly polished thick sections (approximately 10 mm by 10 mm square thick wafers of 200-400 μm thickness) from representative samples from each mineralization stage were prepared for fluid inclusion study. More than 300 fluid inclusions from 24 samples containing quartz, sphalerite and anhydrite crystals were subjected to petrography and microthermometry. The identification of fluid inclusion assemblages (FIAs) was conducted using a Nikon ECLIPSE LV100NPOL polarizing microscope. The microthermometry measurement was conducted using a LINKAM THMS600 stage attached to a Nikon ECLIPSE LV100NPOL polarizing microscope at Akita University. Microthermometric analysis included the freezing temperature T_f, the ice melting temperature T_m, and the homogenization temperature of the fluid phase by vapor

disappearance T_h. Salinity was calculated using the equations of Bodnar (1993): Salinity = $0.00+1.78\theta-0.0442\theta^2+0.000557\theta^3$, where θ is the depression of the freezing point in degrees Celsius (Bodnar, 1993).

Quantitative gas analysis of fluid inclusions was conducted on 5 pure quartz samples. Microthermometry data were also collected from these samples. Quartz chips of 1.1 to 1.2 g were cleaned using 16 M nitric acid for 2 to 4 hours, were rinsed repeatedly with distilled water in ultrasonic bath, and then, were dried at 60 °C overnight. The samples were analyzed at the New Mexico Institute of Mining and Technology using an incremental crush scan method. The samples were crushed 8 to 10 times incrementally under 10^{-8} Torr vacuum at room temperature. The released gases, which included H_2, He, CH_4, H_2O, N_2, H_2S, Ar, and CO_2 (in mol %), were analyzed using dual quadrupole mass spectrometers. The precision for measuring CO_2, CH_4, N_2, and Ar is around 5% and for the other minor gas species around 10% (Blamey, 2012). The details of the methodology were previously described in Blamey (2012).

6.3 Fluid inclusion petrography and microthermometry

Fluid inclusion petrography and microthermometry were conducted on fluid inclusion assemblages (FIAs) in quartz crystals from the Stage 1 quartz veins, Stage 2 quartz veins, Stage 4 quartz-base metal sulfide veins, and the matrix of the Stage 4 hydrothermal breccias. Fluid inclusion assemblages in sphalerite crystals from the Stage 4 and Stage 6 veins and the matrix of the Stage 4 and Stage 6 hydrothermal breccias were also analyzed. Solitary primary fluid inclusions were also observed and analyzed from Stage 6 anhydrite crystals. There was no collected sample from the Stage 3 veins. The Stage 5 epidote-carbonate veins were very thin and did not contain workable fluid inclusions. Both primary and pseudosecondary fluid inclusions were documented. Primary fluid inclusions are those found along the growth zones of the crystals and represent the fluids that were trapped during crystal growth (Roedder, 1979). Pseudosecondary fluid inclusions are found along fractures that terminate within the crystals and

represent the fluids that were trapped along fractures that formed and healed during crystal growth (Roedder, 1979).

Fluid inclusions in quartz and anhydrite are generally smaller (around 10 to 20 µm) compared to those in sphalerite (around 10 to 100 µm). The analysis of fluid inclusions in sphalerite was challenging due to the high refractive index contrast between the fluid inclusions and the host mineral which made the inclusion walls appear very dark and thick. The analysis of fluid inclusions in anhydrite was also difficult because the majority of the fluid inclusions decrepitated before reaching homogenization. Fluid inclusions found in quartz, sphalerite and anhydrite crystals are dominantly liquid-rich liquid-vapor aqueous fluid inclusions though vapor-rich liquid-vapor fluid inclusions, liquid inclusions and vapor inclusions were also found in some samples. Abundant liquid inclusions were also observed in anhydrite crystals. Visible CO_2 was not found in any of the fluid inclusions analyzed. All analyzed fluid inclusions homogenized to liquid phase upon heating.

A summary of the microthermometry measurements of each fluid inclusion assemblage is shown in Table 6.1. A more detailed list of all fluid inclusions and their measurements are shown in Appendix E. Histograms of salinity and homogenization temperatures per sample per mineralization stage are also shown in Figures 6.1 and 6.2.

Table 6.1 Fluid inclusion microthermometry data of each fluid inclusion assemblage (FIA) in the Stage 1 quartz, Stage 2 quartz, Stage 4 quartz and sphalerite, and Stage 6 sphalerite and anhydrite.

Sample ID	Depth from present-day surface (m)	Elevation relative to present-day mean sea level (m)	Sample type	FIA number	Number of fluid inclusions	T_m range (°C)	T_m average (°C)	Salinity range (wt% NaCl eq.)	Salinity average (wt% NaCl eq.)	T_h range (°C)	T_h average (°C)	Homogenization phase
KTDH24 6.50m (F01)	6.1	+275.9	vein	1Qp1	4	-5.4	-5.4	8.4	8.4	246 to 268	258	Liquid
KTDH24 6.50m (F01)	6.1	+275.9	vein	1Qp2	7	-3.5 to -3.1	-3.4	5.1 to 5.7	5.5	208 to 248	238	Liquid
KTDH24 9.20m (F02)	8.6	+273.3	vein	1Qd1	3	-3.7 to -3.6	-3.6	5.9 to 6.0	5.9	203 to 238	221	Liquid
KTDH24 9.20m (F02)	8.6	+273.3	vein	1Qd2	3	-3.8 to -3.4	-3.6	5.6 to 6.2	5.8	207 to 221	216	Liquid
KTDH24 9.20m (F02)	8.6	+273.3	vein	1Qd3	4	-3.3	-3.3	3.4	3.4	204 to 242	223	Liquid
KTDH24 9.20m (F02)	8.6	+273.3	vein	1Qd4	3	-3.9 to -3.7	-3.8	6.0 to 6.3	6.2	222 to 263	240	Liquid
KTDH24 18.70 m (F05)	17.6	+264.4	vein	1Qd5	4	-3.8 to -3.1	-3.4	5.1 to 6.2	5.6	272 to 279	275	Liquid
KTDH24 18.70 m (F05)	17.6	+264.4	vein	1Qd6	2	-3.4 to -3.1	-3.3	5.1 to 5.6	5.3	227 to 241	234	Liquid
KTDH24 18.70 m (F05)	17.6	+264.4	vein	1Qd7	2	-3.7	-3.7	6.0	6.0	255 to 256	255	Liquid
KTDH23 29.25 m (J01)	24.8	+256.1	vein	2Qp12	5	-2.8 to -2.7	-2.7	4.5 to 4.7	4.5	237 to 280	251	Liquid
KTDH23 29.25 m (J01)	24.8	+256.1	vein	2Qd1	2	-3.0	-3.0	5.0	5.0	256 to 261	259	Liquid
KTDH23 29.25 m (J01)	24.8	+256.1	vein	2Qd2	2	-3.0	-3.0	5.0	5.0	263 to 267	265	Liquid
KTDH23 49.80m (J03)	42.2	+238.7	vein	2Qp4	3	-3.0 to -2.9	-3.0	4.8 to 5.0	4.9	264 to 268	266	Liquid
KTDH23 49.80m (J03)	42.2	+238.7	vein	2Qp5	2	-4.1 to -3.0	-3.5	5.0 to 6.6	5.8	261 to 271	266	Liquid
KTDH23 53.50m (J05)	45.4	+235.6	vein	2Qp6	2	-4.0 to -2.4	-3.2	4.0 to 6.5	5.2	255 to 262	259	Liquid
KTDH23 53.50m (J05)	45.4	+235.6	vein	2Qp7	7	-3.9 to -2.7	-3.6	4.5 to 6.3	5.9	253 to 330	289	Liquid
KTDH23 53.50m (J05)	45.4	+235.6	vein	2Qp8	2	-5.2 to -3.9	-4.6	6.3 to 8.1	7.2	263 to 267	265	Liquid
KTDH23 54.55m (J08)	46.3	+234.7	vein	2Qp9	4	-4.3 to -4.0	-4.1	6.5 to 6.9	6.6	298 to 310	304	Liquid
KTDH23 54.55m (J08)	46.3	+234.7	vein	2Qp10	2	-4.2 to -4.1	-4.2	6.6 to 6.7	6.7	306 to 311	309	Liquid
KTDH23 54.55m (J08)	46.3	+234.7	vein	2Qp11	3	-4.1	-4.1	6.6	6.6	262 to 266	264	Liquid
KTDH04 18.40m (C02)	18.4	+207.1	hbx	2Qp1	3	-3.0	-3.0	5.0	5.0	281 to 284	283	Liquid
KTDH04 18.40m (C02)	18.4	+207.1	hbx	2Qp2	5	-3.1 to -3.0	-3.1	5.0 to 5.1	5.0	302 to 315	307	Liquid

Sample ID	Depth from present-day surface (m)	Elevation relative to present-day mean sea level (m)	Sample type	FIA number	Number of fluid inclusions	T_m range (°C)	T_m average (°C)	Salinity range (wt% NaCl eq.)	Salinity average (wt% NaCl eq.)	T_h range (°C)	T_h average (°C)	Homogenization phase
KTDH04 18.40m (C02)	18.4	+207.1	hbx	2Qp3	3	-4.1 to -3.9	-4.1	6.3 to 6.6	6.5	304 to 320	314	Liquid
KTDH23 108.30m (J16)	91.9	+189.1	vein	4Qp17	2	-3.8 to -3.4	-3.6	5.6 to 6.2	5.9	265 to 296	281	Liquid
KTDH23 108.30m (J16)	91.9	+189.1	vein	4Qp18	6	-3.9	-3.9	6.3	6.3	255 to 272	262	Liquid
KTDH23 108.30m (J16)	91.9	+189.1	vein	4Qp19	7	-3.6 to -3.2	-3.4	5.3 to 5.9	5.6	267 to 304	278	Liquid
KTD194-12 110.45m (A13)	99.1	+165.9	vein	4Sp1	5	-3.1	-3.1	5.1	5.1	270 to 280	275	Liquid
KTD194-12 110.45m (A13)	99.1	+165.9	vein	4Qp1	2	-3.5 to -3.3	-3.4	5.4 to 5.7	5.6	320 to 324	322	Liquid
KTD194-12 110.45m (A13)	99.1	+165.9	vein	4Qp2	4	-3.5 to -3.0	-3.3	5.0 to 5.7	5.4	304 to 317	311	Liquid
KTD194-12 110.45m (A13)	99.1	+165.9	vein	4Qp3	2	-3.8 to -3.2	-3.5	5.3 to 6.2	5.7	322 to 360	341	Liquid
KTDH23 156.00m (J21)	132.5	+148.4	vein	4Qp20	3	-3.1	-3.1	5.1	5.1	286 to 292	289	Liquid
KTDH23 156.00m (J21)	132.5	+148.4	vein	4Qp21	2	-3.4	-3.4	5.6	5.6	316 to 318	317	Liquid
KTDH23 156.00m (J21)	132.5	+148.4	vein	4Qp22	7	-3.4 to -3.2	-3.3	5.3 to 5.6	5.4	298 to 310	304	Liquid
KTDH04 84.40m (C10)	84.4	+141.1	vein	4Qp4	4	-3.4 to -3.2	-3.4	5.3 to 5.6	5.5	307 to 340	326	Liquid
KTDH04 84.40m (C10)	84.4	+141.1	vein	4Qp5	4	-4.0 to -3.1	-3.5	5.1 to 6.5	5.7	303 to 309	305	Liquid
KTDH04 84.40m (C10)	84.4	+141.1	vein	4Qp6	10	-4.2 to -3.2	-3.4	5.3 to 6.7	5.6	254 to 299	267	Liquid
KTDH04 84.40m (C10)	84.4	+141.1	vein	4Qp7	7	-3.4 to -2.8	-3.3	4.7 to 5.6	5.4	267 to 274	270	Liquid
KTDH04 93.50m (C16)	93.5	+132.0	hbx	4Sp2	5	-3.9 to -3.1	-3.4	5.1 to 6.3	5.4	265 to 282	274	Liquid
KTDH04 93.85m (C17)	93.9	+131.7	hbx	4Sp3	4	-4.0 to -3.9	-3.9	6.3 to 6.5	6.3	253 to 277	265	Liquid
KTDH04 93.85m (C17)	93.9	+131.7	hbx	4Qd1	9	-4.0 to -3.3	-3.5	5.4 to 6.5	5.7	283 to 335	305	Liquid
KTDH04 101.40m (C20)	101.4	+124.1	hbx	4Sp4	17	-4.6 to -3.8	-4.1	6.2 to 7.3	6.5	290 to 308	301	Liquid
KTDH04 114.80m (C28)	114.8	+110.7	hbx	4Sp5	15	-4.1 to -3.6	-3.9	5.9 to 6.6	6.3	293 to 367	312	Liquid
KTDH04 114.80m (C28)	114.8	+110.7	hbx	4Qp8	5	-4.5 to -4.1	-4.2	6.6 to 7.2	6.7	296 to 315	307	Liquid
KTDH04 117.90m (C29)	117.9	+107.6	hbx	4Qp9	2	-2.9	-2.9	4.8	4.8	284 to 292	288	Liquid
KTDH04 117.90m (C29)	117.9	+107.6	hbx	4Qp10	4	-3.1 to -3.0	-3.0	5.0 to 5.1	5.0	293 to 295	294	Liquid
KTDH04 117.90m (C29)	117.9	+107.6	hbx	4Qp11	2	-3.1 to -3.0	-3.1	5.0 to 5.1	5.0	265 to 270	267	Liquid
KTDH04 117.90m (C29)	117.9	+107.6	hbx	4Qp12	2	-3.9 to -3.8	-3.8	6.2 to 6.3	6.2	287 to 288	288	Liquid

Sample ID	Depth from present-day surface (m)	Elevation relative to present-day mean sea level (m)	Sample type	FIA number	Number of fluid inclusions	T_m range (°C)	T_m average (°C)	Salinity range (wt% NaCl eq.)	Salinity average (wt% NaCl eq.)	T_h range (°C)	T_h average (°C)	Homogenization phase
KTDH04 169.20m (C33)	169.2	+56.3	vein	4Sp6	4	-4.1 to -3.8	-3.9	6.2 to 6.6	6.4	298 to 303	301	Liquid
KTDH04 169.20m (C33)	169.2	+56.3	vein	4Sp7	5	-3.5 to -3.3	-3.4	5.4 to 5.7	5.6	285 to 343	299	Liquid
KTDH04 169.20m (C33)	169.2	+56.3	vein	4Qp13	7	-3.6 to -3.3	-3.5	5.4 to 5.9	5.7	292 to 296	294	Liquid
KTDH04 169.20m (C33)	169.2	+56.3	vein	4Qp14	5	-4.1 to -3.4	-3.6	5.6 to 6.6	5.8	280 to 331	303	Liquid
KTDH04 169.20m (C33)	169.2	+56.3	vein	4Qp15	2	-3.7 to -3.4	-3.5	5.6 to 6.0	5.8	292 to 297	294	Liquid
KTDH04 169.20m (C33)	169.2	+56.3	vein	4Qp16	10	-3.6 to -2.9	-3.4	4.8 to 5.9	5.6	295 to 301	298	Liquid
KTDH04 169.20m (C33)	169.2	+56.3	vein	4Qd2	4	-3.3	-3.3	5.4	5.4	292 to 296	295	Liquid
KTDH04 228.60m (C42)*	228.6	-3.1	vein	6Ao*	4	-2.1 to -1.6	-1.7	2.7 to 3.6	2.9	196 to 270	238	Liquid
KTDH04 229.80m (C43)	229.8	-4.3	hbx	6Sp1	6	-3.1 to -2.8	-2.9	4.7 to 5.1	4.8	278 to 309	295	Liquid
KTDH04 229.80m (C43)	229.8	-4.3	hbx	6Sp2	10	-3.1 to -3.0	-3.1	5.0 to 5.1	5.1	272 to 285	279	Liquid
KTDH04 229.80 m (C43-1)	229.8	-4.3	hbx	6Sp4	2	-3.1	-3.1	5.1	5.1	278 to 284	281	Liquid
KTDH04 229.80 m (C43-1)	229.8	-4.3	hbx	6Sp5	2	3.5 to -3.1	-3.3	5.1 to 5.7	5.4	263 to 290	276	Liquid
KTDH04 229.80 m (C43-1)	229.8	-4.3	hbx	6Sp6	7	-3.1 to -2.8	-2.8	4.7 to 5.1	4.8	261 to 275	270	Liquid
KTDH04 229.80 m (C43-1)	229.8	-4.3	hbx	6Sp7	2	-3.0 to -2.8	-2.9	4.7 to 5.0	4.8	241 to 253	247	Liquid
KTDH04 232.30 m (C44)	232.3	-6.8	hbx	6Sp3	7	-2.8 to -2.5	-2.7	4.2 to 4.7	4.5	279 to 334	293	Liquid
KTDH04 232.30 m (C44-1)	232.3	-6.8	hbx	6Sp8	14	-2.9 to -2.7	-2.8	4.5 to 4.8	4.7	268 to 297	282	Liquid
KTDH04 232.30 m (C44-1)	232.3	-6.8	hbx	6Sp9	3	-3.2 to -2.8	-3.0	4.7 to 5.3	4.9	262 to 293	279	Liquid
KTDH04 232.30 m (C44-1)	232.3	-6.8	hbx	6Sp10	2	-2.8	-2.8	4.7	4.7	284 to 296	290	Liquid
KTDH04 239.70m (C45)*	239.7	-14.2	vein	6Ao*	2	-2.1 to -2.8	-2.5	3.6 to 4.7	4.1	175 to 318	246	Liquid

Note: *The fluid inclusions measured from Stage 6 anhydrite crystals are solitary (6Ao*) and do not exist as fluid inclusion assemblages.

Explanation: hbx – matrix of hydrothermal breccia, FIA number: 1st number – mineralization stage, 1st letter – Q for quartz, S for sphalerite, and A for anhydrite, 2nd letter – p for primary fluid inclusion, d for pseudosecondary fluid inclusion, and o for solitary fluid inclusions, 2nd number – number of fluid inclusion assemblage, T_m – ice melting temperature, T_h – homogenization temperature.

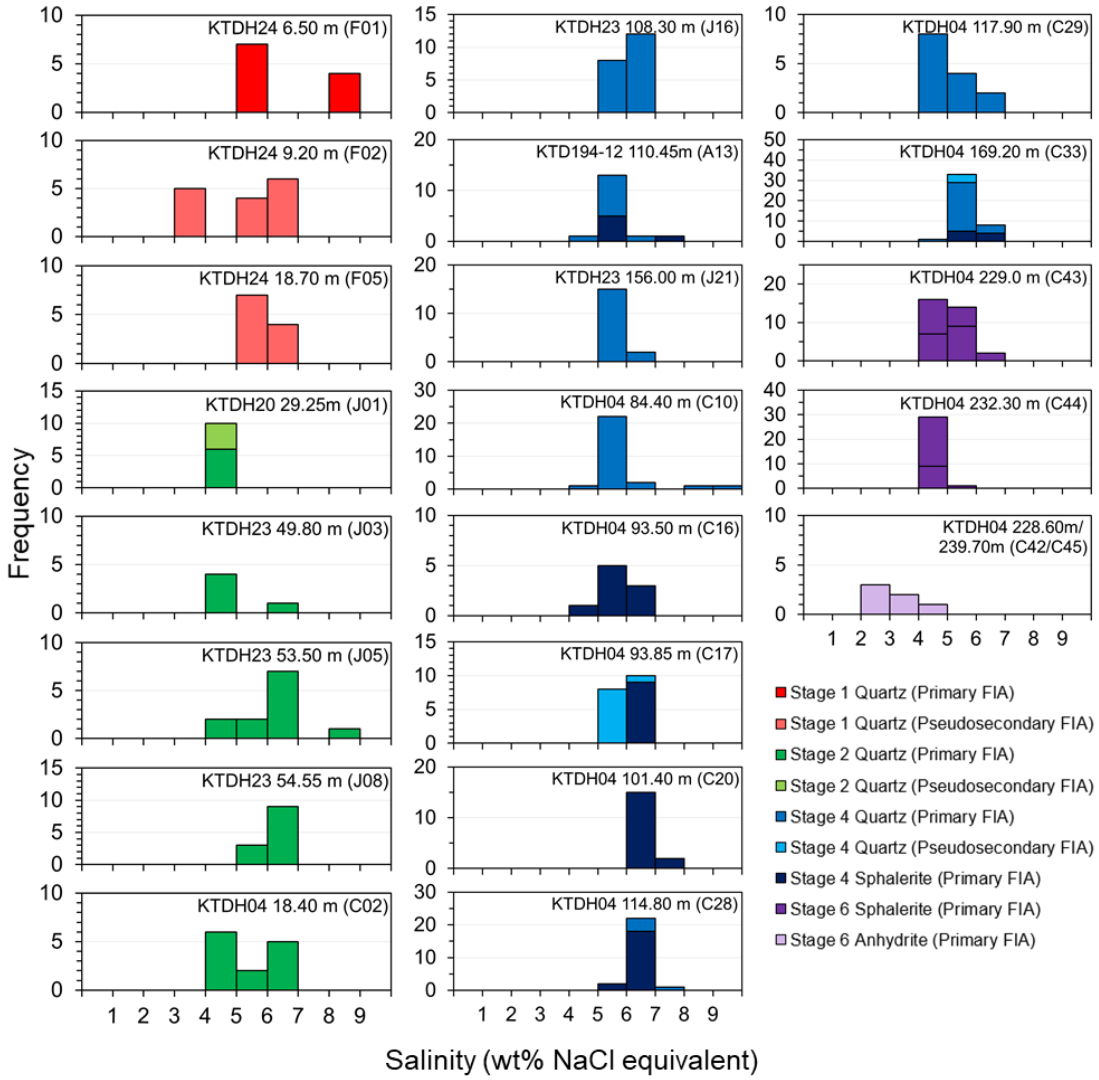

Fig. 6.1 Salinity histograms of measured fluid inclusions from the Stage 1, Stage 2, Stage 4 and Stage 6 mineralization.

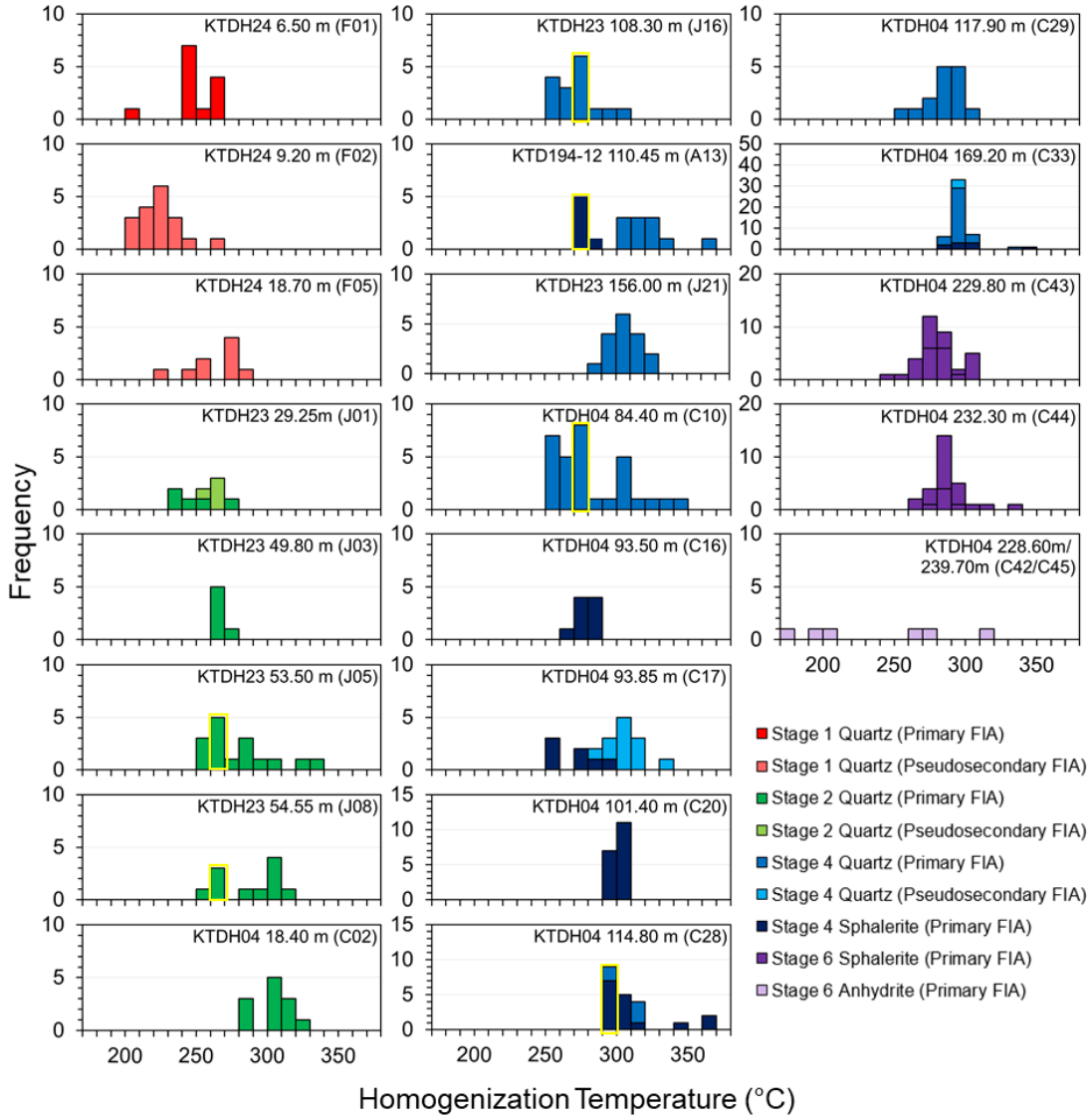

Fig. 6.2 Homogenization temperature histograms of the fluid inclusions from the Stage 1, Stage 2, Stage 4 and Stage 6 mineralizations. Skewness to higher temperatures indicate boiling condition. The yellow boxes indicate the trapping temperature for the histograms showing boiling condition.

6.3.1 Stage 1

Fluid inclusions in quartz crystals from crustiform quartz veins were examined. A total of 11 primary fluid inclusions from 2 FIAs and 21 pseudosecondary fluid inclusions (Fig. 6.3A-B) from 7 FIAs were analyzed from 3 Stage 1 quartz veins. Both primary and pseudosecondary fluid inclusions are liquid-rich liquid-vapor fluid inclusions and are generally around 10 µm in size. The salinity of primary fluid inclusions ranges from 5.1 to 8.4 wt% NaCl equivalent while the salinity of the pseudosecondary fluid inclusions ranges from 3.4 to 6.3 wt% NaCl equivalent (Fig. 6.1). The average salinity of Stage 1 fluid inclusions is 5.8 wt% NaCl equivalent. The homogenization temperature of primary and pseudosecondary fluid inclusions ranges from 208 °C to 268 °C and 203 °C to 279 °C, respectively. The mode of the homogenization temperature of primary fluid inclusions is from 240 °C to 250 °C and mode of the pseudosecondary fluid inclusions varies from 220 °C to 230 °C and 270 °C to 280 °C (Fig. 6.2). The average homogenization temperature of Stage 1 fluid inclusions is 241 °C.

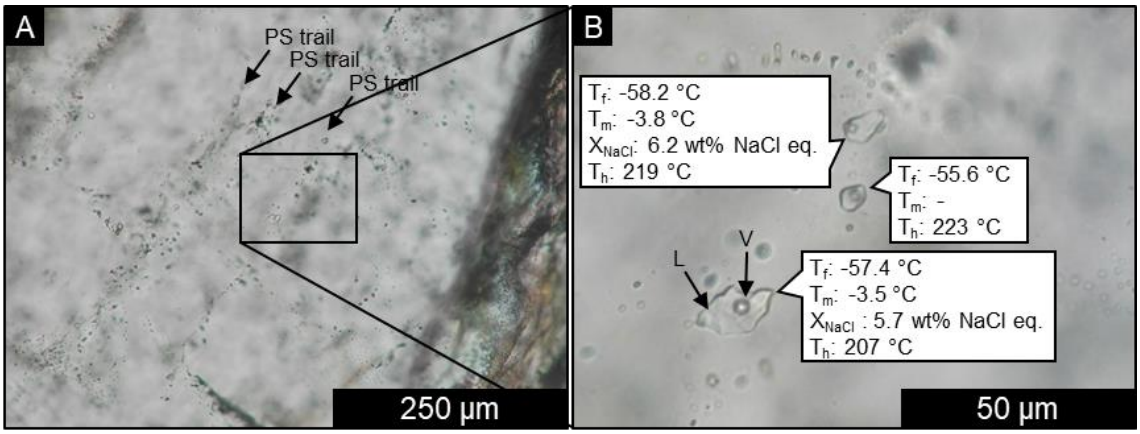

Fig. 6.3 Representative photomicrographs of fluid inclusions from the Stage 1 mineralization. (A) Trails of pseudosecondary fluid inclusions in a quartz crystal from a Stage 1 quartz vein. (B) Pseudosecondary FIA in a Stage 1 quartz vein (Sample: KTDH24 9.20m, F02). Abbreviations: eq. – equivalent, L – liquid, V – vapor, PS – pseudosecondary fluid inclusion, T_f – freezing temperature, T_m – melting temperature, X_{NaCl} – salinity, T_h – homogenization temperature.

6.3.2 Stage 2

A total of 41 primary fluid inclusions from 12 FIAs (Fig. 6.4A-C) and 4 pseudosecondary fluid inclusions from 2 FIAs (Fig. 6.4D) were identified and analyzed from 5 Stage 2 crustiform veins. The majority of the fluid inclusions are liquid-rich liquid-vapor inclusions but some are vapor-rich liquid-vapor fluid inclusions (Fig. 6.4B-C). Their sizes range from 10 to 20 µm. The salinity of the primary and pseudosecondary inclusions ranges from 4.0 to 8.1 wt% NaCl equivalent with an average of 5.7 wt% NaCl equivalent (Fig. 6.1). The homogenization temperature of the primary fluid inclusions and the pseudosecondary fluid inclusions ranges from 237 °C to 330 °C and 256 °C to 267 °C, respectively. The mode of the homogenization temperature from 3 samples is from 260 °C to 270 °C, while the other 2 samples is from 300 °C to 310 °C (Fig. 6.2). The average homogenization temperature of Stage 2 fluid inclusions is 279 °C.

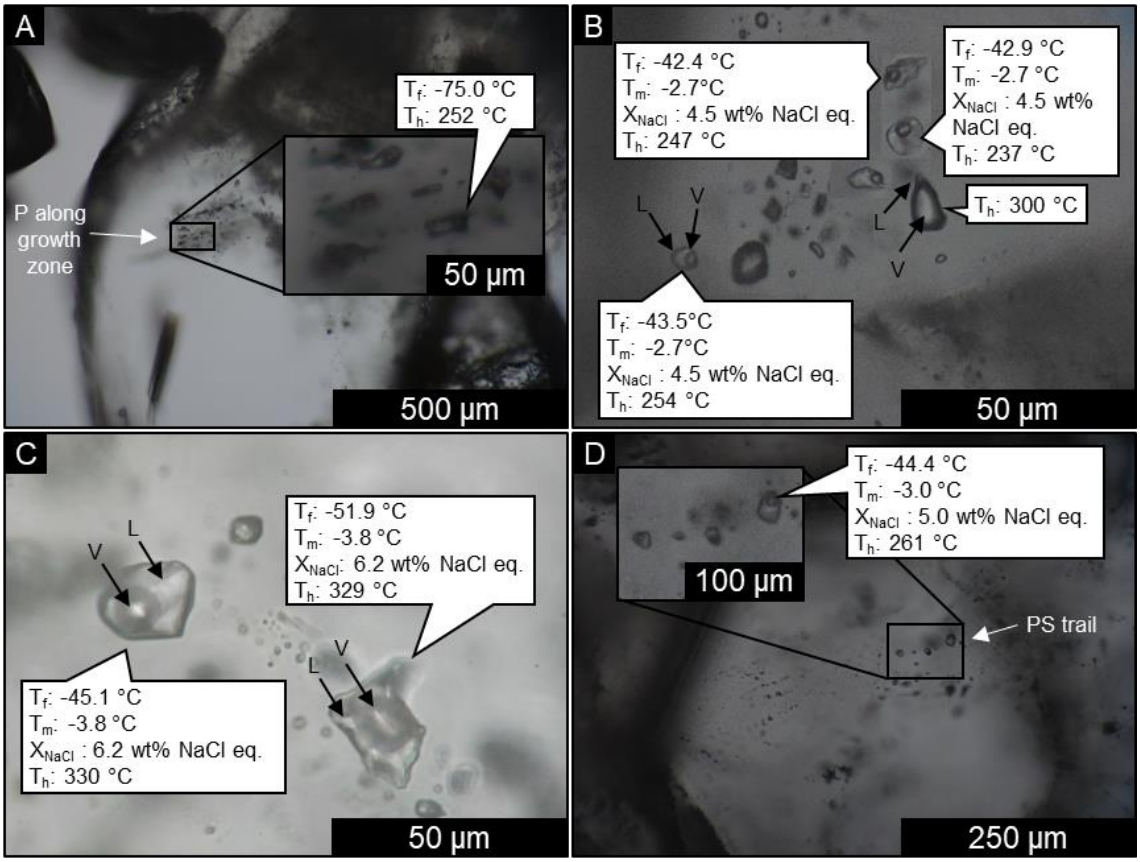

Fig. 6.4 Representative photomicrographs of fluid inclusions from the Stage 2 mineralization. (A) Primary FIA along growth zones in a quartz crystal from a Stage 2 vein (Sample: KTDH23 29.25 m, J01) (B) Heterogeneous trapping of liquid-vapor, liquid, and vapor inclusions in a quartz crystal from a Stage 2 quartz vein (Sample: KTDH23 29.25 m, J01) (C) Fluid inclusions

with variable liquid and vapor proportions in a quartz crystal from a Stage 2 quartz vein (Sample: KTDH23 53.50m, J05). (D) Trail of pseudosecondary FIA in a quartz crystal from a Stage 2 quartz vein (Sample: KTDH23 29.25 m, J01). Abbreviations: eq. – equivalent, L – liquid, V – vapor, P – primary fluid inclusion, PS – pseudosecondary fluid inclusion, T_f – freezing temperature, T_m – melting temperature, X_{NaCl} – salinity, T_h – homogenization temperature.

6.3.3 Stage 4

Fluid inclusions in quartz and sphalerite crystals from the Stage 4 veins (Fig. 6.5A-B) and the matrix of the Stage 4 hydrothermal breccias were analyzed (Fig. 6.5C-D). A total of 99 primary fluid inclusions from 22 FIAs and 13 pseudosecondary fluid inclusions from 2 FIAs from quartz crystals were observed, while 55 primary fluid inclusions from 7 FIAs from sphalerite crystals were observed. The fluid inclusions in quartz crystals are generally smaller (around 10 to 50 µm in diameter, but are commonly 10 to 20 µm across) than those in sphalerite crystals (around 10 to 100 µm in diameter, but are commonly 10 to 20 µm across). The majority of the fluid inclusions are liquid-rich liquid-vapor fluid inclusions but some are vapor-rich liquid-vapor fluid inclusions, vapor inclusions and liquid inclusions (Fig. 6.5A, C). The majority of the fluid inclusions in sphalerite exhibit negative crystal shape (Fig. 6.5B, D). The salinity obtained from primary fluid inclusions in quartz crystals ranges from 4.7 to 7.2 wt% NaCl equivalent, while the salinity from the pseudosecondary fluid inclusions ranges from 5.4 to 6.5 wt% NaCl equivalent (Fig. 6.1). The homogenization temperature from primary fluid inclusions in quartz ranges from 254 °C to 360 °C, while those from pseudosecondary fluid inclusions ranges from 283 °C to 335 °C (Fig. 6.2). The salinity and homogenization temperature obtained from primary fluid inclusions from sphalerite crystals ranges from 5.1 to 7.3 wt% NaCl equivalent (Fig. 6.1) and 253 °C to 367 °C (Fig. 6.2), respectively. The average homogenization temperature of the primary fluid inclusions in quartz, pseudosecondary fluid inclusions in quartz, and primary fluid inclusions in sphalerite are 296 °C, 300 °C, and 289 °C, respectively. The average salinity is 5.7 wt% NaCl equivalent.

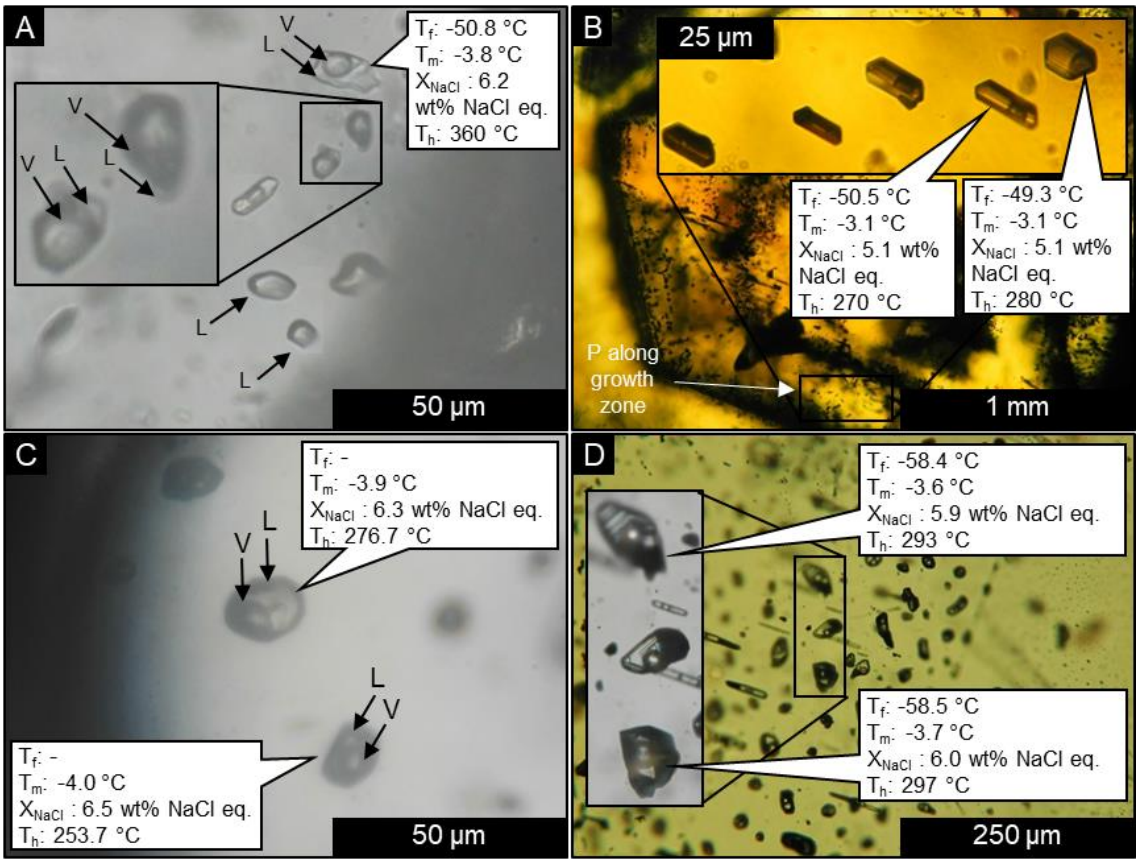

Fig. 6.5 Representative photomicrographs of fluid inclusions from the Stage 4 mineralization. (A) Heterogeneous trapping of liquid-vapor, liquid, and vapor inclusions in quartz crystal from a Stage 4 quartz ± adularia ± calcite vein (Sample: KTD194-12 110.45m, A13). (B) Primary FIA along the growth zones of a sphalerite crystal from a Stage 4 quartz ± adularia ± calcite vein (Sample: KTD194-12 110.45m, A13). (C) Fluid inclusions of variable liquid and vapor proportions in a sphalerite crystal from Stage 4 hydrothermal breccia (Sample: KTDH04 93.85m, C17). (D) Primary FIA along the growth zone of a sphalerite crystal from Stage 4 hydrothermal breccia (Sample: KTDH04 114.80m, C28). Abbreviations: eq. – equivalent, L – liquid, V – vapor, P – primary fluid inclusion, T_f – freezing temperature, T_m – melting temperature, X_{NaCl} – salinity, T_h – homogenization temperature.

6.3.4 Stage 6

Fluid inclusions in sphalerite from the Stage 6 veins and the matrix of the Stage 6 hydrothermal breccias (Fig. 6.6A) were observed. A total of 55 primary fluid inclusions from 10 FIAs were analyzed. The fluid inclusion sizes range from 10 to 70 µm but the majority are about 10 to 20 µm. The majority of the fluid inclusions are liquid-rich liquid-vapor fluid inclusions but some are vapor-rich fluid inclusions. The salinity ranges from 4.2 to 5.7 wt% NaCl equivalent and the average is 4.8 wt% NaCl equivalent (Fig. 6.1). The homogenization temperature ranges from 241 °C to 334 °C. The mode of the homogenization temperature of Stage 6 fluid inclusions is 270 °C to 290 °C while the average is 279 °C (Fig. 6.2). A total of 15 solitary primary fluid inclusions were measured in coarse-grained anhydrite crystals from Stage 6 veins and hydrothermal breccia samples (Fig. 6.6B). Nine fluid inclusions decrepitated before reaching homogenization. Their sizes range from 10 to 25 µm. These samples show a cubic to rectangular shape and are mostly liquid-rich liquid-vapor fluid inclusions. Abundant liquid fluid inclusions were also found. The salinity ranges from 2.7 to 4.7 wt% NaCl equivalent with an average of 3.3 wt % NaCl equivalent while the homogenization temperature ranges from 175 to 318 °C with an average of 241 °C.

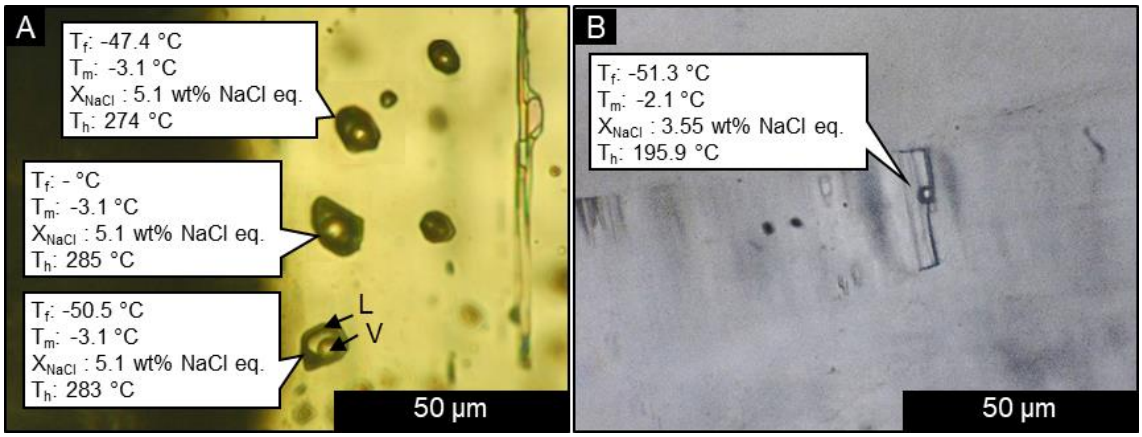

Fig. 6.6 Representative photomicrographs of fluid inclusions from the Stage 6 mineralization. (A) Primary FIA in a sphalerite crystal from Stage 6 hydrothermal breccia (Sample: KTDH04 229.80m, C43). (B) Solitary primary fluid inclusions in anhydrite crystal from Stage 6 vein (Sample: KTDH04 228.60m, C42). Abbreviations: eq. – equivalent, L – liquid, V – vapor, T_f – freezing temperature, T_m – melting temperature, X_{NaCl} – salinity, T_h – homogenization temperature.

6.4 Fluid inclusion gas analysis

Quantitative fluid inclusion gas analysis was conducted on several quartz crystals obtained from the Stage 2 (2 samples) and Stage 4 (3 samples) veins. Fluid inclusion gas compositions, which includes H_2, He, CH_4, H_2O, N_2, H_2S, Ar, and CO_2, and gas content ratios, which includes N_2/Ar, CO_2/CH_4, Ar/He, and CO_2/N_2, are summarized in Table 6.2. The fluid inclusion gas analysis data were plotted on discrimination diagrams of Norman and Moore (1999), Blamey and Norman (2002), Norman and Musgrave (1994), Giggenbach (1986), and Giggenbach and Poreda (1993) which may be used to determine possible fluid sources (Fig. 6.7) and fluid processes (Fig. 6.8).

The fluid inclusion gas content of the Stage 2 and Stage 4 have the same order of magnitude. The dominant gases in both stages are H_2O and CO_2. The H_2O content of the Stage 4 fluid inclusions is slightly higher than the Stage 2 fluid inclusions. The H_2O content of the Stage 4 fluid inclusions is 99.69-99.79 mol% while the H_2O content of the Stage 2 fluid inclusions is 99.45-99.63 mol%. On the other hand, the Stage 2 fluid inclusions contain slightly higher amounts of non-aqueous gas (0.37-0.55%) than the Stage 4 fluid inclusions (0.21-0.31%). The Stage 2 fluid inclusion gases contain 0.2841-0.4095 mol% CO_2, 0.0778-0.1370 mol% N_2, 0.0023-0.0038 mol% CH_4, 0.0011-0.0017 mol% Ar and 0.0001-0.0003 mol% H_2S while Stage 4 contains 0.2018-0.2701 mol% CO_2, 0.0084-0.0349 mol% N_2, 0.0012-0.0027 mol% CH_4, 0.002-0.007 mol% Ar and 0.0001-0.0002 mol% H_2S.

Table 6.2 Quantitative fluid inclusion gas analysis data from the Stage 2 quartz and Stage 4 quartz.

	KTDH23 53.50m (J05)	**KTDH23 54.55m (J08)**	**KTDH23 108.30m (J16)**	**KTDH23 156.00m (J21)**	**KTDH04 117.90m (C29)**
Mineralization stage	2	2	4	4	4
Crush number	10	10	8	8	9
Weighted mean (mol%)					
H_2	0.0000	0.0002	0.0031	0.0005	0.0002
He	0.0000	0.0000	0.0000	0.0000	0.0000
CH_4	0.0038	0.0023	0.0027	0.0013	0.0012
H_2O	99.63	99.45	99.75	99.79	99.69
N_2	0.0778	0.1370	0.0122	0.0084	0.0349
H_2S	0.0003	0.0001	0.0002	0.0001	0.0002
Ar	0.0011	0.0017	0.0003	0.0002	0.0007
CO_2	0.2841	0.4095	0.2322	0.2018	0.2701
Total non-aqueous gas (mol)	6.27E-10	2.84E-10	1.35E-10	1.10E-10	1.14E-10
N_2/Ar	73.70	81.30	48.79	37.14	52.32
CO_2/CH_4	74.61	178.25	84.78	150.35	222.50
Ar/He	31.93	71.05	18.86	11.78	46.94
CO_2/N_2	3.65	2.99	18.99	24.04	7.74
Total non-aqueous gas (mol%)	0.37	0.55	0.25	0.21	0.31

6.5 Discussion

6.5.1 Source of hydrothermal fluids

The gas composition of fluid inclusions can be utilized to determine potential sources of hydrothermal fluids in ore deposits (Giggenbach, 1986; Giggenbach & Poreda, 1993; Norman & Musgrave, 1994; Blamey, 2012; Takahashi et al., 2017). Fluid inclusion gas analysis data on the Stage 2 and Stage 4 quartz veins, which represent the two mineralization styles in Kay Tanda, suggest that shallow meteoric water is an important component of the hydrothermal system of Kay Tanda (Fig. 6.7A-E). Shallow meteoric waters are characterized by similar gas ratios as air-saturated water (ASW) with a N_2/Ar ratio of 38 and a high CO_2/CH_4 ratio due to the low concentrations of CH_4 in meteoric waters (Norman & Musgrave, 1994; Blamey, 2012). The majority of the data plotted in the meteoric water field in both CO_2/CH_4 vs N_2/Ar diagram by Norman and Moore (1999) and Ar/He vs N_2/Ar diagram by Blamey and Norman (2002) which discriminate potential fluid sources (Fig. 6.7 A-B) (Blamey, 2012). One sample from the Stage 2 mineralization plot closer to the boundary between shallow meteoric water and magmatic water which may also indicate a contribution from magmatic fluid which may be derived from the Dacite Porphyry Intrusives at depth (Fig. 6.7C). The circulation of the hydrothermal fluids in the fractured host rocks of the Talahib Volcanic Sequence formed the pervasive argillic alteration in the early stages. On the contrary, most of the data from Stage 4 mineralization plotted within the meteoric water field. Meteoric water later circulated into the deeper levels of the deposit. This can also be seen in the N_2/100-10He-Ar ternary plot by Norman and Musgrave (1994), where most of the data from Stage 2 mineralization plotted closer to the magmatic field while most of the data from the Stage 4 mineralization plotted within the shallow- and deeply-circulated meteoric water field (Fig. 6.7C).

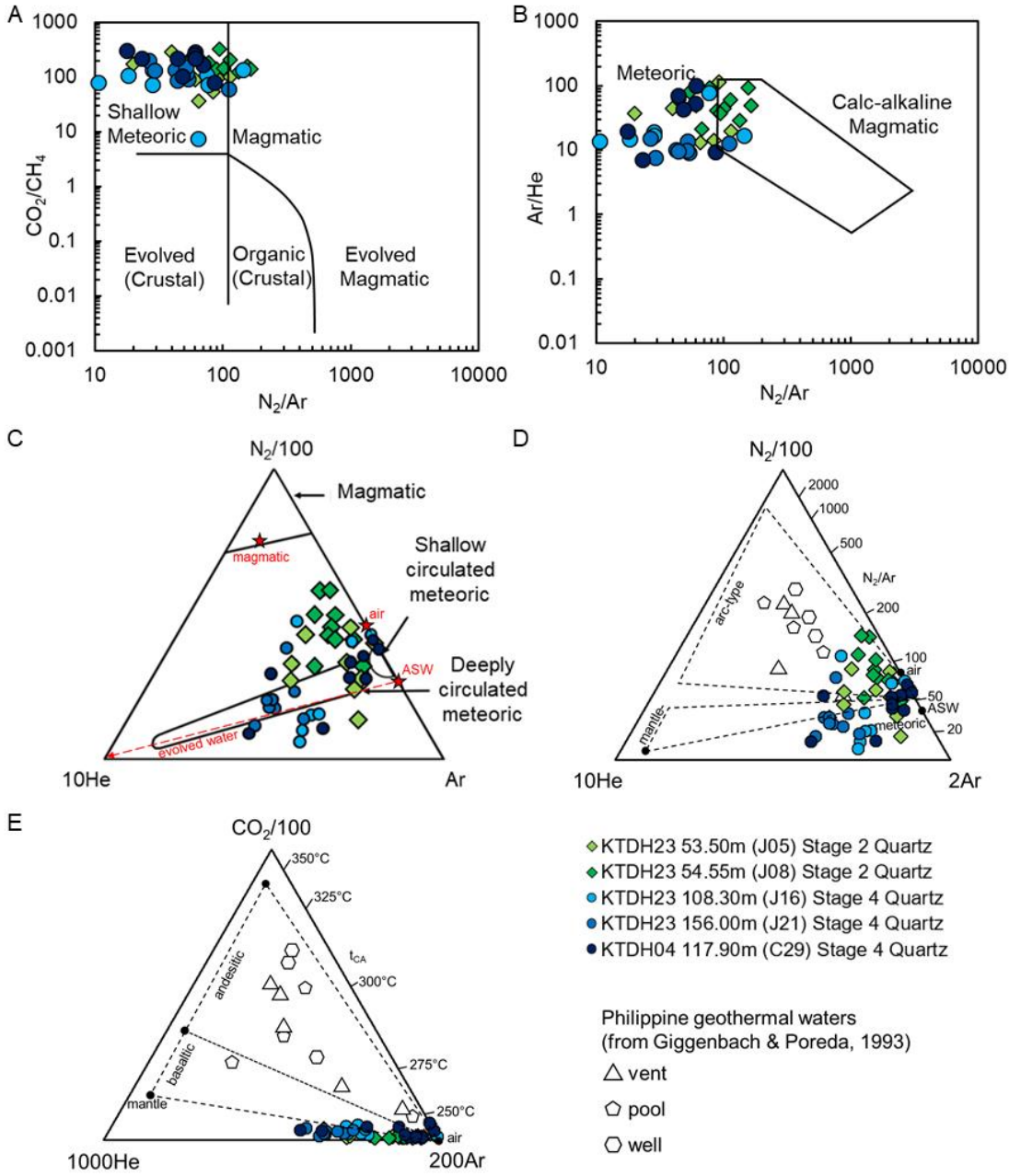

Fig. 6.7 Quantitative fluid inclusion gas analysis data from Stage 2 quartz and Stage 4 quartz plotted on discrimination diagrams. (A) CO_2/CH_4 vs N_2/Ar diagram by Norman and Moore (1999) (B) Ar/He vs N_2/Ar diagram by Blamey and Norman (2002), (C) $N_2/100$-10He-Ar ternary diagram by Norman and Musgrave (1994) (black fields) after Giggenbach (1986) (red stars) (D) $N_2/100$-10He-2Ar diagram by Giggenbach and Poreda (1993) and (E) $CO_2/100$-1000He-200Ar ternary diagram by Giggenbach and Poreda (1993). (A) The shallow meteoric water field was delineated based on the similar N_2/Ar ratio as ASW and high CO_2/CH_4 ratio due to low concentrations of CH_4 in meteoric fluids (Norman & Musgrave, 1994). The magmatic field was delineated based on the collected volcanic gases from various volcanoes around the world as reported by Giggenbach (1996) which showed N_2/Ar ratios exceeding 100s and high CO_2/CH_4 ratio (Norman & Musgrave, 1994). The evolved crustal and evolved magmatic fields are characterized by the high CH_4 content of basinal fluids as shown in the study of fluid inclusion gases from Hansonburg MVT deposit (Norman et al., 1985; Blamey, 2012). The

organic (crustal) field was included due to the reported occurrences of excess nitrogen derived from breakdown of protein in some geothermal systems (Norman & Moore, 1999). (B) The magmatic field was labelled specifically as "calc-alkaline magmatic" because the field was derived from the empirical data collected by Giggenbach (1996) from various calc-alkaline systems (Blamey & Norman, 2002). (C) Giggenbach (1986) reported the N_2, He and Ar composition of the principal sources of geothermal fluids (red stars) based on his study in the Taupo Volcanic Zone. Norman and Musgrave (1994) extended the magmatic field based on the collected data from Copper Flat and Questa porphyry copper deposits, and the deeply circulating meteoric water field based on the collected data from Valles and Rotorua geothermal fields. (D) This diagram discriminates the potential sources of N_2 into arc-type (subducted sediments) and mantle-derived. Upper mantle-derived fluids are characterized by high He content and N_2 is primarily derived from subducted sediments (Giggenbach & Poreda, 1993). (E) This diagram shows the compositional fields of gases derived from andesitic and basaltic magmatism. Also, t_{CA} is the temperature representing attainment of equilibrium during the removal of CO_2 in the form of bicarbonate or carbonate mineral (Giggenbach, 1992b; Giggenbach & Poreda, 1993). The variations in the plots from the same mineralization stage may be attributed to the sequential extraction of FI population per crush sequence (Blamey, 2010).

The N_2/100-10He-2Ar and CO_2/100-1000He-200Ar ternary diagrams by Giggenbach and Poreda (1993) demonstrated the application of gas compositions in determining the sources of hydrothermal fluids in several volcanic-hydrothermal systems in the Philippines. Similar to Figure 6.7C, most of the data plotted in the N_2/100-10He-2Ar ternary diagram approach the meteoric water composition which has similar gas ratios as end-members air and air-saturated water (ASW) (Fig. 6.7D). Like the gas composition of the several Philippine geothermal water samples presented by Giggenbach and Poreda (1993), most of the samples from Kay Tanda plot within the arc-type-derived fluid field approaching meteoric water composition which is consistent to the tectonic setting of the southern Batangas area (Fig. 6.7D). The higher Ar content in Stage 4 quartz may be caused by a higher proportion of meteoric water during its vein formation. In the CO_2/100-1000He-200Ar ternary diagram, the both Stage 2 and 4 data clustered towards the meteoric water composition along the basaltic magmatism field which indicates a possible mixing of basaltic magma-derived component and a larger proportion of meteoric water during vein formation (Fig. 6.7E).

Fluid inclusion data also show that the hydrothermal fluids of Kay Tanda have moderate salinity (>4 wt% NaCl equivalent). This moderate salinity and the deposit's proximity to the sea

(less than 1 km from the coastline of southern Batangas) suggest a possible incorporation of seawater into the hydrothermal system of Kay Tanda. Such incorporation of seawater has been observed in some active geothermal systems such as in Milos Island, Greece (Naden et al, 2005).

6.5.2 Mechanism of ore deposition

Boiling of hydrothermal fluids is an effective mechanism for ore deposition in epithermal deposits. This has been documented in several studies conducted on a number of epithermal deposits around the world (Bodnar et al., 1985; Cooke & Simmons, 2000; André-Mayer et al., 2002; Canet et al., 2011; Shimizu, 2014; Takahashi et al., 2017). In this study, boiling has been found to be an important mechanism for the Au-Ag mineralization in the Stage 2 veins and the Au-base metal mineralization in the Stage 4 veins and hydrothermal breccias. The evidence include the documented adularia textures (Dong & Morrison, 1995), the fluid inclusion assemblages which show heterogeneous trapping or the coexistence of liquid-rich and vapor-rich fluid inclusions (Bodnar et al., 1985; Moncada et al., 2012), and the skewness of homogenization temperature histograms to higher temperatures (Brown, 1998).

The Stage 2 mineralization is hosted by Au-Ag-bearing crustiform and colloform quartz veins which were mainly controlled by NE-trending extensional structures (Rohrlach & Fredericksen, 2008, unpublished data). The formation of the NE-trending structures caused a sudden release in the pressure of the hydrothermal fluids which eventually led to boiling and precipitation of ore minerals. Several evidence for boiling conditions were observed in the Stage 2 veins. The coexistence of liquid-rich and vapor-rich liquid-vapor fluid inclusions were observed in some quartz crystals (Fig. 6.4B-C). The corresponding homogenization temperature histograms also show skewness to higher temperatures which indicates that the fluids were trapped under boiling conditions (Fig. 6.2). Since temperature corrections were negligible at pressures <10 MPa for a 5 wt% NaCl solution (Potter, 1977), the mode of the homogenization temperature is regarded as the trapping temperature under boiling condition. In Stage 2 veins, the trapping temperature of the fluid inclusions is approximately around 260 °C to 270 °C. Moreover, the samples which

exhibited boiling conditions contain 1 ppm to 4 ppm Au based on company's assay data (by every 1 meter of core) which shows the relationship of boiling and Au mineralization in Stage 2 veins.

The Stage 4 veins and hydrothermal breccias also show different evidence of boiling conditions. Adularia may indicate boiling conditions based on the studies done in active geothermal systems (Browne & Ellis, 1970; Browne, 1978; Hedenquist & Henley, 1985; Hedenquist, 1990). Adularia, especially with a rhombic shape, is a good indicator for prolonged extensive boiling and is associated with effective Au mineralization (Dong & Morrison, 1995). Rhombic adularia was observed in several Stage 4 quartz veins (Fig. 4.5E, 4.6A-D). The corresponding histograms of the quartz crystals coexisting with the rhombic adularia also showed skewness to higher temperatures (Fig. 6.2). Fluid inclusion assemblages of quartz crystals coexisting with the rhombic adularia also show coexistence of liquid inclusions, liquid-rich liquid-vapor fluid inclusions, vapor inclusions, and vapor-rich liquid-vapor inclusions (Fig. 6.5A). Multiple events of crosscutting brecciation was observed in a hydrothermal breccia intercepted by drill hole KTDH04. The hydrothermal breccias show rounded clasts of silicified host rock which indicate a very high energy to transport the fragments away from the country rock. Fractures were also observed in the sulfide minerals which were later filled and replaced by later sulfide or quartz. The multiple episodes of hydrothermal brecciation is a manifestation of repeated episodes of release of pressure which may trigger multiple episodes of boiling. The hydrothermal breccia zone intercepted in KTDH04 contains the majority of the bonanza-grade Au which exhibits the strong relationship between boiling and Au precipitation. Based on fluid inclusion petrography, both analyzed quartz and sphalerite crystals from the Stage 4 hydrothermal breccias show heterogeneous trapping of fluid inclusions of varied liquid-vapor proportions (Fig. 6.5A-D). Skewed histograms of homogenization temperature were also observed which indicate trapping temperatures varying from 270 °C to 290 °C (Fig. 6.2). The samples which show evidence of boiling conditions contain abundant base metal sulfides and Au grades that reach up to 55 ppm Au.

Boiling is also suggested in the gas plots of the selected Stage 2 and Stage 4 quartz crystals (Fig. 6.8). One Stage 2 quartz sample and 2 Stage 4 samples showed a negative-trending slope in the CO_2/N_2 vs total gas content diagram which indicates boiling (Fig. 6.8A, D, E). Boiling resulted to a rapid depletion of N_2 which causes the CO_2/N_2 ratio to increase as the volatiles escape from the system (Blamey, 2012).

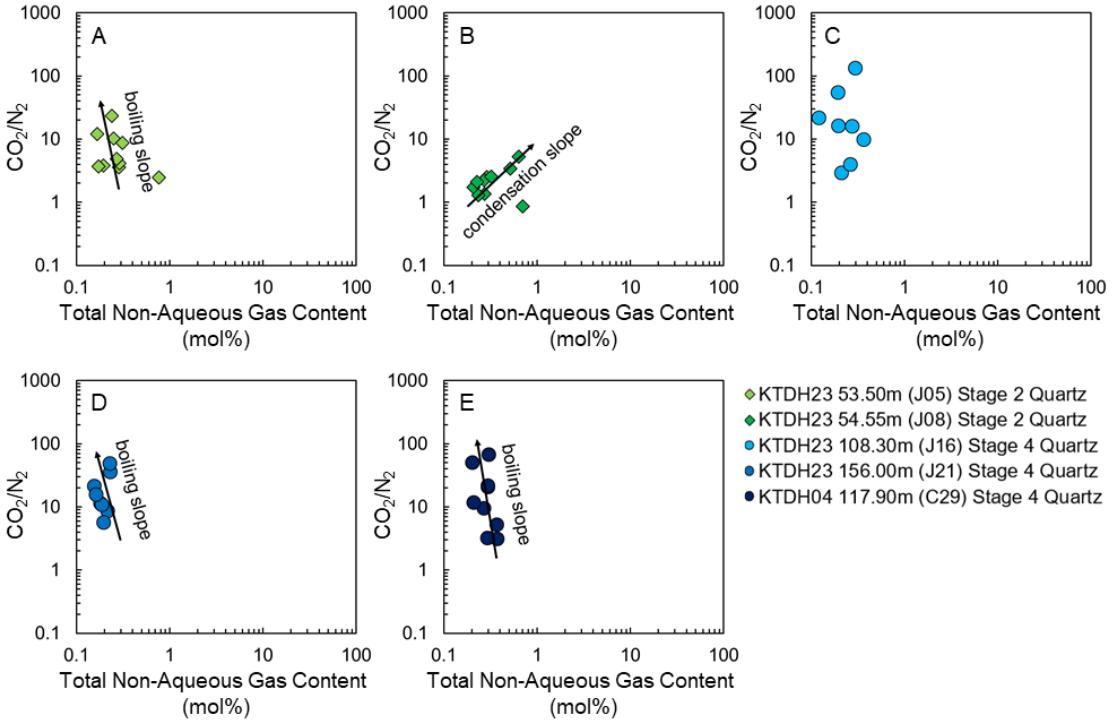

Fig. 6.8 CO_2/N_2 vs total gas content plot of fluid inclusions from Stage 2 quartz and Stage 4 quartz showing boiling trend (A, D and E) and condensation trend (B). Diagram modified from Blamey (2012).

The homogenization temperature and salinity of fluid inclusion assemblages from the different mineralization stages were also plotted to determine other mechanisms that could have influenced the mineralization in Kay Tanda (Fig. 6.9). The temperature of the system started at lower temperatures during Stage 1, gradually increased during Stage 2 to Stage 4, and then started to cool down during Stage 6. The intrusion of the Middle Miocene to Late Miocene Balibago Intrusive Complex into the host rocks released magmatic volatiles which later condensed into the groundwater. This generated strongly acidic solutions which formed a localized advanced argillic alteration and was later cut by Stage 1 Au-bearing quartz veins. This is consistent with the trend of the salinity and homogenization temperature of Stage 1 fluid inclusions. The salinity of the Stage 1 fluid inclusions widely decreases as the temperature decreases which suggests a dilution by surface fluid (Fig. 6.9A) (Wilkinson, 2001). With the intrusion of the Late Miocene to Early Pliocene Dacite Porphyry Intrusives, the temperature of the system continued to increase and the hydrothermal system developed over a wider area which formed the pervasive argillic alteration and Stage 2 Au-Ag quartz stockworks. The system sustained the high temperature condition during the Stage 4 mineralization due to the continuous intrusion of the Dacite Porphyry Intrusives but the salinity started to decrease because of the increasing contribution of deep meteoric water circulation. At the later stages, the temperature and salinity of the system started to decrease as a consequence of the cooling Dacite Porphyry Intrusives and incorporation of more meteoric water into the hydrothermal system. This mixing trend is also observed in the homogenization temperature versus salinity diagram of Stage 6 fluid inclusions from coexisting sphalerite and anhydrite crystals (Fig. 6.9D).

On the other hand, Stage 2 and 4 homogenization vs salinity diagrams do not show a clear trend (Fig. 6.9B-C). If boiling occurred in the system, the homogenization temperature vs salinity diagram would show a steep negative slope corresponding to the increase in the salinity of the fluid inclusions as the temperature decreases (Wilkinson, 2001). This is not clearly seen in Stage 2 and 4 diagrams because of the plots of fluid inclusion assemblages that were trapped below the boiling level.

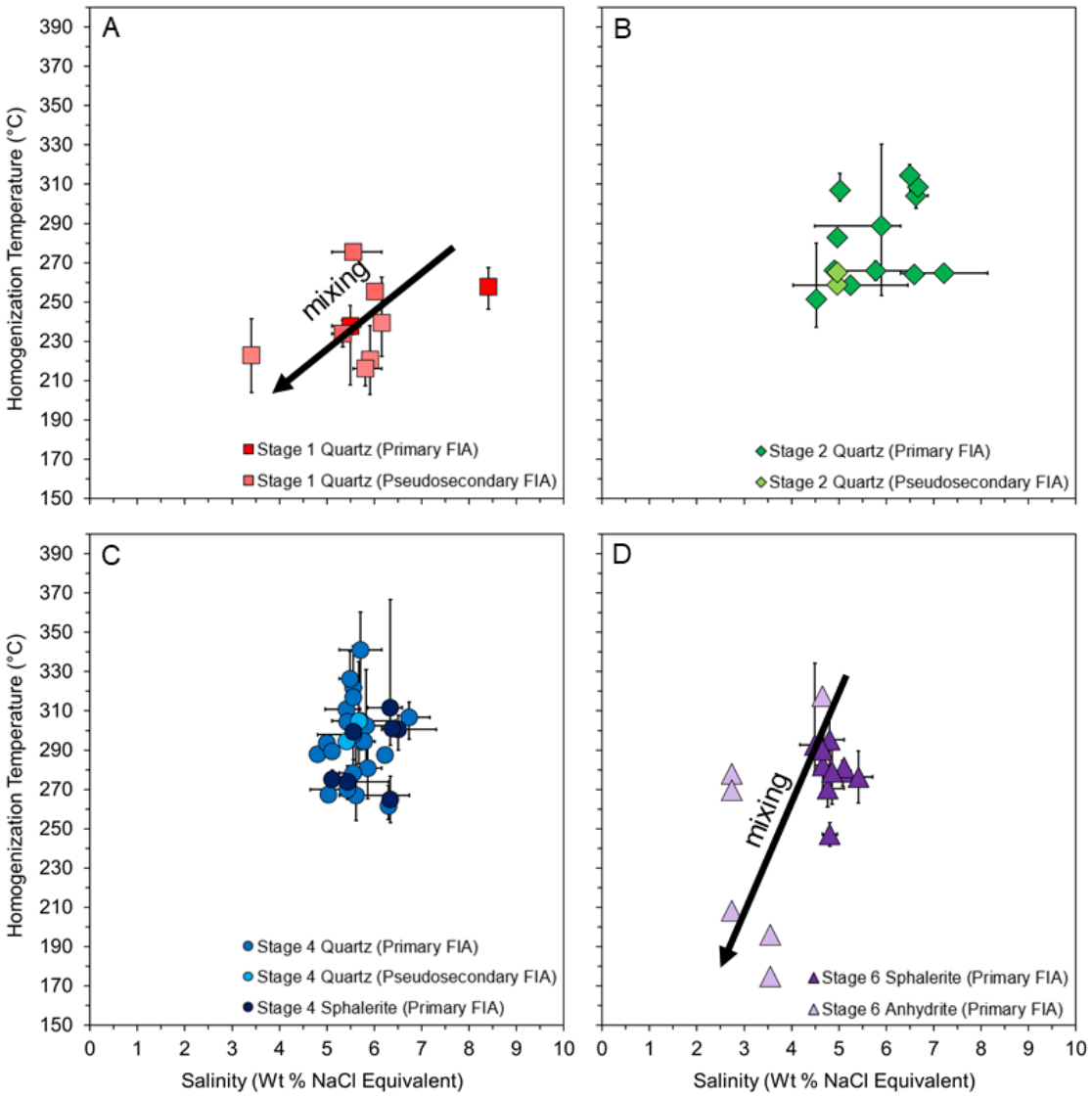

Fig. 6.9 Fluid inclusion assemblages plotted on homogenization temperature vs salinity diagram. Each data point represents the average homogenization temperature and salinity for the fluid inclusion assemblage and the error bars represent the minimum and maximum values for each fluid inclusion assemblage.

The difference in the range and trends of the salinity and homogenization temperature between the mineralization stages may be attributed to the difference in the heat source during the formation of the mineralization stage which is the Balibago Intrusive Complex and the Dacite Porphyry Intrusives, respectively, and the amount of meteoric water as the system evolved through time.

6.5.3 Depth of ore deposition and minimum amount of erosion

Boiling of hydrothermal fluids in Kay Tanda was observed in some of the analyzed quartz and sphalerite from Stages 2 and 4. On the basis of the hydrostatic boiling point curves for brines of constant composition by Haas (1971), the minimum depth of ore deposition below the paleowater table and consequently, an approximate minimum amount of erosion can be estimated. The microthermometry data (the mode of homogenization temperature and salinity), sampling depth relative to the present-day surface and theoretical boiling depth based on the boiling point curve from Haas (1971) are presented in Table 6.3. Based on these data, a boiling condition under hydrostatic pressure was estimated to be approximately around 500 m below the paleowater table for the shallow Au-Ag mineralization in the Stage 2 quartz veins, while more than 600 m below the paleowater table for the deeper base metal-Au mineralization in the Stage 4 veins and hydrothermal breccias. The deeper boiling level for the Stage 4 mineralization is attributed to the continued deposition of sedimentary rocks of the Calatagan Formation at the timing of the later base metal-Au mineralization. This implies that approximately at least 460 m of overlying volcaniclastic-sedimentary sequences has been eroded since the formation of the deposit.

The modes of homogenization temperature (with the range of homogenization temperature represented as horizontal error bars) of the analyzed quartz and sphalerite samples were plotted on a boiling depth vs homogenization temperature diagram (Fig. 6.10). The boiling point curves are given for pure water (H_2O), 5 wt% NaCl equivalent solution, 10 wt% NaCl equivalent solution (Haas, 1971) under hydrostatic condition, and under lithostatic condition with a host rock density of 2.65 g/cm^3. In Figure 6.2, the distribution of homogenization temperature of fluid inclusions of Stage 2 quartz at 236 m a.s.l. (Sample: KTDH23 53.50m, J05) shows evidence of boiling condition where the mode of the homogenization temperature was estimated to be between 260 °C to 270 °C. Based on the calculated salinity which is around 5 to 6 wt% NaCl equivalent in a H_2O-NaCl system, the boiling condition under hydrostatic pressure was estimated at 512 m below the paleowater table at 4.55 MPa (Haas, 1971). The ore-forming depth of the other samples were also

calculated and plotted on the diagram. The majority of the mode of homogenization temperature of the samples plotted near or slightly above the hydrostatic boiling curves.

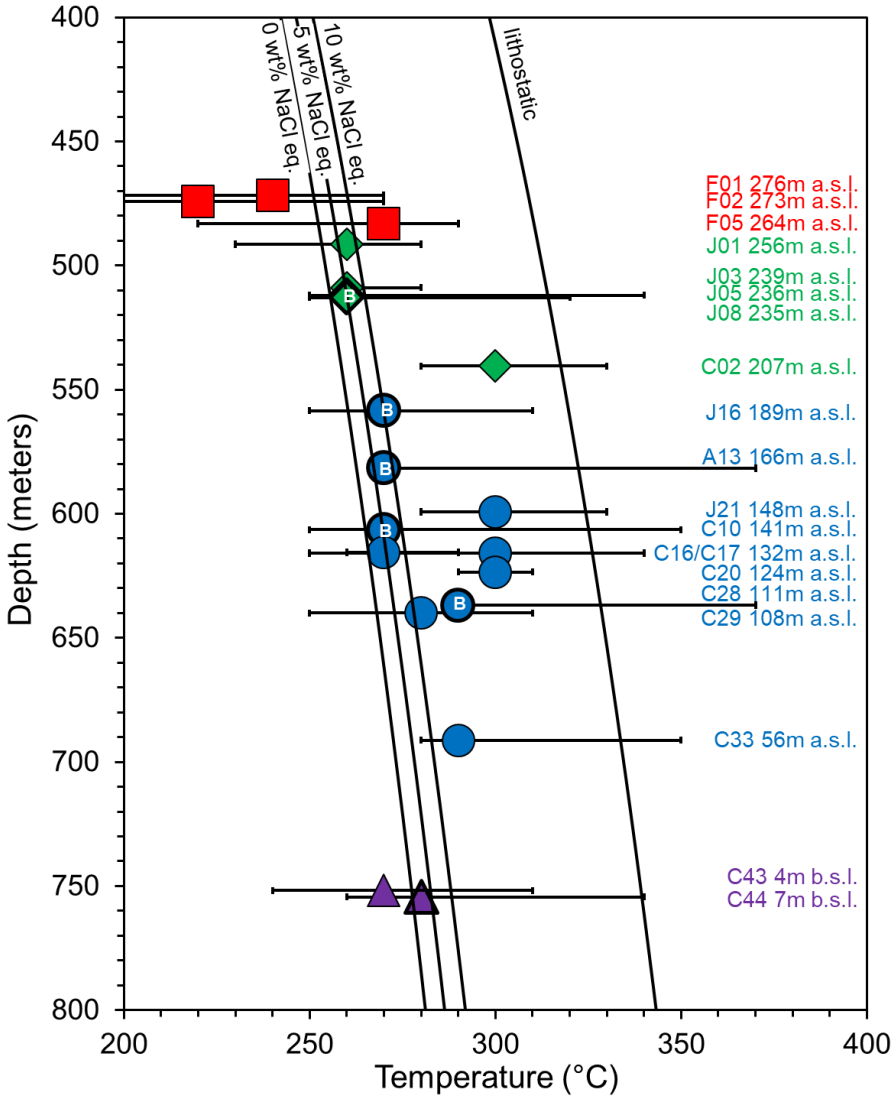

Fig. 6.10 Boiling depth vs temperature diagram. Each data point represents the mode of the homogenization temperature histograms and the error bars represent the lower and upper range of the homogenization temperature per sample. ”B” marks the samples which show boiling condition. Boiling point curves are given for pure water (H_2O), 5 wt% NaCl equivalent solution, 10 wt% NaCl equivalent solution (Haas, 1971) under hydrostatic condition and under lithostatic condition (2.65 g/cm^3). Abbreviation: a.s.l. – above mean sea level, b.s.l. – below sea level.

Table 6.3 Calculated boiling depths and corresponding minimum amount of erosion obtained from fluid inclusion assemblages showing evidence of boiling condition.

Sample ID	Host mineral	Mineralization stage	Mode of salinity (wt% NaCl eq.)	Mode of homogenization temperature (°C)	Depth from present-day surface (m)	Elevation relative to present-day mean sea level (m)	Boiling depth (m)	Minimum amount of erosion (m)
KTDH23 53.50m (J05)	quartz	2	6	260	45.4	+235.6	512	467
KTDH23 54.55m (J08)	quartz	2	6	260	46.3	+234.7	512	466
KTDH23 108.30m (J16)	quartz	4	6	270	91.9	+189.1	610	518
KTD194-12 110.45m (A13)	quartz and sphalerite	4	5	270	99.1	+165.9	610	511
KTDH04 84.40m (C10)	quartz	4	5	270	84.4	+141.1	610	526
KTDH04 114.80m (C28)	quartz and sphalerite	4	6	290	114.8	+110.7	849	734

Note: Samples are arranged according to decreasing elevation from the present-day mean sea level. Boiling depth values were calculated based on Haas (1971).

6.6 Conclusions

Fluid inclusion microthermometry indicates that the temperature of the system increased from Stage 1 (220-270 °C) to Stage 2 (260-310 °C) and remained at high temperatures towards Stage 4 (270-310 °C) and started to cool down at Stage 6 (240-290 °C). The increase in the temperature of the system is attributed to the intrusion of two intrusive units in Kay Tanda, the Balibago Intrusive Complex and the Dacite Porphyry Intrusives.

Based on fluid inclusion gas analysis, shallow meteoric water is an important component of the hydrothermal system of Kay Tanda. The gas ratios of the Stage 2 and Stage 4 fluid inclusions cluster towards the composition of meteoric water, which have similar gas ratios as air-saturated water. A mixing of a magmatic component of basaltic character with meteoric water is also suggested by the gas compositions plotted on the N_2/100-10He-2Ar diagram. The salinity of the system slightly decreased from 5.8 wt% NaCl equivalent in Stage 1 to 5.7 wt% NaCl equivalent in Stages 2 and 4 to 4.7 wt% NaCl equivalent in Stage 6 due to the increasing contribution of deeply circulating meteoric water into the hydrothermal system. This moderate salinity and the deposit's proximity to the sea suggests a possible incorporation of seawater into the hydrothermal system.

Boiling is the main mechanism of ore deposition in Kay Tanda. Boiling evidence found in Stages 2 quartz samples include heterogeneous trapping of fluid inclusions of variable liquid-vapor ratios and homogenization temperature histograms showing skewness to higher temperatures. These evidence were also found in Stage 4 quartz and sphalerite samples including the occurrence of rhombic adularia. A trapping temperature of 260-270 °C and 270-280 °C were determined for Stage 2 and Stage 4 mineralization, respectively. Negative-trending slope in the CO_2/N_2 vs total gas content diagram which indicates boiling conditions were also found in Stage 2 and Stage 4 quartz. On the other hand, surface fluid dilution or mixing is the main mechanism of ore deposition in Stage 1 and Stage 6 which is shown in the decreasing trend of the measurements of homogenization temperature and salinity.

A boiling condition under hydrostatic pressure was estimated in Kay Tanda. It is approximately around 500 m below the paleowater table for the shallow Au-Ag mineralization in the Stage 2 quartz veins, while more than 600 m below the paleowater table for the deeper base metal-Au mineralization in the Stage 4 veins and hydrothermal breccias. Based on the present sampling depth, the minimum amount of eroded volcano-sedimentary overburden was estimated to be around 460 m.

CHAPTER 7

STABLE ISOTOPE SYSTEMATICS

7.1 Introduction

The fluid inclusion study presented in the previous chapter suggested various possible sources of the hydrothermal fluids in Kay Tanda. This chapter aims to provide additional evidence by presenting the results of the stable isotope study which involves (1) the oxygen isotope analysis on illite, quartz, and gypsum, (2) the hydrogen isotope analyses on illite, and (3) the sulfur isotope analysis on sulfides and sulfates. The samples were collected from different stages of mineralization in Kay Tanda. The oxygen and hydrogen isotope studies aim to (1) determine the sources of the hydrothermal fluids and (2) provide information on the possibility of water-rock interaction in the deposit. The sulfur isotope study aims to (1) calculate the temperature of mineral deposition based on sulfur isotopic geothermometry, (2) determine the dominant aqueous sulfur species, (3) determine the source(s) of the sulfur, and (4) determine the chemical conditions and mechanisms of ore deposition.

7.2 Methodology

The oxygen isotopic compositions of 4 illite samples (all from alteration halos around Stage 2 veins), 4 quartz samples (1 from Stage 1 quartz vein, 1 from Stage 2 quartz vein, 1 from Stage 4 quartz vein and 1 from Stage 4 hydrothermal breccia) and 5 gypsum samples (2 from Stage 6 anhydrite-gypsum veins and 3 from Stage 6 hydrothermal breccias) were determined. The hydrogen isotopic compositions of the illite samples were also determined. Illite was separated from the sample by hydraulic elutriation. Approximately 50 g of lightly crushed sample was mixed with 300 ml distilled water and was left for 3 hours and 54 minutes at 20 °C before extracting the clay fraction in the suspension at a settling distance of 5 cm from the water surface.

The air dried oriented clay fraction was analyzed using a Rigaku Multiflex X-ray diffractometer with CuKα tube in Akita University. The quartz and gypsum samples from lightly crushed veins and hydrothermal breccia samples were manually picked under a binocular microscope. At least 20 mg of illite and quartz samples and at least 10 mg of gypsum samples were sent to GNS Science in New Zealand for the stable isotope analysis. The results are presented in the conventional $\delta^{18}O$ per mil (‰) and δD per mil (‰) notation relative to Standard Mean Ocean Water (SMOW) (Craig, 1961).

The sulfur isotopic compositions of sulfides and sulfates collected from the veins and matrix of hydrothermal breccias from the different mineralization stages in Kay Tanda were determined. At least 20 mg sulfide mineral separates and at least 100 mg sulfate mineral separates from lightly crushed samples were manually picked under a binocular microscope. A total of 10 sulfide samples were collected from 7 Stage 2 veins (n_{pyrite} = 7) and 3 Stage 2 hydrothermal breccias (n_{pyrite} = 3), 33 sulfide samples from 5 Stage 4 veins (n_{pyrite} = 4, $n_{sphalerite}$ = 2) and 15 Stage 4 hydrothermal breccias ($n_{chalcopyrite}$ = 1, n_{galena} = 3, n_{pyrite} = 13, $n_{sphalerite}$ = 10), and 11 sulfides samples and 9 sulfate samples from 3 Stage 6 veins (n_{pyrite} = 1, $n_{sphalerite}$ = 1, n_{gypsum} = 4) and 5 Stage 6 hydrothermal breccias ($n_{chalcopyrite}$ = 3, n_{pyrite} = 3, $n_{sphalerite}$ = 3, $n_{anhydrite}$ = 1, n_{gypsum} = 4). The sulfides were decomposed and oxidized to sulfate by adding 20 ml 14M HNO_3 and 4 ml Br_2 under a ventilator system. The solution was heated at 98 °C. After the complete dissolution of the sulfides and evaporation of Br_2, the remaining solution was left to evaporate. The residue was dissolved with 10 ml 50% HCl solution and 90 ml distilled water was added to make a 100 ml solution. The solution was filtered to remove any residue such as undissolved silicate minerals. The cations in the solution were extracted using cation exchange procedure. The dissolved sulfate in the solution was fixed as barite ($BaSO_4$) by adding 10 ml 10% $BaCl_2 \cdot 2H_2O$ solution. On the other hand, the sulfates were dissolved in 200 ml 4N HCl solution overnight at room temperature. Then, the solution was filtered to remove any residue before adding 10 ml 10% $BaCl_2 \cdot 2H_2O$ solution to fix the dissolved sulfate as barite ($BaSO_4$). The barite converted from both sulfide and sulfate samples was later collected by filtration and then dried overnight. Then, a 1:5 ratio of $BaSO_4$ (approximately 0.4-0.5 mg) and V_2O_5 was mixed and sealed in a tin foil capsule. The liberation

of SO_2 gas from barite ($BaSO_4$) was based on the procedure by Yanagisawa and Sakai (1983). The samples were analyzed using a Thermo Scientific FLASH 2000 Organic Elemental Analyzer connected to a Thermo Scientific Delta V Advantage Isotope Ratio Mass Spectrometer at Akita University. The results are presented in the conventional $\delta^{34}S$ per mil (‰) notation relative to Cañon Diablo Troilite standard (Ault & Jensen, 1963). The accuracy of the results is estimated within ± 0.2‰.

7.3 Results

7.3.1 Hydrogen and oxygen isotopes

Two illite samples collected from the same samples used for the determination of the age of mineralization of Kay Tanda using K-Ar method, and two illite samples associated with Stage 2 quartz veins were subjected to hydrogen and oxygen isotope analyses. The $\delta^{18}O$ and δD values of the illite samples showed two different sets of isotopic signature: the $\delta^{18}O$ values of the former two are +5.1‰ and +5.7‰ and the δD values are -37.7‰ and -37.3‰, while the $\delta^{18}O$ values of the latter two are +12.2‰ and +13.1‰ and the δD values are -51.2‰ and -62.0‰, respectively. The oxygen isotopic composition of the quartz samples from Stage 1, 2, and 4 mineralization and the gypsum samples from Stage 6 mineralization were also analyzed. The $\delta^{18}O$ values of the quartz samples range from +9.7‰ to +12.0‰ while those from the gypsum samples range from +5.3‰ to +11.5‰. The isotopic values of water in equilibrium with illite, quartz and gypsum were calculated on the basis of fractional equation by Sheppard and Gilg (1996) for illite, Matsuhisa et al. (1979) for quartz, and Friedman and O'Neil (1977) for gypsum. The temperature used for the calculation was from the measured homogenization temperatures from fluid inclusion microthermometry and estimated temperatures from sulfur isotope thermometry. The results are summarized in Table 7.1.

Table 7.1 Oxygen and hydrogen isotopic data of illite, and oxygen isotope data of quartz and gypsum obtained from different mineralization stages of Kay Tanda.

Sample ID	Depth from present-day surface (m)	Elevation relative to present-day mean sea level (m)	Mineralization Stage	Type	Mineral	$\delta^{18}O_{mineral}$ (‰)	$\delta D_{mineral}$ (‰)	$\delta^{18}O_{water}$ (‰)	δD_{water} (‰)	T_h from Fluid Inclusion Micro-thermometry (°C)	T from Sulfur Isotope Thermometry (°C)
KTD191-12 26.00m (EE05)	21.3	+258.1	Stage 2	alteration	illite	+12.2	-51.2	+7.6	-26.2	260	
KTDH23 55.00m (J10)	46.6	+234.3	Stage 2	alteration	illite	+13.1	-62.0	+8.4	-37.0	260	
KTD183 106.15m (G03)*	90.1	+199.9	Stage 2	alteration	illite	+5.1	-37.7	+0.5	-12.7	260	
KTD183 106.50m (G04)*	90.4	+199.6	Stage 2	alteration	illite	+5.7	-37.3	+1.0	-12.3	260	
KTDH24 9.20m (F02)	8.6	+273.3	Stage 1	vein	quartz	+12.0		+1.5		220	
KTDH23 53.50m (J05)	45.4	+235.6	Stage 2	vein	quartz	+10.8		+2.3		260	
KTDH04 84.40m (C10)	84.4	+141.1	Stage 4	vein	quartz	+9.7		+1.7		270	
KTDH04 93.85m (C17)	93.9	+131.7	Stage 4	hbx	quartz	+11.1		+4.2		300	
KTDH04 227.40m (C411)	227.4	-1.9	Stage 6	hbx	gypsum	+8.0		-1.7			281
KTDH04 227.40m (C412)	227.4	-1.9	Stage 6	vein	gypsum	+5.3		-4.4			281
KTDH04 228.60m (C421)	228.6	-3.1	Stage 6	hbx	gypsum	+11.5		+1.5			274
KTDH04 228.60m (C422)	228.6	-3.1	Stage 6	vein	gypsum	+6.6		-3.5			274
KTDH04 240.80m (C47)	240.8	-15.3	Stage 6	hbx	gypsum	+9.4		-0.1			286

Note: *Illite samples that were used for the determination of the age of mineralization of Kay Tanda using K-Ar method. Calculated values of water in equilibrium with illite, quartz and gypsum on the basis of fractional equation by Sheppard and Gilg (1996) for illite, Matsuhisa et al. (1979) for quartz, and Friedman and O'Neil (1977) for gypsum.

7.3.2 Sulfur isotopes

Sulfur isotope analysis was conducted on a number of sulfides and sulfates collected from the Stage 2 mineralization, which represents the shallow Au-Ag epithermal mineralization, and the Stages 4 and 6 mineralization, which represent the deep base metal mineralization in Kay Tanda. Table 7.2 shows the sulfur isotopic composition of the sulfides and sulfates expressed in $\delta^{34}S$ (‰) and Table 7.3 shows the summary of the sulfur isotope data which includes the minimum, maximum, and median values per mineralization stage. The $\delta^{34}S$ values per mineral per stage is shown in Figure 7.1. The $\delta^{34}S$ are also plotted with respect to elevation relative to present-day mean sea level in Figure 7.2.

A total of 54 sulfide minerals and 9 sulfate minerals collected from Stage 2, Stage 4, and Stage 6 veins and matrix of hydrothermal breccias underwent sulfur isotope analysis. The $\delta^{34}S$ of the Stage 2 sulfides and the Stage 4 sulfides have a much wider range compared to that of the Stage 6 sulfides and sulfates (Fig. 7.1). The $\delta^{34}S$ range of the Stage 2 and the Stage 4 sulfides vary significantly from -5.8‰ to +2.8‰ with a mean at 0‰ and -2.1‰ to +3.3‰ with a mean at +0.7‰, respectively, while that of the Stage 6 sulfides and sulfates are fairly constant from +0.1‰ to +2.3‰ with a mean at +1.1‰ and +21.6‰ to +22.9‰ with a mean at +22.3‰, respectively. Also, the $\delta^{34}S$ of the Stage 6 sulfides are higher than that of the Stage 2 and 4 sulfides. The $\delta^{34}S$ of the minerals collected from veins and hydrothermal breccias belonging to the same mineralization stage are of the same range (Fig. 7.2). The $\delta^{34}S$ of pyrite collected from Stage 2 veins ranges from -5.8‰ to +2.4‰ with a mean at -0.7‰ while that of the pyrite collected from Stage 2 hydrothermal breccias ranges from -0.5‰ to +2.8‰ with a mean at +1.6‰. The $\delta^{34}S$ of sulfides collected from Stage 4 veins ranges from -0.9‰ to +3.3‰ with a mean at +1.4‰ while that of the sulfides collected from Stage 4 hydrothermal breccias ranges from -2.1‰ to +2.5‰ with a mean at +0.6‰. The $\delta^{34}S$ of sulfides collected from Stage 6 veins ranges from +0.5‰ to +1.0‰ with a mean at +0.8‰ while that of the sulfides collected from Stage 6 hydrothermal breccias ranges from +0.1‰ to +2.3‰ with a mean at +1.1‰. The $\delta^{34}S$ of sulfates collected from Stage 6 veins ranges from +21.6‰ to +22.5‰ with a mean at +22.2‰ while that of the sulfates

collected from Stage 6 hydrothermal breccias ranges from +21.9‰ to +22.9‰ with a mean at +22.4‰.

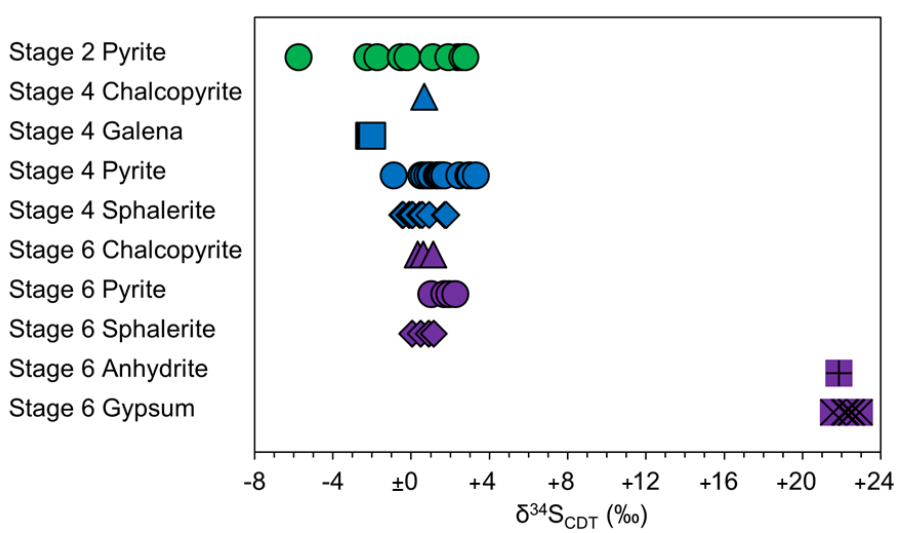

Fig. 7.1 $\delta^{34}S_{CDT}$ (‰) values of sulfides and sulfates per mineralization stage in Kay Tanda.

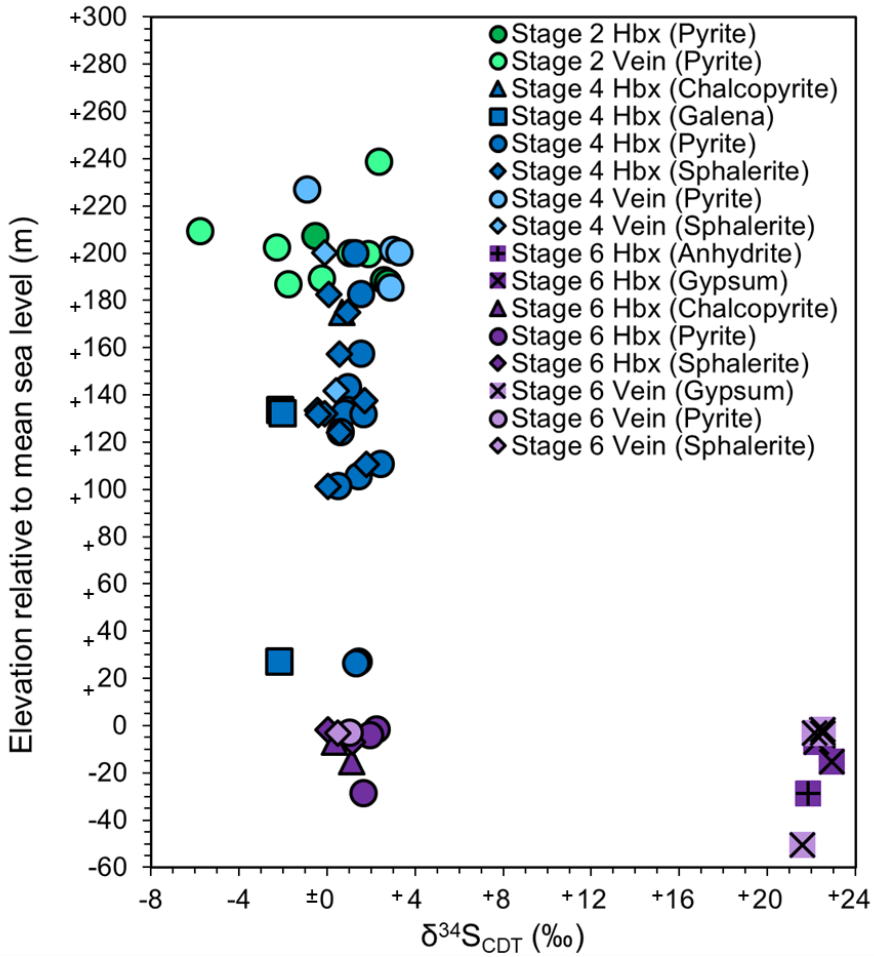

Fig. 7.2 $\delta^{34}S$ (‰) values of sulfides and sulfates projected with respect to elevation from mean sea level (m).

Table 7.2 Sulfur isotopic composition of sulfides and sulfates in Kay Tanda.

Sample ID	Depth from present-day surface (m)	Elevation relative to present-day mean sea level (m)	Mineralization Stage	Sample Type	Mineral	$\delta^{34}S$ (‰)
KTD194-12 86.55m (A09)	77.5	+187.4	Stage 2	Hbx	Pyrite	+2.8
KTD194-12 135.60m (A16)	121.7	+143.2	Stage 4	Hbx	Pyrite	+1.0
KTD194-12 182.05m (A22)	163.8	+101.2	Stage 4	Hbx	Pyrite	+0.5
KTD194-12 182.05m (A22)	163.8	+101.2	Stage 4	Hbx	Sphalerite	±0.0
KTD197-12 101.20m (B15)	93.4	+226.7	Stage 4	Vein	Pyrite	-0.9
KTD197-12 128.85m (B20)	119.0	+201.1	Stage 4	Vein	Pyrite	+3.0
KTD197-12 130.00m (B21)	120.0	+200.0	Stage 4	Vein	Pyrite	+3.3
KTD197-12 130.00m (B21)	120.0	+200.0	Stage 4	Vein	Sphalerite	-0.1
KTDH04 16.30m (C01)	16.3	+209.2	Stage 2	Vein	Pyrite	-5.8
KTDH04 18.40m (C02)	18.4	+207.1	Stage 2	Hbx	Pyrite	-0.5
KTDH04 50.55m (C03)	50.6	+175.0	Stage 4	Hbx	Chalcopyrite	+0.7
KTDH04 50.55m (C03)	50.6	+175.0	Stage 4	Hbx	Sphalerite	+0.9
KTDH04 68.30m (C06)	68.3	+157.2	Stage 4	Hbx	Pyrite	+1.6
KTDH04 68.30m (C06)	68.3	+157.2	Stage 4	Hbx	Sphalerite	+0.6
KTDH04 83.90m (C09)	83.9	+141.6	Stage 4	Vein	Sphalerite	+0.4
KTDH04 87.80m (C12)	87.8	+137.7	Stage 4	Hbx	Sphalerite	+1.7
KTDH04 92.05m (C15)	92.1	+133.5	Stage 4	Hbx	Galena	-2.1
KTDH04 92.05m (C15)	92.1	+133.5	Stage 4	Hbx	Pyrite	+1.0
KTDH04 92.05m (C15)	92.1	+133.5	Stage 4	Hbx	Sphalerite	-0.5
KTDH04 93.50m (C16)	93.5	+132.0	Stage 4	Hbx	Galena	-2.0
KTDH04 93.50m (C16)	93.5	+132.0	Stage 4	Hbx	Pyrite	+0.8
KTDH04 93.50m (C16)	93.5	+132.0	Stage 4	Hbx	Sphalerite	-0.1
KTDH04 93.85m (C17)	93.9	+131.7	Stage 4	Hbx	Pyrite	+1.7
KTDH04 93.85m (C17)	93.9	+131.7	Stage 4	Hbx	Sphalerite	-0.4
KTDH04 101.40m (C20)	101.4	+124.1	Stage 4	Hbx	Pyrite	+0.6
KTDH04 101.40m (C20)	101.4	+124.1	Stage 4	Hbx	Sphalerite	+0.6
KTDH04 114.80m (C28)	114.8	+110.7	Stage 4	Hbx	Pyrite	+2.5
KTDH04 114.80m (C28)	114.8	+110.7	Stage 4	Hbx	Sphalerite	+1.8
KTDH04 120.20m (C31)	120.2	+105.3	Stage 4	Hbx	Pyrite	+1.5
KTDH04 198.50m (C36)	198.5	+27.0	Stage 4	Hbx	Galena	-2.1
KTDH04 198.50m (C36)	198.5	+27.0	Stage 4	Hbx	Pyrite	+1.4
KTDH04 199.30m (C37)	199.3	+26.2	Stage 4	Hbx	Pyrite	+1.3
KTDH04 227.40m (C41)	227.4	-1.9	Stage 6	Hbx	Gypsum	+22.5
KTDH04 227.40m (C41)	227.4	-1.9	Stage 6	Hbx	Pyrite	+2.3
KTDH04 227.40m (C41)	227.4	-1.9	Stage 6	Hbx	Sphalerite	+0.1
KTDH04 227.40m (C41)	227.4	-1.9	Stage 6	Vein	Gypsum	+22.5
KTDH04 228.60m (C42)	228.6	-3.1	Stage 6	Vein	Gypsum	+22.5
KTDH04 228.60m (C42)	228.6	-3.1	Stage 6	Vein	Gypsum	+22.1
KTDH04 228.60m (C42)	228.6	-3.1	Stage 6	Vein	Pyrite	+1.0
KTDH04 228.60m (C42)	228.6	-3.1	Stage 6	Vein	Sphalerite	+0.5
KTDH04 229.80m (C43)	229.8	-4.3	Stage 6	Hbx	Chalcopyrite	+0.6
KTDH04 229.80m (C43)	229.8	-4.3	Stage 6	Hbx	Gypsum	+22.5
KTDH04 229.80m (C43)	229.8	-4.3	Stage 6	Hbx	Pyrite	+2.0

Sample ID	Depth from present-day surface (m)	Elevation relative to present-day mean sea level (m)	Mineralization Stage	Sample Type	Mineral	$\delta^{34}S$ (‰)
KTDH04 229.80m (C43)	229.8	-4.3	Stage 6	Hbx	Sphalerite	+0.9
KTDH04 232.30m (C44)	232.3	-6.8	Stage 6	Hbx	Chalcopyrite	+0.3
KTDH04 232.30m (C44)	232.3	-6.8	Stage 6	Hbx	Gypsum	+22.2
KTDH04 232.30m (C44)	232.3	-6.8	Stage 6	Hbx	Sphalerite	+1.2
KTDH04 240.80m (C47)	240.8	-15.3	Stage 6	Hbx	Chalcopyrite	+1.1
KTDH04 240.80m (C47)	240.8	-15.3	Stage 6	Hbx	Gypsum	+22.9
KTDH04 254.10m (C48)	254.1	-28.6	Stage 6	Hbx	Anhydrite	+21.9
KTDH04 254.10m (C48)	254.1	-28.6	Stage 6	Hbx	Pyrite	+1.7
KTDH04 276.10m (C50)	276.1	-50.6	Stage 6	Vein	Gypsum	+21.6
KTDH19 141.50m (E30)	117.4	+202.2	Stage 2	Vein	Pyrite	-2.3
KTDH24 87.50m (F20)	82.2	+199.8	Stage 4	Hbx	Pyrite	+1.3
KTDH24 105.75m (F22)	99.4	+182.6	Stage 4	Hbx	Pyrite	+1.6
KTDH24 105.75m (F22)	99.4	+182.6	Stage 4	Hbx	Sphalerite	+0.1
KTD183 106.15m (G03)	90.1	+199.9	Stage 2	Vein	Pyrite	+1.1
KTD183 106.50m (G04)	90.4	+199.6	Stage 2	Vein	Pyrite	+1.9
KTDH23 49.80m (J03)	42.2	+238.7	Stage 2	Vein	Pyrite	+2.4
KTDH23 108.30m (J16)	91.9	+189.1	Stage 2	Vein	Pyrite	-0.2
KTDH23 109.00m (J17)	92.5	+188.5	Stage 2	Hbx	Pyrite	+2.6
KTDH23 111.00m (J18)	94.2	+186.8	Stage 2	Vein	Pyrite	-1.7
KTDH23 112.50m (J19)	95.5	+185.5	Stage 4	Vein	Pyrite	+2.9

Note: Hbx – matrix of hydrothermal breccia

Table 7.3 Summary of sulfur isotope data of Kay Tanda.

Mineralization Stage	Type (Number)	Mineral	Number	Minimum $\delta^{34}S$ (‰)	Maximum $\delta^{34}S$ (‰)	Average $\delta^{34}S$ (‰)
Stage 2	Vein (n=7)	Pyrite	7	-5.8	+2.4	-0.7
	Hbx (n=3)	Pyrite	3	-0.5	+2.8	+1.6
		All Stage 2 Sulfides	10	-5.8	+2.8	0.0
Stage 4	Vein (n=5)	Pyrite	4	-0.9	+3.3	+2.1
		Sphalerite	2	-0.1	+0.4	+0.2
		All Stage 4 Vein Sulfides	6	-0.9	+3.3	+1.4
	Hbx (n=15)	Chalcopyrite	1	+0.7	+0.7	+0.7
		Galena	3	-2.1	-2.0	-2.1
		Pyrite	13	+0.5	+2.5	+1.3
		Sphalerite	10	-0.5	+1.8	+0.5
		All Stage 4 Hbx Sulfides	27	-2.1	+2.5	+0.6
		All Stage 4 Chalcopyrite	1	+0.7	+0.7	+0.7
		All Stage 4 Galena	3	-2.1	-2.0	-2.1
		All Stage 4 Pyrite	17	-0.9	+3.3	+1.5
		All Stage 4 Sphalerite	12	-0.5	+1.8	+0.4
		All Stage 4 Sulfides	33	-2.1	+3.3	+0.7
Stage 6	Vein (n=3)	Gypsum	4	+21.6	+22.5	+22.2
		Pyrite	1	+1.0	+1.0	+1.0
		Sphalerite	1	+0.5	+0.5	+0.5
		All Stage 6 Vein Sulfates	4	+21.6	+22.5	+22.2
		All Stage 6 Vein Sulfides	2	+0.5	+1.0	+0.8
	Hbx (n=5)	Anhydrite	1	+21.9	+21.9	+21.9
		Gypsum	4	+22.2	+22.9	+22.5
		Chalcopyrite	3	+0.3	+1.1	+0.7
		Pyrite	3	+1.7	+2.3	+2.0
		Sphalerite	3	+0.1	+1.2	+0.7
		All Stage 6 Hbx Sulfates	5	+21.9	+22.9	+22.4
		All Stage 6 Hbx Sulfides	9	+0.1	+2.3	+1.1
		All Stage 6 Anhydrite	1	+21.9	+21.9	+21.9
		All Stage 6 Gypsum	8	+21.6	+22.9	+22.4
		All Stage 6 Chalcopyrite	3	+0.3	+1.1	+0.7
		All Stage 6 Pyrite	4	+1.0	+2.3	+1.7
		All Stage 6 Sphalerite	4	+0.1	+1.2	+0.6
		All Stage 6 Sulfates	9	+21.6	+22.9	+22.3
		All Stage 6 Sulfides	11	+0.1	+2.3	+1.1
All Stages		All Sulfides	54	-5.8	+3.3	+0.7
		All Sulfates	9	+21.6	+22.9	+22.3

Note: Hbx – matrix of hydrothermal breccia

7.4 Discussion

7.4.1 Source of hydrothermal fluids and water-rock interaction

The fluid inclusion studies presented in the previous chapter suggested that the hydrothermal fluids in Kay Tanda may have been derived from different sources: meteoric water, magmatic fluid and seawater. Stable isotope studies have shown that the hydrothermal fluids in epithermal deposits contain meteoric- and magmatic-derived fluids of varying proportions; magmatic fluids are more dominant in high-sulfidation epithermal deposits, with a minor to moderate component of meteoric water, while meteoric water is more prevalent in low-sulfidation epithermal deposits, with nil to small amounts of magmatic water (Arribas, 1995; Simmons, 1995; Hedenquist et al., 1998; Sillitoe & Hedenquist, 2003; Simmons et al., 2005). However, the amount and significance of seawater input to epithermal deposits, especially those in proximity to the sea, still need further investigation. There are a few stable isotope studies on epithermal deposits where seawater contribution was suggested. In the Ladolam alkali epithermal Au deposit in Papua New Guinea, the sulfur isotopic composition of anhydrite samples is the same as coeval seawater sulfate which was interpreted as incorporation of seawater into the hydrothermal system (Gemmell et al., 2004). In an epithermal deposit in Milos Island, Greece, the hydrogen and oxygen isotopic composition of analyzed fluid inclusions lie in the zone between the meteoric water line and the intermediate zone between seawater and volcanic arc gases (Naden et al., 2005). Moreover, the strontium isotopic composition of barite is close to the strontium isotopic composition of Pliocene seawater (Naden et al., 2005). In an epithermal deposit in SE Afar Rift, Djibouti, sulfur and strontium isotopic composition of sulfate minerals suggested mixing of volcanic- and seawater-derived sulfate (Moussa et al., 2017). In Kay Tanda, the evidence of seawater input is suggested from the hydrogen and oxygen isotopic compositions of illite samples collected from the Stage 2 mineralization (Table 7.1). In Figure 7.3, the calculated $\delta^{18}O_{water}$ and δD_{water} values of the 2 illite samples that were also used for the determination of the age of mineralization using K-Ar method approach the $\delta^{18}O$ and δD value of SMOW and are within the same isotopic composition as the mentioned cases above.

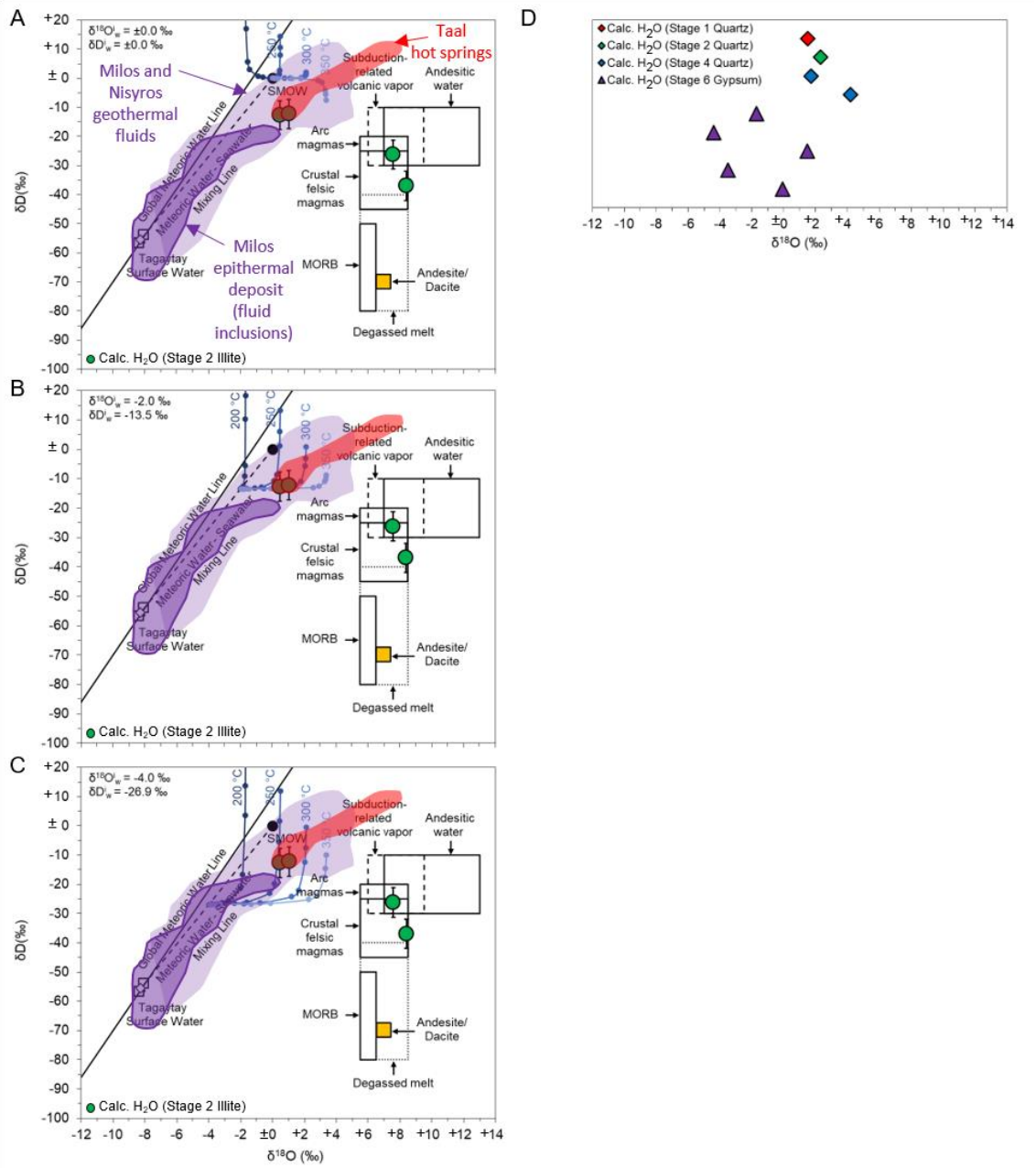

Fig. 7.3 (A-C) $\delta^{18}O$ (‰) versus δD (‰) diagram of the calculated values of water in equilibrium with Stage 2 illite and (D) $\delta^{18}O$ (‰) diagram of the calculated values of water in equilibrium with Stage 1, 2, and 4 quartz and Stage 6 gypsum. Three scenarios are presented: (A) seawater (initial or unexchanged isotopic composition of the water, $\delta^{18}O_{iw}$= 0.0 ‰, δD_{iw}= 0.0 ‰) that has undergone isotopic exchange with andesitic/dacitic host rocks, (B) a mixture of seawater and meteoric water ($\delta^{18}O_{iw}$= -2.0 ‰, δD_{iw}= -13.5 ‰) that has undergone isotopic exchange with andesitic/dacitic host rocks, and (C) a mixture of seawater and meteoric water ($\delta^{18}O_{iw}$= -4.0 ‰, δD_{iw}= -26.9 ‰) that has undergone isotopic exchange with andesitic/dacitic host rocks. The isotopic composition of the unaltered host rock (δ_{ir}) was approximated to be similar to the reported value for andesites/dacites by Nockolds et al. (1978). The fields for subduction-related volcanic vapor, arc magmas, crustal felsic magmas, MORB and degassed melt are from Hedenquist and Lowenstern (1994), for andesitic water (water associated with andesitic volcanism) from Giggenbach (1992a). The values for illite and quartz were calculated using temperatures obtained from fluid inclusion microthermometry while for gypsum using

temperatures obtained from sulfur isotope thermometry of sulfate-sulfide pairs. Oxygen and hydrogen data of Milos and Nisyros from Naden et al. (2005) and of Taal hot springs from Delmelle et al. (1998).

The calculated $\delta^{18}O_{water}$ and δD_{water} values in equilibrium with Stage 2 illite can be explained by water-rock interaction after Field and Fifarek (1985) (Fig. 7.3). A meteoric water-seawater mixing line was produced using the oxygen and hydrogen isotopic data of SMOW and the surface waters collected from two rivers and one cold spring in Tagaytay, Batangas (Delmelle et al., 1998). These are the nearest surface waters to Kay Tanda with reported oxygen and hydrogen isotopic values. Three scenarios were considered: seawater (initial or unexchanged isotopic composition of the water, $\delta^{18}O_{iw}$= 0.0 ‰, δD_{iw}= 0.0 ‰) that has undergone isotopic exchange with andesitic/dacitic host rocks (Fig. 7.3A), a mixture of seawater and meteoric water ($\delta^{18}O_{iw}$= -2.0 ‰, δD_{iw}= -13.5 ‰) that has undergone isotopic exchange with andesitic/dacitic host rocks (Fig 7.3B), and a mixture of seawater and meteoric water ($\delta^{18}O_{iw}$= -4.0 ‰, δD_{iw}= -26.9 ‰) that has undergone isotopic exchange with andesitic/dacitic host rocks (Fig. 7.3C). The isotopic composition of the unaltered host rock (δ_{ir}) of Kay Tanda was approximated to be similar to the reported value for andesites/dacites by Nockolds et al. (1978). The fractionation of oxygen isotopes between rock and water ($\Delta_{r\text{-}w}$) was derived from the plagioclase feldspar (An_{30})-H_2O equation of O'Neil and Taylor (1976) while the fractionation of hydrogen isotopes between rock and water was derived from biotite-H_2O equation of Suzuoki and Epstein (1976).

The calculated $\delta^{18}O_{water}$ and δD_{water} values in equilibrium with Stage 2 illite cannot be produced in the model involving only seawater that has undergone isotopic exchange with the host rocks (Fig. 7.3A). However, two illite samples coincided with the calculated theoretical final composition of water at temperatures between 250 °C and 300 °C and at water-rock ratios (w/r or R) of 0.1 to 0.5 (Fig. 7.3B) and of 1 to 5 (Fig. 7.3 C). This is consistent with the temperature of formation estimated from fluid inclusion microthermometry for the Stage 2 mineralization. The calculated $\delta^{18}O_{water}$ and δD_{water} values of the 2 illite samples are also within the same field as the isotopic composition of Taal hot spring waters, Taal Lake and Taal Main Crater Lake which were interpreted to be generated by a three-component hydrothermal system (Delmelle et al., 1998).

Moreover, the two points which coincided with the water-rock interaction model are the same illite samples used for K-Ar dating. This indicates that seawater had been incorporated into the hydrothermal system of Kay Tanda since the early mineralization stages (Stage 2). The other two samples which plotted away from the two points discussed above may demonstrate isotopic disequilibrium. These samples were collected from shallower depths within the oxidized zone of the deposit which might have affected the original isotopic composition of the illite (Sheppard & Gilg, 1996).

7.4.2 Sulfur isotope thermometry

One of the useful applications of sulfur isotope data is it can provide information on the temperature of ore deposition (Ohmoto & Rye, 1979). The isotopic fractionation factor between two minerals depends on temperature and by measuring the difference between the $\delta^{34}S$ values of two sulfur-bearing compounds, the temperature of equilibration may be estimated (Ohmoto & Rye, 1979; Ohmoto & Lasaga, 1982; Campbell & Larson, 1998). Among the mineral pairs, those which have the largest temperature dependence of fractionation are the most sensitive geothermometers (e.g. sulfide-sulfate, pyrite-galena, sphalerite-galena, pyrite-chalcopyrite) (Ohmoto & Rye, 1979; Campbell & Larson, 1998). In this study, several mineral pairs were used for sulfur isotope geothermometry. The calculated values were compared to the obtained measurements from fluid inclusion microthermometry. This can provide information on the nature of equilibrium between the minerals during ore deposition (Ohmoto & Rye, 1979).

Table 7.4 shows the temperatures calculated from sulfur isotope geothermometry using the following sulfide-sulfide pairs: galena-pyrite, galena-sphalerite, sphalerite-pyrite, and sphalerite-chalcopyrite. The sulfide pairs that show the closest temperature estimates to the temperature obtained from fluid inclusion microthermometry are the galena-pyrite and galena-sphalerite pairs. The temperature of ore deposition estimated by sulfur isotope geothermometry based on the isotopic fractionation between galena and pyrite ranges from 263 to 332 °C. Accounting for the accuracy of the $\delta^{34}S$ values (within ± 0.2‰), the temperature of ore deposition estimated by sulfur

isotope geothermometry based on the isotopic fractionation between galena and sphalerite will range from 290 °C to 490 °C. However, the majority of the calculated temperatures obtained from sphalerite-pyrite and sphalerite-chalcopyrite pairs from both Stage 4 and Stage 6 mineralization show unrealistically low/high values that deviate significantly from those obtained from fluid inclusion microthermometry. This may be caused by two factors. First, the sphalerite-chalcopyrite and sphalerite-chalcopyrite equilibrium fractionation factors versus temperature have gentler slopes, hence, have smaller temperature dependence of fractionation (Ohmoto & Rye, 1979; Campbell & Larson, 1998). These pairs are not as sensitive geothermometers as galena-pyrite and galena-sphalerite pairs (Ohmoto & Rye, 1979; Campbell & Larson, 1998). Second, based on the ore textures, pyrite crystals which were later replaced by chalcopyrite precipitated before the host sphalerite crystal. There may be slight changes in the temperature and fluid composition during mineral precipitation (Campbell & Larson, 1998). The replacement could also have been caused by dissolution and precipitation of the secondary mineral rather than by simple cation substitution (Ohmoto & Rye, 1979).

The majority of the Stage 6 sulfates analyzed in this study is gypsum. Only a few anhydrite crystals which have not yet been completely hydrated to gypsum were observed in the anhydrite-gypsum veins. Based on the $\delta^{34}S$ of anhydrite and gypsum, Stage 6 anhydrite and gypsum have similar isotopic compositions which indicate that the transformation of anhydrite to gypsum via hydration did not affect the $\delta^{34}S$ composition. In this regard, the $\delta^{34}S$ of the Stage 6 gypsum was used to calculate the isotopic fractionation temperature with that of the Stage 6 sulfides that have formed coevally with the original Stage 6 anhydrite. Table 7.5 shows the temperatures calculated from sulfur isotope geothermometry using gypsum-sulfide and anhydrite-sulfide pairs. The largest isotopic fractionation (22.4 ‰) was found in the shallowest sulfide-sulfate pair (sphalerite-gypsum) at 1.9 m below sea level while the smallest isotopic fractionation (20.2 ‰) was found in the deepest sulfide-sulfate pair (pyrite-gypsum) at 28.6 m below sea level. These isotopic fractionation values correspond to about 270 °C and 290 °C, respectively, based on sulfur isotope thermometry (Ohmoto & Rye, 1979; Ohmoto & Lasaga, 1982). These values are similar with the determined homogenization temperatures of primary fluid inclusions in Stage 6 sphalerite.

Table 7.4 Sulfur isotope geothermometry using the $\delta^{34}S$ values of sulfide-sulfide pairs from Stage 4 and Stage 6 mineralization and comparison of temperature obtained from sulfur isotope thermometry and fluid inclusion microthermometry.

Sample ID	Depth from present-day surface (m)	Elevation relative to present-day mean sea level (m)	Mineralization Stage	Mineral	$\delta^{34}S$ (‰)	1000 lnα A-B	Temperature from Sulfur Isotope Thermometry (K)	Temperature from Sulfur Isotope Thermometry (°C)	Temperature from Fluid Inclusion Microthermometry (°C)
Galena-Pyrite Pair									
KTDH04 92.05m (C15)	92.1	+133.5	Stage 4	Galena Pyrite	-2.1 +1.0	-3.1	576.9	303.7	
KTDH04 93.50m (C16)	93.5	+132.0	Stage 4	Galena Pyrite	-2.0 +0.8	-2.8	605.5	332.3	270.0
KTDH04 198.50m (C36)	198.5	+27.0	Stage 4	Galena Pyrite	-2.1 +1.4	-3.6	535.8	262.6	
Galena-Sphalerite Pair									
KTDH04 92.05m (C15)	92.1	+133.5	Stage 4	Galena Sphalerite	-2.1 -0.5	-1.7	665.1	391.9	
KTDH04 93.50m (C16)	93.5	+132.0	Stage 4	Galena Sphalerite	-2.0 -0.1	-1.9	622.6	349.4	270.0
Sphalerite-Pyrite Pair									
KTD197-12 130.00m (B21)	120.0	+200.0	Stage 4	Sphalerite Pyrite	-0.1 +3.3	-3.4	295.9	22.8	
KTDH24 105.75m (F22)	99.4	+182.6	Stage 4	Sphalerite Pyrite	+0.1 +1.6	-1.5	448.0	174.9	
KTDH04 68.30m (C06)	68.3	+157.2	Stage 4	Sphalerite Pyrite	+0.6 +1.6	-1.0	543.1	270.0	
KTDH04 92.05m (C15)	92.1	+133.5	Stage 4	Sphalerite Pyrite	-0.5 +1.0	-1.4	455.7	182.6	

Sample ID	Depth from present-day surface (m)	Elevation relative to present-day mean sea level (m)	Mineralization Stage	Mineral	$\delta^{34}S$ (‰)	1000 lnα A-B	Temperature from Sulfur Isotope Thermometry (K)	Temperature from Sulfur Isotope Thermometry (°C)	Temperature from Fluid Inclusion Microthermometry (°C)
KTDH04 93.50m (C16)	93.5	+132.0	Stage 4	Sphalerite	-0.1	-0.9	569.2	296.0	270.0
				Pyrite	+0.8				
KTDH04 93.85m (C17)	93.9	+131.7	Stage 4	Sphalerite	-0.4	-2.1	378.2	105.1	300.0
				Pyrite	+1.7				
KTDH04 101.40m (C20)	101.4	+124.1	Stage 4	Sphalerite	+0.6	-0.1	1878.5	1605.4	300.0
				Pyrite	+0.6				
KTDH04 114.80m (C28)	114.8	+110.7	Stage 4	Sphalerite	+1.8	-0.7	669.3	396.1	290.0
				Pyrite	+2.5				
KTD194-12 182.05m (A22)	163.8	+101.2	Stage 4	Sphalerite	±0.0	-0.5	790.2	517.1	
				Pyrite	+0.5				
KTDH04 227.40m (C41)	227.4	-1.9	Stage 6	Sphalerite	+0.1	-2.2	368.9	95.8	
				Pyrite	+2.3				
KTDH04 228.60m (C42)	228.6	-3.1	Stage 6	Sphalerite	+0.5	-0.5	748.0	474.8	
				Pyrite	+1.0				
KTDH04 229.80m (C43)	229.8	-4.3	Stage 6	Sphalerite	+0.9	-1.1	529.7	256.5	270.0
				Pyrite	+2.0				
Chalcopyrite-Sphalerite Pair									
KTDH04 50.55m (C03)	50.6	+175.0	Stage 4	Chalcopyrite	+0.7	-0.3	766.9	493.7	
				Sphalerite	+0.9				
KTDH04 229.80m (C43)	229.8	-4.3	Stage 6	Chalcopyrite	+0.6	-0.3	741.5	468.3	270.0
				Sphalerite	+0.9				
KTDH04 232.30m (C44)	232.3	-6.8	Stage 6	Chalcopyrite	+0.3	-0.8	431.5	158.4	280.0
				Sphalerite	+1.2				

Note: Equilibrium isotopic fractionation factors of sulfur compounds with respect to H_2S from Ohmoto and Rye (1979) and Ohmoto and Lasaga (1982).

Table 7.5 Sulfur isotope geothermometry using the $\delta^{34}S$ values of sulfide-sulfate pairs from Stage 6 mineralization and comparison of temperature obtained from sulfur isotope thermometry and fluid inclusion microthermometry.

Sample ID	Depth from present-day surface (m)	Elevation relative to present-day mean sea level (m)	Mineralization Stage	Mineral	$\delta^{34}S$ (‰)	$\Delta^{34}S$ [SO_4^{2-} - H_2S] (‰)	Temperature from Sulfur Isotope Thermometry (K)	Temperature from Sulfur Isotope Thermometry (°C)	Temperature from Fluid Inclusion Microthermometry (°C)
KTDH04 227.40m (C41)	227.4	-1.9	Stage 6	Gypsum	+22.5	22.4	545.6	272.5	
				Sphalerite	+0.1				
KTDH04 227.40m (C41)	227.4	-1.9	Stage 6	Gypsum	+22.5	20.2	561.9	288.8	
				Pyrite	+2.3				
KTDH04 228.60m (C42)	228.6	-3.1	Stage 6	Gypsum	+22.5	21.5	544.2	271.1	
				Pyrite	+1.0				
KTDH04 228.60m (C42)	228.6	-3.1	Stage 6	Gypsum	+22.5	22.0	550.7	277.6	
				Sphalerite	+0.5				
KTDH04 229.80m (C43)	229.8	-4.3	Stage 6	Gypsum	+22.5	21.9	558.3	285.2	270.0
				Chalcopyrite	+0.6				
KTDH04 229.80m (C43)	229.8	-4.3	Stage 6	Gypsum	+22.5	20.6	556.3	283.2	270.0
				Pyrite	+2.0				
KTDH04 229.80m (C43)	229.8	-4.3	Stage 6	Gypsum	+22.5	21.6	555.9	282.8	270.0
				Sphalerite	+0.9				
KTDH04 232.30m (C44)	232.3	-6.8	Stage 6	Gypsum	+22.2	21.9	558.7	285.5	280.0
				Chalcopyrite	+0.3				
KTDH04 232.30m (C44)	232.3	-6.8	Stage 6	Gypsum	+22.2	21.1	562.6	289.5	280.0
				Sphalerite	+1.2				
KTDH04 240.80m (C47)	240.8	-15.3	Stage 6	Gypsum	+22.9	21.8	559.6	286.5	
				Chalcopyrite	+1.1				
KTDH04 254.10m (C48)	254.1	-28.6	Stage 6	Anhydrite	+21.9	20.2	561.9	288.8	
				Pyrite	+1.7				

Note: Equilibrium isotopic fractionation factors of sulfur compounds with respect to H_2S from Ohmoto and Rye (1979) and Ohmoto and Lasaga (1982).

7.4.3 Aqueous sulfur species

Sulfate minerals, specifically gypsum and anhydrite, were only observed in Stage 6 mineralization. They coexist and were in contact with the base metal sulfides sphalerite, galena, chalcopyrite and pyrite. Though the analyzed Stage 6 sulfide-sulfate pairs are restricted in only one drill hole (KTDH04) and were collected from about 30 m vertical interval, the estimated isotopic fractionation between the coexisting aqueous sulfide and aqueous sulfate from the sulfide-sulfate pairs showed variation that allowed the determination of the dominant aqueous sulfur species (Ohmoto & Rye, 1979; Ohmoto & Lasaga, 1982). The data were plotted in a $\delta^{34}S$ vs $\Delta^{34}S$ [SO_4^{2-} - H_2S] diagram (Fig. 7.4). Arbitrary regression lines were generated and a steeper slope is observed in the aqueous sulfide plot while the aqueous sulfate plot has a gentler slope which is consistent with the more homogenous $\delta^{34}S$ of sulfates compared to sulfides. This indicates that aqueous species of sulfur in hydrothermal fluid during Stage 6 mineralization was dominated by sulfate. However, since no sulfate minerals were found in the early mineralization stages, it is assumed that sulfide is the dominant aqueous sulfur species from Stages 1 to 5.

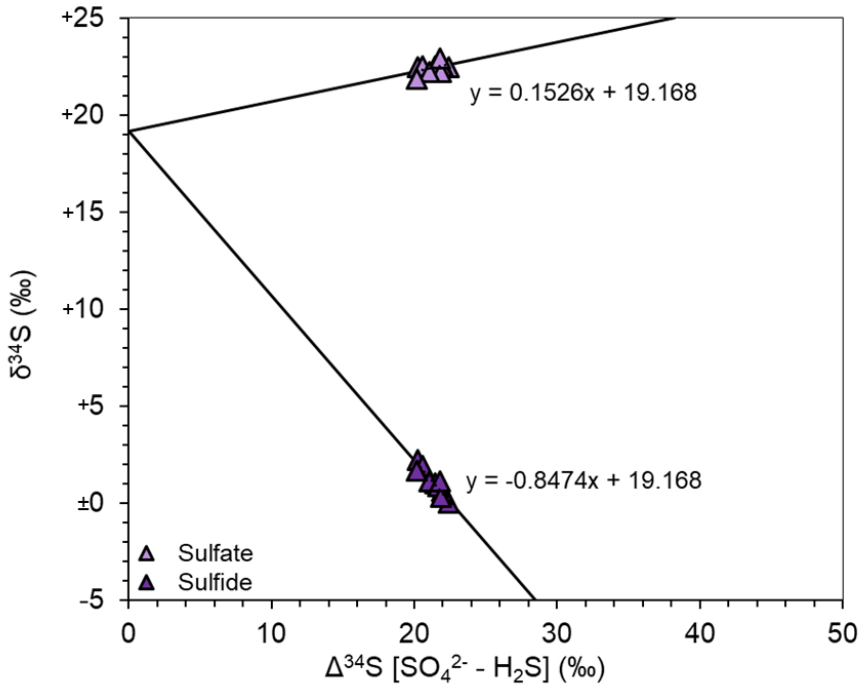

Fig. 7.3 $\delta^{34}S$ (‰) versus $\Delta^{34}S$ [SO_4^{2-} - H_2S] (‰) diagram of Stage 6 sulfate-sulfide mineral pairs of Kay Tanda.

7.4.4 Source of sulfur and mechanism for sulfide-sulfate deposition

There is a multitude of sulfur isotope studies on epithermal deposits which documented the range of $\delta^{34}S$ values for different types of epithermal systems. The $\delta^{34}S$ values of sulfides from low sulfidation, high sulfidation, and alkalic epithermal systems range from -6‰ to +5‰, -10 to +8‰, and -15‰ to +8‰, respectively, which all point to a ^{34}S-depleted source of probable magmatic origin (Ohmoto & Rye, 1979; Field & Fifarek, 1985; Arribas, 1995; Richards, 1995; Jensen & Barton, 2000; Cooke & Simmons, 2000; Gemmell et al., 2004). The sulfur isotopic composition of the sulfide and sulfate minerals of Kay Tanda are within the same range of the sulfur isotopic composition of other Philippine deposits, specifically the epithermal, skarn and porphyry copper deposits from the Western Luzon Arc (Fig. 7.5). The light sulfur isotopic composition of the sulfides analyzed in Kay Tanda ($\delta^{34}S$ = -5.8‰ to +3.3‰, n = 54) coincides with the reported values of known epithermal deposits and also indicates magmatic sulfur as the principal sulfur source.

In the Stage 6 mineralization, however, the fairly constant and heavy isotopic composition of the sulfates ($\delta^{34}S$ = +21.6‰ to +22.9‰, n = 9) indicate a second possible sulfur source. The narrow range of isotopic composition of the sulfates are similar to the sulfur isotopic composition of Late Miocene seawater (~+22‰) (Paytan et al., 2004), to the present-day seawater (~+21‰) (Rees et al., 1978). Interaction between magmatic hydrothermal fluids and seawater attributed to the precipitation of sulfate minerals with $\delta^{34}S$ values similar to Kay Tanda was documented in the Ladolam deposit in Lihir Island ($\delta^{34}S_{anhydrite}$ = +20 to +22‰) (Gemmell et al., 2004). Also, some porphyry deposits in the Philippines documented elevated $\delta^{34}S_{sulfide}$ values which have been interpreted to represent seawater sulfur contribution (Sasaki et al., 1984).

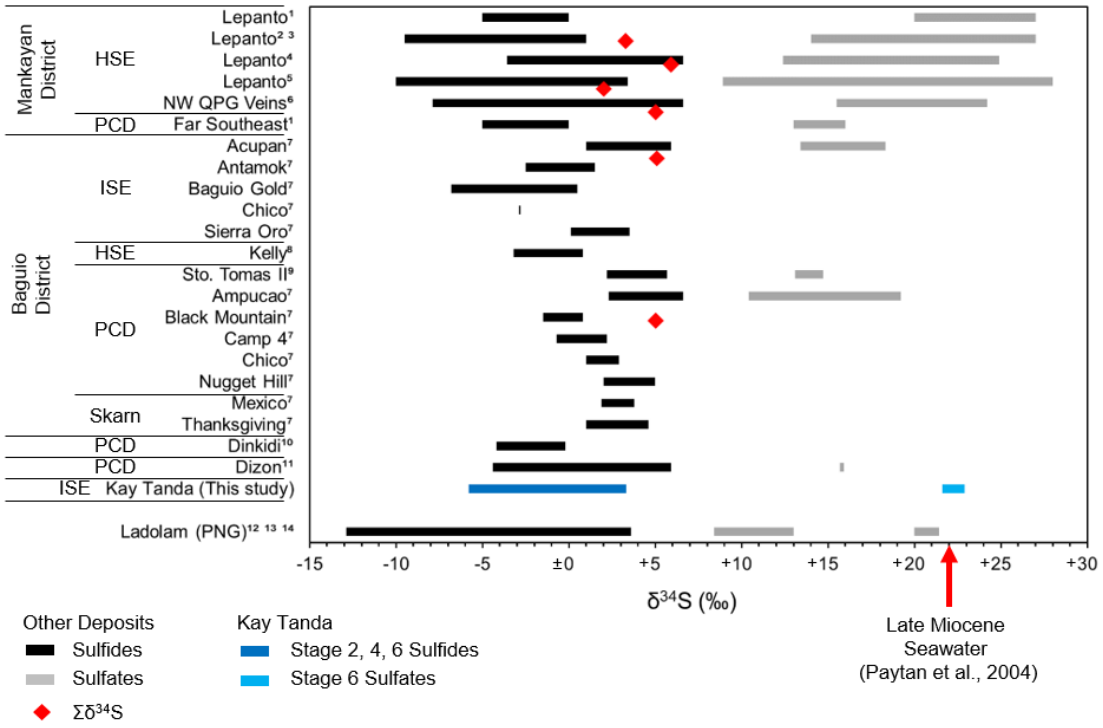

Fig. 7.5 Range of $\delta^{34}S$ (per mil) values for sulfides and sulfates from different ore deposits in Luzon Island, Philippines. Also shown are the calculated values of the $\Sigma\delta^{34}S$ determined from sulfide-sulfate pairs. The data for the Lepanto high sulfidation epithermal (HSE) deposit are from [1]Hedenquist and Garcia (1990), [2]Arribas (1995), [3]Hedenquist et al. (1998), [4]Imai (2000), and [5]Hedenquist et al. (2017); for the NW QPG veins are from [6]Manalo et al. (2018); for the Far Southeast porphyry copper deposit (PCD) are from [1]Hedenquist and Garcia (1990); for the intermediate sulfidation epithermal (ISE) deposits in the Baguio District are from [7]Cooke et al. (2011a); for the Kelly high sulfidation epithermal (HSE) deposit are from [8]Deyell and Cooke (2003); for the porphyry copper deposits (PCD) in the Baguio District are from [9]Imai (2001) and [7]Cooke et al. (2011a); for the [10]Dinkidi porphyry copper deposit (PCD) in Nueva Vizcaya are from Wolfe and Cooke (2011); for the [11]Dizon porphyry copper deposit (PCD) in Zambales are from Imai (2005); for the Ladolam epithermal deposit are from [12]Gemmell et al. (2004), [13]Carman (2003), [14]Muller et al. (2002).

Based on the stable isotope study, several evidence for the incorporation of meteoric-, magmatic- and seawater-derived fluids were presented. Based on the oxygen and hydrogen isotope analyses of illite samples which were used for the determination of the age of the mineralization at Kay Tanda, seawater is involved in the hydrothermal system since the early mineralization stages. However, seawater-derived sulfate minerals did not precipitate in the early stages of the mineralization towards the Stage 4 mineralization where increasing temperature were observed from fluid inclusion microthermometry. This is caused by the retrograde solubility of anhydrite with respect to temperature especially within the temperature regime of the

epithermal environment (Blount & Dickson, 1969). During these stages, seawater sulfate from the entering seawater was consumed via sulfate precipitation at the recharge zone where it encountered increasing temperature. The resulting hydrothermal fluids would then be sulfate-depleted and no sulfate minerals precipitated at Kay Tanda. This is consistent with the dominance of aqueous sulfide species and absence of sulfate minerals in the early mineralization stages where temperature was observed to increase from Stage 1 to Stage 4. The sulfur source is primarily magmatic in origin but there is still seawater component in the hydrothermal system as shown by the oxygen and hydrogen isotopic compositions of illite.

Seawater and magmatic fluid interaction is best demonstrated by Kuroko deposits, a type of hydrothermal ore deposit which lies within the same temperature range as epithermal deposits and also contains large quantities of anhydrite (and gypsum that was derived from hydration of anhydrite) (Ohmoto & Rye, 1974, 1979; Ripley & Ohmoto, 1977). Sulfur isotopic studies on Kuruko deposits suggest that anhydrite precipitated at the recharge zone as the seawater penetrate into the volcanic sequences where it was heated up by the intrusions (Tatsumi, 1970; Farrell et al., 1978; Farrell, 1979). Heated seawater reaches anhydrite saturation at temperatures approximately 110 °C along the vapor pressure curve (Marshall & Slusher, 1973; Glater & Schwartz, 1976). The basaltic rocks in the seafloor releases high amounts of calcium which react with the heated seawater sulfate and precipitates anhydrite with inherent sulfur isotope composition as seawater (Mottl et al., 1974; Hajash, 1975; Bischoff & Dickson, 1975; Mottl & Holland, 1978). The final solution is therefore saturated with respect to anhydrite and depleted with sulfate (Mottl et al., 1974; Hajash, 1975; Bischoff & Dickson, 1975; Mottl & Holland, 1978).

However, during the Stage 6 mineralization, meteoric water contribution increased as the temperature of the system started to cool down. This may have caused the seawater-derived sulfate minerals at the recharge zone to dissolve as a consequence of the retrograde solubility of anhydrite (Blount & Dickson, 1969). The fluids enriched with seawater-derived sulfate started to circulate into the hydrothermal system and interacted with the higher temperature hydrothermal fluids. The hydrothermal system became more sulfate-dominant which is shown by the sulfur isotopic composition of Stage 6 sulfides and sulfates (Fig. 7.4). Stage 6 sulfides also have a higher

and more positive $\delta^{34}S$ compared to the Stages 1, 2 and 4 sulfides. The isotopic disequilibrium can be explained by mixing of sulfide-rich solutions of magmatic origin and sulfate-rich solutions derived from the dissolution of sulfate minerals originally precipitated from seawater at or near the depositional sites (Ohmoto & Lasaga, 1982). This is consistent with the mixing trend observed from the homogenization temperature and salinity of Stage 6 fluid inclusions. This temperature contrast of the sulfate-rich and sulfide-rich solutions is a very effective mechanism for the coprecipitation of sulfate and sulfide minerals. The disequilibrium signature during mixing were inherited simultaneously by the sulfates and sulfides during ore deposition. This has been shown in the experimental studies conducted by Drummond (1981).

7.5 Conclusions

Hydrogen, oxygen and sulfur isotope studies presented evidence of the complex interaction of magmatic fluids, meteoric water, and seawater in Kay Tanda.

The Stage 2 illite samples which were used to determine the age of the mineralization in Kay Tanda have hydrogen and oxygen isotopic compositions approaching SMOW. Their calculated $\delta 18O_{water}$ and δD_{water} values coincided with the calculated theoretical final composition of water that has undergone isotopic exchange with andesitic-dacitic host rocks at temperatures between 250 °C and 300 °C and at water-rock ratios 0.1 to 5. This suggests a water-rock interaction between the andesitic-dacitic volcaniclastic sequences of Kay Tanda and a mixture of meteoric water and seawater. Moreover, this also suggests that seawater has been incorporated into the hydrothermal system of Kay Tanda since the early mineralization stages.

The sulfur isotope analysis of sulfide and sulfate minerals collected from different mineralization stages in Kay Tanda showed the following isotopic compositions: Stage 2 sulfides $\delta^{34}S$ values from -5.8‰ to +2.8‰, Stage 4 sulfides $\delta^{34}S$ values from -2.1‰ to +3.3‰, Stage 6 sulfides $\delta^{34}S$ values from +0.1‰ to +2.3‰ and Stage 6 sulfates $\delta^{34}S$ values from +21.6‰ to +22.9‰. These values are within the reported values of other magmatic-hydrothermal deposits in the Philippines which report magmatic sulfur as the primary sulfur source. Stage 6 sulfides,

however, showed elevated $\delta^{34}S$ values which also indicate a possible contribution of seawater sulfur as documented in several Philippine porphyry deposits. The fairly uniform $\delta^{34}S$ composition of the anhydrite and gypsum crystals also approach the sulfur isotopic composition of seawater.

There are two sources of sulfur in Kay Tanda: (1) a magmatic source which was derived from the intrusive rocks and (2) seawater. The precipitation of anhydrite during the late stage of the mineralization is explained by anhydrite's retrograde solubility. During the early mineralization stages as the seawater enter the deposit, seawater-derived sulfate minerals precipitate at the recharge zone where the seawater-derived fluids encounter increasing temperatures. The resulting fluids became seawater sulfate-depleted which later circulated in the system. This is consistent with absence of sulfates and dominance of sulfides from Stages 1 to 4 where temperature was observed to increased based on fluid inclusion microthermometry. However, at the last mineralization stage where the temperature of the system decreased and the meteoric water circulated into the deeper levels, the seawater-derived sulfate minerals started to dissolve which contributed seawater-derived sulfate into the hydrothermal fluids. The mixing of these fluids is an effective mechanism for the co-precipitation of the Stage 6 sulfates and sulfides.

CHAPTER 8

PHYSICOCHEMICAL CONDITIONS OF ORE DEPOSITION

8.1 Introduction

One of the notable features of the mineralization in Kay Tanda is its local bonanza Au-grade which is associated with the Stage 4 base-metal mineralization. This characteristic is well documented in drill hole intercepts of KTDH04, where assay results of Stage 4 hydrothermal breccias reach up to 100 g/t Au (Rohrlach & Fredericksen, 2008, unpublished data). In Chapter 5: Ore Mineral Chemistry, the major and minor element composition of Stage 4 and Stage 6 sphalerite were analyzed which allowed for the calculation of the FeS content of sphalerite. In Chapter 6: Fluid Inclusion Studies, fluid inclusion microthermometry conducted on quartz, sphalerite and anhydrite crystals from different stages of the mineralization provided information on the temperature, salinity and pressure during ore deposition. In Chapter 7: Stable Isotope Systematics, the dominant aqueous sulfur species were determined based on the sulfur isotopic composition of the sulfide and sulfate minerals.

This chapter aims to determine other physicochemical variables that are fundamental to ore transport and deposition which include *pH*, total sulfur content, sulfur fugacity, oxygen fugacity, and the concentrations and activities of dissolved components (alkali ions and sulfur-bearing species) through thermodynamic calculations. This chapter also aims to determine the dominant gold-bearing species and the possible mechanisms of gold deposition during Stage 4 bonanza Au mineralization.

Because the thermodynamic calculations in this chapter will be discussed in detail, the methodology part is omitted. The assumptions, equations and constants used for the calculations are presented throughout the discussion or listed in the Appendices.

8.2 Temperature, salinity and pressure

The homogenization temperature of the primary and pseudosecondary fluid inclusions from Stage 4 quartz crystals and the primary inclusions from Stage 4 sphalerite crystals ranges from 253 °C to 367 °C. The trapping temperature is estimated to vary between 270 °C to 290 °C based on the samples indicating boiling conditions. The salinity varies from 4.7 to 7.3 wt% NaCl equivalent with an average of 5.7 wt% NaCl equivalent. Vapor-saturated pressure is assumed because of the coexistence of primary liquid-rich and vapor-rich fluid inclusions. A boiling condition under hydrostatic pressure was estimated at 512 m below the paleowater table at 4.55 MPa (Haas, 1971). At these conditions, temperature corrections were negligible (Potter, 1977).

8.3 Sulfur fugacity

The sulfidation state of Kay Tanda was determined by (1) observing the ore mineral assemblages and their textures, and (2) by determining the chemical composition of sphalerite. Since Stages 1 and 2 have low base metal sulfide content, the sulfidation state was only determined for the base metal sulfide-rich stages (Stage 4 and Stage 6).

The FeS content of sphalerite coexisting with pyrite or pyrrhotite has been used to determine the sulfidation state of epithermal deposits (Barton & Skinner, 1979). The FeS content of sphalerite deposited in low sulfidation state typically ranges from 40 to 20 mol % FeS, in intermediate sulfidation state from 20 to 1 mol % FeS, in high sulfidation state from 1.0 to 0.05 mol % FeS, while in very high-sulfidation state from <0.05 mol % FeS (Scott & Barnes, 1971; Czamanske, 1974; Einaudi et al., 2003). In this study, the FeS content in sphalerite from Stages 4 and 6 were determined. The data were combined with the homogenization temperature of primary fluid inclusions trapped in the Stages 4 and 6 sphalerite and plotted on $logf_{S_2}$ vs 1000/T diagram to determine the sulfidation state of the hydrothermal fluids in Kay Tanda.

In Stage 4 hydrothermal breccias, fractured pyrite crystals contain inclusions of chalcopyrite and bornite. The bornite inclusions commonly show exsolution lamellae of chalcopyrite and both were later altered to secondary covellite (Fig. 4.5K-L). The exsolution of chalcopyrite from

bornite inclusions formed from the reaction of the host pyrite crystal and bornite solid solution occurring as inclusions as the temperature decreased (Craig & Scott, 1974). This texture indicates that the host mineral (pyrite) and the inclusions were formed at the same time under high sulfidation conditions (Craig & Scott, 1974). Though the temperature conditions at which these textures were formed cannot be determined specifically and be plotted in the $logf_{S_2}$ vs *1000/T* diagram, this texture is an evidence of the high sulfidation conditions during the formation of this initial mineral assemblage.

The fractured pyrite crystals were later replaced and filled in by chalcopyrite along its fractures and were surrounded or hosted by large sphalerite crystals. The Stage 4 and Stage 6 sphalerite that commonly host the fractured pyrite contained 0.72 to 2.9 mol% FeS and 0.97 to 2.1 mol % FeS, respectively. The FeS content of sphalerite is related to temperature and sulfur fugacity through Equation 8.1:

$$logX_{FeS} = 7.16 - \frac{7730}{T} - \frac{1}{2} logf_{s_2} \qquad \text{(Eq. 8.1)}$$

where X_{FeS} is the FeS content of sphalerite in mole fraction, T is temperature in K, and f_{S_2} is the sulfur fugacity in atm (Barton & Skinner, 1979). When plotted in the $logf_{S_2}$ vs *1000/T* diagram, it shows that the minerals were formed under intermediate sulfidation conditions but close to the high sulfidation border ($logf_{S_2}$ = -9 to -12 atm at 250°C to 310 °C) (Fig. 8.1).

This indicates that the mineralization was initially formed under high sulfidation conditions and then the sulfidation state decreased as the mineralization progressed. The ore mineral assemblage in Kay Tanda, which is composed primarily of low Fe sphalerite, galena, chalcopyrite and pyrite, also coincides with intermediate sulfidation conditions (Einaudi et al., 2003).

For the purposes of thermodynamic calculations, the sulfur fugacity values to be used for the succeeding calculations are shown in Table 8.1.

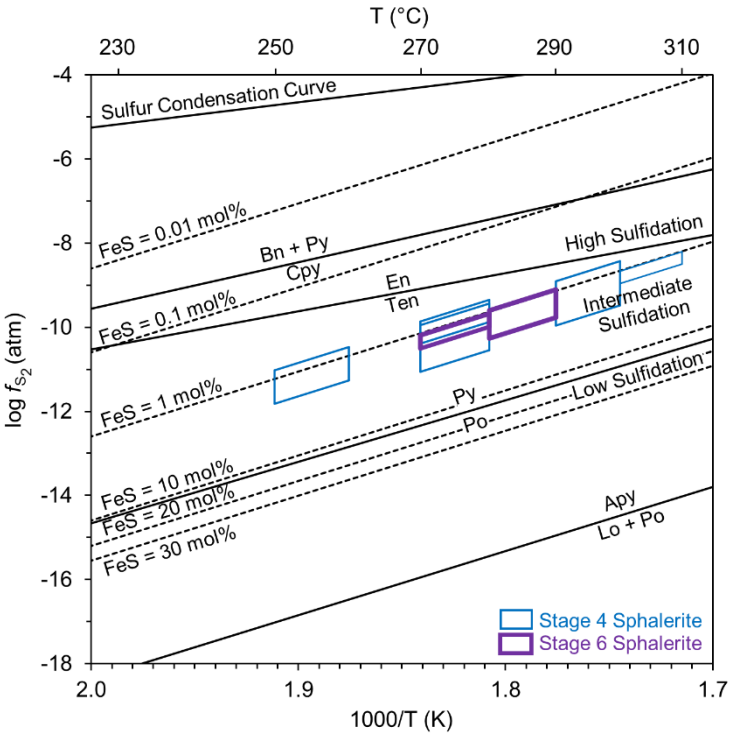

Fig. 8.1 $Logf_{S_2}$ vs temperature diagram showing the sulfidation state of the Stages 4 and 6 mineralization at Kay Tanda from FeS content of sphalerite and homogenization temperature of fluid inclusions in the corresponding sphalerite from the Stage 4 and Stage 6 veins. Sulfidation reactions used to define sulfidation states are from Barton and Skinner (1979). Abbreviations: Apy – Arsenopyrite, Bn – bornite, Cpy – chalcopyrite, En – enargite, Lo – loellingite, Po – pyrrhotite, Py – pyrite, Ten – Tennantite.

Table 8.1 FeS content range in sphalerite and the representative sulfur fugacity values at T = 250 °C and T = 300 °C

	T = 250 °C	**T = 300 °C**
X_{FeS} (mol%)	0.79 to 1.96	0.77 to 2.59
$logf_{S_2}$ average (atm)	-11.4	-9.0

8.4 pH

The average salinity calculated from the ice melting temperature of fluid inclusions is around 5.7 wt% NaCl equivalent. Assuming that the salinity of the hydrothermal fluid is dependent on the concentrations of Na^+, Ca^{2+}, K^+, and Cl^- ions, the concentrations of these ions can be calculated using the following alkali geothermometer equations: (1) Na/K geothermometer by Fournier (1981) (Eq. 8.2) and (2) Na-K-Ca geothermometer by Fournier and Truesdell (1973) (Eq. 8.3) (Henley et al., 1984b):

$$T\,(°C) = \frac{1217}{\log\left(\frac{Na}{K}\right) + 1.483} - 273.15 \quad \text{(Eq. 8.2)}$$

$$T\,(°C) = \frac{1647}{\log\left(\frac{Na}{K}\right) + \beta\left[\log\left(\frac{\sqrt{Ca}}{Na}\right) + 2.06\right] + 2.47} - 273.15 \quad \text{(Eq. 8.3)}$$

The activities of each dissolved alkali ion a_i is also calculated by multiplying the activity coefficient γ_i derived from the Debye-Huckel equation (Eq. 8.4) to the concentration of the dissolved alkali ions m_i (Eq. 8.5) (Henley et al., 1984a).

$$-log\gamma_i = \frac{Az_i^2\sqrt{I}}{1 + B\text{å}_i\sqrt{I}} + bI \quad where \quad I = \frac{1}{2}\sum_i m_i z_i^2 \quad \text{(Eq. 8.4)}$$

$$a_i = \gamma_i m_i \quad \text{(Eq. 8.5)}$$

The list of the Debye-Huckel coefficients (*A* and *B*), ionic charge (z_i), and ion size parameter å_i are listed in Appendix F. Considering the temperature range obtained from fluid inclusion microthermometry, the alkali ion concentrations and activities are calculated at T = 250°C and T = 300 °C (Table 8.2).

Table 8.2 Calculated alkali concentrations and activities at T = 250°C and T = 300 °C

	T = 250 °C	**T = 300 °C**
Alkali ion concentration (mol/L)		
Na^+	0.88	0.83
K^+	0.07	0.11
Ca^{2+}	$7.9\text{x}10^{-5}$	$2.6\text{x}10^{-5}$
Cl^-	0.95	0.94
log alkali ion activity		
$log\ a_{Na^+}$	-0.39	-0.49
$log\ a_{K^+}$	-1.51	-1.43
$log\ a_{Ca^{2+}}$	-5.15	-5.89
$log\ a_{Cl^-}$	-0.37	-0.47

The *pH* of the mineralizing fluids during the deposition ore minerals can be inferred from the observed alteration minerals. The activity of K^+ and *pH* are related through the mineral equilibria between adularia and sericite (Henley et al., 1984c). These are common alteration minerals associated to the Au and base metal mineralization at Kay Tanda. For the reaction,

$$3Kfeldspar + 2H^+ = Kmica + 6quartz + 2K^+$$

the standard free energy change ($\Delta G°_R$) at T = 250°C and T = 300 °C can be calculated using the following Equation 8.6:

$$\Delta G°_R = \left(\Delta G°_{Kmica} + 6\Delta G°_{quartz} + 2\Delta G°_{K^+}\right) - (3\Delta G°_{Kspar} + 2\Delta G°_{H^+}) \quad \text{(Eq. 8.6)}$$

The relationship between K^+ and *pH* is shown in Equation 8.8 from the calculation of the equilibrium constant *k* for this reaction using Equation 8.7.

$$\Delta G°_R = -RTlnk = -RT2.303logk \quad \text{(Eq. 8.7)}$$

$$\log k = 2\log(\frac{[K^+]}{[H^+]}) \quad \text{(Eq. 8.8)}$$

$$pH = -log[H^+] \quad \text{(Eq. 8.9)}$$

Using the free energies of formation ($\Delta G°_R$) of potassium feldspar (Kfeldspar), Kmica, quartz, H^+ and K^+ (Helgeson et al., 1978; Henley et al., 1984c) and the activity of K^+, the *pH* of the hydrothermal fluid can be calculated from Equations 8.8 to 8.9. The same is done for the mineral equilibria between kaolinite and sericite using the reaction:

$$2Kmica + 3H_2O + 2H^+ = 3kaolinite + 2K^+$$

The free energies of formation ($\Delta G°_f$) of minerals and aqueous species (Helgeson et al., 1978; Henley et al., 1984c) in kJ/mol at the saturated vapor pressure of pure water are listed in Appendix G. The *pH* of the hydrothermal fluids calculated at T = 250°C and T = 300 °C are shown in Table 8.3.

The *pH* at Stage 4 mineralization is approximately equal to the *pH* at the sericite-adularia boundary. Stage 4 mineralization is characterized by near neutral-*pH* alteration assemblage (neutral *pH* = 5.54 at 250 °C and 5.64 at 300 °C) which indicates that the mineralizing fluids are in equilibrium with the host rocks.

Table 8.3 Calculated *pH* at the sericite-adularia and kaolinite-sericite boundaries at T = 250°C and T = 300 °C

	T = 250°C	**T = 300 °C**
$pH_{\text{sericite-adularia}}$	5.48	5.21
$pH_{\text{kaolinite-sericite}}$	3.49	3.14

8.5 Total sulfur concentration

The total sulfur concentration is also an important variable controlling metal transport and oxide and sulfide mineral stabilities (Barnes, 1979). The total sulfur content in Kay Tanda is estimated at $\Sigma S = 10^{-2}$ mol. This is based on the estimations for Ag- and base-metal rich adularia-sericite-style epithermal deposits such as Creede, Colorado ($\Sigma S = 10^{-3.8}$ to $10^{-3.7}$ m, Barton et al., 1997), Yatani, Japan ($\Sigma S = 10^{-2}$ m, Hattori, 1975), Toyoha, Japan ($\Sigma S = 10^{-2}$-$10^{-2.5}$ m, Tsushima, 1997), Eureka, Colorado ($\Sigma S = 10^{-1.4}$ m, Casadevall & Ohmoto, 1977), and Round Mountain, Nevada (ΣS = 0.0014 m, Sander & Einaudi, 1990). Base metal-rich deposits, especially those containing economic concentrations of base metals, have higher ΣS compared to base metal-poor deposits such as Acupan, Philippines (ΣS = 0.004 m, Cooke et al., 1996). The dominant sulfur species in Kay Tanda is H_2S.

8.6 Oxygen fugacity

Assuming that (1) the total sulfur content is estimated at $\Sigma S = 10^{-2}$ mol, (2) the dominant sulfur species is H_2S, and (3) the sulfur fugacity is estimated at $logf_{S_2}$ = -11.4 atm at 250 °C and at $logf_{S_2}$ = -9.0 atm at 300 °C, the oxygen fugacity at T = 250 ° C and T = 300 °C were determined from the reaction:

$$2H_2S + O_{2(g)} = S_{2(g)} + 2H_2O$$

The relationship between oxygen fugacity, sulfur fugacity and H_2S content is shown in Equation 8.10.

$$logf_{O_2} = logf_{S_2} - 2\log[H_2S] - logk \quad \text{(Eq. 8.10)}$$

The equilibrium constants (*log k* values) used are 30.06 at T = 250 °C and 27.21 at T = 300 °C based on the data of Helgeson et al. (1978), Robie et al. (1978) and Fisher and Barnes (1972) (Henley et al., 1984d). The calculated oxygen fugacity values are shown in Table 8.4. The data were plotted on a $logf_{S_2}$ vs $logf_{O_2}$ diagram (Fig. 8.2). Stage 4 mineralization is in the sulfide dominant field. This is consistent with the sulfur isotope data of Stage 4 sulfides. The data were also plotted on the $logf_{O_2}$ vs *pH* diagram (Fig. 8.3). The mineral stability fields of several minerals were also superimposed on the diagrams. The chemical reactions and equilibrium constants used for the construction of the mineral stability fields in the $logf_{S_2}$ vs $logf_{O_2}$ diagram and $logf_{O_2}$ vs *pH* diagram are listed in Appendix H.

Table 8.4 Calculated oxygen fugacity values at T = 250°C and T = 300 °C

	T = 250 °C	**T = 300 °C**
$logf_{O_2}$	-37.5	-32.2

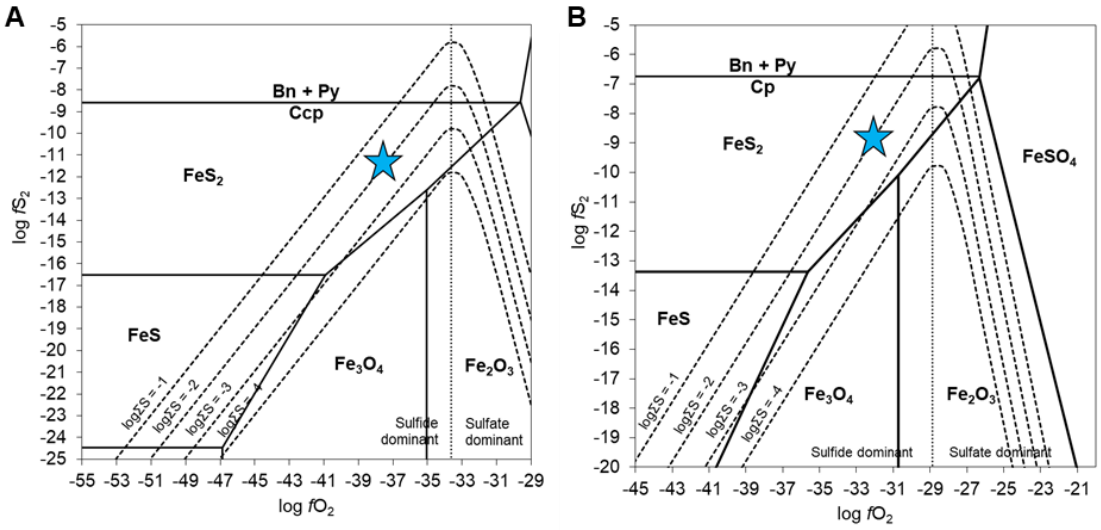

Fig. 8.2 Estimated ore-forming conditions on $logf_{S_2}$ vs $logf_{O_2}$ diagram at 250 °C (A) and at 300 °C (B). The phase relation of minerals in Fe-O-S system are also plotted. Mineral stabilities were derived from Barton and Skinner (1979).

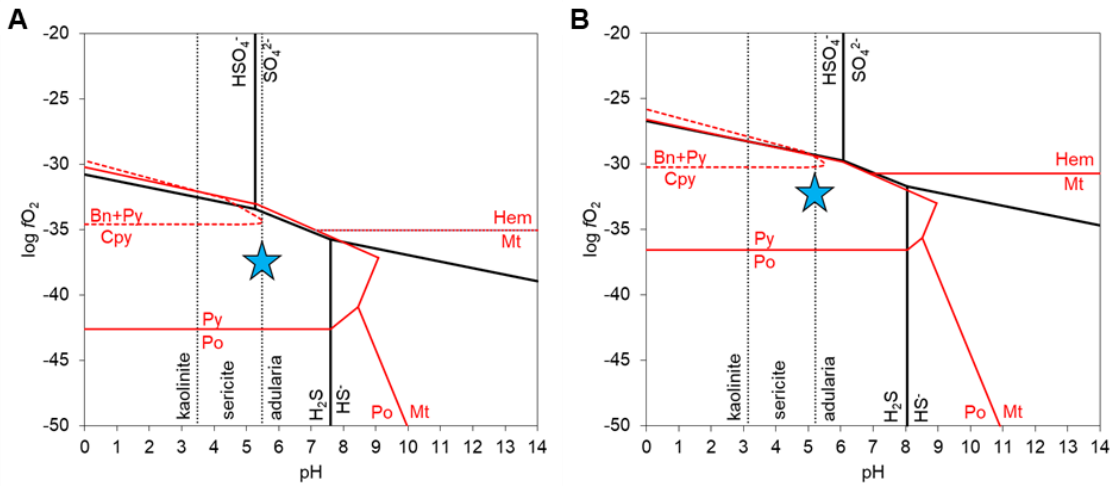

Fig. 8.3 Estimated ore-forming conditions on $logf_{O_2}$ vs *pH* diagram at 250 °C (A) and at 300 °C (B). The phase relation of minerals in Fe-O-S system are also plotted. Mineral stabilities were derived from Barton and Skinner (1979).

8.7 Concentration and activity of sulfur-bearing species

Using the calculated *pH*, ΣS, $logf_{S_2}$, and $logf_{O_2}$, the concentrations of the different sulfur-bearing species in solution were also determined. The reactions and their corresponding equilibrium constants (*log k* values) at T = 250 °C and T = 300 °C that were used in the calculations are shown in Appendix H. The activities of the sulfur-bearing species are also calculated using Equations 8.4 and 8.5. The results are shown in Table 8.5.

8.8 Au speciation and mechanism for deposition

The two most important ligands that form complexes with gold are Cl^- and HS^- which forms $AuCl_2^-$ and $Au(HS)_2^-$ complexes, respectively (Seward, 1989; Seward, 1991). The behavior of these complexes in response to changes in the physicochemical conditions during ore formation affects metal transport and deposition (Seward, 1989; Seward, 1991).

The solubility fields of $AuCl_2^-$ and $Au(HS)_2^-$ complexes at T = 300 °C and T = 250 °C are superimposed on $log\, f_{O_2}$ vs *pH* diagram (Fig. 8.4). The reactions and their corresponding equilibrium constants (*log k* values) at T = 250 °C and T = 300 °C obtained from Shenberger and Barnes (1989) and Helgeson (1969) are listed in Appendix H.

Table 8.5 Calculated concentrations and activities of sulfur-bearing species at T = 250°C and T = 300 °C

	T = 250 °C	**T = 300 °C**
log concentration		
log H_2S	-1.98	-2.01
log HS^-	-3.77	-4.44
log SO_4^{2-}	-8.40	-7.01
log HSO_4^-	-9.60	-7.38
log activity		
log aH_2S	-1.98	-2.01
log aHS^-	-2.31	-2.42
log aSO_4^{2-}	-3.30	-3.66
log $aHSO_4^-$	-2.31	-2.42

$AuCl_2^-$ complexes are probably insignificant in Kay Tanda because of the $AuCl_2^-$ complexes are predominant at high temperatures (450-500°C), high pressures (0.5-2.0 kbars) and high salinities (3 m KCl) (Cooke et al., 1996). Based on the diagram, the dominant Au-bearing complex is $Au(HS)_2^-$ which is the predominant Au(I)-bisulfide complex at weakly acidic to weakly basic *pH* (Seward, 1973; Shenberger & Barnes, 1989; Benning & Seward, 1996; Wood & Samson, 1998). A decrease in temperature can cause an increase in the solubility of $Au(HS)_2^-$ which can transport large amounts of gold into the system. In the H_2S field, the gold solubility is controlled by the reaction (Benning & Seward, 1996):

$$Au(HS)_{2(aq)}^- + \frac{1}{2}H_2 = Au + H_2S_{aq} + HS_{aq}^-$$

Several mechanisms can lead to gold precipitation such as increase in H_2 and $Au(HS)_2^-$ concentrations, or decrease in *pH* and ΣS. In Kay Tanda, evidences of boiling conditions were observed. Boiling might have caused the removal of H_2S which lead to the decomposition of $Au(HS)_2^-$ complex leading to the precipitation of gold (Benning & Seward, 1996). This mechanism, coupled with the transport of large amounts of gold by $Au(HS)_2^-$ complex during temperature decrease may be responsible for the bonanza-Au grade in Stage 4 mineralization.

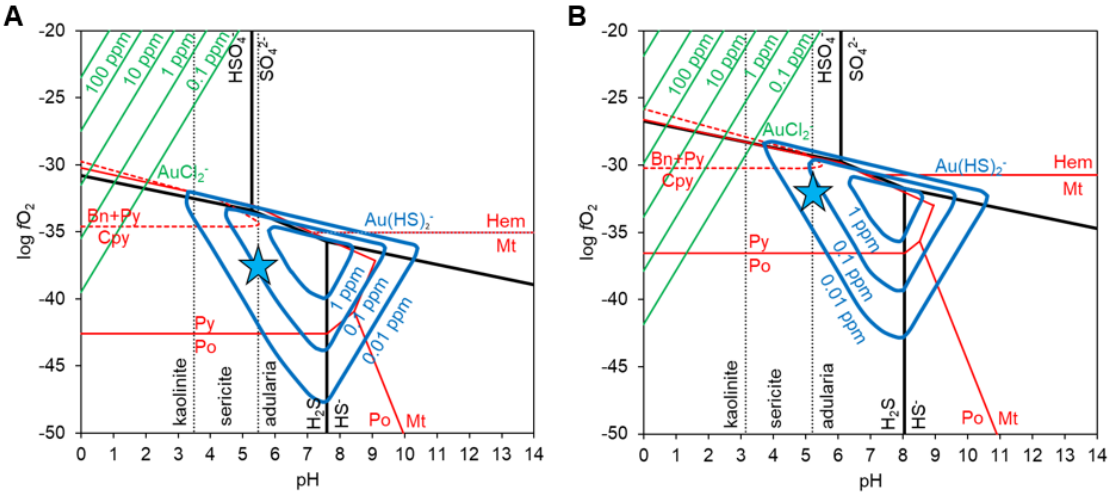

Fig. 8.4 Solubility of Au complexes superimposed on $logf_{O_2}$ vs *pH* diagram. (A) Solubility fields of $AuCl_2^-$ and $Au(HS)_2^-$ complexes at T = 250 °C. (B) Solubility fields of $AuCl_2^-$ and $Au(HS)_2^-$ complexes at T = 300 °C.

8.9 Conclusions

Incorporating the acquired homogenization temperature from the fluid inclusion microthermometry, the calculated FeS content of sphalerite from the major and minor element composition, and the observed ore mineral assemblage and ore textures from ore microscopy, the sulfur fugacity was determined for the Stage 4 bonanza Au mineralization at Kay Tanda. Bornite inclusions with exsolution lamellae of chalcopyrite in host fractured pyrite indicate ore formation at high sulfidation conditions. The host sphalerite crystals of the fractured pyrite crystals indicate ore formation at intermediate sulfidation conditions based on the FeS content of sphalerite at temperatures estimated by fluid inclusion microthermometry. These indicate an evolution from a high sulfidation condition to an intermediate sulfidation condition during Stage 4 ore deposition.

The average salinity was estimated at 5.7 wt% NaCl equivalent and was used to determine the *pH* during Stage 4 mineralization using sericite-adularia as the *pH* control factor. Assuming that the system is in equilibrium, the $logf_{O_2}$ varies from -32.2 to -37.5 atm from T = 300 to 250 °C at *pH* = 5.11 and $\Sigma S = 10^{-2}$ mol/kg. Based on the $logf_{S_2}$ vs $logf_{O_2}$ and $logf_{O_2}$ vs *pH* diagrams, the Stage 4 mineralization occurred in a sulfide-dominant condition where H_2S is the dominant aqueous sulfur species. Gold was mainly transported as $Au(HS)_2^-$ complex. In Kay Tanda,

evidence of boiling conditions was observed. Boiling might have caused the removal of H_2S which triggered the decomposition of $Au(HS)_2^-$ complex leading to the precipitation of gold.

CHAPTER 9

GENETIC MODEL

This study has investigated the characteristics, genesis, and evolution of the gold and base metal mineralization at the Kay Tanda epithermal gold deposit. The formation of the deposit is attributed to the circulation of the hydrothermal fluids derived from several sources, which were heated up by several intrusive bodies at depth, and interacted with the andesitic to dacitic volcaniclastic rocks and volcanic-derived sedimentary host rocks. This chapter aims to present the genetic model of Kay Tanda as it evolved through time. The genetic model highlights the interpretation of the results that were presented in the previous chapters. These include: (1) the geologic framework of the deposit, (2) the characteristics, occurrence and paragenetic sequence of the different alteration and mineralization stages, (3) the sources of the components of the hydrothermal system, (4) the changes in the physicochemical conditions during ore deposition, and (5) the mechanisms responsible for ore deposition. At the end of the chapter, implications for exploration and several recommendations for future work will be suggested.

9.1 Genetic Model

The epithermal mineralization in Kay Tanda is mainly linked to the emplacement of the Balibago Intrusive Complex and the Dacite Porphyry Intrusives, which intruded the Talahib Volcanic Sequence and the Calatagan Formation during the Late Miocene to Early Pliocene. The circulating hydrothermal fluids derived from multiple sources generated an epithermal system that evolved through time.

The epithermal system in Kay Tanda commenced after the emplacement of the coeval Balibago Intrusive Complex and its associated breccia pipes into the Talahib Volcanic Sequence during the Middle Miocene to Late Miocene (Fig. 9.1). The deposition of the andesitic to dacitic

volcaniclastic rocks of the Talahib Volcanic Sequence and the emplacement of the Balibago Intrusive Complex are attributed to the Neogene volcanism at the southern tip of the Western Luzon Arc consequent to the subduction of the South China Sea Basin along the Manila Trench (Hayes & Lewis, 1985; Defant et al., 1991; Aurelio, 2000). The dioritic bodies of the Balibago Intrusive Complex formed a domal intrusive complex which caused extensive fracturing and brecciation due to the release of pressure on the overlying dacitic to andesitic volcaniclastic rocks (Rohrlach & Fredericksen, 2008, unpublished data). Magmatic volatiles, such as SO_2, H_2S, CO_2, and HCl, were exsolved from the intrusions which ascended through the fractured volcaniclastic rocks and breccia pipes and later condensed into the groundwater. This interaction caused the formation of strongly acidic solutions due to the disproportionation of SO_2 to form H_2SO_4 and H_2S and the dissociation of HCl (Arribas, 1995). The passage of strongly acidic solutions caused the intensive leaching of the host rocks and the formation of vuggy silica which were mostly mapped in and around the breccia pipes. The petrography of these altered host rocks showed the presence of high temperature vug-filling pyrophyllite, dickite/kaolinite and diaspore crystals which indicate that the alteration is of hypogene origin and that the fluids were also silica-undersaturated (Simmons et al., 2005). After the leaching, silica-saturated hydrothermal fluids ascended through the fractured volcaniclastic rocks and breccias and deposited the Stage 1 quartz veins and the associated silicification in the advanced argillic-altered zones. These quartz veins were formed at lower temperatures compared to the other younger veins. Based on fluid inclusion microthermometry, the homogenization temperature of primary and secondary fluid inclusions in the Stage 1 quartz veins ranges from 200 °C to 280 °C with the mode varying between 220 °C to 250 °C and 270 °C to 280 °C. The main mechanism of ore deposition in the Stage 1 veins is surface fluid dilution based on the trends of the homogenization temperature vs salinity of the measured fluid inclusion assemblages (Wilkinson, 2001). This is consistent with the mixing of the magmatic-derived fluids and the shallow meteoric waters during this stage. Parts of these advanced argillic zones were later removed by erosion and were covered by younger rocks such as the Late Miocene to Early Pliocene sedimentary sequences of the Calatagan Formation and the Pliocene andesitic volcaniclastic rocks of the Balibago Andesite. At present, the advanced argillic

alteration in Kay Tanda is localized in areas in and around the breccia pipes associated with the intrusion of the Balibago Intrusive Complex (Fig. 9.1).

During the Middle Miocene collision of the Palawan Microcontinental Block to the Philippine Mobile Belt, the volcanism decreased in southern Batangas as a consequence of the transformation of the southern tip of the Manila Trench from a subduction zone setting into a collision zone setting (Rangin et al., 1985; Stephan et al., 1986; Rangin et al., 1988; Aurelio et al., 2013). This was observed in Kay Tanda with the deposition of the Late Miocene to Early Pliocene Calatagan Formation which indicates periods of quiescence leading to the deposition of intercalated sedimentary rocks within volcaniclastic rocks. The abundance of texturally immature clastic rocks (conglomerates) over the texturally mature clastic rocks (siltstones and shales) and their compositional similarity to the older volcaniclastic rocks indicate local derivation (Tucker, 2001). Lenses of limestones within the Calatagan Formation also indicate that the rocks were deposited in a volcanic environment transitioning to a shallow marine environment (Tucker, 2001). The report by Avila (1980) also suggested that there was partial subsidence at the southern part of Batangas which resulted to tilting towards the south during Late Miocene to Early Pliocene. This led to the deposition of marine limestones on the volcaniclastic-sedimentary rocks (Avila, 1980).

The evolution of the hydrothermal system continued in the Late Miocene to Early Pliocene with the intrusion of the Dacite Porphyry Intrusives. The temperature of the system started to increase, and the interaction between the fractured volcaniclastic rocks and the circulating hydrothermal fluids progressed. The hydrothermal system developed over a broader area which formed the pervasive argillic alteration dominated by illite and quartz. K-Ar dating of Stage 2 illite samples collected from haloes around Stage 2 quartz veins indicates that the mineralization occurred at the end of Late Miocene (5.9 to 5.5 ± 0.2 Ma). Also, a regional extension event occurred in the southern Batangas region during the Late Miocene to Early Pliocene which later propagated northwards and became more focused along the Macolod Corridor further north of Kay Tanda (Rohrlach & Fredericksen, 2008, unpublished data). The crustal extension formed NE-trending normal faults which controlled the formation of the quartz veins at the shallower

levels of Kay Tanda (Rohrlach & Fredericksen, 2008, unpublished data). The silica-saturated hydrothermal fluids formed the extensive Stage 2 quartz stockworks composed of banded crustiform to colloform quartz veins, quartz-pyrite veins, and silicified hydrothermal breccias which form the bulk Au-Ag mineralization in Kay Tanda. The measured homogenization temperature from primary fluid inclusions ranges from 250 °C to 330 °C with mode around 260 °C to 270 °C which is higher than the measured temperatures of Stage 1 veins. Boiling is the main mechanism of ore deposition in Stage 2 which is supported by the following evidence from fluid inclusion studies: (1) heterogeneous trapping of fluid inclusions of variable liquid-vapor ratios (Bodnar et al., 1985; Moncada et al., 2012), (2) homogenization temperature histograms showing skewness to higher temperatures (Brown, 1998), and (3) negative-trending slope in the CO_2/N_2 vs total gas content diagram (Blamey, 2010). A boiling condition under hydrostatic pressure was estimated approximately around 500 m below the paleowater table for the shallow Au-Ag mineralization (Haas, 1971). Based on the fluid inclusion gas compositions, meteoric water is an important component of the hydrothermal fluids (Giggenbach & Poreda, 1993; Norman & Musgrave, 1994; Norman & Moore, 1999; Blamey and Norman, 2002; Blamey, 2010). One sample from the Stage 2 mineralization plotted closer to the boundary between shallow meteoric water and magmatic water which may indicate that the hydrothermal fluids were dominated by meteoric water but with a contribution from magmatic fluid which may be derived from the Dacite Porphyry Intrusives at depth (Blamey, 2010). Like the gas composition of the several Philippine geothermal water samples presented by Giggenbach and Poreda (1993), most of the samples from Kay Tanda plotted within the arc-type-derived fluid field approaching meteoric water composition which is consistent with the tectonic setting of the southern Batangas area. In the CO_2/100-1000He-200Ar ternary diagram by Giggenbach and Poreda (1993), the Stage 2 fluid inclusion gas composition clustered towards the meteoric water composition along the basaltic magmatism field which indicates a possible mixing of basaltic magma-derived component and a larger proportion of meteoric water during vein formation. The magmatic component in the hydrothermal fluids was also observed in the sulfur isotopic composition of Stage 2 sulfides which point to a magmatic sulfur origin. Also, the Stage 2 illite samples used for the K-Ar dating show

oxygen and hydrogen isotope compositions close to SMOW which may suggest a mixture of seawater and meteoric water that has undergone isotopic exchange with the andesitic and dacitic host rocks. During the early mineralization stages, seawater sulfate from the entering seawater was consumed via sulfate precipitation at the recharge zone where it encounters increasing temperature. This is because of retrograde solubility of anhydrite, i.e. increasing temperature causes the solubility of anhydrite to decrease (Blount & Dickson, 1969). The resulting fluids became seawater sulfate-depleted which later circulated in the system. This is consistent with absence of sulfates in the early mineralization stages (Fig. 9.2). The sulfur source is primarily magmatic in origin but there is still seawater component in the hydrothermal system as shown by the oxygen and hydrogen isotopic compositions of illite.

Meteoric water and seawater continued to be incorporated into the hydrothermal system as the mineralization in Kay Tanda evolved from a shallow quartz-Au-Ag mineralization to a deeper quartz-base metal-Au mineralization (Fig. 9.3). Despite the increase in surface water influx, the high temperature of the epithermal system was sustained because of the continuous emplacement of the Dacite Porphyry Intrusives. This increasing temperature inhibited the incorporation of seawater sulfate into the hydrothermal system. Seawater sulfate continued to be consumed at the recharge zone. The pH of the circulating hydrothermal fluids also continued to increase from the early to the later stages of the mineralization which is exhibited by the acidic alteration assemblage associated with Stage 1 mineralization, weakly acidic alteration assemblage in Stage 2, to a near neutral pH alteration assemblage in Stage 4 which formed the illite – chlorite – quartz alteration. The absence of illite/sericite haloes around the Stage 4 base metal sulfide veins indicate that the mineralization was in equilibrium with the host rocks. The homogenization temperature from varied from 250 °C to 360 °C with a mode from 270 °C to 280 °C. This is a 10 °C increase from the trapping temperature at Stage 2. Boiling is also the main mechanism for ore deposition in Stage 4. This is supported by the following evidence: (1) occurrence of rhombic adularia in Stage 4 veins and hydrothermal breccia (Dong & Morrison, 1995), (2) heterogeneous trapping of fluid inclusions of variable liquid-vapor ratios (Bodnar et al., 1985; Moncada et al., 2012), (3) homogenization temperature histograms showing skewness to higher temperatures (Brown, 1998),

and (4) negative-trending slope in the CO_2/N_2 vs total gas content diagram (Blamey, 2010). The boiling depth is estimated at around 600 m below the paleowater table (Haas, 1971). The deeper boiling level for the Stage 4 and Stage 6 mineralization is attributed to the continued deposition of sedimentary rocks of the Calatagan Formation at the timing of the later base metal-Au mineralization (Fig. 9.3). This implies that approximately at least 460 m of overlying volcaniclastic-sedimentary sequences has been eroded since the formation of the deposit.

One of the notable characteristics during Stage 4 mineralization is its base metal mineralization and bonanza grade Au-mineralization. Petrographic, microthermometric and chemical analysis of Stage 4 sphalerite revealed important information on the physicochemical conditions (temperature, salinity, sulfur fugacity) during the Stage 4 mineralization. Sphalerite crystals typically host fractured pyrite crystals which contains bornite inclusions with exsolution lamellae of chalcopyrite. This texture reveals that the sulfidation conditions during Stage 4 mineralization evolved from a high sulfidation state (based on the bornite and chalcopyrite inclusion textures in pyrite) to an intermediate sulfidation state (based on the FeS content and trapping temperature of fluid inclusions in host sphalerite) (Craig & Scott, 1974; Barton & Skinner, 1979). Using these data, thermodynamic calculations of physicochemical conditions (pH, $logf_{S_2}$, $logf_{O_2}$) during the Stage 4 bonanza grade Au mineralization were conducted at temperatures 300 °C to 250 °C. The pH was calculated using sericite-adularia as the pH control factor. The pH during Stage 4 mineralization is estimated at pH = 5.11 which is near neutral pH conditions at the mentioned temperatures. Assuming ΣS = 10^{-2} mol/kg, the oxygen fugacity was estimated at $logf_{O_2}$ = -32.2 to -37.5 atm. This is within the H_2S stability field, which is the dominant sulfur-bearing species in the hydrothermal fluids. Based on the solubility field of different Au complexes plotted on the $logf_{O_2}$ vs pH diagram, gold was mainly transported as $Au(HS)_2^-$ complex. In Kay Tanda, evidence of boiling conditions were observed. Boiling might have caused the removal of H_2S which triggered to the decomposition of $Au(HS)_2^-$ complex leading to the precipitation of gold (Benning & Seward, 1996).

During the last stage of the mineralization, the temperature of the system started to decrease. Increasing meteoric water contribution and decreasing temperature caused the seawater-derived sulfates to dissolve as a consequence of the retrograde solubility of anhydrite. The fluids enriched with seawater-derived sulfate started to circulate into the hydrothermal system and interacted with the higher temperature hydrothermal fluids (Fig. 9.4). The hydrothermal system became more sulfate-dominant which is shown by the sulfur isotopic composition of Stage 6 sulfides and sulfates. The mixing of hydrothermal fluids caused the precipitation of anhydrite-base metal veins. The homogenization temperature obtained from fluid inclusions in sphalerite crystals range from 240 °C to 340 °C with a mode at 270 °C to 280 °C, while that of the anhydrite crystals range from 175 to 320 °C. The salinity of the system also decreased to 4.6 wt% NaCl equivalent. The decreasing trend of salinity as the homogenization temperature decreases suggests surface fluid dilution or mixing. The pH of the deposit also remained at near neutral conditions similar to Stage 4 mineralization. Hydration textures were observed in the anhydrite veins which indicates the transformation of anhydrite to gypsum attributed to the circulation of meteoric water into the deposit.

The propylitic alteration recorded in the Late Miocene to Early Pliocene Calatagan Formation indicates that the thermal activity contributed by the Dacite Porphyry Intrusives continued after the deposition of the sedimentary-volcaniclastic sequences. The hydrothermal activity in Kay Tanda eventually ceased during the Middle to Late Pliocene, which was reflected to the deposition of the post-mineralization Pliocene-age Lobo Agglomerate and Balibago Andesite which were not affected by hydrothermal alteration. Erosion exposed some of the mineralized and hydrothermally altered areas in Kay Tanda which is observed in the present-day location.

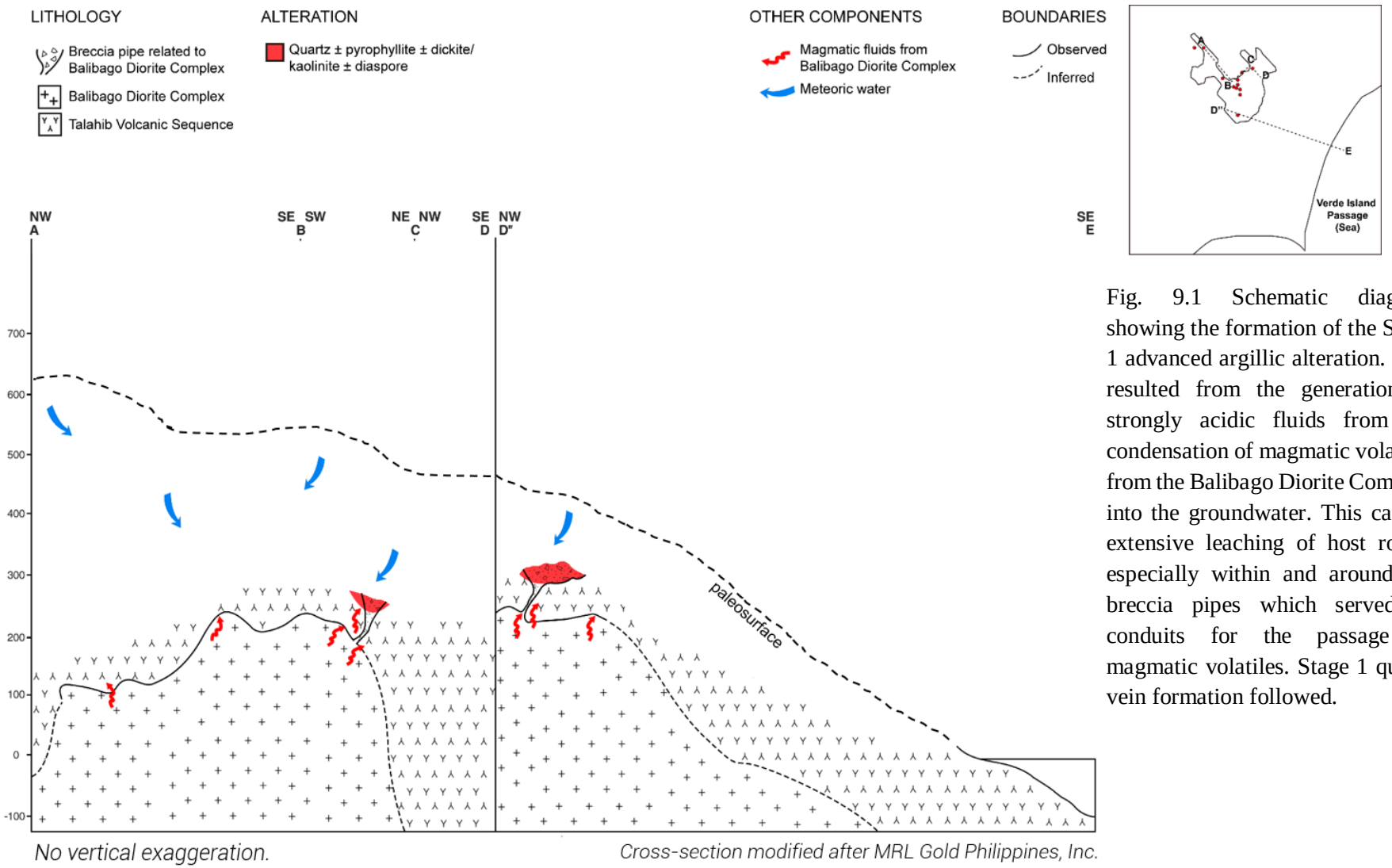

Fig. 9.1 Schematic diagram showing the formation of the Stage 1 advanced argillic alteration. This resulted from the generation of strongly acidic fluids from the condensation of magmatic volatiles from the Balibago Diorite Complex into the groundwater. This caused extensive leaching of host rocks, especially within and around the breccia pipes which served as conduits for the passage of magmatic volatiles. Stage 1 quartz vein formation followed.

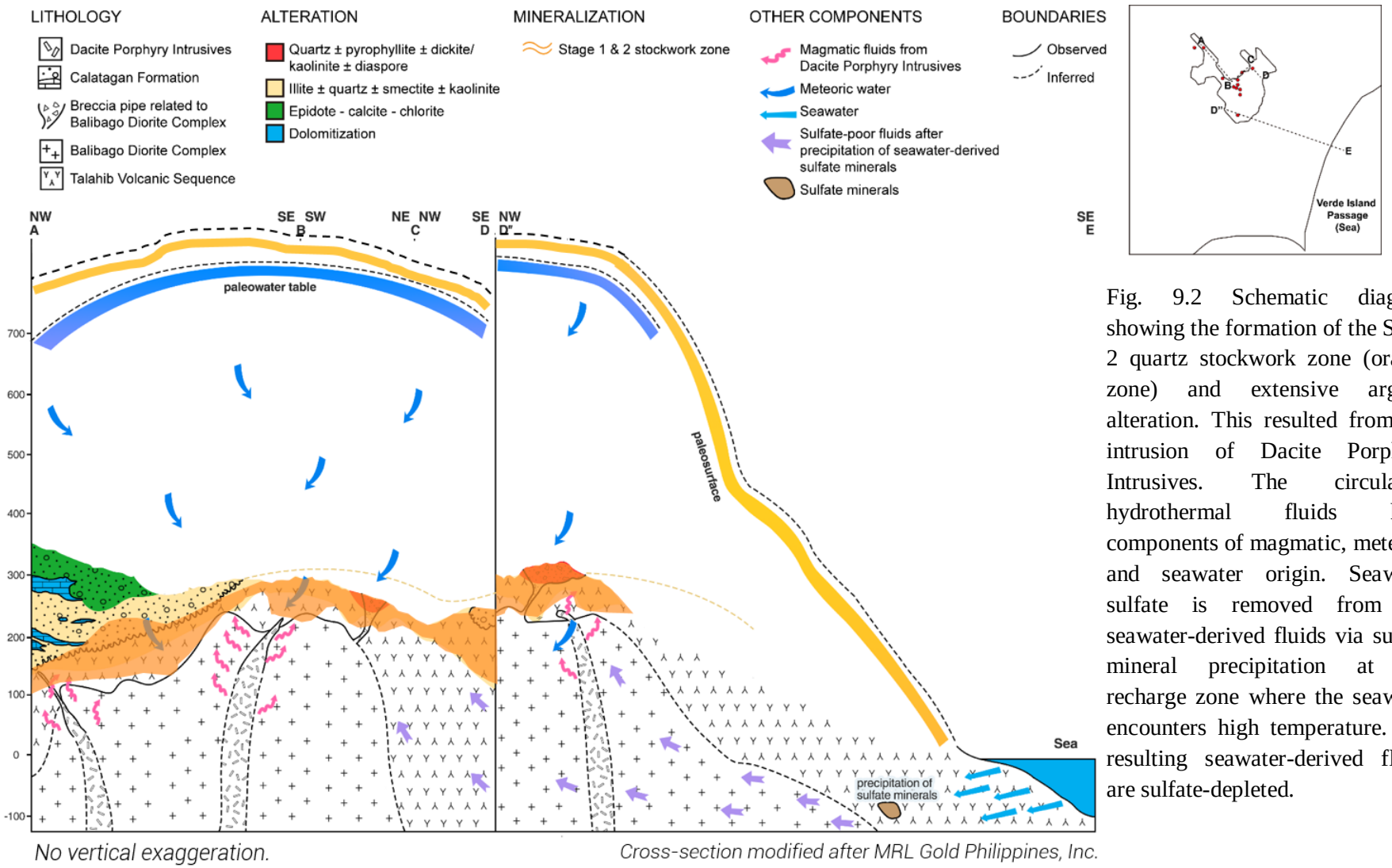

Fig. 9.2 Schematic diagram showing the formation of the Stage 2 quartz stockwork zone (orange zone) and extensive argillic alteration. This resulted from the intrusion of Dacite Porphyry Intrusives. The circulating hydrothermal fluids have components of magmatic, meteoric and seawater origin. Seawater sulfate is removed from the seawater-derived fluids via sulfate mineral precipitation at the recharge zone where the seawater encounters high temperature. The resulting seawater-derived fluids are sulfate-depleted.

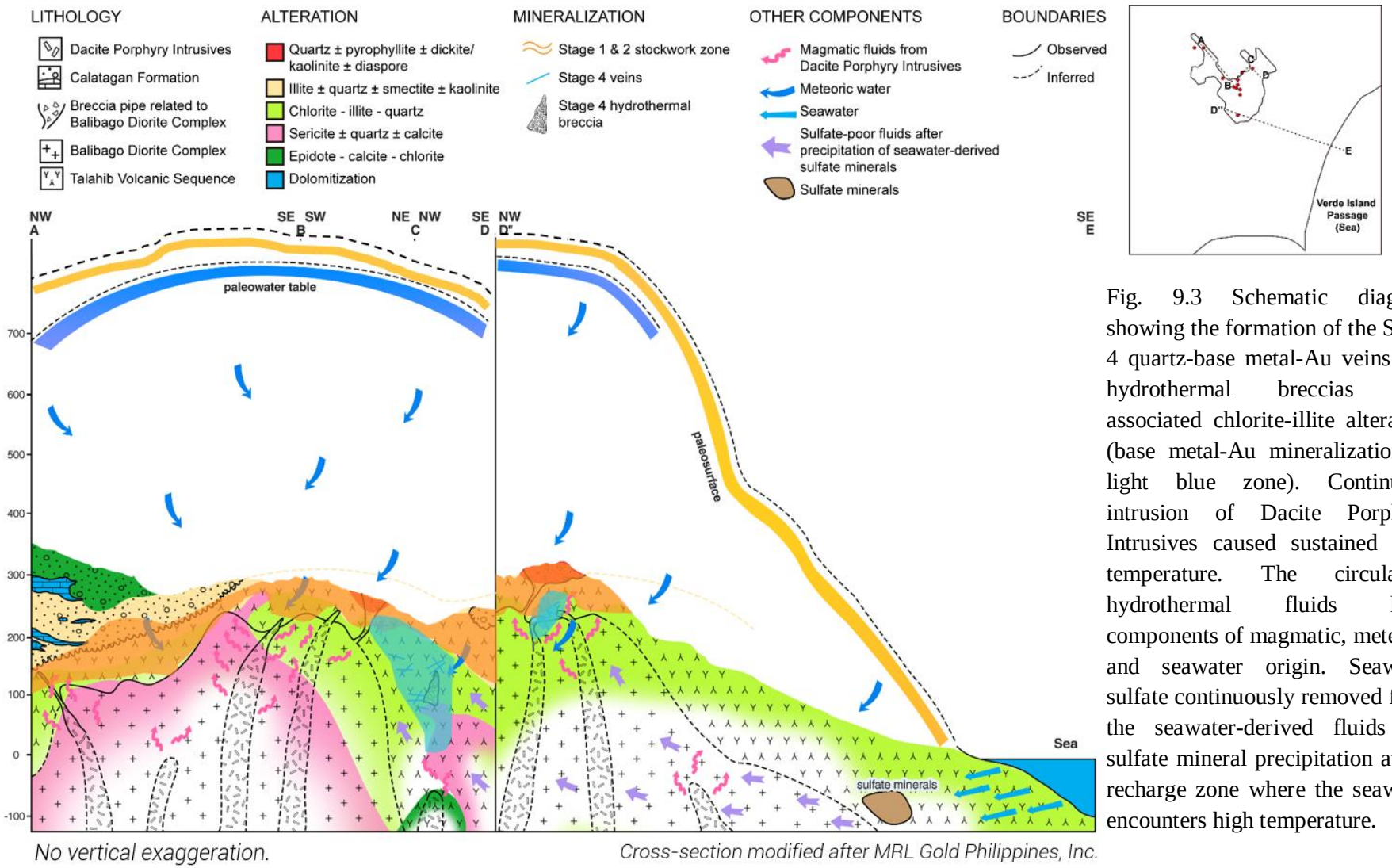

Fig. 9.3 Schematic diagram showing the formation of the Stage 4 quartz-base metal-Au veins and hydrothermal breccias and associated chlorite-illite alteration (base metal-Au mineralization in light blue zone). Continuous intrusion of Dacite Porphyry Intrusives caused sustained high temperature. The circulating hydrothermal fluids have components of magmatic, meteoric and seawater origin. Seawater sulfate continuously removed from the seawater-derived fluids via sulfate mineral precipitation at the recharge zone where the seawater encounters high temperature.

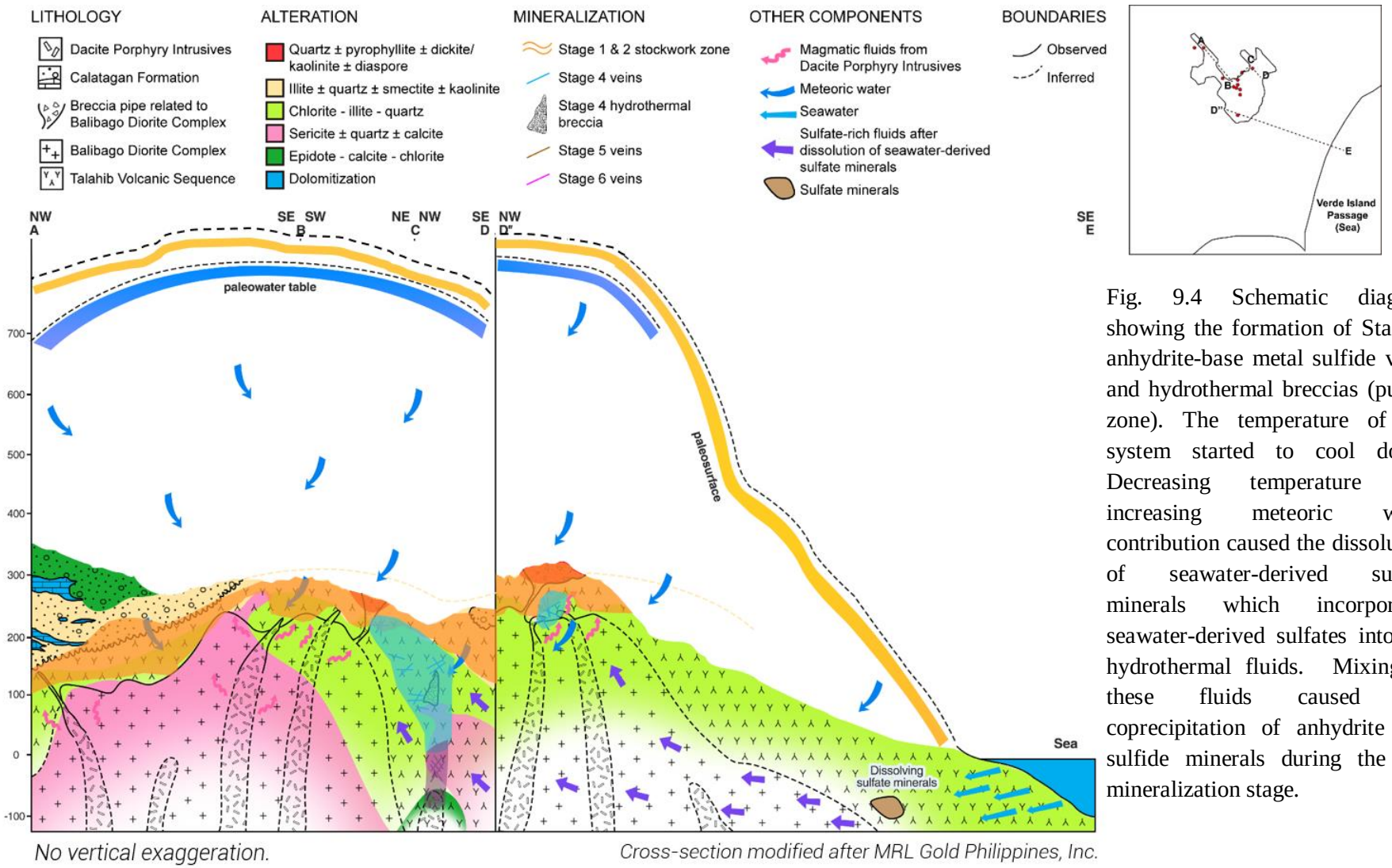

Fig. 9.4 Schematic diagram showing the formation of Stage 6 anhydrite-base metal sulfide veins and hydrothermal breccias (purple zone). The temperature of the system started to cool down. Decreasing temperature and increasing meteoric water contribution caused the dissolution of seawater-derived sulfate minerals which incorporated seawater-derived sulfates into the hydrothermal fluids. Mixing of these fluids caused the coprecipitation of anhydrite and sulfide minerals during the last mineralization stage.

9.2 Implications to Exploration

The Batangas Mineral District is one of the least-studied mining districts in the Philippines. This study on the geologic framework and evolution of the mineralization at Kay Tanda hopes to serve as an impetus for further exploration in the region.

1. Based on the surface mapping and drilling at Kay Tanda, the mineralization is continuous towards the north, northeast, and southwest of the deposit. The main structural trend of the stockwork zone is northeast-southwest and this may continue towards the northeast and southwest of Kay Tanda.
2. Hydrothermally altered rocks are exposed towards the northeast and southwest of the deposit which indicates that mineralization may be intercepted at shallower levels (within a few tens of meters), while mineralization is covered by post-mineralization rocks towards the north and may be encountered at deeper levels (within tens of meters to a few hundred meters).
3. Though the bulk Au mineralization is hosted in the shallow stockwork zone, the bonanza Au-grade veins and hydrothermal breccias associated with the deeper base-metal mineralization is also an attractive target for drilling. Deeper drilling may help delineate and estimate the resource potential of the deeper base metal-Au mineralization.
4. The spatial and temporal relationships between epithermal deposits and porphyry Cu deposits have been documented in several deposits around the world. Exploration for buried porphyry Cu deposits in the region should document carefully the characteristics and origin of the exposed advanced argillic alteration in Kay Tanda and in other prospects in the immediate vicinity.

9.3 Recommendations for Future Work

The epithermal system in Kay Tanda exhibits unique characteristics attributed to the complex evolution of its geologic framework and tectonic setting. Some of the highlighted characteristics of the deposit are (1) an increasing temperature as the system evolved from a Au-Ag epithermal

mineralization to a base-metal with bonanza Au grade epithermal mineralization, (2) a decreasing temperature documented at the last stage of mineralization which influenced the formation of anhydrite-base metal veins, (3) a mixture of meteoric water (dominant), magmatic water and seawater component in the circulating hydrothermal fluids, and (4) boiling as the main mechanism for ore deposition. This PhD study and the MSc thesis by the same author are just two of a few of studies conducted in Kay Tanda. There is still so much to learn about the deposit and below are some suggestions for future work:

(1) There is still a poor understanding of the structural controls on ore mineralization in Kay Tanda. Company data are limited to measurements of structures and veins but their continuity is not reflected in any of the generated maps. A detailed structural study may help constrain the role of structures in the formation of the deposit.

(2) Seawater contribution to the hydrothermal system is suggested from the sulfur, oxygen and hydrogen isotope work conducted in this study, though the amount of seawater in the system is unquantified. Strontium isotope studies can also help trace potential sources of hydrothermal fluids and may provide additional evidence for the incorporation of seawater in the deposit.

(3) The age of the mineralization reported in this study is obtained from K-Ar dating of Stage 2 illite. K-Ar or Ar-Ar dating on Stage 4 adularia may provide additional information on the age of the mineralization of Kay Tanda.

(4) The age of the intrusive units, namely the Balibago Intrusive Complex and the Dacite Porphyry Intrusives, are yet to be determined. Collecting samples from a deeper level may be a challenge but the determination of the age of emplacement of these intrusive units using unaltered rock samples may help improve the genetic model of the deposit.

(5) Surface mapping was not conducted in this study and only a few drill holes were used. An independent surface mapping activity may help improve and update the existing geologic and alteration map of the deposit.

REFERENCES

Ahmad, M. (1979) Fluid inclusion and geochemical studies at the Emperor Gold Mine, Fiji [Ph.D. Thesis]. University of Tasmania, Hobart, Australia, 334p.

Albino, G. V. and Margolis, J. (1991) Different styles of adularia-sericite epithermal deposits – constrasts in geological setting and mineralogy [Abstract]. Geological Society of America Abstracts with Program, 23, A230.

Allen, C. R. (1962) Circum-Pacific faulting in the Philippines-Taiwan Region. Journal of Geophysical Research, 67, 4795-4812.

André-Mayer, A., Leroy, J. L., Bailly, L. et al. (2002) Boiling and vertical mineralization zoning: A case study from the Apacheta low-sulfidation epithermal gold-silver deposit, southern Peru. Mineralium Deposita, 37, 452-464.

Aoki, M., Comsti, E. C., Lazo, F. B. and Matsuhisa, Y. (1993) Advanced argillic alteration and geochemistry of alunite in an evolving hydrothermal system at Baguio, northern Luzon, Philippines. Resource Geology, 43, 155-164.

Aquino, D. J. P. (2004) Surface structure analysis for the Bulalo geothermal field: Possible implications to local and regional tectonics [M.Sc. Thesis]. National Institute of Geological Sciences, University of the Philippines Diliman, Quezon City, Philippines, 116p.

Arpa, M. C. B., Patino, L. C. and Vogel, T. A. (2008) The basaltic to trachydacitic upper Diliman Tuff in Manila: Petrogenesis and comparison with deposits from Taal and Laguna Calderas. Journal of Volcanology and Geothermal Research, 177, 1020–1034.

Arribas, A., Jr. (1995) Characteristics of high-sulfidation epithermal deposits, and their relation to magmatic fluid. In Magmas, Fluids and Ore Deposits: Mineralogical Association of Canada Short Course, 23, 419-454.

Arribas, A., Jr., Hedenquist, J. W., Itaya, T., Okada, T., Concepcion, R. A. and Garcia, J. S., Jr. (1995) Contemporaneous formation of adjacent porphyry and epithermal Cu-Au deposits over 300 ka in northern Luzon, Philippines. Geology, 23, 337-340.

Ashley, R. P. (1982) Occurrence model for enargite-gold deposit. US Geological Survey Open-File Report 82-795, 144-147.

Ault, W. V. and Jensen, M. L. (1963) Summary of sulfur isotope standards [Proceedings]. In Jensen, M. L. (ed.) Biogeochemistry of Sulfur Isotopes. National Science Foundation. Yale University.

Aurelio, M. A. (2000) Tectonics of the Philippines revisited. Journal of the Geologic Society of the Philippines, 55, 119-183.

Aurelio, M. A., Peña, R. E. and Taguibao, K. J. L. (2013) Sculpting the Philippine archipelago since the Cretaceous through rifting, oceanic spreading, subduction, obduction, collision and strike-slip faulting: Contribution to IGMA5000. Journal of Asian Earth Sciences, 72, 102-107.

Avila, E. T., Jr. (1980) Report on the geology and mineral resources of southern Batangas covering Lobo, Batangas City, Malabrigo and San Juan Quadrangles. Philippine Bureau of Mines and Geosciences Technical Information Series No. 14-80. Mines and Geosciences Bureau, Quezon City, 28p.

Barnes, H. L. (1979) Solubilities of ore minerals. In Barnes, H. L. (ed.) Geochemistry of Hydrothermal Ore Deposits. 2nd edn. John Wiley & Sons, Inc., New York, 404-460.

Barrier, E., Huchon, P. and Aurelio, M. (1991) Philippine Fault: A key for Philippine kinematics. Geology, 19, 32-35.

Barton, P. B., Jr. and Bethke P. M. (1987) Chalcopyrite disease in sphalerite: Pathology and epidemiology. American Mineralogist, 72, 451–467.

Barton, P. B., Jr. and Skinner, B. J. (1979) Sulfide mineral stabilities. In Barnes, H. L. (ed.) Geochemistry of Hydrothermal Ore Deposits. 2nd edn. John Wiley & Sons, Inc., New York, 278-403.

Barton, P. B., Jr., Bethke P. M. and Roedder, E. (1977) Environment of ore deposition in the Creede Mining District, San Juan Mountains, Colorado: Part III: Progress toward interpretation of the chemistry of the ore-forming fluid for the OH vein. Economic Geology, 72, 1-24.

Benning, L. G. and Seward, T. M. (1996) Hydrosulphide complexing of Au(I) in hydrothermal solutions from 150°-400°C and 500-1500 bar. Geochimica et Cosmochimica Acta, 60, 1849-1871.

Berger, B. R. and Henley, R. W. (1989) Advances in the understanding of epithermal gold-silver deposits, with special reference to the western United States. Economic Geology Monograph 6, 405-423.

Bischoff, J. L. and Dickson, F. W. (1975) Seawater-basalt interaction at 200°C and 500 bar: Implications for origin of seafloor heavy-metal deposits and regulation of sea-water chemistry. Earth Planetary Science Letters, 25, 385-397.

Blamey, N. J. F. (2012) Composition and evolution of crustal, geothermal and hydrothermal fluids interpreted using quantitative fluid inclusion gas analysis. Journal of Geochemical Exploration, 116-117, 17-27.

Blamey, N. J. F. and Norman, D. I. (2002). New interpretations of geothermal volatiles: Ar/He and N_2/Ar ratios — better indicator of magmatic volatiles, and equilibrium gas geothermometry [Proceedings]. Twenty-seventh Workshop of Geothermal Reservoir Engineering, Stanford University, Stanford, California, January 28–30, 2002, 188–197.

Blount, C. W. and Dickson, F. W. (1969) The solubility of anhydrite ($CaSO_4$) in NaCl-H_2O from 100 to 450 °C and 1 to 1000 bars. Geochimica et Cosmochimica Acta, 33, 227-245.

Bodnar, R. J. (1993) Revised equation and table for determining the freezing point depression of H_2O-NaCl solutions. Geochimica et Cosmochimica Acta, 57, 683-684.

Bodnar, R. J., Reynolds, T. J. and Kuehn, C. A. (1985) Fluid inclusion systematics in epithermal systems. In Berger, B. R. and Bethke, P. M. (eds.) Reviews in Economic Geology Volume 2: Geology and Geochemistry of Epithermal Systems. Society of Economic Geologists, Michigan, 73-97.

Bonham, H. F., Jr. (1986) Models for volcanic-hosted epithermal precious metal deposits: A review [Proceedings]. Volcanism, Hydrothermal Systems and Related Mineralisation, 5th International Volcanological Congress, University of Auckland, Auckland, New Zealand, 13-17.

Bonham, H. F., Jr. (1988) Models for volcanic-hosted precious metal deposit: A review. In Schafer, R. W., Cooper, J. J. and Vikre, P. G. (eds.) Bulk Mineable Precious Metal Deposits of the western United States. Geological Society of Nevada, Reno, 259-271.

Brown, P. E. (1998) Fluid inclusion modeling for hydrothermal systems. In Richards, J. P. and Larson, P. B. (eds.) Reviews in Economic Geology Volume 10: Techniques in Hydrothermal Ore Deposits Geology. Society of Economic Geologists, Michigan, 151-171.

Browne, P. R. L. (1978) Hydrothermal alteration in active geothermal fields. Annual Reviews Earth Planetary Science, 6, 229-250.

Browne, P. R. L. and Ellis, A. J. (1970) The Ohaki-Broadlands hydrothermal area, New Zealand: Mineralogy and related geochemistry. American Journal of Science, 269, 97-131.

Buchanan, L. J. (1981) Precious metal deposits associated with volcanic environments in the southwest. Arizona Geological Society Digest, 14, 237-262.

Bureau of Mines and Geo-Sciences (1985a) Geological Map of Batangas Quadrangle (Sheet 3261 III). Map, 1st edn. Scale 1:50,000, Bureau of Mines and Geo-Sciences, Ministry of Natural Resources, Quezon City.

Bureau of Mines and Geo-Sciences (1985b) Geological Map of Lobo Quadrangle (Sheet 3260 IV). Map, 1st edn. Scale 1:50,000, Bureau of Mines and Geo-Sciences, Ministry of Natural Resources, Quezon City.

Bureau of Mines and Geo-Sciences (1985c) Geological Map of Malabrigo Quadrangle (Sheet 3260 I). Map, 1st edn. Scale 1:50,000, Bureau of Mines and Geo-Sciences, Ministry of Natural Resources, Quezon City.

Bureau of Mines and Geo-Sciences (1985d) Geological Map of San Juan Quadrangle (Sheet 3261 II). Map, 1st edn. Scale 1:50,000, Bureau of Mines and Geo-Sciences, Ministry of Natural Resources, Quezon City.

Campbell, A. R. and Larson, P. B. (1998) Introduction to stable isotope applications in hydrothermal systems. In Richards, J. P. and Larson, P. B. (eds.) Reviews in Economic Geology Volume 10: Techniques in Hydrothermal Ore Deposits Geology. Society of Economic Geologists, Colorado, 173-194.

Canet, C., Franco, S. I., Prol-Ledesma, R. M., González-Partida, E. and Villanueva-Estrada, R. E. (2011) A model of boiling for fluid inclusion studies: Application to the Bolaños Ag-Au-Pb-Zn epithermal deposit, Western Mexico. Journal of Geochemical Exploration, 110, 118-125.

Carman, G. G. (2003) Geology, mineralization and hydrothermal evolution of the Ladolam gold deposit, Lihir Island, Papua New Guinea. Society of Economic Geologists Special Publication 10, 247-284.

Cardwell, R. K., Isacks, B. L. and Karig, D. E. (1980) The spatial distribution of earthquakes, focal mechanism solutions and subducted lithosphere in the Philippine and Northern Indonesian regions. In Hayes, D. E. (ed.) The Tectonic and Geologic Evolution of Southeast Asian Seas and Islands. American Geophysical Union Monograph, 23, 1-35.

Casadevall, T. and Ohmoto, H. (1977) Sunnyside Mine, Eureka Mining District, San Juan County, Colorado: Geochemistry of gold and base metal ore deposition in a volcanic environment. Economic Geology, 72, 1285-1320.

Castillo, P. R. and Newhall, C. G. (2004) Geochemical constraints on possible subduction components in lavas of Mayon and Taal Volcanoes, Southern Luzon, Philippines. Journal of Petrology, 45, 1089–1108.

Castillo, P. R., Rigby, S. J. and Solidum, R. U. (2007) Origin of high field strength element enrichment in volcanic arcs: Geochemical evidence from the Sulu Arc, southern Philippines. Lithos, 97, 271-288.

Chen, W. W., Zhang, J. M., Ardell., A. J. and Dunn, B. (1988) Solid-state phase equilibria in the ZnS-CdS system. Materials Research Bulletin, Los Angeles, 10p.

Chutas, N. I., Kress, V. C., Ghiorso, M. S. and Sack, R. O. (2008) A solution model for high-temperature PbS-$AgSbS_2$-$AgBiS_2$ galena. American Mineralogist, 93, 1630–1640.

Concepcion, R. A. B., Dimalanta, C. B., Yumul, G. P., Jr., Faustino-Eslava, D. V., Queaño, K. L., Tamayo, R. A., Jr. and Imai, A. (2012) Petrography, geochemistry and tectonics of a rifted fragment of Mainland Asia: Evidence from the Lasala Formation, Mindoro Island, Philippines. International Journal Earth Science (Geologische Rundschau), 101, 273–290.

Cook N. J., Ciobanu C. L., Pring, A. et al. (2009) Trace and minor elements in sphalerite: A LA-ICPMS study. Geochimica et Cosmochimica Acta, 73, 4761–4791.

Cooke, D. R. and Bloom, M. S. (1990) Epithermal and subjacent porphyry mineralization, Acupan, Baguio District, Philippines: A fluid inclusion and paragenetic study. Journal of Geochemical Exploration, 35, 297-340.

Cooke, D. R. and Deyell, C. L. (2003) Descriptive names for epithermal deposits: Their genetic implications for genetic classifications and inferring ore fluid chemistry. In Eliopoulos, D. et al. (eds.) Mineral Exploration and Sustainable Development. Millpress, Rotterdam, 1, 457-460.

Cooke, D. R. and Simmons, S. F. (2000) Characteristics and genesis of epithermal gold deposits. In Hagemann, S. G. and Brown, P. E. (eds.) Reviews in Economic Geology Volume 13: Gold in 2000. Society of Economic Geologists Inc., Colorado, 221-244.

Cooke D. R., Deyell, C. L., Waters, P. J., Gonzales, R. I. and Zaw, K. (2011a) Evidence for magmatic-hydrothermal fluids and ore-forming processes in epithermal and porphyry deposits of the Baguio District, Philippines. Economic Geology, 106, 1399-1424.

Cooke, D. R., Hollings, P. and Chang, Z. (2011b) Philippine porphyry and epithermal deposits: An Introduction. Economic Geology, 106, 1253-1256.

Cooke D. R., McPhail, D. C. and Bloom, M. S. (1996) Epithermal gold mineralization, Acupan, Baguio District, Philippines: Geology, mineralization, alteration, and the thermochemical environment of ore deposition. Economic Geology, 91, 243-272.

Corby, G. W., Kleinpell, R. M., Popence, W. P. et al. (1951) Geology and oil possibilities in the Philippines. Technical Bulletin 21, Bureau of Mines, Quezon City, 365p.

Cox, D. M. (2010) NI 43-101 Report: Mineral resource estimate upgrade on the Kay Tanda Project, Luzon, Philippines. Unpublished Report, 128p.

Craig, H. (1961) Isotopic variations in meteoric waters. Science, 133, 1702-1703.

Craig, J. R. (1973) The Cu–Zn–S system. Mineralium Deposita, 8, 81–91.

Craig, J. R. and Scott, S. D. (1974) Sulfide phase equilibria. In Ribbe, P. H. (ed.) Sulfide Mineralogy. Mineralogical Society of America. Virginia, CS-1-110.

Czamanske, G. K. (1974) The FeS content of sphalerite along the chalcopyrite-pyrite-bornite sulfur fugacity buffer. Economic Geology, 69, 1328-1334.

De Boer, J., Odom, L. A., Ragland, P. C., Snider, F. G. and Tilford, N. R. (1980) The Bataan orogene: Eastward subduction, tectonic rotations, and volcanism in the western Pacific (Philippines). Tectonophysics, 67, 251-282.

Defant, M. J., De Boer, J. Z. and Oles, D. (1988) The western Central Luzon volcanic arc, the Philippines: Two arcs divided by rifting? Tectonophysics, 145, 305-317.

Defant, M. J., Maury, R. C., Ripley, E. M., Feigenson, M. D. and Jacques, D. (1991) An example of island-arc petrogenesis: Geochemistry and petrology of the southern Luzon Arc, Philippines. Journal of Petrology, 32, 455-500.

Delmelle, P., Kusakabe, M., Bernard, A., Fischer, T., de Brouwer, S. and del Mundo, E. (1998) Geochemical and isotopic evidence for seawater contamination of the hydrothermal system of Taal Volcano, Luzon, the Philippines. Bulletin of Volcanology, 59, 562-576.

Deyell, C. L. and Cooke, D. R. (2003) Mineralogical and isotopic evidence for the genesis of the Kelly gold-silver deposit, Baguio district, Philippines: Diverse mineral assemblages in a hybrid epithermal system. In Eliopoulos, D. et al. Mineral Exploration and Sustainable Development–Proceedings of the Seventh Biennial SGA Meeting: Millpress, Rotterdam, 1, 469–472.

Dimalanta, C. B., Ramos, E. G. L., Yumul, G. P., Jr. and Bellon, H. (2009) New features from the Romblon Island Group: Key to understanding the arc–continent collision in Central Philippines. Tectonophysics, 479, 120-129.

Dong, G. and Morrison, G. W. (1995) Adularia in epithermal veins, Queensland: Morphology, structural state and origin. Mineralium Deposita, 30, 11-19.

Drummond S. E. (1981) Boiling and mixing of hydrothermal fluids: Chemical effects on mineral precipitation [Ph.D. Thesis]. Pennsylvania State University, USA.

Einaudi, M. T., Hedenquist, J. W. and Inan, E. E. (2003) Sulfidation state of fluids in active and extinct hydrothermal systems: Transitions from porphyry to epithermal environments. Society of Economic Geologists Special Publication, 10, 285-313.

Executive Order No. 79 (2016). Malacañan Palace, Manila, Republic of the Philippines.

Farrell, C. W. (1979) Strontium Isotopes of Kuroko Deposits [Ph. D. Thesis]. Harvard University, USA.

Farrell. C. W., Holland, H. D. and Petersen, U. (1978) The isotopic composition of strontium in barites and anhydrites from Kuroko Deposits. Mining Geology, 28, 281-291.

Faure, M., Marchadier, Y. and Rangin, C. (1989) Pre-Eocene synmetamorphic structure in the Mindoro-Romblon-Palawan area, west Philippines, and implications for the history of Southeast Asia. Tectonics, 8, 963-979.

Fernandez, H. E., Damasco, F. V. and Sangalang, L. A. (1979) Gold ore shoot development in the Antamok Mines, Philippines. Economic Geology, 74, 606-627.

Field, C. W. and Fifarek, R. H. (1985) Light stable-isotope systematics in the epithermal environment. In Roberston, J. M. (ed.) Reviews in Economic Geology Volume 2: Geology and Geochemistry of Epithermal Systems. Society of Economic Geologists, Michigan, 99-128.

Fisher, J. R. and Barnes, H. L. (1972) The ion-product constant of water to 350°. Journal of Physical Chemistry, 76, 90-99.

Fitch, T. J. (1972) Plate convergence, transcurrent faults, and internal deformation adjacent to Southeast Asia and the Western Pacific. Journal of Geophysical Research, 77, 4432-4460.

Förster, H., Oles, D., Knittel, U., Defant, M. J. and Torres, R. C. (1990) The Macolod Corridor: A rift crossing the Philippine island arc. Tectonophysics, 183, 265-271.

Fournier, R. O. (1981) Application of water geochemistry to geothermal exploration and reservoir engineering. In Ryback L. and Muffler, L. J. P. (eds.) Geothermal Systems: Principles and Case Histories, New York, 109-143.

Fournier, R. O. and Truesdell, A. H. (1973) An empirical Na-K-Ca geothermometer for natural waters. Geochimica et Cosmochimica Acta, 371, 1255-1275.

Friedman, I. and O'Neil, J. R. (1977) Compilation of stable isotope fractionation factors of geochemical interest. In Fleischer, M. (ed.) Data of Geochemistry, 6th Edition: U.S. Geological Survey, Professional Paper 440-KK, KK1-KK12.

Garwin, S., Hall, R. and Watanabe, Y. (2005) Tectonic setting, geology and gold and copper mineralization in Cenozoic magmatic arcs of Southeast Asia and the West Pacific. Economic Geology, 100, 891-930.

Gemmell, J. B., Sharpe, R., Jonasson, I. R. and Herzig, P. M. (2004) Sulfur isotope evidence for magmatic contributions to submarine and subaerial gold mineralization: Conical Seamount and the Ladolam Gold Deposit, Papua New Guinea. Society of Economic Geologists, 99, 1711-1725.

George, L., Cook, N. J., Ciobanu, C. L. and Wade, B. P. (2015) Trace and minor elements in galena: A reconnaissance LA-ICP-MS study. American Mineralogist, 100, 548-569.

Gervasio, F. C. (1966) The age and nature of orogenesis of the Philippines. The Philippine Geologist, 20, 121-140.

Giggenbach, W.F. (1986) The use of gas chemistry in delineating the origin of flui discharges over the Taupo Volcanic Zone: A review [Proceedings]. International Volcanology Congress, New Zealand, 5, 47-50.

Giggenbach, W. F. (1992a) Isotopic shifts in waters from geothermal and volcanic systems along convergent plate boundaries and their origin. Earth and Planetary Science Letters, 113, 495-510.

Giggenbach, W. F. (1992b) The composition of gases in geothermal and volcanic systems as a function of tectonic setting [Proceedings]. 7th International Symposium on Water-Rock Interaction, Park City, U.S.A., 873-878.

Giggenbach, W. F. (1996) Chemical composition of volcanic gases. In Scarpa, R. and Tilling, R. I (eds.) Monitoring and Mitigation of Volcano Hazards. Springer Verlag, Berlin-Heidelberg, 221–256.

Giggenbach, W. F. and Poreda, R. J. (1993) Helium isotopic and chemical composition of gases from volcanic-hydrothermal systems in the Philippines. Geothermics, 22, 369-380.

Giles, D. I. and Nelson, C. E. (1982) Principal features of epithermal lode gold deposits of the circum-Pacific rim [Transactions]. 3rd Circum-Pacific Energy and Minerals Resources Conference. American Association of Petroleum Geologists, Honolulu, Hawaii, 273-278.

Glater, J. and Schwartz, J. (1976) High-temperature solubility of calcium sulfate hemihydrate and anhydrite in natural seawater concentrates. Journal of Chemical Engineering Data, 21, 47-52.

Haas, J. L., Jr. (1971) The effect of salinity on the maximum thermal gradient of a hydrothermal system at hydrostatic pressure. Economic Geology, 66, 940-946.

Hall, R. (2002) Cenozoic geological and plate tectonic evolution of SE Asia and the SW Pacific: Computer-based reconstructions, model and animations. Journal of Asian Earth Sciences, 20, 353-431.

Hajash, A., Jr. (1975) Hydrothermal processes along mid-oceanic ridges: An experimental investigation [Ph.D. Thesis]. Texas A&M University, USA.

Hamburger, M. W., Cardwell, R. K. and Isacks, B. L. (1983) Seismotectonics of the northern Philippine Island Arc. In Hayes, D. E. (ed.) The Tectonic and Geologic Evolution of Southeast Asian Seas and Islands: Part 2. American Geophysical Union Monograph, 27, 1-22.

Hamilton, W. (1979) Tectonics of the Indonesian Region. U.S. Geological Survey Professional Paper, 1078.

Hardie, L. A. (1967) Gypsum-anhydrite equilibrium at one atmosphere pressure. American Mineralogist, 52, 171-200.

Hattori, K. (1975) Geochemistry of ore deposition at the Yatani-lead-zinc and gold-silver deposit, Japan. Economic Geology. 70, 677-693.

Hayba, D. O., Bethke, P. M., Heald, P. and Foley, N. K. (1985) Geologic, mineralogic and geochemical characteristics of volcanic-hosted epithermal precious metal deposits. In Berger, B. R. and Bethke, P. M. (eds.) Reviews in Economic Geology Volume 2: Geology and Geochemistry of Epithermal Systems. Society of Economic Geologists, Michigan, 129-167.

Hayes, D. E. and Lewis, S. D. (1984) A geophysical study of the Manila Trench, Luzon, Philippines, Part 1: Crustal signature gravity and regional tectonic evolution. Journal of Geophysical Research, 89, 9171-9195.

Hayes, D. E. and Lewis, S. D. (1985) Structure and tectonics of the Manila Trench System, Western Luzon, Philippines. Energy, 10, 263-279.

Heald, P., Hayba, D. O. and Foley, N. K. (1987) Comparative anatomy of volcanic-hosted epithermal deposits: Acid-sulfate and adularia-sericite types. Economic Geology, 82, 1-26.

Hedenquist, J. W. (1987) Mineralization associated with volcanic-related hydrothermal systems in the Circum-Pacific basin [Transactions]. Fourth Circum Pacific Conference on Energy and Mineral Resources Conference, American Association of Petroleum Geologists, Singapore, 513-524.

Hedenquist, J. W. (1990) The thermal and geochemical structure of the Broadlands-Ohaaki geothermal system, New Zealand. Geothermics, 19, 151-185.

Hedenquist, J. W. and Garcia, J. S., Jr. (1990) Sulfur isotope systematics in the Lepanto mining district, northern Luzon, Philippines [Abstract]. Mining Geology, 40, 67.

Hedenquist, J. W. and Henley, R. W. (1985) Hydrothermal eruptions in the Waiotapu geothermal system, New Zealand: Their origin, associated breccias, and relation to precious metal mineralization. Economic Geology, 80, 1640-1668.

Hedenquist, J. W. and Lowenstern, J. B. (1994) The role of magmas in the formation of hydrothermal ore deposits. Nature, 370, 519-527.

Hedenquist, J. W., Arribas, A., Jr. and Aoki, M. (2017) Zonation of sulfate and sulfide minerals and isotopic composition in the Far Southeast Porphyry and Lepanto Epithermal Cu–Au Deposits, Philippines. Resource Geology, 67, 174-196.

Hedenquist, J. W., Arribas, A., Jr. and Gonzales-Urien, E. (2000) Exploration for epithermal gold deposits. In Hagemann, S. G. and Brown, P. E. (eds.) Reviews in Economic Geology Volume 13: Gold in 2000. Society of Economic Geologists Inc., Colorado, 245-277.

Hedenquist, J. W., Arribas, A., Jr. and Reynolds, T. J. (1998) Evolution of an intrusion-centered hydrothermal system: Far Southeast-Lepanto Porphyry and Epithermal Cu-Au Deposits, Philippines. Economic Geology, 93, 373-404.

Hedenquist, J. W., Reyes, A. G., Simmons, S. F. and Taguchi, S. (1992) The thermal and geochemical structure of geothermal and epithermal systems: A framework for interpreting fluid inclusion data. European Journal of Mineralogy, 4, 989-1015.

Helgeson, H. C. (1969) Thermodynamics of hydrothermal systems at elevated temperatures and pressures. American Journal of Geosciences, 267, 729-804.

Helgeson, H. C., Delany, J. M., Nesbitt, H. W. and Bird, D. K. (1978) Summary and critique of the thermodynamic properties of rock forming minerals. American Journal of Science, 2784, 1-229.

Henley, R. W. (1985) The geothermal framework of epithermal deposits. In Berger, B. R. and Bethke, P. M. (eds.) Reviews in Economic Geology Volume 2: Geology and Geochemistry of Epithermal Systems. Society of Economic Geologists, Michigan, 1-24.

Henley, R. W., Truesdell, A. H., Barton, P. B., Jr. and Whitney, J. A. (1984a) Introduction to chemical calculations. In Roberston, J. M. (ed.) Reviews in Economic Geology Volume 1: Fluid-Mineral Equilibria in Hydrothermal Systems. Society of Economic Geologists, Michigan, 1-8.

Henley, R. W., Truesdell, A. H., Barton, P. B., Jr. and Whitney, J. A. (1984b) Chemical geothermometers for geothermal exploration. In Roberston, J. M. (ed.) Reviews in Economic Geology Volume 1: Fluid-Mineral Equilibria in Hydrothermal Systems. Society of Economic Geologists, Michigan, 31-44.

Henley, R. W., Truesdell, A. H., Barton, P. B., Jr. and Whitney, J. A. (1984c) Hydrolysis reactions in hydrothermal fluids. In Roberston, J. M. (ed.) Reviews in Economic Geology Volume 1: Fluid-Mineral Equilibria in Hydrothermal Systems. Society of Economic Geologists, Michigan, 65-82.

Henley, R. W., Truesdell, A. H., Barton, P. B., Jr. and Whitney, J. A. (1984d) Redox reactions in hydrothermal fluids. In Roberston, J. M. (ed.) Reviews in Economic Geology Volume 1: Fluid-Mineral Equilibria in Hydrothermal Systems. Society of Economic Geologists, Michigan, 99-114.

Hirowatari, F. and Taguchi, S. (1978) Quantitative analytical method of native gold using EPMA. In Matsukuma, T. and Urashima, Y. (eds.) Gold and Silver Ores of Japan. 2nd edn. Japan Mining Association, Tokyo, 101-115.

Hollings, P., Baker, M. J., Orovan, E. and Rinne, M. (2018) A special issue devoted to porphyry and epithermal deposits of the Southwest Pacific: An Introduction. Economic Geology, 113, 1-6.

Holloway, N. H. (1982) North Palawan block, Philippines: Its relation to Asian mainland and role in evolution of the South China Sea. American Association of Petroleum Geologists Bulletin, 16, 1355–1383.

Imai, A. (2000) Mineral paragenesis, fluid inclusions and sulfur isotope systematics of the Lepanto Far Southeast Porphyry Cu-Au Deposit, Mankayan, Philippines. Resource Geology, 50, 151-168.

Imai, A. (2001) Generation and evolution of ore fluids for the porphyry Cu-Au mineralization of the Santo Tomas II (Philex) Deposit, Philippines. Resource Geology, 51, 71-96.

Imai, A. (2002) Metallogenesis of porphyry Cu deposits of the Western Luzon Arc, Philippines: K-Ar ages, SO_3 contents of microphenocrystic apatite and significance of intrusive rocks. Resource Geology, 52, 147-161.

Imai, A. (2005) Evolution of hydrothermal system at the Dizon porphyry Cu-Au deposit, Zambales, Philippines. Resource Geology, 55, 73-90.

Imai, A., Listanco, E. L. and Fujii, T. (1996) Highly oxidized and sulfur-rich dacitic magma of Mount Pinatubo: Implication for metallogenesis of porphyry copper mineralization in the Western Luzon Arc. In Newhall, C. G. and Punongbayan, R. S. (eds.) Fire and Mud: Eruptions and Lahars of Mount Pinatubo, Philippines. Philippine Institute of Volcanology and Seismology, Quezon City, 865-84.

Jensen, E. P. and Barton, M. D. (2000) Gold deposits related to alkaline magmatism. In Hagemann, S. G. and Brown, P. E. (eds.) Reviews in Economic Geology Volume 13: Gold in 2000. Society of Economic Geologists Inc., Colorado, 279–314.

Kamilli, R. J. and Ohmoto, H. (1977) Paragenesis, zoning, fluid inclusion and isotopic studies of the Finlandia Vein, Colqui District, Central Peru. Economic Geology, 72, 950-982.

Knittel, U. and Oles, D. (1995) Basaltic volcanism associated with extensional tectonics in the Taiwan-Luzon island arc: Evidence for non-depleted sources and subduction zone enrichment. In Smellie, J. L. (ed.) Volcanism Associated with Extension at Consuming Plate Margins. Geological Society Special Publication, 81, 77–93.

Kojima, S. and Sugaki, A. (1985) Phase relations in the Cu-Fe-Zn-S system between 500 °C and 300 °C under hydrothermal conditions. Economic Geology, 80, 158-171.

Kramer, V., Hirth, H., Hofherr, M. and Trah, H. P. (1987) Phase studies in the systems Ag_2Te–Ga_2Te_3, ZnSe–In_2Se_3 and ZnS–Ga_2S_3. Thermochimica Acta, 112, 89–94.

Lab-oyan, F. T. and Climie, J. A. (2010) The Kay Tanda Low- to Intermediate Sulfidation Epithermal Gold-Silver Deposit, Batangas Province, Philippines [Conference Abstract]. Hunt for Ore Deposits. Baguio, Philippines.

Large, R. R., Danyushevsky, L., Hollit, C. et al. (2009) Gold and trace element zonation in pyrite using a laser imaging technique: Implications for the timing of gold in orogenic and Carlin-style sediment-hosted deposits. Economic Geology, 104, 635-668.

Lewis, S. D. and Hayes, D. E. (1983) The tectonics of northward propagating subduction along Eastern Luzon, Philippine Islands. In Hayes, D. E. (ed.) Tectonic and Geologic Evolution of Southeast Asian Seas and Islands: Part 2, American Geophysical Union. Monograph 27, 57-78.

Lin, Y. and Tiegeng, L. (1999) Sphalerite chemistry, Niujiaotang Cd-rich Zinc Deposit, Guizhou, Southwest China. Chinese Journal of Geochemistry, 18, 62-68.

Lindgren, W. (1933) Mineral deposits. McGraw-Hill, New York, 930p.

Loudon, A. G. (1976) Marcopper porphyry copper deposit, Philippines. Economic Geology, 71, 721-732.

Manalo, P. C., Imai, A., Subang, L. L., de los Santos, M. C., Yanagi, K., Takahashi, R. and Blamey, N. J. F. (2018) Mineralization of the Northwest Quartz-Pyrite-Gold Veins:

Implications for multiple mineralization events at Lepanto, Mankayan Mineral District, Northern Luzon, Philippines. Economic Geology, 113, 1609-1629.

Manalo, P. C., Dimalanta, C. B., Ramos, N. T., Faustino-Eslava, D. V., Queaño, K. L. and Yumul, G. P., Jr. (2016) Magnetic signatures and Curie surface trend across an arc-continent collision zone: An example from Central Philippines. Surveys in Geophysics, 37, 557-578.

Marchadier, Y. and Rangin, C. (1990) Polyphase tectonics at the southern tip of the Manila trench, Mindoro-Tablas Islands, Philippines. Tectonophysics, 183, 273-287.

Marshall, W. L. and Slusher, R. (1973) Debye-Huckel correlated solubilities of calcium sulfate in water and in aqueous sodium nitrate and lithium nitrate solutions of molality 0 to 6 mol kg^{-1} and at temperatures from 398 to 623 K. Journal of Chemical Thermodynamics, 5, 189-197.

Matsuhisa, Y., Goldsmith, J. R. and Clayton, R. N. (1979) Oxygen isotopic fractionation in the system quartz-albite-anorthite-water. Geochimica et Cosmochimica Acta, 43, 1131-1140.

Milsom, J., Ali, J. R. and Queaño, K. L. (2006) Peculiar geometry of northern Luzon, Philippines: Implications for regional tectonics of new gravity and paleomagnetic data. Tectonics, 25, 1-14.

Mines and Geosciences Bureau (2004) Mineral Resource Information Series No. 6: Gold and Silver. Mines and Geosciences Bureau, Quezon City, 26p.

Mines and Geosciences Bureau (2010) Geology of the Philippines. Mines and Geosciences Bureau, Quezon City, 532p.

Mines and Geosciences Bureau (2018) Mineral Production Sharing Agreement (MPSA) as of December 31, 2018 [Online]. Available at: http://mgb.gov.ph/attachments/article/51/R2_MTSR_DEC_2018.pdf (Accessed: 01 February 2019).

Mitchell, A. H. G. and Balce, G. R. (1990) Geological features of some epithermal gold systems, Philippines. Journal of Geochemical Exploration, 35, 241-296.

Mitchell, A. H. G., Hernandez, F. and dela Cruz, A. P. (1986) Cenozoic evolution of the Philippine archipelago. Journal of Southeast Asian Earth Sciences, 1, 3-22.

Mottl, M. and Holland, H. D. (1978) Chemical exchange during hydrothermal alteration of basalt by seawater-I. Experimental results for major and minor components of seawater. Geochimica Cosmochimica Acta, 42, 1103-1115.

Mottl, M., Corr, R. F. and Holland, H. D. (1974) Chemical exchange between sea water and mid-ocean ridge basalt during hydrothermal alteration [Abstract]. Geological Society of America, GAAPBC, 6, 879-880.

Moncada, D., Mutchler, S., Nieto, A., Reynolds, T. J., Rimstidt, J. D. and Bodnar, R. J. (2012) Mineral textures and fluid inclusion petrography of the epithermal Ag-Au deposits at Guanajuato, Mexico: Application to exploration. Journal of Geochemical Exploration, 114, 20-35.

Moussa N., Rouxel, O., Grassineau, N. V., Ponzevera, E., Nonnotte, P., Fouquet, Y. and Le Gall B. (2017) Sulfur and strontium isotopic study of epithermal mineralization: A case study from the SE Afar Rift, Djibouti. Ore Geology Reviews, 21, 358-368.

Muller, D., Herzig, P. M., Scholten, J. C., and Hunt, S. (2002) Ladolam gold deposit, Lihir Island, Papua New Guinea: Gold mineralization hosted by alkaline rocks: Society of Economic Geologists Special Publication 9, 367-382.

MSN Weather (2019). Records and Averages [Online]. Available at: https://www.msn.com/en-ph/weather/records/lobocalabarzonphilippines/we-city?q=lobo-calabarzon&form=PRWLAS&iso=PH&el=6nEN35iV87Vzq3YcBrJAmw%3d%3d (Accessed: 27 January 2019)

Naden, J., Kilias, S.P. and Darbyshire, D. P. F. (2005) Active geothermal systems with entrained seawater as modern analogs for transitional volcanic-hosted massive sulfide and continental magmato-hydrothermal mineralization: The example of Milos, Island, Greece. Geology, 33, 541-544.

Nichols, G., Hall, R., Milsom, J. et al. (1990) The southern termination of the Philippine Trench. Tectonophysics, 183, 289-303.

Nockolds, S. R., Knox, R. W. O'B. and Chinner, G. A. (1978) Petrology: Cambridge University Press, New York, 435p.

Norman, D. I. and Moore, J. N. (1999) Methane and excess N_2 and Ar in geothermal fluid inclusions [Proceedings]. Twenty-fourthWorkshop on Geothermal Reservoir Engineering, Stanford University, Stanford, California, January 22-24, 1999, 233-240.

Norman, D. I. and Musgrave, J. A. (1994) N_2–Ar–He compositions in fluids inclusions: Indicators of fluid source. Geochimica et Cosmochimica Acta, 58, 1119-1131.

Norman, D. I., Ting, W., Putnam, B. R. and Smith, R. W. (1985) Mineralization of the Hansonburg Mississippi-Valley-type deposit, New Mexico: Insights from composition of gases in fluid inclusions. The Canadian Mineralogist, 23, 353-368.

Ohmoto, H. and Lasaga, A. C. (1982) Kinetics of reactions between aqueous sulfates and sulfides in hydrothermal systems. Geochimica et Cosmochimica Acta, 46, 1727-1745.

Ohmoto, H. and Rye, R. O. (1974) Hydrogen and oxygen isotopic compositions of fluid inclusions in the Kuroko deposits, Japan. Economic Geology, 69, 947-953.

Ohmoto, H. and Rye, R. O. (1979) Isotopes of sulfur and carbon. In Barnes, H. L. (ed.) Geochemistry of Hydrothermal Ore Deposits. 2nd edn. John Wiley & Sons, Inc. New York, 509-567.

O'Neil, J. R. and Silberman, M. L. (1974) Stable isotope relations in epithermal Au-Ag deposits. Economic Geology. 69, 902-909.

O'Neil, J. R. and Taylor, H. P., Jr. (1967) The oxygen isotope and cation exchange chemistry of feldspars. American Mineralogist, 52, 1414-1437.

Ozawa, A., Tagami, T., Listanco, E. L., Arpa, C. B. and Sudo, M. (2004) Initiation and propagation of subduction along the Philippine Trench: Evidence from the temporal and spatial distribution of volcanoes. Journal of Asian Earth Sciences, 23, 105-111.

Paytan, A., Kastner, M., Campbell, D., and Thiemes, M. H. (2004) Seawater sulfur isotope fluctuations in the Cretaceous. Science, 304, 1663-1665.

PhilGIS (2011) Country Basemaps [Online]. Available at: http://philgis.org/general-country-datasets/country-basemaps (Accessed: 14 February 2018).

Philippine Institute for Volcanology and Seismology (2008) PHIVOLCS Volcano Monitoring [Online]. Available at:

https://www.phivolcs.dost.gov.ph/index.php?option=com_content&view=article&id=50&Itemid=86 (Accessed: 13 February 2018).

Philippine Institute for Volcanology and Seismology (2015) Active Faults and Trenches in the Philippines [Online]. Available at: https://www.phivolcs.dost.gov.ph/index.php?option=com_content&view=article&id=78&Itemid=500024 (Accessed: 13 February 2018).

Potter, R. W. (1977) Pressure corrections for fluid-inclusion homogenization temperatures based on the volumetric properties of the system NaCl-H_2O. Journal of Research of the U.S. Geological Survey, 5, 603-607.

Pubellier, M., Garcia, F., Loevenbruck, A. and Chorowicz, J. (2000) Recent deformation at the junction between the North Luzon block and the Central Philippines from ERS-1 Images. Island Arc, 9, 598–610.

Rai, K. (1978) Micromineralogy and geochemistry of sphalerites from Sulitjelma mining district, Norway. Norsk Geologisk Tidsskrift, 1, 17-31.

Rangin, C., Stephan, J. F. and Muller, C. (1985) Middle Oligocene oceanic crust of South China Sea jammed into Mindoro collision zone (Philippines). Geology, 13, 425-428.

Rangin, C., Stephan, J. F., Blanchet, R. et al. (1988) Seabeam survey at the southern end of the Manila trench: Transition between subduction and collision process, offshore Mindoro Island, Philippines. Tectonophysics, 146, 261-278.

Rees, C. E., Jenkins, W. J. and Monster, J. (1978) The sulphur isotopic composition of ocean water sulphate. Geochimica et Cosmochimica Acta, 42, 377-381.

Renock, D. and Becker, U. (2011) A first principles study of coupled substitution in galena. Ore Geology Reviews, 42, 71–83.

Richards, J. P. (1995) Alkalic-type epithermal gold deposits - A review. In Magmas, Fluids and Ore Deposits: Mineralogical Association of Canada Short Course, 23, 367–400.

Ripley, E. M. and Ohmoto, H. (1977) Mineralogic, sulfur isotope, and fluid inclusion studies of the stratabound copper deposits at the Raul Mine, Peru. Economic Geology, 72, 1017-1041.

Robie, R. A., Hemingway, B. S. and Fisher, J. R. (1978) Thermodynamic properties of minerals and related substances at 298.15 K and 1 bar (105 Pascals) and at higher temperatures. U.S. Geological Survey Bulletin, 1452, 456p.

Roedder, E. (1979) Fluid inclusions as samples of ore fluids. In Barnes, H. L. (ed.) Geochemistry of Hydrothermal Ore Deposits. 2nd edn. John Wiley & Sons, Inc. New York, 684-737.

Rohrlach, B. D. and Fredericksen, D. C. (2008) Independent geological report on the epithermal gold-silver resource at Kay Tanda Prospect Area, Southern Luzon, Philippines: A report for Mindoro Resources Limited. Unpublished Report. 377p.

Sajona, F. G., Izawa, E., Motomura, Y., Imai, A., Sakakibara, H. and Watanabe, K. (2002) Victoria carbonate-base metal gold deposit and its significance in the Mankayan Mineral District, Luzon, Philippines. Resource Geology, 52, 312-328.

Sander, M. V. and Einaudi, M. T. (1990) Epithermal deposition of gold during transition from propylitic to potassic alteration at Round Mountain, Nevada. Economic Geology, 85, 285-311.

Sasaki, A., Ulriksen, C. E., Sato, K. and Ishihara, S. (1984) Sulphur isotope recoinnaissance of porphyry copper and manto-tye deposits in Chile and the Philippines. Bulletin of Geological Survey of Japan, 35, 615-622.

Sato, J., Maeda, H., Kinryu, Y. and Ono, S. (1980) Mineral paragenesis and fluid inclusion data of the Ohe polymetallic vein-type deposits, Hokkaido, Japan. Mining Geology, 30, 277-288.

Sawkins, F. J., O'Neil, J. R. and Thompson, J. M. (1979) Fluid inclusion and geochemical studies of vein gold deposits, Baguio District, Philippines. Economic Geology, 74, 1420-1434.

Scott, S. D. and Barnes, H. L. (1971) Sphalerite geothermometry and geobarometry. Economic Geology, 66, 653-669.

Seward, T. M. (1973) Thiocomplexes of gold and the transport of gold in hydrothermal ore solutions. Geochimica et Cosmochimica Acta, 37, 379-399.

Seward, T. M. (1989) The hydrothermal chemistry of gold and its implications for ore formation: Boiling and conductive cooling as examples. Economic Geology Monograph, 6, 398-404.

Seward, T. M. (1991) The hydrothermal geochemistry of gold. In Forster, R. P. (ed.) Gold Metallogeny and Exploration. Blackie and Son Ltd., London, 37-62.

Shenberger D. M. and Barnes, H. L. (1989) Solubility of gold in aqueous sulfide solutions from 150 to 350 °C. Geochimica et Cosmochimica Acta, 53, 269-278.

Sheppard, S. M. F. and Gilg, H. A. (1996) Stable isotope geochemistry of clay minerals. Clay Minerals, 31, 1-24.

Shimizu, T. (2014) Reinterpretation of quartz textures in terms of hydrothermal fluid evolution at the Koryu Au-Ag deposit, Japan. Economic Geology, 109, 2051-2065.

Sillitoe, R. H. (1977) Metallic mineralization affiliated to subaerial volcanism: A review. In Volcanic processes in ore-genesis. Institution of Mining and Metallurgy and Geological Society, London, 99-116.

Sillitoe, R. H. (1989) Gold deposits in western Pacific island arcs: The magmatic connection. Economic Geology Monograph 6, 274-291.

Sillitoe, R. H. (1993a) Giant and bonanza gold deposits in the epithermal environment: Assessment of potential factors. Economic Geology Special Publication 2, 125-156.

Sillitoe, R. H. (1993b) Epithermal models: Genetic types, geometrical controls and shallow features. Geological Association of Canada Special Paper 40, 403-417.

Sillitoe, R. H. (1995) Exploration and discovery of base- and precious metal deposits in the circum-Pacific region during the last 25 years. Resource Geology Special Issue, 19, 119p.

Sillitoe, R. H. (2000) Exploration and discovery of base- and precious metal deposits in the circum-Pacific region - a late 1990s update. Resource Geology Special Issue, 21, 65p.

Sillitoe, R. H. and Gappe, I. M., Jr. (1984) Philippine porphyry copper deposits: Geologic setting and characteristics. CCOP Project Office, UNDP Technical Support for Regional Offshore Prospecting in East Asia (RAS/81/120), Bangkok, 89p.

Sillitoe, R. H. and Hedenquist, J. W. (2003) Linkages between volcanotectonic settings, ore fluid compositions, and epithermal precious metal deposits. In Simmons, S. F. and Graham, I. (eds.) Volcanic, Geothermal, and Ore-forming fluids: Rulers and Witnesses of Processes within the Earth, Society of Economic Geologists Special Publication, 10, 315-343.

Simmons, S. F. (1995) Magmatic contributions to low-sulfidation epithermal deposits. In Magmas, Fluids and Ore Deposits: Mineralogical Association of Canada Short Course, 23, 455-477.

Simmons, S. F., White, N. C. and John D. A. (2005) Geological characteristics of epithermal precious and base metal deposits. Economic Geology, 100, 485-522.

Solidum, R. U., Castillo, P. R. and James W. H. (2003) Geochemistry of lavas from Negros Arc, west central Philippines: Insights into the contribution from the subducting slab. Geochemisty Geophysics Geosystems, 4, 1-26.

Sosa, L. (2014) Lobo and Archangel Gold Projects: Final Exploration Report. Unpublished Report. 183p.

Stephan, J. F., Blanchet, R., Rangin, C., Pelletier, B., Letouzey, J. and Muller, C. (1986) Geodynamic evolution of the Taiwan-Luzon-Mindoro Belt since the Late Eocene. Tectonophysics, 125, 245-268.

Sudo, M., Listanco, E. L., Ishikawa, N., Tagami, T., Kamata, H. and Tatsumi, Y. (2000) K-Ar dating of the volcanic rocks from Macolod Corridor in southwestern Luzon, Philippines: Toward understanding the Quaternary volcanism and tectonics. Journal of the Geologic Society of the Philippines, 55, 89-104.

Sugaki, A., Kitakaze, A. and Kojima, S. (1987) Bulk compositions of intimate intergrowths of chalcopyrite and sphalerite and their genetic implications. Mineralium Deposita, 22, 26–32.

Suzuoki, T. and Epstein, S. (1976) Hydrogen isotope fractionation between OH-bearing minerals and waters. Geochimica et Cosmochimica Acta, 40, 1229-1240.

Taguchi, S. and Hirowatari, F. (1976) Quantitative electron microanalysis of electrum by Bence and Albee method. Journal of the Mineralogical Society of Japan, 12, 82-85.

Takahashi, R., Tagiri, R., Blamey, N. J. F., Imai, A., Watanabe, Y. and Takeuchi, A. (2017) Characteristics and behavior of hydrothermal fluids for gold mineralization at the Hishikari Deposits, Kyushu, Japan. Resource Geology, 67, 279-299.

Tatsumi, T. (1970) Volcanism and Ore Genesis. University of Tokyo Press, Tokyo.

Taylor, H. P., Jr. (1974) The application of oxygen and hydrogen isotope studies to problems of hydrothermal alteration and ore deposition. Economic Geology, 69, 843-883.

Taylor, B. and Hayes, D. E. (1980) The tectonic evolution of the South China Basin. In Hayes, D. E. (ed.) The Tectonic and Geologic Evolution of Southeast Asian Seas and Islands. Geophysical Monograph, Part 1, 23, 89–104.

Tsushima, N. (1997) Characteristics and formation process of tin-polymetallic mineralization at the Shinano vein, Toyoha mine [Ph.D. Thesis]. Hokkaido University, Japan, 203p.

Tucker, M. E. (2001) Sedimentary Petrology: An Introduction to the Origin of Sedimentary Rocks. 3rd edn. Blackwell Publishing, Massachussetts, 272p.

Vogel, T. A., Flood, T. P., Patino, L. C. et al. (2006) Geochemistry of silicic magmas in the Macolod Corridor, SW Luzon, Philippines: Evidence of distinct, mantle-derived, crustal sources for silicic magmas. Contributions to Mineralogy and Petrology, 151, 267-281.

Waters, P. J., Cooke, D. R., Gonzales, R. I. and Phillips, D. (2011) Porphyry and epithermal deposits and $^{40}Ar/^{39}Ar$ geochronology of the Baguio District, Philippines. Economic Geology, 106, 1335-1363.

Wen, H., Zhu, C., Zhang, Y., Cloquet, C., Fan, H., and Fu, S. (2016) Zn/Cd ratios and cadmium isotope evidence for the classification of lead-zinc deposits. Scientific Reports, 6, 1-7

White, N. C. (1991) High sulfidation epithermal gold deposits: Characteristics, and a model for their origin. Geological Survey of Japan Report, 277, 9-20.

White, N. C. and Hedenquist, J. W. (1990) Epithermal environments and styles of mineralization: Variations and their causes, and guidelines for exploration. Journal of Geochemical Exploration, 36, 445-474.

White, N. C. and Hedenquist, J. W. (1995) Epithermal gold deposits: Styles, characteristics and exploration. Society of Economic Geologists Newsletter, 23, 1-13.

White, N. C. and Poizat, V. (1995) Epithermal deposits: Diverse styles, diverse origins? [Proceedings]. Exploring the Rim, PACRIM 1995 Congress, Auckland, New Zealand, 623-628.

White, N. C., Leake, M. J., McCaughey, S. N. and Parris, B. W. (1995) Epithermal gold deposits of the southwest Pacific. Journal of Geochemical Exploration, 54, 87-136.

Wilkinson, J. J. (2001) Fluid inclusions in hydrothermal ore deposits. Lithos, 55, 229-272.

Wolfe, J. A. (1981) Philippine geochronology. Journal of the Geological Society of the Philippines, 35, 1-30.

Wolfe, J. A. and Self, S. (1983) Structural lineaments and Neogene volcanism in southwestern Luzon. Geophysical Monograph Series: The Tectonic and Geologic Evolution of Southeast Asian Seas and Islands: Part 2, 27, 157-172.

Wolfe, J. A., Manuzon, M. S. and Divis, A. F. (1978) The Taysan porphyry Cu deposit, southern Luzon Island, Philippines. Economic Geology, 73, 608-617.

Wolfe, R. C. and Cooke, D. R. (2011) Geology of the Didipio Region and genesis of the Dinkidi Alkalic Porphyry Cu-Au Deposit and related pegmatites, Northern Luzon, Philippines. Economic Geology, 106, 1279-1315.

Wood, S. A. and Samson, I. M. (1998) Solubility of ore minerals and complexation of ore metals in hydrorthermal solutions. In Richards, J. P. and Larson, P. B. (eds.) Reviews in Economic Geology Volume 10: Techniques in Hydrothermal Ore Deposits Geology. Society of Economic Geologists, Michigan, 33-80.

Yanasigawa, F. and Sakai, H. (1983) Thermal decomposition of barium sulfate-vanadium pentaoxide-silica glass mixtures for preparation of sulfur dioxide in sulfur isotope ratio measurements. Analytical Chemistry, 55, 985-987.

Yang, J., Li, Y., Liu, S., Tian, H., Chen, C., Liu, J., Shi, Y. (2015) Theoretical calculations of Cd isotope fractionation in hydrothermal fluids. Chemical Geology, 391, 74-82.

Yang, T. F., Lee, T., Chen, C., Cheng, S., Knittel, U., Punongbayan, R. S., and Rasdas, A. R. (1996) A double island arc between Taiwan and Luzon: Consequence of ridge subduction. Tectonophysics, 258, 85-101.

Ye, L., Cook, N. J., Ciobanu, C. L. et al. (2011) Trace and minor elements in sphalerite from base metal deposits in South China: A LA-ICPMS study. Ore Geology Reviews, 39, 188-217.

Yumul, G. P., Jr., Dimalanta, C. B., Maglambayan, V. B. and Marquez, E. J. (2008) Tectonic setting of a composite terrain: A review of the Philippine island arc system. Geosciences Journal, 12, 7-17.

Zanoria, A. S., Domingo, E. G., Bacuta, G. C. and Almeda, R. L. (1984) Geology and tectonic setting of copper and chromite deposits of the Philippines. Geologic Survey of Japan Report, 263, 209-233.

Zaw, K. and Large R. R. (1996) Petrology and geochemistry of sphalerite from the Cambrian VHMS deposits in the Rosebery-Hercules district, western Tasmania: Implications for gold mineralisation and Devonian metamorphic-metasomatic process. Mineralogy and Petrology, 57, 97-118.

Zhou, H., Sun, X., Fu, Y., Lin, H. and Jiang, L. (2016) Mineralogy and mineral chemistry of Bi-minerals: Constraints on ore genesis of the Beiya giant porphyry-skarn gold deposit, southwestern China. Ore Geology Reviews, 79, 408-424.

Zhu, Y., An, F. and Tan, J. (2011) Geochemistry of hydrothermal gold deposits: A review. Geoscience Frontiers, 2, 367-374.

APPENDICES

APPENDIX A

DRILL HOLE DATA AND LOCATION MAP

Drill Hole ID	UTM Northing	UTM Easting	Elevation	Drill Hole Length	Depth	Azimuth	Dip
KTD175	1506924.88	316834.46	295.3	160	0	50	57
KTD176	1506869.27	316803.35	290.6	99.2	0	50	57
KTD182	1506941.1	316712.45	298.26	159.85	0	50	57
					50	51	59
					100	50	58
					158	50	60
KTD183	1506808.12	316854.66	289.97	175.4	0	50	57
					50	50	59
					100	49	60
					150	46	61
KTD191-12	1506851.4	316850.71	279.39	92.6	0	320	55
KTD194-12	1506985.52	316869.65	264.96	217.75	0	48	63
					50	48.8	64.4
					100	48.3	64.4
					150	49.3	65
					200	50.3	65.4
KTD197-12	1506644.8	316832.75	320.06	150.95	0	294	67
					50	293.4	67.7
					100	292.4	67.7
					150	292.8	68.2
KTD198-12	1506861.62	316826.69	281.18	153.5	0	48	45
					50	45.6	46.3
					100	45.8	46.3
					150	45.7	45.9
KTDH-04	1507019.63	316956.01	225.51	304	0	0	90
KTDH-10	1507187.56	316485.01	340.86	519.3	0	140	60
					100	145	60
					150	145	60
					200	145	61.5
					250	143	62.5
					299.6	145	63
					350	145.5	64
					400	143	65
					450	142	65
					519.3	141	65
KTDH-19	1507184.9	316557.07	319.63	500.1	0	320	55
					50	324	56
					100	320	57.5
					150	325	58
					200	325	58
					250	325.5	60
					300	322.5	62
					350	325	62.5
					400	322	64
					450	325	63.5
					500.1	320	63.5
KTDH-23	1506859.72	316827.69	280.94	164.3	0	142	58

					50	145	58
					100	145.5	58.5
					164.3	145	60
KTDH-24	1506886.71	316836.38	281.99	126	0	143	70
					50	146	70
					120	146.5	69.5

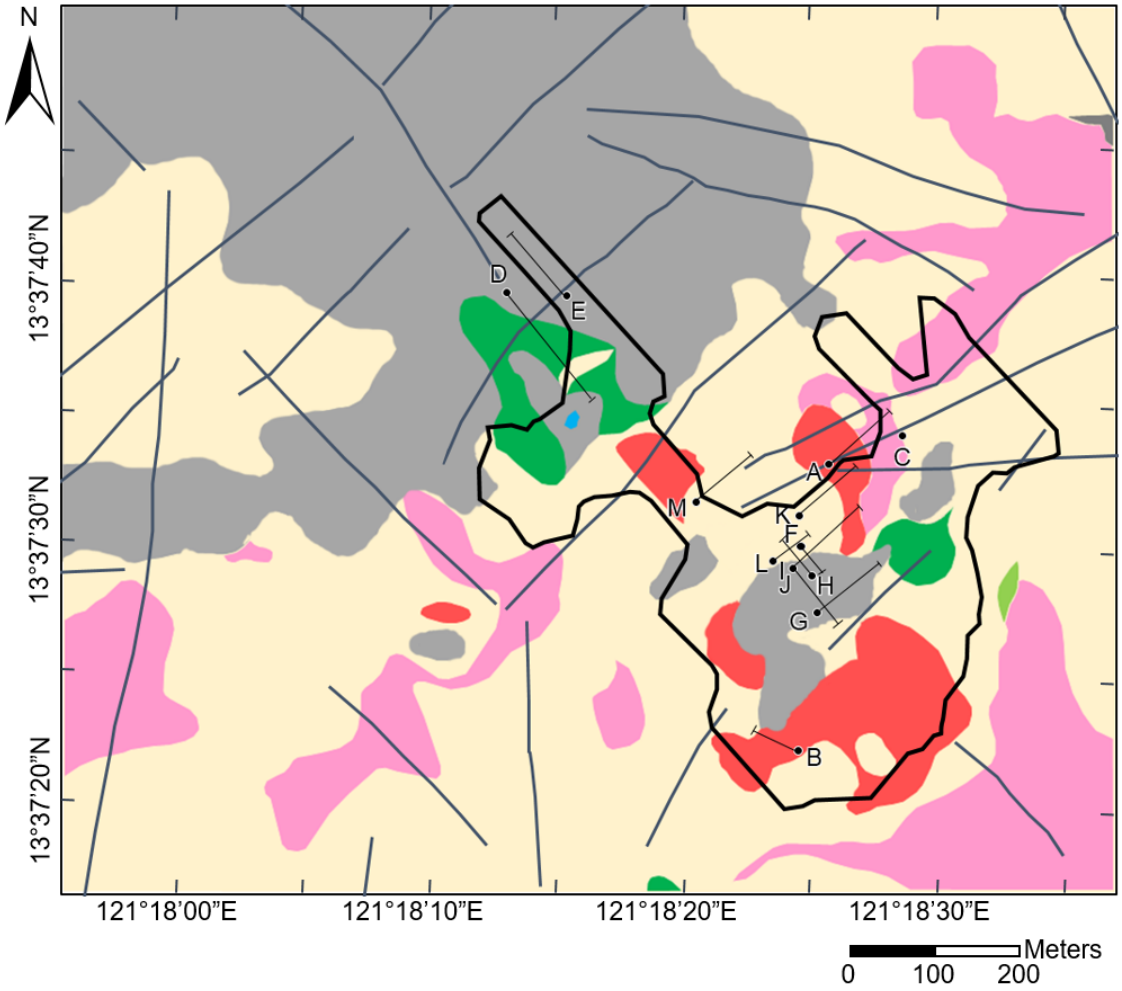

Alteration

- Quartz ± pyrophyllite ± dickite/kaolinite ± diaspore
- Illite ± quartz ± smectite ± kaolinite
- Chlorite-illite-quartz
- Sericite-quartz-calcite
- Epidote-calcite-chlorite
- Dolomitization
- Not hydrothermally altered

Mineralization (Sampling Point)

- Stage 1
- Stage 2
- Stage 4
- Stage 5
- Stage 6

Other Features

- Resource Area
- Interpreted structures from SRTM data of Rohrlach and Fredericksen (2008)

Drill Hole Name

- Collar
- End

Drill Hole Nomenclature

- **A** – KTD194-12
- **B** – KTD197-12
- **C** – KTDH04
- **D** – KTDH10
- **E** – KTDH19
- **F** – KTDH24
- **G** – KTD183
- **H** – KTD191-12
- **I** – KTD198-12
- **J** – KTDH23
- **K** – KTD175
- **L** – KTD176
- **M** – KTD182

APPENDIX B

NATIVE GOLD/ELECTRUM AU AND AG COMPOSITION

Sample	Sample point	Sample type	Au (Atomic %)	Ag (Atomic %)	Mineral ID
KTD194-12 186.60m (A23)	TSA23-C1-3	vein	92.12	7.88	Native Gold
KTD194-12 186.60m (A23)	TSA23-C1-4	vein	91.50	8.50	Native Gold
KTD194-12 186.60m (A23)	TSA23-C1-5	vein	92.55	7.45	Native Gold
KTD194-12 186.60m (A23)	TSA23-C1-6	vein	92.27	7.73	Native Gold
KTDH04 85.30m (C11)	TSC11-C3-1	vein	91.66	8.34	Native Gold
KTDH04 85.30m (C11)	TSC11-C3-2	vein	91.56	8.44	Native Gold
KTDH04 85.30m (C11)	TSC11-C3-3	vein	91.25	8.75	Native Gold
KTDH04 85.30m (C11)	TSC11-C3-4	vein	91.82	8.18	Native Gold
KTDH04 85.30m (C11)	TSC11-C4-2	vein	90.71	9.29	Native Gold
KTDH04 85.30m (C11)	TSC11-C1-1	vein	91.00	9.00	Native Gold
KTDH04 85.30m (C11)	TSC11-C1-3	vein	91.14	8.86	Native Gold
KTDH04 85.30m (C11)	TSC11-C1-5	vein	90.64	9.36	Native Gold
KTDH04 85.30m (C11)	TSC11-C1-6	vein	91.01	8.99	Native Gold
KTDH04 85.30m (C11)	PSC11-C1-3	vein	90.65	9.35	Native Gold
KTDH04 85.30m (C11)	PSC11-C1-4	vein	90.46	9.54	Native Gold
KTDH04 85.30m (C11)	PSC11-C1-5	vein	90.60	9.40	Native Gold
KTDH04 85.30m (C11)	PSC11-C1-6	vein	90.36	9.64	Native Gold
KTDH04 85.30m (C11)	PSC11-C1-7	vein	89.76	10.24	Native Gold
KTDH04 85.30m (C11)	PSC11-C1-8	vein	88.49	11.51	Native Gold
KTDH04 101.40m (C20)	TSC20-C1-1	hbx	93.22	6.78	Native Gold
KTDH04 101.40m (C20)	TSC20-C1-2	hbx	92.97	7.03	Native Gold
KTDH04 101.40m (C20)	TSC20-C1-6	hbx	93.30	6.70	Native Gold
KTDH04 101.40m (C20)	TSC20-C1-7	hbx	93.43	6.57	Native Gold
KTDH04 101.40m (C20)	TSC20-C1-8	hbx	93.16	6.84	Native Gold
KTDH04 101.40m (C20)	TSC20-C1-12	hbx	93.60	6.40	Native Gold
KTDH04 101.40m (C20)	TSC20-C1-13	hbx	93.40	6.60	Native Gold
KTDH04 101.40m (C20)	TSC20-C1-14	hbx	93.38	6.62	Native Gold
KTDH04 101.40m (C20)	TSC20-C2-6	hbx	93.32	6.68	Native Gold
KTDH04 101.40m (C20)	TSC20-C2-9	hbx	93.27	6.73	Native Gold
KTDH04 101.40m (C20)	TSC20-C2-10	hbx	93.10	6.90	Native Gold
KTDH04 101.40m (C20)	TSC20-C2-11	hbx	93.33	6.67	Native Gold
KTDH04 101.40m (C20)	TSC20-C2-12	hbx	93.30	6.70	Native Gold
KTDH04 101.40m (C20)	TSC20-C2-20	hbx	93.33	6.67	Native Gold
KTDH04 101.40m (C20)	TSC20-C2-21	hbx	93.26	6.74	Native Gold
KTDH04 101.40m (C20)	TSC20-C2-22	hbx	93.42	6.58	Native Gold
KTDH04 101.40m (C20)	TSC20-C2-23	hbx	93.20	6.80	Native Gold
KTDH04 101.40m (C20)	TSC20-C3-1	hbx	93.22	6.78	Native Gold
KTDH04 101.40m (C20)	TSC20-C3-6	hbx	93.15	6.85	Native Gold
KTDH04 101.40m (C20)	TSC20-C3-10	hbx	93.06	6.94	Native Gold
KTDH04 101.40m (C20)	TSC20-C5-2	hbx	93.07	6.93	Native Gold
KTDH04 101.40m (C20)	TSC20-C5-3	hbx	93.14	6.86	Native Gold
KTDH04 101.40m (C20)	TSC20-C5-4	hbx	93.26	6.74	Native Gold
KTDH04 101.40m (C20)	TSC20-C5-5	hbx	92.98	7.02	Native Gold
KTDH04 101.40m (C20)	TSC20-C5-6	hbx	93.26	6.74	Native Gold
KTDH04 101.40m (C20)	TSC20-C5-9	hbx	93.16	6.84	Native Gold
KTDH04 101.40m (C20)	TSC20-C5-16	hbx	93.39	6.61	Native Gold
KTDH04 101.40m (C20)	TSC20-C6-2	hbx	92.98	7.02	Native Gold
KTDH04 101.40m (C20)	TSC20-C6-3	hbx	93.09	6.91	Native Gold
KTDH04 101.40m (C20)	TSC20-C7-2	hbx	93.10	6.90	Native Gold

KTDH04 101.40m (C20)	TSC20-C7-3	hbx	92.79	7.21	Native Gold
KTDH04 101.40m (C20)	TSC20-C7-4	hbx	92.99	7.01	Native Gold
KTDH04 101.40m (C20)	TSC20-C7-6	hbx	92.91	7.09	Native Gold
KTDH04 101.40m (C20)	TSC20-C7-7	hbx	92.82	7.18	Native Gold
KTDH04 101.40m (C20)	TSC20-C7-8	hbx	93.19	6.81	Native Gold
KTDH04 101.40m (C20)	TSC20-C8-1	hbx	93.17	6.83	Native Gold
KTDH04 101.40m (C20)	TSC20-C8-8	hbx	93.32	6.68	Native Gold
KTDH04 101.40m (C20)	TSC20-C8-10	hbx	93.26	6.74	Native Gold
KTDH04 101.40m (C20)	TSC20-C8-11	hbx	92.95	7.05	Native Gold
KTDH04 101.40m (C20)	TSC20-C9-1	hbx	92.76	7.24	Native Gold
KTDH04 101.40m (C20)	TSC20-C9-2	hbx	92.92	7.08	Native Gold
KTDH04 101.40m (C20)	TSC20-C9-3	hbx	92.61	7.39	Native Gold
KTDH04 101.40m (C20)	TSC20-C9-4	hbx	92.59	7.41	Native Gold
KTDH04 101.40m (C20)	TSC20-C9-12	hbx	92.75	7.25	Native Gold
KTDH04 101.40m (C20)	TSC20-C9-13	hbx	92.99	7.01	Native Gold
KTDH04 101.40m (C20)	TSC20-C9-14	hbx	92.85	7.15	Native Gold
KTDH04 101.40m (C20)	TSC20-C9-15	hbx	92.65	7.35	Native Gold
KTDH04 101.40m (C20)	TSC20-C9-16	hbx	92.58	7.42	Native Gold
KTDH04 101.40m (C20)	TSC20-C9-17	hbx	92.68	7.32	Native Gold
KTDH04 101.40m (C20)	TSC20-C9-18	hbx	92.72	7.28	Native Gold
KTDH04 101.40m (C20)	TSC20-C10-3	hbx	93.04	6.96	Native Gold
KTDH04 101.40m (C20)	TSC20-C10-4	hbx	92.94	7.06	Native Gold
KTDH04 101.40m (C20)	PSC20-C1-3	hbx	92.61	7.39	Native Gold
KTDH04 101.40m (C20)	PSC20-C1-4	hbx	92.46	7.54	Native Gold
KTDH04 101.40m (C20)	PSC20-C1-6	hbx	92.74	7.26	Native Gold
KTDH04 101.40m (C20)	PSC20-C1-11	hbx	93.17	6.83	Native Gold
KTDH04 101.40m (C20)	PSC20-C2-1	hbx	92.37	7.63	Native Gold
KTDH04 101.40m (C20)	PSC20-C2-2	hbx	92.89	7.11	Native Gold
KTDH04 101.40m (C20)	PSC20-C2-3	hbx	92.26	7.74	Native Gold
KTDH04 101.40m (C20)	PSC20-C3-1	hbx	92.29	7.71	Native Gold
KTDH04 101.40m (C20)	PSC20-C3-3	hbx	92.35	7.65	Native Gold
KTDH04 101.40m (C20)	PSC20-C3-4	hbx	92.46	7.54	Native Gold
KTDH04 101.40m (C20)	PSC20-C4-1	hbx	92.05	7.95	Native Gold
KTDH04 101.40m (C20)	PSC20-C5-1	hbx	92.61	7.39	Native Gold
KTDH04 101.40m (C20)	PSC20-C5-2	hbx	92.33	7.67	Native Gold
KTDH04 101.40m (C20)	PSC20-C6-2	hbx	92.52	7.48	Native Gold
KTDH04 101.40m (C20)	PSC20-C7-4	hbx	93.06	6.94	Native Gold
KTDH04 101.40m (C20)	PSC20-C7-5	hbx	92.97	7.03	Native Gold
KTDH04 101.40m (C20)	PSC20-C7-6	hbx	92.94	7.06	Native Gold
KTDH04 101.40m (C20)	PSC20-C7-7	hbx	92.43	7.57	Native Gold
KTDH04 101.40m (C20)	PSC20-C8-1	hbx	92.60	7.40	Native Gold
KTDH04 101.40m (C20)	PSC20-C8-6	hbx	91.87	8.13	Native Gold
KTDH04 101.40m (C20)	PSC20-C9-1	hbx	92.85	7.15	Native Gold
KTDH04 101.40m (C20)	PSC20-C9-4	hbx	92.79	7.21	Native Gold
KTDH04 101.40m (C20)	PSC20-C11-2	hbx	92.70	7.30	Native Gold
KTDH04 101.40m (C20)	PSC20-C11-4	hbx	92.84	7.16	Native Gold
KTDH04 101.40m (C20)	PSC20-C11-6	hbx	92.74	7.26	Native Gold
KTDH04 101.40m (C20)	PSC20-C11-7	hbx	92.37	7.63	Native Gold
KTDH04 101.40m (C20)	PSC20-C12-1	hbx	92.59	7.41	Native Gold
KTDH04 101.40m (C20)	PSC20-C12-2	hbx	92.79	7.21	Native Gold

KTDH04 101.40m (C20)	PSC20-C12-3	hbx	93.02	6.98	Native Gold
KTDH04 101.40m (C20)	PSC20-C12-4	hbx	92.99	7.01	Native Gold
KTDH04 101.40m (C20)	PSC20-C12-5	hbx	92.85	7.15	Native Gold
KTDH04 101.40m (C20)	PSC20-C13-1	hbx	92.89	7.11	Native Gold
KTDH04 101.40m (C20)	PSC20-C13-2	hbx	92.90	7.10	Native Gold
KTDH04 101.40m (C20)	PSC20-C13-3	hbx	92.89	7.11	Native Gold
KTDH04 101.40m (C20)	PSC20-C14-1	hbx	92.74	7.26	Native Gold
KTDH04 101.40m (C20)	PSC20-C14-2	hbx	92.76	7.24	Native Gold
KTDH04 101.40m (C20)	PSC20-C14-4	hbx	92.81	7.19	Native Gold
KTDH04 101.40m (C20)	PSC20-C14-5	hbx	92.73	7.27	Native Gold
KTDH04 101.40m (C20)	PSC20-C14-6	hbx	92.82	7.18	Native Gold
KTDH04 101.40m (C20)	PSC20-C14-9	hbx	92.16	7.84	Native Gold
KTDH04 101.40m (C20)	PSC20-C14-10	hbx	92.60	7.40	Native Gold
KTDH04 101.40m (C20)	PSC20-C14-11	hbx	92.64	7.36	Native Gold
KTDH04 101.40m (C20)	PSC20-C14-12	hbx	92.86	7.14	Native Gold
KTDH04 101.40m (C20)	PSC20-C15-1	hbx	92.71	7.29	Native Gold
KTDH04 101.40m (C20)	PSC20-C15-2	hbx	92.81	7.19	Native Gold
KTDH04 101.40m (C20)	PSC20-C15-3	hbx	92.99	7.01	Native Gold
KTDH04 101.40m (C20)	PSC20-C15-4	hbx	92.81	7.19	Native Gold
KTDH04 101.40m (C20)	PSC20-C116-1	hbx	92.44	7.56	Native Gold
KTDH04 101.40m (C20)	PSC20-C116-2	hbx	92.77	7.23	Native Gold
KTDH04 101.40m (C20)	PSC20-C116-3	hbx	92.79	7.21	Native Gold
KTDH04 101.40m (C20)	PSC20-C116-4	hbx	92.62	7.38	Native Gold
KTDH04 101.40m (C20)	PSC20-C116-5	hbx	92.58	7.42	Native Gold
KTDH04 101.40m (C20)	PSC20-C116-7	hbx	92.32	7.68	Native Gold
KTDH04 101.40m (C20)	PSC20-C116-8	hbx	92.45	7.55	Native Gold
KTDH04 101.40m (C20)	PSC20-C116-9	hbx	92.85	7.15	Native Gold
KTDH04 101.40m (C20)	PSC20-C17-2	hbx	92.89	7.11	Native Gold
KTDH04 101.40m (C20)	PSC20-C17-4	hbx	92.97	7.03	Native Gold
KTDH04 101.40m (C20)	PSC20-C18-1	hbx	92.93	7.07	Native Gold
KTDH04 101.40m (C20)	PSC20-C18-2	hbx	92.44	7.56	Native Gold
KTDH04 101.40m (C20)	PSC20-C19-2	hbx	92.93	7.07	Native Gold
KTDH04 101.40m (C20)	PSC20-C19-3	hbx	92.98	7.02	Native Gold
KTDH04 101.40m (C20)	PSC20-C19-6	hbx	92.96	7.04	Native Gold
KTDH04 102.95m (C21)	PSC21-C1-1	hbx	92.49	7.51	Native Gold
KTDH04 102.95m (C21)	PSC21-C2-1	hbx	92.39	7.61	Native Gold
KTDH04 102.95m (C21)	PSC21-C2-2	hbx	92.36	7.64	Native Gold
KTDH04 102.95m (C21)	PSC21-C2-4	hbx	92.21	7.79	Native Gold
KTDH04 102.95m (C21)	PSC21-C2-5	hbx	92.08	7.92	Native Gold
KTDH04 102.95m (C21)	PSC21-C3-1	hbx	92.38	7.62	Native Gold
KTDH04 102.95m (C21)	PSC21-C3-2	hbx	92.14	7.86	Native Gold
KTDH04 102.95m (C21)	PSC21-C3-3	hbx	92.04	7.96	Native Gold
KTDH04 102.95m (C21)	PSC21-C3-4	hbx	92.13	7.87	Native Gold
KTDH04 102.95m (C21)	PSC21-C3-5	hbx	92.16	7.84	Native Gold
KTDH04 102.95m (C21)	PSC21-C3-7	hbx	92.46	7.54	Native Gold
KTDH04 105.50m (C23)	TSC23-C1-4	vein	93.52	6.48	Native Gold
KTDH04 105.50m (C23)	TSC23-C1-6	vein	93.70	6.30	Native Gold
KTDH04 105.50m (C23)	TSC23-C2-1	vein	81.20	18.80	Native Gold
KTDH04 105.50m (C23)	TSC23-C3-1	vein	87.70	12.30	Native Gold
KTDH04 105.50m (C23)	TSC23-C4-5	vein	93.58	6.42	Native Gold

KTDH04 105.50m (C23)	TSC23-C4-9	vein	88.19	11.81	Native Gold
KTDH04 105.50m (C23)	TSC23-C4-11	vein	78.44	21.56	Electrum
KTDH04 105.50m (C23)	TSC23-C5-1	vein	78.65	21.35	Electrum
KTDH04 105.50m (C23)	TSC23-C5-2	vein	78.97	21.03	Electrum
KTDH04 105.50m (C23)	TSC23-C5-9	vein	93.84	6.16	Native Gold
KTDH04 105.50m (C23)	TSC23-C5-11	vein	94.10	5.90	Native Gold
KTDH04 105.50m (C23)	TSC23-C5-12	vein	94.21	5.79	Native Gold
KTDH04 105.50m (C23)	TSC23-C5-15	vein	93.96	6.04	Native Gold
KTDH04 119.10m (C30)	PSC30-C1-1	hbx	92.60	7.40	Native Gold
KTDH04 119.10m (C30)	PSC30-C1-5	hbx	92.82	7.18	Native Gold
KTDH04 119.10m (C30)	PSC30-C1-6	hbx	92.67	7.33	Native Gold
KTDH04 119.10m (C30)	PSC30-C1-10	hbx	92.96	7.04	Native Gold
KTDH04 119.10m (C30)	PSC30-C1-11	hbx	92.94	7.06	Native Gold
KTDH04 119.10m (C30)	PSC30-C1-12	hbx	93.13	6.87	Native Gold
KTDH04 119.10m (C30)	PSC30-C1-19	hbx	92.73	7.27	Native Gold
KTDH04 119.10m (C30)	PSC30-C1-20	hbx	92.79	7.21	Native Gold
KTDH04 119.10m (C30)	PSC30-C1-21	hbx	92.86	7.14	Native Gold
KTDH04 119.10m (C30)	PSC30-C2-2	hbx	92.15	7.85	Native Gold
KTDH04 119.10m (C30)	PSC30-C2-3	hbx	92.44	7.56	Native Gold
KTDH04 119.10m (C30)	PSC30-C2-4	hbx	92.03	7.97	Native Gold
KTDH04 119.10m (C30)	PSC30-C2-5	hbx	91.99	8.01	Native Gold
KTDH04 119.10m (C30)	PSC30-C3-1	hbx	92.77	7.23	Native Gold
KTDH04 119.10m (C30)	PSC30-C3-2	hbx	92.60	7.40	Native Gold
KTDH04 119.10m (C30)	PSC30-C3-3	hbx	92.37	7.63	Native Gold
KTDH04 119.10m (C30)	PSC30-C3-4	hbx	92.25	7.75	Native Gold
KTDH04 119.10m (C30)	PSC30-C3-5	hbx	92.16	7.84	Native Gold
KTDH04 119.10m (C30)	PSC30-C4-1	hbx	92.38	7.62	Native Gold
KTDH04 119.10m (C30)	PSC30-C4-2	hbx	92.49	7.51	Native Gold
KTDH04 119.10m (C30)	PSC30-C4-3	hbx	92.57	7.43	Native Gold
KTDH04 119.10m (C30)	PSC30-C4-4	hbx	92.67	7.33	Native Gold
KTDH04 119.10m (C30)	PSC30-C4-5	hbx	92.73	7.27	Native Gold
KTDH04 119.10m (C30)	PSC30-C4-6	hbx	93.21	6.79	Native Gold
KTDH04 169.20m (C33)	PSC33-C1-2	vein	86.09	13.91	Native Gold
KTDH04 169.20m (C33)	PSC33-C1-3	vein	86.45	13.55	Native Gold
KTDH04 169.20m (C33)	PSC33-C1-6	vein	94.06	5.94	Native Gold

APPENDIX C

SPHALERITE MINOR AND MAJOR ELEMENT COMPOSITION

Sample Name		KTD194-12 110.45m (A13)													KTD194-12 194.00m (A24)			KTDH04 87.80m (C12)			
Sample Point		A13-C1-2	A13-C1-5	A13-C1-9	A13-C1-23	A13-C2-02	A13-C2-03	A13-C2-04	A13-C2-05	A13-C2-06	A13-C2-07	A13-C2-12	A13-C2-13	A13-C2-14	A24-C1-12	A24-C1-16	A24-C1-27	C12-C1-1	C12-C1-2	C12-C1-3	C12-C1-4
Weight %	L.L.D. %																				
Zn	0.08	63.91	63.65	63.54	65.04	64.76	64.80	65.17	65.11	64.88	65.09	65.76	65.13	65.30	63.94	64.57	63.78	64.48	64.92	65.50	66.30
Fe	0.04	1.16	1.40	1.61	0.72	0.67	0.57	0.55	0.45	0.47	0.52	0.55	0.50	0.66	0.79	0.48	0.44	0.77	0.65	0.54	0.46
Mn	0.02	0.06	0.07	0.09	0.08	0.07	0.07	0.09	0.06	0.06	0.10	0.06	0.10	0.08	0.13	0.16	0.12	0.08	0.08	0.05	0.07
Cd	0.02	0.16	0.18	0.23	0.29	0.29	0.35	0.31	0.33	0.35	0.36	0.31	0.30	0.29	0.26	0.29	0.31	0.39	0.42	0.45	0.40
Cu	0.06	<0.06	<0.06	<0.06	0.09	<0.06	<0.06	<0.06	<0.06	0.09	<0.06	<0.06	<0.06	<0.06	<0.06	<0.06	<0.06	<0.06	<0.06	<0.06	<0.06
Sn	0.04	<0.04	<0.04	<0.04	<0.04	<0.04	<0.04	<0.04	0.09	0.05	<0.04	<0.04	<0.04	<0.04	<0.04	<0.04	<0.04	<0.04	<0.04	<0.04	<0.04
In	0.04	<0.04	<0.04	<0.04	<0.04	<0.04	<0.04	<0.04	<0.04	<0.04	<0.04	<0.04	<0.04	<0.04	<0.04	<0.04	<0.04	<0.04	<0.04	<0.04	<0.04
Ag	0.03	<0.03	<0.03	0.08	<0.03	<0.03	<0.03	<0.03	<0.03	<0.03	<0.03	<0.03	<0.03	<0.03	0.03	0.06	0.07	<0.03	0.08	<0.03	<0.03
Ga	0.02	0.15	0.16	0.16	0.23	<0.02	0.07	0.14	0.21	0.07	0.17	0.05	0.06	0.22	0.29	0.04	<0.02	0.25	0.06	0.17	<0.02
S	0.02	32.67	33.39	32.63	32.67	32.53	32.34	32.18	32.13	32.15	32.07	31.73	32.43	31.62	31.78	31.95	32.75	32.51	32.69	32.97	32.76
Total		98.11	98.84	98.34	99.12	98.32	98.19	98.44	98.38	98.13	98.31	98.46	98.51	98.16	97.21	97.54	97.47	98.48	98.90	99.68	99.99
Atomic %																					
Zn		48.33	47.60	47.99	48.88	49.01	49.18	49.43	49.44	49.35	49.44	50.02	49.26	49.82	49.09	49.39	48.52	48.75	48.89	48.93	49.49
Fe		1.03	1.22	1.43	0.63	0.59	0.50	0.48	0.40	0.42	0.46	0.49	0.44	0.59	0.71	0.43	0.40	0.68	0.57	0.47	0.40
Mn		0.06	0.06	0.08	0.07	0.06	0.06	0.08	0.05	0.06	0.09	0.05	0.09	0.07	0.11	0.14	0.11	0.07	0.07	0.05	0.06
Cd		0.07	0.08	0.10	0.13	0.13	0.15	0.14	0.15	0.16	0.16	0.14	0.13	0.13	0.12	0.13	0.14	0.17	0.18	0.20	0.17
Cu		0.04		0.00	0.07		0.00		0.04	0.07	0.04	0.04	0.02	0.03				0.02			
Sn				0.00				0.01	0.04	0.02				0.01		0.00	0.01				
In			0.01													0.00		0.00		0.02	
Ag			0.01	0.04			0.01				0.01	0.01	0.01		0.02	0.03	0.03		0.04		
Ga		0.10	0.11	0.11	0.16	0.00	0.05	0.10	0.15	0.05	0.12	0.03	0.04	0.15	0.21	0.03		0.18	0.04	0.12	0.01
S		50.37	50.91	50.25	50.06	50.20	50.04	49.76	49.74	49.87	49.67	49.21	50.01	49.19	49.75	49.84	50.79	50.12	50.20	50.22	49.86
Total		100.00	100.00	100.00	100.00	100.00	100.00	100.00	100.00	100.00	100.00	100.00	100.00	100.00	100.00	100.00	100.00	100.00	100.00	100.00	100.00
FeS		2.07	2.49	2.87	1.27	1.19	1.00	0.97	0.80	0.83	0.92	0.97	0.89	1.15	1.41	0.86	0.80	1.37	1.15	0.94	0.80
MnS		0.11	0.13	0.17	0.14	0.12	0.12	0.16	0.10	0.12	0.19	0.11	0.17	0.14	0.23	0.28	0.22	0.15	0.14	0.09	0.13
CdS		0.14	0.16	0.20	0.26	0.26	0.31	0.27	0.29	0.31	0.32	0.27	0.27	0.26	0.23	0.26	0.28	0.34	0.37	0.39	0.35

Sample Name		KTDH04 87.80m (C12)																		
Sample Point		C12-C1-5	C12-C1-6	C12-C1-7	C12-C1-8	C12-C1-9	C12-C1-10	C12-C1-11	C12-C1-12	C12-C1-13	C12-C1-14	C12-C1-15	C12-C1-16	C12-C2-1	C12-C2-2	C12-C2-3	C12-C2-4	C12-C2-5	C12-C2-6	C12-C2-7	C12-C2-8
Weight %	L.L.D. %																				
Zn	0.08	65.77	65.72	65.74	66.30	65.75	66.10	65.50	66.19	65.16	65.83	65.55	65.24	64.14	64.88	64.43	65.84	66.45	66.03	66.07	65.15
Fe	0.04	0.45	0.38	0.46	0.43	0.40	0.42	0.46	0.46	0.48	0.61	0.58	0.56	0.62	1.01	0.69	0.60	0.37	0.70	0.63	0.63
Mn	0.02	0.06	0.07	0.05	0.03	0.08	0.04	0.04	0.03	0.07	0.03	0.06	0.08	0.07	0.10	0.06	0.08	0.03	0.06	0.08	0.07
Cd	0.02	0.37	0.36	0.34	0.31	0.27	0.30	0.25	0.32	0.36	0.38	0.40	0.32	0.37	0.39	0.39	0.40	0.40	0.41	0.42	0.49
Cu	0.06	<0.06	<0.06	<0.06	<0.06	<0.06	<0.06	<0.06	<0.06	<0.06	<0.06	0.06	0.08	<0.06	0.38	<0.06	<0.06	0.13	<0.06	<0.06	0.06
Sn	0.04	<0.04	<0.04	<0.04	<0.04	<0.04	<0.04	<0.04	0.08	<0.04	<0.04	<0.04	<0.04	<0.04	<0.04	<0.04	<0.04	<0.04	<0.04	0.05	<0.04
In	0.04	<0.04	<0.04	<0.04	<0.04	<0.04	<0.04	<0.04	<0.04	<0.04	<0.04	<0.04	<0.04	<0.04	<0.04	<0.04	<0.04	<0.04	<0.04	<0.04	<0.04
Ag	0.03	0.06	<0.03	<0.03	<0.03	<0.03	<0.03	<0.03	<0.03	<0.03	<0.03	<0.03	<0.03	<0.03	<0.03	<0.03	<0.03	<0.03	0.03	<0.03	<0.03
Ga	0.02	0.22	0.29	0.08	0.15	0.10	0.12	0.16	0.16	0.22	0.17	0.05	0.17	0.02	0.16	0.19	<0.02	0.06	0.10	0.17	0.20
S	0.02	32.91	32.97	33.39	33.21	33.40	34.10	33.63	33.22	33.59	33.40	33.70	33.00	33.67	33.50	33.69	32.92	33.68	33.54	33.86	33.23
Total		99.83	99.79	100.06	100.42	100.00	101.09	100.03	100.46	99.87	100.42	100.39	99.45	98.89	100.42	99.44	99.84	101.11	100.87	101.29	99.82
Atomic %																					
Zn		49.10	49.06	48.80	49.16	48.81	48.44	48.52	49.07	48.37	48.73	48.43	48.79	47.91	47.96	47.94	49.13	48.86	48.66	48.44	48.53
Fe		0.39	0.33	0.40	0.37	0.35	0.36	0.40	0.40	0.41	0.53	0.50	0.49	0.55	0.87	0.60	0.52	0.32	0.60	0.54	0.55
Mn		0.05	0.06	0.04	0.02	0.07	0.04	0.04	0.02	0.06	0.03	0.05	0.07	0.06	0.09	0.05	0.07	0.02	0.05	0.07	0.06
Cd		0.16	0.16	0.15	0.13	0.12	0.13	0.11	0.14	0.15	0.16	0.17	0.14	0.16	0.17	0.17	0.17	0.17	0.18	0.18	0.21
Cu				0.01		0.03		0.04				0.05	0.06	0.03	0.29			0.09			0.05
Sn									0.03				0.00				0.01		0.01	0.02	
In		0.01		0.01					0.00			0.01	0.01		0.01				0.02		
Ag		0.02			0.00		0.01		0.01						0.01	0.01	0.00		0.01		
Ga		0.15	0.20	0.06	0.10	0.07	0.08	0.11	0.11	0.15	0.12	0.03	0.12	0.01	0.11	0.13	0.00	0.04	0.07	0.12	0.14
S		50.10	50.18	50.53	50.21	50.55	50.94	50.79	50.21	50.85	50.43	50.77	50.31	51.28	50.50	51.11	50.08	50.49	50.40	50.62	50.47
Total		100.00	100.00	100.00	100.00	100.00	100.00	100.00	100.00	100.00	100.00	100.00	100.00	100.00	100.00	100.00	100.00	100.00	100.00	100.00	100.00
FeS		0.79	0.67	0.81	0.74	0.70	0.74	0.81	0.81	0.84	1.07	1.01	0.99	1.12	1.77	1.22	1.05	0.64	1.21	1.10	1.11
MnS		0.10	0.13	0.08	0.05	0.14	0.07	0.08	0.05	0.12	0.05	0.10	0.15	0.12	0.18	0.10	0.15	0.05	0.11	0.14	0.12
CdS		0.33	0.31	0.30	0.27	0.24	0.26	0.22	0.27	0.31	0.33	0.35	0.28	0.33	0.34	0.34	0.35	0.35	0.35	0.36	0.43

Sample Name		KTDH04 87.80m (C12)																		
Sample Point		C12-C2-9	C12-C2-10	C12-C2-11	C12-C2-12	C12-C2-13	C12-C2-14	C12-C2-15	C12-C3-1	C12-C3-2	C12-C3-3	C12-C3-4	C12-C3-5	C12-C3-6	C12-C3-7	C12-C3-8	C12-C3-9	C12-C3-10	C12-C3-11	C12-C3-12	C12-C3-13
Weight %	L.L.D. %																				
Zn	0.08	66.24	64.05	65.73	64.61	64.98	64.53	64.28	65.79	66.04	66.68	65.15	66.08	66.49	65.69	64.52	65.35	65.54	65.54	65.07	66.49
Fe	0.04	0.64	0.66	0.58	0.73	0.55	0.62	0.56	0.69	0.68	0.67	0.51	0.47	0.56	0.55	0.70	0.68	0.51	0.59	0.55	0.56
Mn	0.02	0.02	0.06	0.08	0.06	0.03	0.06	0.04	0.05	0.07	0.06	0.05	0.04	0.04	0.03	0.07	<0.02	0.04	0.05	0.06	0.06
Cd	0.02	0.50	0.50	0.43	0.41	0.42	0.39	0.41	0.36	0.39	0.40	0.40	0.39	0.41	0.42	0.38	0.41	0.38	0.37	0.40	0.36
Cu	0.06	<0.06	<0.06	<0.06	0.22	0.09	0.19	0.10	0.12	<0.06	<0.06	<0.06	<0.06	<0.06	<0.06	<0.06	0.14	<0.06	<0.06	<0.06	0.07
Sn	0.04	<0.04	<0.04	<0.04	<0.04	<0.04	<0.04	<0.04	<0.04	<0.04	<0.04	<0.04	<0.04	0.04	0.07	<0.04	<0.04	<0.04	<0.04	<0.04	0.07
In	0.04	<0.04	0.06	<0.04	0.04	<0.04	<0.04	<0.04	<0.04	<0.04	<0.04	<0.04	<0.04	<0.04	0.04	0.09	<0.04	<0.04	<0.04	<0.04	<0.04
Ag	0.03	0.04	<0.03	<0.03	<0.03	0.03	0.04	0.05	<0.03	<0.03	0.04	<0.03	<0.03	0.08	<0.03	0.03	0.06	0.04	<0.03	<0.03	0.06
Ga	0.02	0.14	0.07	0.09	0.20	0.08	0.23	0.09	<0.02	0.14	0.05	0.26	0.12	<0.02	0.08	0.11	0.13	0.11	<0.02	0.22	0.08
S	0.02	33.45	33.28	33.11	33.99	33.79	33.82	33.83	33.33	33.66	33.16	32.90	33.47	33.06	34.12	33.48	33.45	33.49	32.91	33.71	33.24
Total		101.03	98.68	100.03	100.27	99.96	99.87	99.37	100.34	100.97	101.06	99.26	100.56	100.69	101.00	99.39	100.22	100.12	99.46	99.99	100.99
Atomic %																					
Zn		48.83	48.10	48.92	47.68	48.14	47.82	47.82	48.74	48.59	49.23	48.85	48.85	49.28	48.17	48.12	48.44	48.61	49.05	48.21	49.10
Fe		0.55	0.58	0.50	0.63	0.47	0.54	0.49	0.60	0.58	0.58	0.45	0.40	0.49	0.47	0.61	0.59	0.45	0.52	0.47	0.48
Mn		0.02	0.06	0.07	0.05	0.02	0.05	0.04	0.04	0.06	0.05	0.05	0.03	0.04	0.03	0.06	0.01	0.04	0.05	0.05	0.05
Cd		0.21	0.22	0.19	0.17	0.18	0.17	0.18	0.15	0.16	0.17	0.17	0.17	0.18	0.18	0.17	0.18	0.16	0.16	0.17	0.15
Cu			0.01		0.17	0.07	0.14	0.08	0.09				0.01		0.02		0.11				0.05
Sn				0.00					0.01			0.00		0.02	0.03				0.00	0.01	0.03
In		0.00	0.03	0.01	0.02	0.01						0.01	0.01		0.02	0.04	0.00	0.00	0.01	0.00	
Ag		0.02				0.01	0.02	0.02		0.01	0.02			0.04	0.01	0.01	0.03	0.02			0.03
Ga		0.10	0.05	0.06	0.14	0.05	0.16	0.07	0.01	0.10	0.04	0.18	0.08		0.05	0.08	0.09	0.07		0.15	0.06
S		50.27	50.96	50.25	51.14	51.04	51.10	51.31	50.35	50.49	49.92	50.29	50.45	49.96	51.02	50.91	50.56	50.65	50.21	50.93	50.05
Total		100.00	100.00	100.00	100.00	100.00	100.00	100.00	100.00	100.00	100.00	100.00	100.00	100.00	100.00	100.00	100.00	100.00	100.00	100.00	100.00
FeS		1.11	1.18	1.01	1.30	0.97	1.10	1.00	1.21	1.17	1.15	0.90	0.82	0.97	0.97	1.25	1.19	0.90	1.04	0.97	0.97
MnS		0.04	0.11	0.15	0.11	0.05	0.10	0.07	0.09	0.12	0.10	0.09	0.06	0.07	0.06	0.13	0.03	0.07	0.09	0.10	0.10
CdS		0.43	0.44	0.38	0.36	0.37	0.35	0.37	0.31	0.33	0.34	0.35	0.34	0.35	0.37	0.34	0.36	0.33	0.33	0.35	0.31

Sample Name		KTDH04 87.80m (C12)				KTDH04 92.05m (C15)														
Sample Point		C12-C3-14	C12-C3-15	C12-C3-16	C12-C3-17	C15-C1-1	C15-C1-2	C15-C1-3	C15-C1-4	C15-C1-5	C15-C1-6	C15-C1-7	C15-C1-8	C15-C1-9	C15-C1-10	C15-C1-11	C15-C1-12	C15-C1-13	C15-C1-14	C15-C1-15	C15-C1-16
Weight %	L.L.D. %																				
Zn	0.08	65.78	66.32	66.83	64.36	65.33	64.84	65.34	65.66	65.62	65.91	65.19	65.50	64.94	64.85	65.01	65.60	64.22	65.33	64.29	65.81
Fe	0.04	0.63	0.67	0.41	1.18	0.77	0.64	1.02	0.58	0.76	0.73	0.65	0.62	0.64	0.62	0.60	0.64	0.67	0.65	0.95	0.68
Mn	0.02	0.07	0.06	0.04	0.09	0.11	0.12	0.11	0.09	0.11	0.07	0.09	0.11	0.08	0.09	0.12	0.11	0.06	0.09	0.11	0.20
Cd	0.02	0.38	0.35	0.40	0.40	0.31	0.33	0.32	0.28	0.28	0.31	0.32	0.33	0.35	0.33	0.31	0.29	0.30	0.34	0.27	0.33
Cu	0.06	<0.06	<0.06	<0.06	0.72	<0.06	<0.06	0.52	0.11	0.16	<0.06	0.16	0.10	<0.06	<0.06	<0.06	<0.06	0.30	0.34	0.41	<0.06
Sn	0.04	<0.04	<0.04	<0.04	<0.04	<0.04	<0.04	0.06	<0.04	0.11	<0.04	<0.04	0.05	<0.04	<0.04	0.07	<0.04	<0.04	<0.04	<0.04	<0.04
In	0.04	<0.04	0.09	<0.04	<0.04	<0.04	<0.04	<0.04	<0.04	<0.04	<0.04	<0.04	<0.04	<0.04	<0.04	<0.04	<0.04	<0.04	<0.04	<0.04	<0.04
Ag	0.03	0.04	<0.03	0.04	<0.03	<0.03	0.09	<0.03	0.07	0.04	0.06	<0.03	<0.03	<0.03	0.08	0.05	<0.03	<0.03	0.05	<0.03	<0.03
Ga	0.02	0.09	0.18	0.03	0.06	0.18	0.07	0.06	0.10	0.11	0.10	0.20	0.11	<0.02	0.25	0.12	0.21	0.04	0.05	0.18	<0.02
S	0.02	33.69	33.58	34.18	33.77	33.05	33.70	33.44	33.51	34.18	34.42	32.85	33.74	33.77	33.13	33.42	33.53	32.94	33.01	33.81	33.52
Total		100.70	101.25	101.92	100.58	99.74	99.77	100.87	100.40	101.37	101.60	99.46	100.54	99.78	99.34	99.70	100.37	98.52	99.86	100.03	100.54
Atomic %																					
Zn		48.49	48.74	48.66	47.41	48.71	48.12	48.16	48.57	47.95	47.99	48.79	48.32	48.14	48.49	48.37	48.52	48.36	48.70	47.54	48.60
Fe		0.54	0.57	0.35	1.01	0.67	0.55	0.88	0.51	0.65	0.62	0.57	0.53	0.55	0.54	0.52	0.55	0.59	0.57	0.82	0.59
Mn		0.06	0.05	0.03	0.08	0.10	0.10	0.10	0.08	0.09	0.06	0.08	0.09	0.07	0.08	0.11	0.09	0.05	0.08	0.10	0.18
Cd		0.16	0.15	0.17	0.17	0.13	0.14	0.14	0.12	0.12	0.13	0.14	0.14	0.15	0.14	0.13	0.12	0.13	0.15	0.12	0.14
Cu				0.00	0.55	0.02		0.40	0.08	0.12	0.01	0.12	0.07	0.02	0.01	0.04		0.23	0.26	0.31	
Sn		0.01	0.01	0.00		0.00		0.02		0.05	0.00		0.02		0.02	0.03		0.01	0.02		
In		0.01	0.04	0.01						0.01		0.01		0.01				0.00			0.01
Ag		0.02	0.01	0.02	0.01	0.00	0.04		0.03	0.02	0.03			0.00	0.04	0.02	0.00	0.00	0.02	0.00	
Ga		0.06	0.12	0.02	0.04	0.12	0.05	0.04	0.07	0.07	0.07	0.14	0.08	0.00	0.18	0.08	0.15	0.03	0.03	0.13	0.01
S		50.64	50.31	50.74	50.73	50.24	51.00	50.26	50.54	50.92	51.09	50.14	50.74	51.04	50.51	50.70	50.57	50.58	50.17	50.98	50.47
Total		100.00	100.00	100.00	100.00	100.00	100.00	100.00	100.00	100.00	100.00	100.00	100.00	100.00	100.00	100.00	100.00	100.00	100.00	100.00	100.00
FeS		1.10	1.15	0.70	2.06	1.35	1.13	1.77	1.02	1.33	1.26	1.15	1.08	1.13	1.09	1.06	1.12	1.19	1.14	1.68	1.19
MnS		0.13	0.10	0.07	0.16	0.19	0.21	0.20	0.16	0.19	0.13	0.16	0.19	0.15	0.16	0.22	0.19	0.11	0.16	0.19	0.36
CdS		0.33	0.30	0.34	0.35	0.27	0.29	0.27	0.24	0.25	0.27	0.28	0.29	0.31	0.29	0.27	0.25	0.27	0.30	0.24	0.29

Sample Name		KTDH04 92.05m (C15)																		
Sample Point		C15-C1-17	C15-C1-18	C15-C1-19	C15-C2-1	C15-C2-2	C15-C2-3	C15-C2-4	C15-C2-5	C15-C2-6	C15-C2-7	C15-C2-8	C15-C2-9	C15-C2-10	C15-C2-11	C15-C2-12	C15-C2-13	C15-C2-14	C15-C2-15	C15-C2-16	C15-C3-1
Weight %	L.L.D. %																				
Zn	0.08	65.08	65.41	65.14	65.40	65.60	65.14	66.29	64.95	64.58	66.18	65.45	64.91	65.86	65.61	64.55	64.66	64.32	64.50	64.54	63.79
Fe	0.04	0.65	0.55	0.52	0.50	0.61	0.56	0.62	0.53	0.66	0.54	0.56	0.52	0.55	0.63	0.66	0.59	0.60	0.67	0.62	0.79
Mn	0.02	0.21	0.21	0.17	0.08	0.12	0.18	0.17	0.26	0.26	0.27	0.26	0.24	0.26	0.21	0.25	0.22	0.13	0.11	0.08	0.05
Cd	0.02	0.30	0.32	0.33	0.30	0.32	0.31	0.35	0.31	0.33	0.34	0.32	0.33	0.34	0.33	0.35	0.33	0.31	0.35	0.29	0.34
Cu	0.06	<0.06	<0.06	<0.06	<0.06	0.08	<0.06	<0.06	<0.06	<0.06	<0.06	<0.06	<0.06	<0.06	<0.06	<0.06	<0.06	0.08	0.23	0.17	0.25
Sn	0.04	<0.04	<0.04	<0.04	<0.04	<0.04	<0.04	<0.04	<0.04	<0.04	0.05	<0.04	<0.04	<0.04	<0.04	<0.04	<0.04	<0.04	<0.04	<0.04	<0.04
In	0.04	0.05	<0.04	<0.04	<0.04	<0.04	<0.04	<0.04	<0.04	<0.04	<0.04	<0.04	<0.04	<0.04	<0.04	0.06	<0.04	<0.04	<0.04	<0.04	0.10
Ag	0.03	<0.03	0.04	<0.03	<0.03	0.06	0.05	<0.03	<0.03	<0.03	<0.03	0.06	<0.03	0.03	<0.03	0.07	<0.03	0.07	<0.03	<0.03	<0.03
Ga	0.02	<0.02	0.14	0.20	0.09	0.11	0.16	0.09	0.20	0.15	0.10	0.12	0.30	0.02	0.17	0.16	<0.02	0.08	0.17	0.14	0.09
S	0.02	33.28	33.33	33.71	33.58	33.77	33.49	33.36	33.48	33.69	33.41	34.06	33.58	33.61	33.55	33.24	33.40	33.04	33.37	33.40	34.21
Total		99.57	100.00	100.07	99.94	100.66	99.89	100.88	99.71	99.68	100.90	100.83	99.88	100.67	100.50	99.33	99.19	98.62	99.40	99.24	99.61
Atomic %																					
Zn		48.48	48.57	48.20	48.50	48.33	48.37	48.91	48.29	47.93	48.81	48.05	48.16	48.57	48.46	48.22	48.29	48.38	48.11	48.17	47.20
Fe		0.57	0.48	0.45	0.43	0.52	0.49	0.54	0.46	0.57	0.47	0.48	0.45	0.47	0.55	0.57	0.51	0.53	0.59	0.54	0.68
Mn		0.19	0.19	0.15	0.07	0.10	0.16	0.15	0.23	0.23	0.23	0.23	0.22	0.23	0.19	0.22	0.20	0.11	0.10	0.07	0.05
Cd		0.13	0.14	0.14	0.13	0.14	0.14	0.15	0.13	0.14	0.15	0.14	0.14	0.15	0.14	0.15	0.14	0.14	0.15	0.12	0.14
Cu		0.04	0.04	0.04	0.03	0.06		0.01		0.03			0.01			0.04		0.06	0.18	0.13	0.19
Sn				0.00							0.02			0.01		0.00	0.00	0.01	0.00	0.01	
In		0.02				0.01	0.00				0.01		0.00		0.01	0.02		0.01		0.01	0.04
Ag		0.01	0.02	0.01		0.03	0.02					0.02	0.01	0.01	0.01	0.03		0.03	0.01		0.01
Ga			0.10	0.14	0.06	0.08	0.11	0.06	0.14	0.11	0.07	0.08	0.21	0.01	0.12	0.11		0.06	0.12	0.10	0.06
S		50.56	50.47	50.87	50.78	50.73	50.71	50.19	50.75	50.99	50.24	50.99	50.80	50.54	50.52	50.64	50.85	50.67	50.75	50.84	51.62
Total		100.00	100.00	100.00	100.00	100.00	100.00	100.00	100.00	100.00	100.00	100.00	100.00	100.00	100.00	100.00	100.00	100.00	100.00	100.00	100.00
FeS		1.15	0.97	0.92	0.88	1.06	0.99	1.08	0.93	1.16	0.94	0.98	0.91	0.96	1.10	1.16	1.04	1.07	1.20	1.11	1.41
MnS		0.38	0.37	0.31	0.14	0.20	0.32	0.30	0.46	0.47	0.47	0.47	0.44	0.46	0.38	0.44	0.40	0.23	0.20	0.14	0.10
CdS		0.26	0.28	0.29	0.26	0.28	0.28	0.30	0.27	0.29	0.30	0.28	0.29	0.29	0.29	0.31	0.29	0.27	0.31	0.25	0.30

Sample Name		KTDH04 92.05m (C15)																		
Sample Point		C15-C3-2	C15-C3-3	C15-C3-4	C15-C3-5	C15-C3-6	C15-C3-7	C15-C3-8	C15-C3-9	C15-C3-10	C15-C3-11	C15-C3-12	C15-C3-13	C15-C3-14	C15-C3-15	C15-C3-16	C15-C4-1	C15-C4-2	C15-C4-3	C15-C4-4	C15-C4-5
Weight %	L.L.D. %																				
Zn	0.08	63.89	65.78	64.84	64.99	65.24	65.14	64.41	65.71	65.26	65.65	65.89	66.04	65.98	65.16	64.71	65.79	65.39	64.87	66.09	66.18
Fe	0.04	0.54	0.62	0.52	0.49	0.59	0.76	0.72	0.58	0.54	0.58	0.55	0.49	0.51	0.44	0.68	0.77	0.82	0.75	0.59	0.60
Mn	0.02	0.11	0.10	0.17	0.17	0.16	0.11	0.09	0.20	0.21	0.19	0.13	0.12	0.07	0.04	0.08	0.05	0.07	0.12	0.23	0.18
Cd	0.02	0.31	0.29	0.30	0.33	0.36	0.26	0.29	0.30	0.35	0.31	0.31	0.30	0.29	0.32	0.30	0.31	0.31	0.33	0.31	0.27
Cu	0.06	<0.06	<0.06	<0.06	<0.06	<0.06	<0.06	0.35	<0.06	0.06	<0.06	<0.06	<0.06	<0.06	<0.06	0.37	0.64	0.39	0.34	0.08	<0.06
Sn	0.04	<0.04	<0.04	<0.04	<0.04	<0.04	<0.04	<0.04	<0.04	<0.04	<0.04	0.06	<0.04	<0.04	<0.04	<0.04	<0.04	<0.04	<0.04	<0.04	<0.04
In	0.04	<0.04	<0.04	<0.04	<0.04	<0.04	<0.04	0.07	0.06	<0.04	<0.04	<0.04	<0.04	<0.04	<0.04	<0.04	<0.04	<0.04	<0.04	<0.04	<0.04
Ag	0.03	0.05	<0.03	<0.03	<0.03	0.05	<0.03	<0.03	<0.03	<0.03	0.12	0.06	<0.03	<0.03	<0.03	<0.03	0.07	<0.03	<0.03	<0.03	<0.03
Ga	0.02	0.25	0.13	0.06	0.06	0.20	0.15	0.14	0.05	0.12	0.07	0.15	0.05	0.25	<0.02	0.07	0.03	0.16	0.09	<0.02	0.06
S	0.02	34.56	34.61	33.23	33.45	34.30	34.29	34.06	33.81	33.74	33.50	34.06	33.56	33.85	33.36	34.93	33.67	33.58	34.15	33.90	34.02
Total		99.70	101.54	99.12	99.49	100.90	100.70	100.13	100.70	100.29	100.42	101.22	100.57	100.94	99.33	101.13	101.32	100.72	100.65	101.20	101.30
Atomic %																					
Zn		47.11	47.82	48.50	48.42	47.80	47.75	47.53	48.37	48.22	48.55	48.24	48.77	48.46	48.64	47.09	48.26	48.21	47.64	48.44	48.40
Fe		0.46	0.53	0.45	0.42	0.51	0.65	0.62	0.50	0.47	0.50	0.47	0.43	0.44	0.38	0.58	0.66	0.71	0.64	0.50	0.51
Mn		0.09	0.09	0.15	0.15	0.14	0.09	0.08	0.17	0.18	0.17	0.11	0.11	0.06	0.04	0.06	0.04	0.06	0.11	0.20	0.16
Cd		0.13	0.12	0.13	0.14	0.15	0.11	0.12	0.13	0.15	0.13	0.13	0.13	0.12	0.14	0.13	0.13	0.13	0.14	0.13	0.12
Cu		0.04	0.04	0.01			0.04	0.27		0.05	0.02	0.03		0.04	0.01	0.27	0.48	0.29	0.26	0.06	0.03
Sn				0.01			0.01	0.00	0.02			0.03							0.00		
In				0.00		0.01		0.03	0.02			0.00	0.01		0.02		0.01	0.01		0.00	0.01
Ag		0.02	0.01			0.02				0.00	0.05	0.03		0.00			0.03		0.01	0.01	
Ga		0.17	0.09	0.04	0.04	0.14	0.10	0.10	0.03	0.09	0.05	0.11	0.03	0.17	0.00	0.05	0.02	0.11	0.06		0.04
S		51.96	51.30	50.69	50.82	51.24	51.25	51.25	50.76	50.84	50.52	50.85	50.53	50.70	50.77	51.82	50.36	50.48	51.14	50.66	50.73
Total		100.00	100.00	100.00	100.00	100.00	100.00	100.00	100.00	100.00	100.00	100.00	100.00	100.00	100.00	100.00	100.00	100.00	100.00	100.00	100.00
FeS		0.97	1.08	0.92	0.86	1.04	1.33	1.28	1.01	0.95	1.01	0.96	0.86	0.88	0.77	1.20	1.32	1.43	1.31	1.02	1.03
MnS		0.20	0.18	0.30	0.30	0.28	0.19	0.16	0.35	0.37	0.33	0.23	0.21	0.13	0.08	0.13	0.08	0.12	0.22	0.40	0.32
CdS		0.28	0.25	0.27	0.29	0.31	0.23	0.26	0.26	0.30	0.27	0.27	0.26	0.25	0.29	0.26	0.26	0.27	0.29	0.27	0.23

Sample Name		KTDH04 92.05m (C15)																		
Sample Point		C15-C4-6	C15-C4-7	C15-C4-8	C15-C4-9	C15-C4-10	C15-C4-11	C15-C4-12	C15-C4-13	C15-C4-14	C15-C4-15	C15-C4-16	C15-C4-17	C15-C4-18	C15-C5-1	C15-C5-2	C15-C5-3	C15-C5-4	C15-C5-5	C15-C5-6	C15-C5-7
Weight %	L.L.D. %																				
Zn	0.08	66.10	65.08	65.92	66.04	65.40	65.43	65.18	65.60	64.66	65.28	65.22	65.58	65.51	64.96	65.73	66.77	65.61	65.44	65.47	65.40
Fe	0.04	0.50	0.80	0.65	0.61	0.71	0.66	0.63	0.58	0.51	0.53	0.62	0.54	0.58	0.84	0.68	0.60	0.58	0.59	0.57	0.75
Mn	0.02	0.23	0.17	0.19	0.17	0.16	0.14	0.15	0.12	0.26	0.28	0.24	0.19	0.22	0.09	0.11	0.13	0.11	0.16	0.16	0.21
Cd	0.02	0.29	0.32	0.29	0.31	0.30	0.30	0.29	0.34	0.28	0.31	0.34	0.29	0.27	0.31	0.31	0.34	0.37	0.32	0.34	0.35
Cu	0.06	<0.06	0.25	0.13	<0.06	<0.06	<0.06	<0.06	0.10	0.08	<0.06	<0.06	0.13	<0.06	0.30	<0.06	0.11	<0.06	0.09	<0.06	0.11
Sn	0.04	<0.04	<0.04	<0.04	0.04	<0.04	<0.04	<0.04	<0.04	<0.04	<0.04	<0.04	0.06	<0.04	<0.04	0.05	<0.04	<0.04	<0.04	<0.04	<0.04
In	0.04	<0.04	<0.04	<0.04	<0.04	<0.04	0.07	<0.04	<0.04	<0.04	<0.04	<0.04	0.06	<0.04	<0.04	<0.04	<0.04	<0.04	<0.04	<0.04	<0.04
Ag	0.03	0.06	0.04	<0.03	0.04	<0.03	<0.03	0.04	<0.03	<0.03	<0.03	<0.03	0.06	<0.03	<0.03	<0.03	0.03	<0.03	0.07	<0.03	<0.03
Ga	0.02	0.14	0.04	0.08	0.12	0.02	0.19	0.09	0.11	0.08	<0.02	0.09	0.09	0.19	0.07	0.22	0.18	0.05	0.04	0.15	0.11
S	0.02	33.77	33.72	33.69	33.03	33.63	33.98	33.76	34.44	33.18	33.92	33.21	33.62	33.16	33.79	33.55	33.62	33.64	33.82	33.60	33.91
Total		101.07	100.42	100.94	100.36	100.24	100.76	100.14	101.29	99.04	100.31	99.72	100.62	99.92	100.36	100.64	101.77	100.35	100.54	100.29	100.82
Atomic %																					
Zn		48.55	48.04	48.48	49.05	48.36	48.09	48.19	47.87	48.42	48.15	48.57	48.41	48.74	47.94	48.51	48.86	48.49	48.24	48.43	48.06
Fe		0.43	0.69	0.56	0.53	0.62	0.57	0.55	0.50	0.45	0.45	0.54	0.47	0.51	0.73	0.59	0.51	0.50	0.51	0.49	0.64
Mn		0.20	0.15	0.16	0.15	0.14	0.12	0.13	0.11	0.24	0.24	0.22	0.17	0.19	0.08	0.09	0.11	0.10	0.14	0.14	0.18
Cd		0.12	0.14	0.12	0.14	0.13	0.13	0.12	0.14	0.12	0.13	0.15	0.12	0.12	0.13	0.13	0.14	0.16	0.14	0.14	0.15
Cu		0.01	0.19	0.10		0.02		0.04	0.07	0.06		0.03	0.09		0.23	0.01	0.08		0.07		0.08
Sn					0.02							0.00	0.02	0.00		0.02		0.01	0.01	0.00	
In		0.00					0.03						0.02			0.01		0.02	0.01		
Ag		0.03	0.02		0.02			0.02	0.00	0.01			0.03	0.01			0.01		0.03		
Ga		0.10	0.03	0.06	0.08	0.02	0.13	0.07	0.08	0.05	0.01	0.06	0.06	0.13	0.05	0.15	0.12	0.03	0.03	0.10	0.08
S		50.57	50.76	50.52	50.02	50.71	50.93	50.89	51.23	50.66	51.01	50.43	50.59	50.30	50.85	50.49	50.16	50.70	50.82	50.68	50.81
Total		100.00	100.00	100.00	100.00	100.00	100.00	100.00	100.00	100.00	100.00	100.00	100.00	100.00	100.00	100.00	100.00	100.00	100.00	100.00	100.00
FeS		0.88	1.40	1.13	1.06	1.25	1.15	1.12	1.02	0.91	0.93	1.09	0.95	1.02	1.48	1.19	1.03	1.01	1.04	1.00	1.30
MnS		0.40	0.30	0.33	0.30	0.29	0.25	0.26	0.22	0.48	0.50	0.44	0.34	0.38	0.16	0.19	0.23	0.20	0.29	0.28	0.37
CdS		0.25	0.28	0.25	0.27	0.26	0.26	0.25	0.29	0.25	0.27	0.29	0.25	0.23	0.27	0.26	0.29	0.32	0.28	0.29	0.30

Sample Name		KTDH04 92.05m (C15)						KTDH04 93.50m (C16)												
Sample Point		C15-C5-8	C15-C5-9	C15-C5-10	C15-C5-11	C15-C5-12	C15-C5-14	C16-C1-2	C16-C1-3	C16-C1-5	C16-C1-6	C16-C1-7	C16-C1-8	C16-C1-9	C16-C1-10	C16-C1-11	C16-C1-12	C16-C1-13	C16-C1-14	C16-C1-15	C16-C1-16
Weight %	L.L.D. %																				
Zn	0.08	65.21	64.98	65.83	65.45	65.66	65.90	65.63	65.11	66.43	65.17	65.17	64.84	65.12	64.63	65.60	65.50	66.72	65.75	65.09	65.31
Fe	0.04	0.61	0.52	0.59	0.60	0.72	0.60	0.70	0.66	0.56	0.61	0.65	0.75	0.55	0.73	0.60	0.54	0.49	0.50	0.59	0.60
Mn	0.02	0.23	0.29	0.25	0.20	0.19	0.10	0.06	0.07	0.05	0.06	0.13	0.10	0.09	0.11	0.07	0.12	0.16	0.11	0.13	0.10
Cd	0.02	0.36	0.29	0.30	0.34	0.33	0.30	0.36	0.32	0.32	0.30	0.31	0.33	0.34	0.35	0.29	0.31	0.37	0.30	0.35	0.38
Cu	0.06	0.10	<0.06	<0.06	<0.06	0.15	<0.06	<0.06	<0.06	<0.06	<0.06	<0.06	0.13	<0.06	<0.06	<0.06	<0.06	<0.06	<0.06	<0.06	<0.06
Sn	0.04	<0.04	<0.04	<0.04	<0.04	<0.04	<0.04	<0.04	<0.04	<0.04	0.09	<0.04	<0.04	<0.04	<0.04	<0.04	<0.04	<0.04	<0.04	<0.04	<0.04
In	0.04	<0.04	<0.04	0.04	<0.04	<0.04	<0.04	<0.04	0.06	0.06	<0.04	<0.04	<0.04	<0.04	<0.04	<0.04	<0.04	<0.04	<0.04	<0.04	<0.04
Ag	0.03	0.08	<0.03	<0.03	<0.03	0.04	<0.03	<0.03	<0.03	<0.03	<0.03	<0.03	<0.03	<0.03	0.05	<0.03	0.04	0.04	<0.03	0.08	<0.03
Ga	0.02	0.14	0.06	0.14	<0.02	0.13	0.11	0.21	0.20	0.09	0.04	0.05	0.26	0.19	0.15	0.02	0.15	0.08	<0.02	0.07	0.12
S	0.02	33.44	33.01	33.12	33.39	33.69	33.64	33.10	31.81	32.63	32.65	31.96	32.22	32.43	32.42	32.31	32.16	32.71	31.95	32.45	31.95
Total		100.16	99.15	100.27	99.98	100.91	100.64	100.06	98.22	100.14	98.91	98.27	98.63	98.72	98.46	98.88	98.81	100.57	98.61	98.74	98.47
Atomic %																					
Zn		48.35	48.67	48.87	48.59	48.31	48.58	48.80	49.61	49.56	49.08	49.56	49.07	49.19	48.92	49.52	49.54	49.61	49.87	49.16	49.59
Fe		0.53	0.46	0.51	0.52	0.62	0.52	0.61	0.59	0.48	0.54	0.57	0.67	0.49	0.65	0.53	0.47	0.43	0.44	0.52	0.54
Mn		0.21	0.26	0.22	0.18	0.17	0.09	0.06	0.06	0.05	0.05	0.12	0.09	0.08	0.10	0.06	0.10	0.14	0.10	0.12	0.09
Cd		0.15	0.13	0.13	0.15	0.14	0.13	0.16	0.14	0.14	0.13	0.14	0.15	0.15	0.16	0.13	0.14	0.16	0.13	0.15	0.17
Cu		0.07	0.03	0.02	0.01	0.11	0.04	0.04	0.00	0.02			0.10			0.03	0.01		0.04		0.04
Sn									0.01	0.01	0.04	0.01	0.01						0.01		0.00
In			0.00	0.02			0.00	0.00	0.02	0.03	0.01		0.00			0.00	0.01			0.01	0.02
Ag		0.04		0.01		0.02		0.01							0.02		0.02	0.02		0.04	
Ga		0.10	0.04	0.10		0.09	0.07	0.14	0.14	0.06	0.03	0.03	0.18	0.14	0.11	0.01	0.10	0.06		0.05	0.09
S		50.56	50.42	50.14	50.55	50.54	50.56	50.18	49.42	49.64	50.13	49.56	49.73	49.95	50.04	49.73	49.60	49.59	49.41	49.97	49.47
Total		100.00	100.00	100.00	100.00	100.00	100.00	100.00	100.00	100.00	100.00	100.00	100.00	100.00	100.00	100.00	100.00	100.00	100.00	100.00	100.00
FeS		1.06	0.93	1.02	1.06	1.26	1.05	1.22	1.16	0.96	1.08	1.14	1.32	0.98	1.30	1.05	0.94	0.85	0.88	1.03	1.06
MnS		0.42	0.52	0.44	0.36	0.34	0.18	0.11	0.13	0.10	0.10	0.23	0.18	0.17	0.20	0.12	0.21	0.28	0.19	0.24	0.18
CdS		0.31	0.26	0.26	0.30	0.29	0.26	0.31	0.28	0.28	0.27	0.27	0.29	0.30	0.31	0.25	0.27	0.32	0.27	0.30	0.33

Sample Name		KTDH04 93.50m (C16)																		
Sample Point		C16-C1-17	C16-C2-1	C16-C2-2	C16-C2-3	C16-C2-5	C16-C2-6	C16-C2-7	C16-C2-8	C16-C2-9	C16-C2-10	C16-C2-11	C16-C2-12	C16-C2-13	C16-C2-14	C16-C2-15	C16-C2-16	C16-C2-17	C16-C2-18	C16-C2-19	C16-C3-1
Weight %	L.L.D. %																				
Zn	0.08	65.98	65.14	64.90	65.90	65.94	64.81	65.62	65.39	65.23	66.23	65.84	65.46	65.39	65.54	65.37	66.21	65.92	66.60	65.01	66.15
Fe	0.04	0.41	0.65	0.58	0.65	0.73	0.48	0.58	0.58	0.48	0.65	0.59	0.62	0.60	0.51	0.52	0.52	0.56	0.60	0.62	0.67
Mn	0.02	0.05	0.09	0.15	0.23	0.29	0.32	0.31	0.31	0.28	0.32	0.30	0.32	0.25	0.23	0.19	0.19	0.17	0.18	0.20	0.15
Cd	0.02	0.33	0.29	0.30	0.31	0.34	0.32	0.32	0.36	0.30	0.31	0.35	0.33	0.39	0.33	0.32	0.33	0.33	0.33	0.34	0.34
Cu	0.06	<0.06	<0.06	<0.06	<0.06	0.10	<0.06	0.07	<0.06	<0.06	<0.06	<0.06	<0.06	<0.06	<0.06	<0.06	<0.06	<0.06	<0.06	<0.06	<0.06
Sn	0.04	<0.04	<0.04	0.09	<0.04	<0.04	<0.04	<0.04	<0.04	0.07	<0.04	<0.04	<0.04	<0.04	<0.04	0.08	<0.04	<0.04	<0.04	<0.04	<0.04
In	0.04	0.05	<0.04	<0.04	<0.04	<0.04	<0.04	0.08	<0.04	<0.04	<0.04	<0.04	<0.04	<0.04	0.07	<0.04	<0.04	0.05	<0.04	<0.04	<0.04
Ag	0.03	<0.03	<0.03	<0.03	<0.03	0.04	0.03	<0.03	<0.03	<0.03	<0.03	<0.03	0.06	<0.03	<0.03	0.06	<0.03	<0.03	0.07	0.07	<0.03
Ga	0.02	0.17	0.05	0.08	0.03	0.07	0.08	0.17	0.09	0.16	0.15	0.02	0.07	0.13	0.10	0.20	0.05	0.06	0.22	0.15	0.08
S	0.02	32.34	32.18	32.13	32.43	32.36	32.41	32.45	32.28	32.19	31.93	32.30	32.95	32.52	32.22	32.01	32.84	32.29	32.58	31.65	32.02
Total		99.33	98.39	98.22	99.56	99.86	98.47	99.60	99.00	98.69	99.59	99.40	99.80	99.28	99.00	98.75	100.15	99.37	100.58	98.04	99.41
Atomic %																					
Zn		49.67	49.39	49.33	49.45	49.39	49.05	49.23	49.33	49.36	49.87	49.51	48.81	49.14	49.49	49.55	49.31	49.60	49.54	49.65	49.86
Fe		0.36	0.58	0.52	0.57	0.64	0.42	0.51	0.51	0.42	0.57	0.52	0.54	0.53	0.45	0.46	0.45	0.49	0.52	0.55	0.59
Mn		0.04	0.08	0.14	0.21	0.26	0.29	0.27	0.28	0.25	0.29	0.27	0.28	0.22	0.21	0.17	0.17	0.15	0.16	0.18	0.13
Cd		0.15	0.13	0.13	0.14	0.15	0.14	0.14	0.16	0.13	0.14	0.15	0.14	0.17	0.15	0.14	0.14	0.14	0.14	0.15	0.15
Cu			0.04			0.08		0.05		0.03			0.03				0.01		0.03	0.03	
Sn				0.04						0.03	0.00		0.01	0.01	0.01	0.03		0.00		0.01	
In		0.02			0.01	0.00	0.00	0.04			0.00		0.01		0.03		0.01	0.02			
Ag					0.00	0.02	0.02		0.00	0.01		0.01	0.03		0.00	0.03		0.01	0.03	0.03	
Ga		0.12	0.03	0.06	0.02	0.05	0.06	0.12	0.06	0.11	0.11	0.02	0.05	0.09	0.07	0.14	0.04	0.05	0.15	0.11	0.05
S		49.63	49.76	49.79	49.60	49.42	50.02	49.64	49.66	49.66	49.02	49.52	50.10	49.84	49.60	49.48	49.87	49.54	49.42	49.29	49.21
Total		100.00	100.00	100.00	100.00	100.00	100.00	100.00	100.00	100.00	100.00	100.00	100.00	100.00	100.00	100.00	100.00	100.00	100.00	100.00	100.00
FeS		0.72	1.15	1.03	1.13	1.26	0.85	1.02	1.01	0.84	1.12	1.03	1.08	1.05	0.89	0.91	0.90	0.98	1.03	1.08	1.17
MnS		0.09	0.17	0.27	0.41	0.51	0.58	0.55	0.56	0.50	0.56	0.54	0.56	0.45	0.41	0.35	0.34	0.29	0.32	0.36	0.26
CdS		0.29	0.25	0.26	0.27	0.29	0.29	0.28	0.31	0.26	0.27	0.30	0.28	0.34	0.29	0.28	0.29	0.28	0.29	0.30	0.29

Sample Name		KTDH04 93.50m (C16)									KTDH04 93.85m (C17)										
Sample Point		C16-C3-3	C16-C3-4	C16-C3-5	C16-C3-6	C16-C3-7	C16-C3-8	C16-C3-9	C16-C3-11	C16-C3-12	C17-C1-1	C17-C1-2	C17-C1-3	C17-C1-4	C17-C1-5	C17-C1-6	C17-C1-7	C17-C1-8	C17-C1-9	C17-C1-10	C17-C1-12
Weight %	L.L.D. %																				
Zn	0.08	65.33	65.69	65.38	65.68	65.85	65.82	66.06	65.34	65.44	64.61	63.23	63.58	64.32	64.63	64.48	63.40	64.80	63.35	65.19	64.47
Fe	0.04	0.60	0.55	0.66	0.59	0.49	0.46	0.52	0.48	0.60	0.60	1.05	0.71	0.76	0.68	0.87	1.04	0.73	0.95	0.73	0.58
Mn	0.02	0.21	0.22	0.13	0.16	0.29	0.30	0.29	0.27	0.16	0.13	0.08	0.11	0.09	0.07	0.07	0.07	0.07	0.13	0.10	0.15
Cd	0.02	0.31	0.34	0.32	0.33	0.36	0.31	0.37	0.33	0.33	0.36	0.32	0.31	0.35	0.30	0.32	0.30	0.30	0.35	0.35	0.33
Cu	0.06	<0.06	<0.06	<0.06	<0.06	<0.06	<0.06	<0.06	<0.06	<0.06	<0.06	0.34	0.33	<0.06	<0.06	0.41	0.84	<0.06	0.46	<0.06	<0.06
Sn	0.04	<0.04	<0.04	<0.04	<0.04	<0.04	<0.04	<0.04	<0.04	<0.04	<0.04	<0.04	<0.04	<0.04	<0.04	0.10	0.05	0.07	<0.04	<0.04	0.07
In	0.04	<0.04	<0.04	0.05	<0.04	<0.04	<0.04	<0.04	0.05	0.06	<0.04	<0.04	<0.04	<0.04	<0.04	<0.04	<0.04	<0.04	<0.04	<0.04	0.06
Ag	0.03	<0.03	0.09	0.09	0.05	<0.03	0.05	<0.03	<0.03	0.08	<0.03	<0.03	<0.03	<0.03	<0.03	<0.03	<0.03	<0.03	0.05	<0.03	0.03
Ga	0.02	0.12	0.09	0.09	0.17	0.19	<0.02	0.19	0.07	0.22	0.08	0.11	0.06	0.23	0.08	0.03	0.03	0.14	0.06	0.13	0.08
S	0.02	31.78	31.66	31.85	32.42	31.99	32.32	32.39	31.53	31.76	33.70	33.35	33.79	33.11	33.25	33.44	32.83	33.26	32.75	31.83	33.00
Total		98.34	98.63	98.58	99.40	99.16	99.26	99.81	98.08	98.66	99.49	98.47	98.88	98.85	99.01	99.73	98.55	99.38	98.09	98.32	98.76
Atomic %																					
Zn		49.72	49.93	49.67	49.36	49.74	49.55	49.50	49.96	49.73	48.04	47.47	47.44	48.27	48.39	47.95	47.76	48.39	47.94	49.61	48.49
Fe		0.53	0.49	0.59	0.52	0.43	0.40	0.45	0.43	0.53	0.53	0.92	0.62	0.66	0.59	0.76	0.92	0.64	0.84	0.65	0.51
Mn		0.19	0.20	0.12	0.14	0.26	0.27	0.26	0.24	0.15	0.12	0.07	0.09	0.08	0.06	0.06	0.06	0.06	0.11	0.09	0.13
Cd		0.14	0.15	0.14	0.14	0.16	0.14	0.16	0.15	0.14	0.16	0.14	0.13	0.15	0.13	0.14	0.13	0.13	0.15	0.15	0.14
Cu			0.04							0.01	0.00	0.26	0.25	0.00		0.32	0.65	0.00	0.35		
Sn		0.01	0.00	0.01		0.01	0.00					0.01				0.04	0.02	0.03		0.01	0.03
In		0.01	0.01	0.02	0.01				0.02	0.03	0.00	0.00	0.01	0.01	0.01	0.01	0.01				0.03
Ag			0.04	0.04	0.02	0.01	0.02	0.01	0.01	0.04			0.01		0.01				0.02	0.01	0.01
Ga		0.08	0.06	0.07	0.12	0.13		0.13	0.05	0.16	0.06	0.08	0.04	0.16	0.05	0.02	0.02	0.10	0.04	0.09	0.06
S		49.32	49.07	49.34	49.68	49.27	49.62	49.48	49.14	49.21	51.10	51.05	51.40	50.66	50.75	50.71	50.42	50.64	50.54	49.39	50.60
Total		100.00	100.00	100.00	100.00	100.00	100.00	100.00	100.00	100.00	100.00	100.00	100.00	100.00	100.00	100.00	100.00	100.00	100.00	100.00	100.00
FeS		1.05	0.96	1.16	1.04	0.86	0.80	0.89	0.84	1.05	1.08	1.89	1.28	1.34	1.21	1.54	1.85	1.30	1.69	1.29	1.03
MnS		0.38	0.38	0.24	0.29	0.50	0.54	0.51	0.47	0.29	0.24	0.15	0.19	0.17	0.13	0.13	0.12	0.13	0.23	0.17	0.26
CdS		0.27	0.29	0.28	0.29	0.31	0.27	0.32	0.29	0.28	0.32	0.28	0.28	0.31	0.27	0.28	0.27	0.27	0.31	0.30	0.29

Sample Name		KTDH04 93.85m (C17)																		
Sample Point		C17-C1-13	C17-C1-14	C17-C2-1	C17-C2-2	C17-C2-3	C17-C2-4	C17-C2-5	C17-C2-6	C17-C2-7	C17-C2-8	C17-C2-9	C17-C2-12	C17-C2-13	C17-C2-14	C17-C2-15	C17-C2-16	C17-C2-17	C17-C3-1	C17-C3-2	C17-C3-3
Weight %	L.L.D. %																				
Zn	0.08	64.87	64.25	64.19	64.77	64.60	65.40	63.94	64.97	64.48	64.66	64.75	63.48	64.14	65.27	64.56	65.24	64.82	65.35	65.97	65.93
Fe	0.04	0.61	0.50	0.64	0.60	0.54	0.56	0.44	0.52	0.52	0.54	0.51	1.10	0.58	0.49	0.57	0.63	0.69	0.66	0.66	0.72
Mn	0.02	0.11	0.11	0.10	0.12	0.21	0.27	0.24	0.26	0.20	0.24	0.19	0.09	0.13	0.21	0.18	0.15	0.11	0.07	0.12	0.15
Cd	0.02	0.32	0.31	0.29	0.32	0.32	0.32	0.32	0.32	0.34	0.32	0.31	0.30	0.33	0.34	0.36	0.32	0.32	0.38	0.35	0.32
Cu	0.06	<0.06	0.07	0.06	<0.06	0.08	<0.06	<0.06	0.11	0.06	<0.06	0.07	0.43	0.07	<0.06	<0.06	0.06	<0.06	<0.06	<0.06	<0.06
Sn	0.04	<0.04	<0.04	<0.04	<0.04	0.10	<0.04	<0.04	<0.04	<0.04	<0.04	<0.04	<0.04	<0.04	<0.04	<0.04	<0.04	<0.04	<0.04	<0.04	<0.04
In	0.04	<0.04	0.04	<0.04	<0.04	0.10	<0.04	<0.04	<0.04	<0.04	<0.04	<0.04	<0.04	0.09	<0.04	<0.04	<0.04	<0.04	<0.04	<0.04	<0.04
Ag	0.03	0.04	0.03	<0.03	<0.03	<0.03	<0.03	<0.03	<0.03	<0.03	<0.03	<0.03	<0.03	<0.03	<0.03	0.08	<0.03	<0.03	<0.03	<0.03	<0.03
Ga	0.02	<0.02	0.22	0.09	0.23	0.04	0.14	0.25	0.23	0.11	0.09	0.02	0.10	0.08	0.03	0.15	0.11	0.17	0.14	<0.02	0.09
S	0.02	32.46	33.20	32.88	33.07	32.64	32.62	32.82	33.05	32.30	32.75	32.61	33.08	32.67	33.12	32.77	33.25	33.05	32.78	33.33	33.01
Total		98.41	98.74	98.27	99.11	98.63	99.32	98.02	99.47	98.01	98.59	98.47	98.58	98.09	99.46	98.67	99.76	99.17	99.38	100.43	100.22
Atomic %																					
Zn		49.09	48.25	48.46	48.54	48.77	49.09	48.40	48.55	49.02	48.74	48.92	47.71	48.60	48.74	48.65	48.57	48.54	48.99	48.84	49.00
Fe		0.54	0.44	0.57	0.52	0.48	0.49	0.39	0.46	0.46	0.48	0.45	0.97	0.52	0.43	0.51	0.55	0.61	0.58	0.57	0.63
Mn		0.10	0.09	0.09	0.11	0.19	0.24	0.22	0.23	0.18	0.21	0.17	0.08	0.12	0.18	0.16	0.13	0.10	0.06	0.11	0.13
Cd		0.14	0.14	0.13	0.14	0.14	0.14	0.14	0.14	0.15	0.14	0.14	0.13	0.15	0.15	0.16	0.14	0.14	0.17	0.15	0.14
Cu		0.02	0.05	0.05		0.07			0.08	0.05	0.04	0.05	0.33	0.05	0.04	0.03	0.05	0.03		0.01	0.02
Sn						0.04	0.00		0.01			0.01	0.01			0.01					
In			0.02	0.02		0.04								0.04	0.00		0.01		0.00		
Ag		0.02	0.02					0.01				0.00		0.01		0.04			0.01	0.01	
Ga		0.01	0.15	0.06	0.16	0.03	0.10	0.18	0.16	0.08	0.06	0.02	0.07	0.06	0.02	0.11	0.08	0.12	0.09		0.06
S		50.08	50.84	50.62	50.53	50.24	49.93	50.65	50.36	50.06	50.33	50.23	50.69	50.46	50.43	50.35	50.47	50.46	50.10	50.31	50.02
Total		100.00	100.00	100.00	100.00	100.00	100.00	100.00	100.00	100.00	100.00	100.00	100.00	100.00	100.00	100.00	100.00	100.00	100.00	100.00	100.00
FeS		1.08	0.90	1.15	1.06	0.96	0.98	0.79	0.92	0.93	0.96	0.90	1.96	1.04	0.87	1.02	1.11	1.23	1.16	1.16	1.25
MnS		0.20	0.19	0.19	0.22	0.38	0.49	0.44	0.47	0.37	0.43	0.35	0.17	0.23	0.37	0.32	0.26	0.21	0.13	0.21	0.26
CdS		0.28	0.28	0.26	0.28	0.28	0.28	0.29	0.28	0.30	0.28	0.28	0.27	0.30	0.29	0.32	0.28	0.28	0.34	0.30	0.28

Sample Name		KTDH04 93.85m (C17)													KTDH04 114.80m (C28)						
Sample Point		C17-C3-4	C17-C3-5	C17-C3-6	C17-C3-7	C17-C3-8	C17-C3-9	C17-C3-10	C17-C3-11	C17-C3-12	C17-C3-13	C17-C3-14	C17-C3-15	C17-C3-16	C28-C1-1	C28-C1-3	C28-C1-4	C28-C1-5	C28-C1-6	C28-C1-8	C28-C1-9
Weight %	L.L.D. %																				
Zn	0.08	64.84	64.89	64.53	65.57	64.71	65.84	65.34	64.70	65.17	64.82	65.53	65.41	64.87	64.99	65.23	65.80	65.99	65.74	65.57	66.16
Fe	0.04	0.61	0.52	0.57	0.50	0.55	0.47	0.59	0.44	0.49	0.71	0.61	0.52	0.76	0.69	0.80	0.83	0.78	0.58	0.72	0.70
Mn	0.02	0.20	0.28	0.26	0.29	0.26	0.30	0.29	0.26	0.28	0.25	0.23	0.17	0.15	0.08	0.13	0.15	0.17	0.12	0.06	0.04
Cd	0.02	0.35	0.30	0.34	0.29	0.33	0.30	0.32	0.36	0.31	0.29	0.30	0.32	0.33	0.20	0.23	0.24	0.21	0.19	0.25	0.25
Cu	0.06	<0.06	<0.06	<0.06	0.07	<0.06	<0.06	<0.06	<0.06	0.12	<0.06	<0.06	<0.06	<0.06	0.37	0.11	0.16	<0.06	<0.06	<0.06	<0.06
Sn	0.04	<0.04	<0.04	<0.04	<0.04	<0.04	<0.04	<0.04	<0.04	<0.04	<0.04	<0.04	<0.04	<0.04	<0.04	<0.04	<0.04	<0.04	<0.04	<0.04	<0.04
In	0.04	<0.04	<0.04	<0.04	0.04	<0.04	<0.04	<0.04	0.11	<0.04	0.07	<0.04	<0.04	0.11	<0.04	<0.04	<0.04	<0.04	<0.04	<0.04	<0.04
Ag	0.03	<0.03	<0.03	0.05	<0.03	<0.03	<0.03	<0.03	<0.03	<0.03	<0.03	0.06	<0.03	0.05	0.06	<0.03	<0.03	0.10	<0.03	<0.03	0.08
Ga	0.02	0.03	<0.02	0.22	0.11	0.23	0.05	0.07	0.11	0.15	<0.02	0.21	0.21	0.12	0.20	0.10	0.26	<0.02	0.19	0.07	0.13
S	0.02	33.58	32.39	32.65	32.55	32.75	32.88	32.92	32.84	32.89	33.19	33.54	32.85	32.39	31.46	32.43	31.76	32.41	31.37	32.06	32.37
Total		99.61	98.38	98.61	99.41	98.83	99.85	99.52	98.82	99.41	99.33	100.46	99.48	98.78	98.05	99.04	99.20	99.65	98.19	98.73	99.71
Atomic %																					
Zn		48.19	49.11	48.69	49.21	48.70	49.12	48.85	48.70	48.78	48.43	48.43	48.96	49.00	49.69	49.11	49.75	49.48	50.24	49.65	49.60
Fe		0.53	0.46	0.50	0.44	0.49	0.41	0.51	0.39	0.43	0.62	0.53	0.46	0.67	0.62	0.71	0.74	0.68	0.52	0.64	0.61
Mn		0.18	0.25	0.24	0.26	0.24	0.27	0.26	0.23	0.25	0.22	0.20	0.15	0.13	0.07	0.12	0.14	0.15	0.10	0.05	0.03
Cd		0.15	0.13	0.15	0.12	0.15	0.13	0.14	0.16	0.14	0.13	0.13	0.14	0.15	0.09	0.10	0.10	0.09	0.09	0.11	0.11
Cu		0.04	0.03		0.05	0.02				0.09					0.29	0.09	0.12		0.04	0.01	0.04
Sn			0.02							0.00	0.01			0.01			0.00			0.00	
In				0.02	0.02		0.01		0.05	0.01	0.03			0.05	0.01	0.02					0.01
Ag		0.00		0.02				0.00	0.01	0.01		0.03	0.01	0.02	0.03			0.04			0.04
Ga		0.02	0.01	0.16	0.08	0.16	0.04	0.05	0.08	0.10	0.01	0.14	0.15	0.08	0.15	0.07	0.18		0.13	0.05	0.09
S		50.89	49.99	50.23	49.81	50.25	50.02	50.18	50.39	50.20	50.56	50.54	50.14	49.89	49.05	49.79	48.96	49.55	48.88	49.49	49.48
Total		100.00	100.00	100.00	100.00	100.00	100.00	100.00	100.00	100.00	100.00	100.00	100.00	100.00	100.00	100.00	100.00	100.00	100.00	100.00	100.00
FeS		1.08	0.92	1.00	0.88	0.98	0.81	1.03	0.79	0.85	1.25	1.06	0.92	1.34	1.22	1.41	1.44	1.35	1.02	1.27	1.21
MnS		0.36	0.50	0.47	0.52	0.48	0.53	0.52	0.47	0.50	0.44	0.40	0.30	0.26	0.14	0.23	0.27	0.30	0.20	0.10	0.07
CdS		0.31	0.26	0.30	0.25	0.29	0.26	0.28	0.31	0.27	0.25	0.26	0.28	0.29	0.18	0.20	0.20	0.18	0.17	0.22	0.21

Sample Name		KTDH04 114.80m (C28)																		
Sample Point		C28-C1-11	C28-C1-12	C28-C1-13	C28-C1-14	C28-C1-15	C28-C1-16	C28-C1-17	C28-C1-18	C28-C1-19	C28-C1-20	C28-C1-21	C28-C1-22	C28-C1-23	C28-C1-24	C28-C1-25	C28-C1-26	C28-C1-27	C28-C1-28	C28-C1-29	C28-C1-30
Weight %	L.L.D. %																				
Zn	0.08	65.19	66.09	65.87	65.45	65.64	64.82	65.15	66.14	65.60	65.82	64.58	65.03	64.63	65.75	65.70	65.67	65.16	66.06	66.26	65.90
Fe	0.04	0.86	0.73	0.77	0.71	0.80	0.86	0.74	0.76	0.79	0.86	0.89	0.74	0.88	0.74	0.66	0.58	0.67	0.66	0.63	0.70
Mn	0.02	0.04	0.03	0.07	0.07	0.05	0.05	<0.02	<0.02	<0.02	0.02	0.04	0.07	0.04	0.04	<0.02	0.06	0.07	0.04	0.09	0.05
Cd	0.02	0.18	0.16	0.22	0.25	0.21	0.18	0.22	0.20	0.24	0.23	0.15	0.21	0.19	0.17	0.21	0.20	0.18	0.22	0.28	0.22
Cu	0.06	<0.06	<0.06	0.08	<0.06	<0.06	<0.06	0.10	<0.06	<0.06	<0.06	0.11	<0.06	<0.06	0.10	<0.06	<0.06	0.12	<0.06	<0.06	<0.06
Sn	0.04	<0.04	<0.04	<0.04	<0.04	<0.04	<0.04	0.04	0.04	0.08	<0.04	<0.04	<0.04	<0.04	<0.04	<0.04	<0.04	<0.04	<0.04	<0.04	0.04
In	0.04	<0.04	<0.04	0.07	<0.04	<0.04	<0.04	0.10	<0.04	<0.04	<0.04	<0.04	0.06	<0.04	<0.04	<0.04	<0.04	<0.04	<0.04	<0.04	<0.04
Ag	0.03	<0.03	<0.03	<0.03	<0.03	0.07	<0.03	0.06	<0.03	<0.03	<0.03	0.06	<0.03	<0.03	<0.03	<0.03	<0.03	0.07	0.05	0.05	<0.03
Ga	0.02	0.06	0.09	0.14	0.18	0.15	0.12	0.13	0.09	0.22	0.16	0.13	0.20	0.22	0.06	0.06	0.09	0.15	0.09	0.05	0.13
S	0.02	32.42	33.07	33.20	33.26	32.69	33.01	32.68	33.87	33.16	33.47	32.58	33.43	33.25	33.80	33.41	32.81	33.12	33.19	32.81	33.54
Total		98.76	100.17	100.42	99.92	99.60	99.05	99.23	101.10	100.09	100.56	98.54	99.74	99.21	100.64	100.03	99.41	99.54	100.31	100.18	100.59
Atomic %																					
Zn		49.18	49.11	48.82	48.66	49.14	48.58	48.94	48.51	48.76	48.61	48.75	48.36	48.29	48.40	48.73	49.17	48.64	49.01	49.35	48.63
Fe		0.76	0.63	0.67	0.62	0.70	0.76	0.65	0.66	0.69	0.74	0.79	0.64	0.77	0.63	0.57	0.51	0.59	0.58	0.55	0.61
Mn		0.04	0.03	0.06	0.07	0.04	0.05	0.01	0.02	0.01	0.02	0.04	0.06	0.04	0.03		0.06	0.06	0.03	0.08	0.05
Cd		0.08	0.07	0.09	0.11	0.09	0.08	0.10	0.08	0.10	0.10	0.07	0.09	0.08	0.07	0.09	0.09	0.08	0.09	0.12	0.10
Cu		0.03		0.06				0.08			0.00	0.08			0.08	0.02	0.03	0.09			0.04
Sn			0.00			0.00	0.01	0.02	0.02	0.03	0.01			0.00			0.01				0.02
In				0.03			0.00	0.04			0.01	0.01	0.03		0.01	0.02				0.01	0.01
Ag			0.00		0.01	0.03	0.00	0.03				0.03			0.00			0.03	0.02	0.02	
Ga		0.05	0.07	0.10	0.13	0.10	0.09	0.09	0.06	0.15	0.11	0.09	0.14	0.15	0.04	0.04	0.06	0.10	0.06	0.04	0.09
S		49.87	50.09	50.17	50.41	49.89	50.44	50.05	50.66	50.26	50.40	50.15	50.68	50.66	50.73	50.53	50.08	50.41	50.21	49.83	50.46
Total		100.00	100.00	100.00	100.00	100.00	100.00	100.00	100.00	100.00	100.00	100.00	100.00	100.00	100.00	100.00	100.00	100.00	100.00	100.00	100.00
FeS		1.52	1.26	1.34	1.24	1.40	1.53	1.30	1.33	1.38	1.50	1.58	1.30	1.56	1.29	1.16	1.02	1.18	1.16	1.09	1.22
MnS		0.07	0.06	0.12	0.13	0.08	0.09	0.02	0.03	0.02	0.04	0.07	0.13	0.07	0.07	0.00	0.11	0.12	0.07	0.16	0.09
CdS		0.16	0.14	0.19	0.22	0.19	0.16	0.20	0.17	0.21	0.20	0.13	0.18	0.17	0.14	0.18	0.18	0.16	0.19	0.25	0.19

Sample Name		KTDH04 114.80m (C28)																		
Sample Point		C28-C1-31	C28-C1-32	C28-C1-33	C28-C1-34	C28-C1-35	C28-C1-36	C28-C1-37	C28-C1-38	C28-C1-39	C28-C1-40	C28-C1-42	C28-C2-1	C28-C2-2	C28-C2-3	C28-C2-4	C28-C2-5	C28-C2-6	C28-C2-7	C28-C2-8	C28-C2-9
Weight %	L.L.D. %																				
Zn	0.08	65.01	65.66	66.12	66.20	65.22	65.80	65.20	65.75	65.78	65.61	64.74	65.56	65.90	64.36	65.56	65.51	65.33	65.77	65.82	65.78
Fe	0.04	0.66	0.79	0.75	0.82	0.82	0.63	0.77	0.91	0.90	0.79	0.77	0.76	0.80	1.48	0.83	0.83	0.85	0.82	0.77	0.73
Mn	0.02	0.05	0.09	0.07	0.06	0.07	0.08	0.09	0.07	0.06	0.07	0.05	0.20	0.24	0.23	0.26	0.23	0.23	0.20	0.21	0.18
Cd	0.02	0.20	0.21	0.21	0.17	0.18	0.16	0.15	0.14	0.13	0.17	0.28	0.22	0.22	0.24	0.21	0.23	0.22	0.25	0.25	0.23
Cu	0.06	<0.06	0.34	0.16	0.19	<0.06	0.23	0.26	<0.06	0.17	<0.06	0.34	<0.06	<0.06	0.59	<0.06	<0.06	<0.06	<0.06	<0.06	0.07
Sn	0.04	<0.04	<0.04	<0.04	<0.04	<0.04	<0.04	<0.04	<0.04	<0.04	<0.04	0.08	<0.04	<0.04	<0.04	<0.04	<0.04	<0.04	<0.04	<0.04	<0.04
In	0.04	<0.04	<0.04	0.05	<0.04	<0.04	<0.04	0.08	<0.04	<0.04	<0.04	<0.04	<0.04	<0.04	<0.04	<0.04	<0.04	<0.04	<0.04	<0.04	<0.04
Ag	0.03	<0.03	<0.03	<0.03	<0.03	<0.03	<0.03	<0.03	<0.03	<0.03	0.06	<0.03	<0.03	<0.03	<0.03	0.04	<0.03	<0.03	<0.03	<0.03	0.06
Ga	0.02	0.21	0.11	0.15	0.18	0.05	0.12	0.16	0.17	0.28	0.11	0.16	0.17	0.19	0.21	0.20	0.15	0.09	0.17	0.20	0.06
S	0.02	33.30	33.10	33.30	33.13	32.79	33.60	32.50	32.88	32.76	33.02	32.35	33.30	33.40	33.56	33.17	33.08	31.96	33.39	33.14	32.65
Total		99.42	100.30	100.80	100.74	99.14	100.62	99.21	99.92	100.07	99.82	98.77	100.21	100.75	100.66	100.27	100.03	98.69	100.61	100.39	99.76
Atomic %																					
Zn		48.49	48.73	48.82	48.95	48.91	48.52	49.01	48.99	49.01	48.89	48.90	48.59	48.61	47.41	48.63	48.68	49.49	48.59	48.80	49.19
Fe		0.57	0.68	0.64	0.71	0.72	0.55	0.68	0.79	0.79	0.69	0.68	0.66	0.69	1.28	0.72	0.72	0.76	0.71	0.67	0.64
Mn		0.04	0.08	0.06	0.06	0.07	0.07	0.08	0.06	0.05	0.07	0.05	0.18	0.21	0.20	0.23	0.20	0.21	0.18	0.18	0.16
Cd		0.09	0.09	0.09	0.07	0.08	0.07	0.06	0.06	0.06	0.07	0.12	0.09	0.10	0.10	0.09	0.10	0.10	0.11	0.11	0.10
Cu		0.01	0.26	0.12	0.14	0.03	0.17	0.20	0.02	0.13	0.03	0.27	0.03	0.01	0.44		0.04		0.00	0.01	0.05
Sn			0.00	0.01			0.01		0.01			0.03	0.01								
In				0.02				0.03				0.01	0.00	0.01	0.01		0.02				
Ag					0.01	0.01	0.00	0.00		0.01	0.03				0.00	0.02	0.01	0.01			0.03
Ga		0.14	0.07	0.11	0.13	0.04	0.08	0.11	0.12	0.20	0.07	0.11	0.11	0.13	0.14	0.14	0.10	0.06	0.12	0.14	0.04
S		50.65	50.08	50.13	49.95	50.14	50.52	49.81	49.95	49.76	50.16	49.82	50.32	50.23	50.41	50.17	50.12	49.37	50.30	50.09	49.78
Total		100.00	100.00	100.00	100.00	100.00	100.00	100.00	100.00	100.00	100.00	100.00	100.00	100.00	100.00	100.00	100.00	100.00	100.00	100.00	100.00
FeS		1.16	1.37	1.29	1.41	1.45	1.11	1.35	1.58	1.56	1.38	1.35	1.33	1.40	2.58	1.45	1.45	1.49	1.42	1.35	1.28
MnS		0.09	0.16	0.12	0.11	0.13	0.14	0.16	0.13	0.11	0.13	0.09	0.36	0.42	0.40	0.45	0.40	0.41	0.36	0.37	0.32
CdS		0.18	0.18	0.18	0.14	0.16	0.14	0.13	0.12	0.11	0.15	0.25	0.19	0.19	0.21	0.18	0.20	0.19	0.21	0.21	0.20

Sample Name		KTDH04 114.80m (C28)																		
Sample Point		C28-C2-10	C28-C2-11	C28-C2-12	C28-C2-13	C28-C2-14	C28-C2-16	C28-C2-17	C28-C3-3	C28-C3-4	C28-C3-5	C28-C3-6	C28-C3-7	C28-C3-8	C28-C3-9	C28-C3-10	C28-C3-11	C28-C3-12	C28-C3-13	C28-C3-14	C28-C3-15
Weight %	L.L.D. %																			
Zn	0.08	66.22	65.90	65.73	66.50	65.82	65.51	65.95	65.72	66.13	65.62	65.69	67.02	65.36	65.62	66.65	64.77	64.72	65.69	65.79	66.41
Fe	0.04	0.74	0.72	0.68	0.75	0.78	0.77	0.60	0.75	0.72	0.71	0.55	0.48	0.44	0.80	0.71	0.78	0.77	0.70	0.78	0.44
Mn	0.02	0.13	0.13	0.12	0.18	0.20	0.12	0.07	0.10	0.07	0.11	0.09	0.10	0.09	0.13	0.14	0.15	0.11	0.12	0.14	0.07
Cd	0.02	0.21	0.20	0.23	0.20	0.19	0.19	0.17	0.25	0.27	0.28	0.27	0.30	0.35	0.25	0.26	0.26	0.28	0.23	0.21	0.26
Cu	0.06	<0.06	0.10	<0.06	0.09	0.11	0.06	0.08	0.14	0.20	0.24	0.28	0.15	<0.06	0.13	<0.06	0.13	0.08	0.10	<0.06	<0.06
Sn	0.04	0.08	<0.04	<0.04	<0.04	<0.04	<0.04	0.07	<0.04	<0.04	<0.04	<0.04	<0.04	<0.04	<0.04	<0.04	<0.04	<0.04	<0.04	<0.04	0.05
In	0.04	<0.04	<0.04	<0.04	<0.04	<0.04	<0.04	<0.04	0.04	<0.04	<0.04	<0.04	<0.04	<0.04	<0.04	<0.04	<0.04	<0.04	<0.04	<0.04	0.06
Ag	0.03	<0.03	0.07	<0.03	<0.03	0.05	0.04	0.07	0.04	<0.03	<0.03	<0.03	0.05	0.08	<0.03	<0.03	0.05	<0.03	<0.03	0.03	0.09
Ga	0.02	0.33	0.23	0.10	0.04	0.13	<0.02	0.09	0.03	0.12	0.26	0.13	0.15	0.11	0.12	0.05	0.02	0.16	<0.02	0.12	0.14
S	0.02	33.09	32.24	32.19	32.29	32.69	32.64	32.17	33.45	32.40	32.48	33.37	32.52	32.63	32.40	33.40	32.51	33.02	32.23	33.48	33.61
Total		100.78	99.57	99.04	100.05	99.96	99.34	99.27	100.52	99.91	99.71	100.38	100.75	99.05	99.44	101.21	98.66	99.13	99.08	100.56	101.13
Atomic %																					
Zn		48.99	49.51	49.60	49.74	49.12	49.15	49.71	48.57	49.49	49.16	48.64	49.83	49.19	49.28	49.03	48.88	48.49	49.53	48.57	48.85
Fe		0.64	0.63	0.60	0.66	0.68	0.68	0.53	0.65	0.63	0.62	0.48	0.42	0.39	0.70	0.61	0.68	0.67	0.62	0.67	0.38
Mn		0.11	0.11	0.11	0.16	0.18	0.11	0.06	0.09	0.06	0.10	0.07	0.09	0.08	0.11	0.13	0.14	0.10	0.11	0.13	0.06
Cd		0.09	0.09	0.10	0.09	0.08	0.08	0.08	0.11	0.12	0.12	0.12	0.13	0.15	0.11	0.11	0.11	0.12	0.10	0.09	0.11
Cu			0.07		0.07	0.09	0.05	0.06	0.11	0.16	0.18	0.22	0.11		0.10		0.10	0.06	0.08	0.03	
Sn		0.03	0.01					0.03	0.02	0.01	0.00			0.01		0.00	0.01	0.01	0.00		0.02
In					0.01				0.02						0.01				0.01	0.01	0.02
Ag		0.00	0.03	0.00		0.02	0.02	0.03	0.02	0.00	0.01	0.01	0.02	0.04	0.00		0.02			0.01	0.04
Ga		0.23	0.16	0.07	0.03	0.09		0.06	0.02	0.09	0.18	0.09	0.10	0.08	0.08	0.03	0.01	0.11		0.09	0.10
S		49.91	49.39	49.52	49.25	49.74	49.92	49.44	50.40	49.44	49.62	50.38	49.30	50.07	49.61	50.09	50.03	50.44	49.55	50.40	50.41
Total		100.00	100.00	100.00	100.00	100.00	100.00	100.00	100.00	100.00	100.00	100.00	100.00	100.00	100.00	100.00	100.00	100.00	100.00	100.00	100.00
FeS		1.27	1.24	1.19	1.29	1.35	1.36	1.05	1.30	1.24	1.24	0.97	0.83	0.78	1.39	1.22	1.37	1.35	1.23	1.36	0.77
MnS		0.23	0.23	0.22	0.31	0.35	0.21	0.12	0.18	0.12	0.20	0.15	0.17	0.15	0.23	0.25	0.27	0.20	0.22	0.26	0.12
CdS		0.18	0.17	0.20	0.17	0.16	0.17	0.15	0.22	0.23	0.24	0.24	0.25	0.31	0.21	0.22	0.23	0.24	0.20	0.18	0.23

Sample Name		KTDH04 114.80m (C28)																KTDH04 232.30m (C44)		
Sample Point		C28-C3-16	C28-C4-1	C28-C4-2	C28-C4-3	C28-C4-4	C28-C4-5	C28-C4-6	C28-C4-7	C28-C4-8	C28-C4-9	C28-C4-10	C28-C4-12	C28-C4-13	C28-C4-14	C28-C4-15	C28-C4-16	C28-C4-17	C44-C1-1	C44-C1-2	C44-C1-3
Weight %	L.L.D. %																			
Zn	0.08	65.23	65.25	65.40	66.13	65.70	66.17	66.17	65.35	64.50	65.91	65.78	65.78	65.91	65.62	66.03	66.40	64.47	63.96	63.94	64.34
Fe	0.04	0.71	0.50	0.73	0.71	0.80	0.72	0.75	0.68	0.80	0.74	0.65	0.62	0.73	0.84	0.69	0.61	1.49	0.73	0.72	0.78
Mn	0.02	0.08	0.10	0.14	0.14	0.14	0.18	0.14	0.13	0.15	0.12	0.12	0.12	0.08	0.07	0.10	0.06	0.06	0.02	0.04	0.05
Cd	0.02	0.25	0.27	0.20	0.20	0.20	0.19	0.35	0.19	0.23	0.21	0.20	0.21	0.17	0.15	0.29	0.22	0.23	0.33	0.32	0.27
Cu	0.06	0.08	0.11	0.13	0.11	<0.06	<0.06	<0.06	0.12	0.23	0.17	<0.06	<0.06	0.08	<0.06	0.16	<0.06	0.88	<0.06	<0.06	<0.06
Sn	0.04	<0.04	<0.04	<0.04	<0.04	<0.04	<0.04	0.04	<0.04	<0.04	<0.04	<0.04	<0.04	<0.04	<0.04	0.08	0.05	<0.04	<0.04	<0.04	<0.04
In	0.04	<0.04	<0.04	0.05	<0.04	<0.04	<0.04	<0.04	0.06	<0.04	<0.04	<0.04	<0.04	<0.04	<0.04	0.06	<0.04	<0.04	<0.04	<0.04	0.08
Ag	0.03	<0.03	<0.03	<0.03	<0.03	<0.03	<0.03	<0.03	<0.03	<0.03	<0.03	<0.03	<0.03	<0.03	0.05	<0.03	<0.03	<0.03	<0.03	<0.03	<0.03
Ga	0.02	0.11	0.21	0.21	0.08	0.28	0.09	0.15	0.13	0.03	0.18	0.12	0.05	0.19	0.12	0.09	0.11	0.19	0.18	0.13	0.06
S	0.02	32.42	33.33	33.44	34.02	33.13	33.18	34.17	33.41	33.13	33.44	34.02	33.96	33.61	33.94	33.59	34.01	33.18	33.97	33.30	33.06
Total		98.89	99.77	100.30	101.40	100.24	100.53	101.77	100.06	99.08	100.77	100.89	100.74	100.78	100.80	101.09	101.45	100.49	99.19	98.45	98.64
Atomic %																					
Zn		49.19	48.55	48.41	48.33	48.77	48.97	48.19	48.48	48.28	48.62	48.25	48.34	48.55	48.20	48.56	48.53	47.70	47.55	48.05	48.37
Fe		0.63	0.44	0.63	0.61	0.69	0.62	0.64	0.59	0.70	0.64	0.56	0.53	0.63	0.72	0.60	0.52	1.29	0.63	0.63	0.69
Mn		0.07	0.09	0.12	0.12	0.13	0.16	0.12	0.11	0.13	0.11	0.10	0.10	0.07	0.06	0.09	0.05	0.05	0.02	0.04	0.05
Cd		0.11	0.12	0.08	0.09	0.08	0.08	0.15	0.08	0.10	0.09	0.09	0.09	0.07	0.07	0.12	0.09	0.10	0.14	0.14	0.12
Cu		0.06	0.08	0.10	0.08		0.02	0.04	0.09	0.18	0.13	0.03		0.06		0.12	0.02	0.67	0.03	0.04	0.02
Sn								0.02		0.01						0.03	0.02	0.00			
In			0.01	0.02	0.02			0.00	0.03	0.01				0.00		0.02	0.02	0.01			0.03
Ag		0.01	0.01	0.00									0.01		0.02	0.01				0.00	
Ga		0.08	0.15	0.15	0.06	0.19	0.06	0.10	0.09	0.02	0.13	0.08	0.03	0.13	0.08	0.06	0.08	0.13	0.13	0.09	0.04
S		49.85	50.56	50.48	50.69	50.14	50.08	50.74	50.54	50.57	50.29	50.89	50.89	50.48	50.84	50.38	50.68	50.05	51.50	51.01	50.68
Total		100.00	100.00	100.00	100.00	100.00	100.00	100.00	100.00	100.00	100.00	100.00	100.00	100.00	100.00	100.00	100.00	100.00	100.00	100.00	100.00
FeS		1.26	0.88	1.28	1.24	1.39	1.24	1.29	1.19	1.42	1.29	1.13	1.08	1.26	1.47	1.20	1.06	2.59	1.31	1.29	1.40
MnS		0.15	0.18	0.25	0.24	0.25	0.31	0.25	0.22	0.26	0.21	0.21	0.21	0.14	0.13	0.17	0.10	0.10	0.04	0.08	0.10
CdS		0.22	0.23	0.17	0.18	0.17	0.16	0.30	0.17	0.21	0.18	0.18	0.18	0.15	0.13	0.25	0.19	0.20	0.29	0.29	0.24

Sample Name		KTDH04 232.30m (C44)																		
Sample Point		C44-C1-4	C44-C1-5	C44-C1-6	C44-C1-7	C44-C1-8	C44-C1-9	C44-C2-1	C44-C2-3	C44-C2-4	C44-C2-6	C44-C2-8	C44-C2-9	C44-C2-10	C44-C2-11	C44-C2-12	C44-C2-13	C44-C2-14	C44-C2-15	C44-C2-16	C44-C2-17
Weight %	L.L.D. %																				
Zn	0.08	64.10	64.36	65.02	64.85	64.97	64.72	65.65	64.65	65.18	65.22	64.46	64.44	64.77	64.17	65.12	64.32	64.73	64.70	64.81	65.65
Fe	0.04	0.90	0.92	0.93	0.82	1.08	0.81	1.07	0.91	1.17	1.02	0.74	0.78	0.90	0.84	0.78	0.87	0.90	0.89	0.92	0.78
Mn	0.02	0.12	0.09	0.09	0.08	0.07	0.04	0.03	0.19	0.26	0.39	0.39	0.38	0.38	0.39	0.31	0.30	0.22	0.18	0.11	0.06
Cd	0.02	0.34	0.34	0.32	0.33	0.33	0.30	0.28	0.32	0.29	0.27	0.30	0.29	0.30	0.31	0.29	0.30	0.31	0.31	0.31	0.28
Cu	0.06	0.07	<0.06	<0.06	0.15	0.21	0.19	0.46	<0.06	0.25	0.15	<0.06	<0.06	0.12	<0.06	<0.06	<0.06	<0.06	<0.06	<0.06	0.11
Sn	0.04	<0.04	<0.04	<0.04	<0.04	<0.04	<0.04	<0.04	<0.04	<0.04	<0.04	<0.04	0.04	<0.04	<0.04	<0.04	0.04	<0.04	<0.04	<0.04	<0.04
In	0.04	<0.04	0.09	<0.04	<0.04	<0.04	0.07	<0.04	<0.04	<0.04	<0.04	<0.04	<0.04	<0.04	<0.04	<0.04	<0.04	<0.04	<0.04	<0.04	<0.04
Ag	0.03	<0.03	<0.03	<0.03	<0.03	<0.03	<0.03	<0.03	<0.03	<0.03	0.04	<0.03	<0.03	0.09	<0.03	<0.03	0.07	<0.03	0.03	0.05	<0.03
Ga	0.02	0.16	0.08	0.10	0.22	0.16	0.15	<0.02	0.23	0.17	0.15	0.16	<0.02	0.22	0.13	0.09	0.18	0.10	0.17	0.08	0.10
S	0.02	32.86	33.13	32.75	32.48	31.98	32.21	32.90	32.80	32.67	31.86	31.99	32.79	32.46	32.79	32.51	32.87	32.25	33.11	32.66	33.25
Total		98.55	99.00	99.20	98.92	98.80	98.49	100.38	99.10	99.98	99.09	98.03	98.71	99.23	98.62	99.11	98.94	98.51	99.40	98.94	100.22
Atomic %																					
Zn		48.30	48.23	48.79	48.87	49.19	49.05	48.75	48.52	48.62	49.29	49.08	48.51	48.69	48.33	48.98	48.30	49.00	48.34	48.77	48.70
Fe		0.79	0.81	0.81	0.72	0.96	0.72	0.93	0.80	1.02	0.90	0.66	0.68	0.79	0.74	0.69	0.76	0.80	0.78	0.81	0.68
Mn		0.11	0.08	0.08	0.07	0.06	0.04	0.03	0.17	0.23	0.35	0.35	0.34	0.34	0.35	0.27	0.27	0.19	0.16	0.10	0.05
Cd		0.15	0.15	0.14	0.15	0.14	0.13	0.12	0.14	0.12	0.12	0.13	0.13	0.13	0.13	0.13	0.13	0.13	0.14	0.14	0.12
Cu		0.06	0.02		0.11	0.17	0.15	0.35	0.01	0.19	0.12		0.01	0.09			0.02	0.01	0.01		0.08
Sn								0.01					0.02	0.00	0.01		0.02	0.02			
In			0.04	0.01	0.00		0.03				0.01	0.01				0.00	0.01			0.02	0.00
Ag						0.00					0.02			0.04			0.03	0.00	0.01	0.02	
Ga		0.11	0.06	0.07	0.15	0.11	0.11		0.16	0.12	0.11	0.12		0.15	0.09	0.07	0.13	0.07	0.12	0.06	0.07
S		50.48	50.62	50.10	49.92	49.37	49.77	49.81	50.20	49.70	49.09	49.66	50.32	49.76	50.35	49.86	50.34	49.78	50.44	50.10	50.29
Total		100.00	100.00	100.00	100.00	100.00	100.00	100.00	100.00	100.00	100.00	100.00	100.00	100.00	100.00	100.00	100.00	100.00	100.00	100.00	100.00
FeS		1.60	1.63	1.63	1.44	1.89	1.44	1.85	1.60	2.03	1.77	1.30	1.37	1.58	1.49	1.37	1.54	1.60	1.58	1.62	1.37
MnS		0.22	0.15	0.15	0.15	0.12	0.08	0.05	0.34	0.46	0.69	0.70	0.68	0.67	0.70	0.55	0.53	0.39	0.33	0.19	0.10
CdS		0.30	0.30	0.28	0.29	0.28	0.27	0.24	0.28	0.25	0.23	0.26	0.25	0.26	0.27	0.26	0.26	0.27	0.27	0.27	0.24

Sample Name		KTDH04 232.30m (C44)															
Sample Point		C44-C3-1	C44-C3-2	C44-C3-4	C44-C3-5	C44-C3-6	C44-C3-7	C44-C3-8	C44-C3-9	C44-C3-10	C44-C3-11	C44-C3-12	C44-C3-13	C44-C3-14	C44-C3-15	C44-C3-16	C44-C3-17
Weight %	L.L.D. %																
Zn	0.08	64.25	64.62	64.70	65.49	66.21	64.60	64.97	64.20	64.87	64.11	64.79	65.62	65.25	64.71	65.19	65.52
Fe	0.04	0.86	0.93	1.15	0.55	0.64	0.77	0.87	0.67	0.88	0.79	1.20	0.81	0.95	0.82	0.76	0.75
Mn	0.02	0.06	0.04	0.05	0.03	0.06	0.08	0.03	0.04	0.14	0.14	0.05	0.11	0.14	0.18	0.07	0.11
Cd	0.02	0.30	0.29	0.29	0.27	0.31	0.27	0.28	0.30	0.32	0.32	0.30	0.34	0.34	0.33	0.31	0.28
Cu	0.06	0.29	0.42	0.60	0.07	0.14	0.13	0.28	0.07	<0.06	<0.06	0.67	0.11	<0.06	<0.06	<0.06	0.09
Sn	0.04	<0.04	<0.04	<0.04	<0.04	<0.04	<0.04	<0.04	<0.04	0.05	<0.04	<0.04	<0.04	<0.04	<0.04	<0.04	<0.04
In	0.04	<0.04	<0.04	<0.04	<0.04	<0.04	<0.04	<0.04	<0.04	<0.04	0.05	<0.04	<0.04	<0.04	<0.04	<0.04	<0.04
Ag	0.03	<0.03	<0.03	<0.03	<0.03	0.04	<0.03	<0.03	<0.03	<0.03	<0.03	<0.03	<0.03	<0.03	0.06	<0.03	<0.03
Ga	0.02	0.11	0.11	0.18	0.09	0.31	0.24	0.10	0.05	0.15	0.03	0.23	0.12	0.25	0.18	0.11	<0.02
S	0.02	32.33	33.19	33.44	33.22	33.48	33.07	33.33	32.92	32.75	33.44	33.02	33.09	33.72	33.94	33.17	33.46
Total		98.22	99.60	100.41	99.72	101.18	99.16	99.87	98.24	99.17	98.87	100.25	100.20	100.65	100.22	99.62	100.21
Atomic %																	
Zn		48.74	48.17	47.84	48.79	48.71	48.38	48.29	48.47	48.70	47.96	48.11	48.75	48.05	47.76	48.60	48.53
Fe		0.76	0.81	0.99	0.48	0.55	0.68	0.76	0.60	0.78	0.69	1.04	0.71	0.82	0.71	0.66	0.65
Mn		0.06	0.04	0.04	0.02	0.05	0.07	0.02	0.04	0.12	0.12	0.05	0.10	0.12	0.16	0.07	0.10
Cd		0.13	0.12	0.12	0.12	0.13	0.12	0.12	0.13	0.14	0.14	0.13	0.15	0.15	0.14	0.13	0.12
Cu		0.23	0.33	0.46	0.06	0.11	0.10	0.22	0.05		0.04	0.51	0.08	0.04		0.03	0.07
Sn							0.00			0.02	0.00			0.01	0.00		
In								0.02		0.01	0.02	0.01				0.01	
Ag			0.01			0.02					0.00	0.01	0.01		0.03		0.01
Ga		0.08	0.08	0.13	0.07	0.22	0.17	0.07	0.03	0.11	0.02	0.16	0.08	0.18	0.12	0.08	0.01
S		50.00	50.45	50.41	50.47	50.22	50.49	50.51	50.68	50.13	51.01	49.99	50.12	50.63	51.08	50.42	50.53
Total		100.00	100.00	100.00	100.00	100.00	100.00	100.00	100.00	100.00	100.00	100.00	100.00	100.00	100.00	100.00	100.00
FeS		1.52	1.63	2.01	0.97	1.11	1.37	1.53	1.21	1.55	1.40	2.08	1.42	1.67	1.45	1.33	1.31
MnS		0.11	0.07	0.09	0.05	0.10	0.14	0.05	0.08	0.25	0.25	0.09	0.20	0.25	0.32	0.13	0.20
CdS		0.27	0.25	0.25	0.24	0.26	0.23	0.25	0.26	0.28	0.28	0.26	0.29	0.30	0.29	0.27	0.24

Sample Name		KTDH04 68.30m (C06)																		
Sample Point		C06-C1-2	C06-C1-3	C06-C1-6	C06-C1-7	C06-C1-8	C06-C1-9	C06-C1-10	C06-C1-11	C06-C1-12	C06-C1-13	C06-C1-15	C06-C1-16	C06-C1-17	C06-C1-18	C06-C1-20	C06-C1-21	C06-C1-22	C06-C1-23	C06-C1-24	C06-C1-25
Weight %	L.L.D. %																				
Zn	0.07	65.39	65.08	64.86	64.82	65.35	64.39	64.95	65.55	65.05	64.64	64.80	64.58	65.02	64.90	65.22	64.92	64.74	64.38	65.23	64.73
Fe	0.03	0.49	0.47	0.54	0.53	0.45	0.56	0.57	0.65	0.52	0.46	0.38	0.48	0.49	0.63	0.50	0.49	0.56	0.55	0.86	0.60
Mn	0.02	0.06	0.05	0.08	0.07	0.04	<0.02	0.06	0.03	0.04	0.05	0.06	0.08	0.04	0.05	0.04	0.03	0.08	0.03	0.06	0.07
Cd	0.03	0.37	0.30	0.37	0.38	0.38	0.40	0.38	0.33	0.36	0.36	0.32	0.39	0.32	0.27	0.43	0.44	<0.03	0.31	0.29	0.30
Cu	0.06	<0.06	<0.06	<0.06	<0.06	<0.06	<0.06	<0.06	<0.06	<0.06	<0.06	0.06	<0.06	<0.06	<0.06	0.22	<0.06	<0.06	<0.06	0.31	0.10
Sn	0.03	<0.03	<0.03	<0.03	<0.03	<0.03	0.04	<0.03	<0.03	<0.03	0.05	<0.03	<0.03	<0.03	0.04	<0.03	0.03	<0.03	<0.03	<0.03	<0.03
In	0.06	<0.06	<0.06	<0.06	<0.06	<0.06	<0.06	<0.06	<0.06	<0.06	0.16	<0.06	<0.06	<0.06	<0.06	<0.06	<0.06	0.18	<0.06	0.10	<0.06
Ag	0.06	<0.06	<0.06	<0.06	<0.06	<0.06	<0.06	<0.06	<0.06	<0.06	<0.06	0.08	0.07	<0.06	<0.06	<0.06	<0.06	<0.06	0.16	<0.06	0.08
Ga	0.02	0.13	0.21	0.16	0.14	0.21	0.09	0.08	0.25	0.03	<0.02	0.13	0.14	0.13	0.03	0.14	0.08	0.09	0.07	0.23	0.11
S	0.03	32.90	32.32	32.78	32.81	31.81	33.07	32.63	32.74	32.17	32.65	32.63	32.48	32.81	32.61	32.53	32.82	32.57	32.92	33.09	32.72
Total		99.35	98.43	98.78	98.74	98.24	98.54	98.66	99.55	98.18	98.35	98.45	98.23	98.80	98.53	99.09	98.81	98.22	98.41	100.17	98.72
Atomic %																					
Zn		48.99	49.31	48.84	48.81	49.79	48.49	49.00	49.06	49.44	48.92	48.99	48.98	48.94	49.02	49.11	48.88	48.99	48.58	48.47	48.79
Fe		0.43	0.42	0.48	0.47	0.40	0.49	0.50	0.57	0.46	0.40	0.33	0.43	0.43	0.56	0.44	0.43	0.49	0.49	0.75	0.53
Mn		0.06	0.04	0.07	0.06	0.04	0.00	0.05	0.03	0.04	0.04	0.06	0.07	0.03	0.04	0.04	0.03	0.07	0.02	0.05	0.06
Cd		0.16	0.13	0.16	0.17	0.17	0.17	0.17	0.14	0.16	0.16	0.14	0.17	0.14	0.12	0.19	0.19		0.14	0.12	0.13
Cu								0.05	0.04	0.00		0.05				0.17	0.01	0.02	0.01	0.24	0.08
Sn					0.00	0.01	0.02		0.01	0.01	0.02	0.01			0.02		0.01				0.00
In		0.01	0.00	0.00		0.02		0.00			0.07		0.01					0.08		0.04	
Ag			0.01	0.00	0.01							0.04	0.03	0.02	0.01			0.02	0.07	0.02	0.04
Ga		0.09	0.15	0.11	0.10	0.15	0.06	0.06	0.18	0.02		0.09	0.10	0.09	0.02	0.10	0.06	0.07	0.05	0.16	0.08
S		50.26	49.94	50.33	50.39	49.42	50.77	50.18	49.97	49.86	50.39	50.30	50.21	50.36	50.22	49.95	50.39	50.26	50.65	50.14	50.29
Total		100.00	100.00	100.00	100.00	100.00	100.00	100.00	100.00	100.00	100.00	100.00	100.00	100.00	100.00	100.00	100.00	100.00	100.00	100.00	100.00
FeS		0.87	0.84	0.96	0.94	0.80	1.00	1.00	1.13	0.92	0.81	0.67	0.86	0.86	1.12	0.88	0.87	0.99	0.99	1.51	1.07
MnS		0.11	0.08	0.14	0.12	0.07	0.00	0.10	0.06	0.07	0.08	0.11	0.15	0.06	0.09	0.07	0.05	0.14	0.05	0.11	0.12
CdS		0.32	0.27	0.33	0.33	0.33	0.35	0.33	0.28	0.32	0.31	0.28	0.35	0.28	0.24	0.37	0.39	0.00	0.28	0.25	0.27

Sample Name			KTDH04 93.50m (C16)																KTDH04 101.40m (C20)	
Sample Point		C06-C1-26	C16-C1-1	C16-C1-2	C16-C1-3	C16-C1-4	C16-C1-6	C16-C1-7	C16-C1-8	C16-C1-10	C16-C1-12	C16-C1-13	C16-C1-15	C16-C1-18	C16-C1-20	C16-C1-21	C16-C1-22	C16-C1-23	C16-C1-25	C20-C1-1	C20-C1-7
Weight %	L.L.D. %																			
Zn	0.07	64.33	64.56	64.71	64.49	64.29	64.54	64.88	64.36	64.69	64.82	64.63	65.38	63.97	64.28	65.31	64.13	64.22	64.67	63.31	64.05
Fe	0.03	0.62	0.54	0.47	0.55	0.55	0.49	0.52	0.49	0.47	0.51	0.49	0.58	0.58	0.55	0.53	0.53	0.57	0.55	0.57	0.69
Mn	0.02	0.04	0.19	0.21	0.19	0.30	0.27	0.25	0.24	0.23	0.24	0.25	0.12	0.29	0.28	0.29	0.25	0.16	0.25	0.10	0.09
Cd	0.03	0.41	0.42	0.39	0.31	0.34	0.24	0.30	0.41	0.45	0.31	0.39	0.25	0.35	0.35	0.34	0.33	0.19	0.56	0.40	0.48
Cu	0.06	0.19	<0.06	<0.06	<0.06	<0.06	<0.06	0.08	<0.06	<0.06	<0.06	0.08	<0.06	<0.06	<0.06	<0.06	<0.06	<0.06	<0.06	0.15	0.32
Sn	0.03	0.05	<0.03	<0.03	<0.03	<0.03	0.06	<0.03	<0.03	<0.03	<0.03	<0.03	<0.03	<0.03	<0.03	0.10	0.04	<0.03	<0.03	<0.03	<0.03
In	0.06	<0.06	<0.06	0.35	<0.06	0.09	<0.06	0.09	<0.06	<0.06	0.07	<0.06	<0.06	<0.06	<0.06	<0.06	<0.06	<0.06	<0.06	<0.06	<0.06
Ag	0.06	<0.06	<0.06	<0.06	0.07	<0.06	<0.06	<0.06	<0.06	<0.06	<0.06	<0.06	<0.06	<0.06	<0.06	<0.06	0.17	<0.06	<0.06	0.10	<0.06
Ga	0.02	0.11	0.10	<0.02	0.17	<0.02	0.05	0.12	0.05	0.10	0.25	0.15	0.18	0.20	0.09	0.18	0.07	0.11	0.13	0.20	0.16
S	0.03	32.53	32.31	32.93	32.58	33.36	32.89	33.06	32.91	32.63	32.87	32.69	32.95	32.79	32.88	32.84	32.65	32.85	32.79	33.23	32.99
Total		98.27	98.13	99.06	98.37	98.92	98.53	99.30	98.46	98.56	99.06	98.69	99.46	98.17	98.43	99.58	98.17	98.11	98.96	98.05	98.79
Atomic %																					
Zn		48.74	49.04	48.61	48.79	48.14	48.61	48.55	48.52	48.86	48.67	48.73	48.88	48.36	48.48	48.85	48.58	48.54	48.63	47.78	48.16
Fe		0.55	0.48	0.42	0.49	0.48	0.43	0.45	0.43	0.42	0.44	0.43	0.51	0.52	0.48	0.46	0.47	0.51	0.49	0.51	0.61
Mn		0.03	0.18	0.19	0.17	0.26	0.24	0.22	0.22	0.20	0.22	0.23	0.11	0.26	0.25	0.25	0.22	0.14	0.22	0.09	0.08
Cd		0.18	0.19	0.17	0.14	0.15	0.11	0.13	0.18	0.20	0.13	0.17	0.11	0.15	0.15	0.15	0.15	0.09	0.25	0.18	0.21
Cu		0.15		0.03			0.02	0.06		0.01		0.06	0.03			0.03		0.01		0.11	0.25
Sn		0.02		0.00			0.02	0.01				0.01		0.00		0.04	0.02		0.01	0.01	
In		0.00	0.01	0.15		0.04	0.02	0.04	0.02		0.03	0.00	0.02	0.02					0.02	0.01	
Ag					0.03		0.02	0.00	0.02	0.01							0.08	0.00		0.04	
Ga		0.08	0.07		0.12		0.03	0.08	0.03	0.07	0.18	0.11	0.12	0.14	0.07	0.13	0.05	0.08	0.09	0.14	0.11
S		50.25	50.03	50.44	50.26	50.93	50.50	50.45	50.57	50.24	50.33	50.26	50.23	50.54	50.57	50.08	50.44	50.63	50.28	51.13	50.58
Total		100.00	100.00	100.00	100.00	100.00	100.00	100.00	100.00	100.00	100.00	100.00	100.00	100.00	100.00	100.00	100.00	100.00	100.00	100.00	100.00
FeS		1.10	0.96	0.84	0.98	0.98	0.87	0.91	0.87	0.84	0.89	0.87	1.02	1.05	0.98	0.93	0.95	1.03	0.98	1.03	1.24
MnS		0.06	0.35	0.38	0.35	0.54	0.48	0.45	0.44	0.41	0.43	0.46	0.21	0.52	0.50	0.51	0.45	0.29	0.45	0.18	0.16
CdS		0.36	0.37	0.34	0.27	0.30	0.22	0.26	0.37	0.39	0.27	0.34	0.22	0.31	0.31	0.29	0.30	0.17	0.50	0.36	0.43

Sample Name		KTDH04 101.40m (C20)			KTDH04 227.40m (C41)														KTDH04 228.60m (C42)	
Sample Point		C20-C1-14	C20-C1-18	C20-C1-23	C41-C1-2	C41-C1-4	C41-C1-5	C41-C1-6	C41-C1-8	C41-C1-10	C41-C1-11	C41-C1-12	C41-C1-13	C41-C1-14	C41-C1-15	C41-C1-16	C41-C1-17	C41-C1-19	C41-C1-20	C42-C1-1	C42-C1-2
Weight %	L.L.D. %																			
Zn	0.07	63.21	63.53	63.77	64.09	63.06	63.76	63.91	63.63	63.47	63.83	63.25	63.56	63.81	62.93	63.52	63.15	63.61	64.05	64.86	65.64
Fe	0.03	0.56	0.62	0.79	0.84	0.92	0.78	0.83	0.90	0.90	0.78	0.94	0.91	0.95	0.92	0.94	0.94	1.00	1.00	0.92	0.84
Mn	0.02	0.06	0.09	0.08	0.24	0.18	0.11	0.22	0.25	0.14	0.17	0.06	0.17	0.27	0.25	0.23	0.20	0.21	0.14	0.17	0.19
Cd	0.03	0.36	0.33	0.35	0.33	0.30	0.29	0.31	0.25	0.28	0.39	0.26	0.37	0.27	0.32	0.33	0.33	0.28	0.31	0.31	0.29
Cu	0.06	0.26	0.30	0.23	0.13	0.09	<0.06	<0.06	<0.06	<0.06	<0.06	0.91	<0.06	<0.06	<0.06	<0.06	<0.06	<0.06	0.23	<0.06	<0.06
Sn	0.03	<0.03	<0.03	<0.03	<0.03	<0.03	0.04	<0.03	<0.03	<0.03	<0.03	<0.03	0.04	<0.03	0.03	<0.03	<0.03	0.05	<0.03	<0.03	<0.03
In	0.06	0.10	<0.06	<0.06	0.06	0.11	<0.06	<0.06	<0.06	<0.06	<0.06	<0.06	<0.06	<0.06	0.07	<0.06	<0.06	<0.06	<0.06	0.06	<0.06
Ag	0.06	0.07	<0.06	0.18	<0.06	<0.06	<0.06	<0.06	<0.06	<0.06	<0.06	<0.06	0.09	<0.06	<0.06	<0.06	<0.06	<0.06	<0.06	<0.06	<0.06
Ga	0.02	<0.02	<0.02	0.08	0.10	0.11	0.22	0.15	0.09	0.13	0.15	0.18	0.10	0.06	0.12	0.04	0.08	0.07	0.04	0.21	0.08
S	0.03	34.03	33.13	32.71	33.34	33.39	33.35	33.08	33.45	33.60	33.99	33.67	33.24	33.35	33.52	33.65	33.50	33.27	33.49	33.58	33.43
Total		98.66	97.98	98.20	99.14	98.15	98.55	98.49	98.56	98.53	99.31	99.27	98.48	98.71	98.15	98.70	98.20	98.49	99.25	100.10	100.47
Atomic %																					
Zn		47.20	47.97	48.27	47.91	47.46	47.84	48.08	47.68	47.54	47.39	47.08	47.77	47.80	47.30	47.50	47.45	47.77	47.73	48.04	48.53
Fe		0.49	0.54	0.70	0.73	0.81	0.68	0.73	0.79	0.79	0.68	0.82	0.80	0.84	0.81	0.82	0.83	0.88	0.87	0.80	0.72
Mn		0.06	0.08	0.07	0.21	0.16	0.10	0.20	0.22	0.13	0.15	0.05	0.15	0.24	0.22	0.20	0.18	0.19	0.12	0.15	0.17
Cd		0.16	0.14	0.15	0.15	0.13	0.13	0.14	0.11	0.12	0.17	0.11	0.16	0.12	0.14	0.14	0.14	0.12	0.13	0.13	0.13
Cu		0.20	0.23	0.18	0.10	0.07	0.05		0.04		0.03	0.70	0.04		0.04			0.03	0.18	0.00	
Sn							0.02	0.01			0.01		0.02	0.01	0.01	0.00		0.02	0.00		
In		0.04			0.03	0.05	0.01			0.00		0.01			0.03		0.00	0.00	0.02	0.03	
Ag		0.03	0.02	0.08						0.01			0.04	0.02			0.01		0.02	0.00	0.01
Ga			0.00	0.06	0.07	0.08	0.15	0.11	0.06	0.09	0.10	0.12	0.07	0.04	0.09	0.02	0.06	0.05	0.03	0.14	0.06
S		51.82	51.01	50.48	50.80	51.24	51.02	50.74	51.10	51.31	51.46	51.10	50.95	50.94	51.37	51.31	51.32	50.93	50.89	50.71	50.39
Total		100.00	100.00	100.00	100.00	100.00	100.00	100.00	100.00	100.00	100.00	100.00	100.00	100.00	100.00	100.00	100.00	100.00	100.00	100.00	100.00
FeS		1.01	1.11	1.42	1.49	1.66	1.40	1.48	1.62	1.62	1.40	1.68	1.62	1.70	1.66	1.69	1.70	1.79	1.78	1.61	1.46
MnS		0.12	0.16	0.14	0.43	0.33	0.21	0.40	0.45	0.26	0.31	0.10	0.32	0.49	0.45	0.41	0.36	0.38	0.25	0.31	0.33
CdS		0.32	0.29	0.31	0.30	0.27	0.26	0.28	0.22	0.25	0.35	0.23	0.33	0.24	0.28	0.29	0.30	0.25	0.27	0.27	0.25

Sample Name		KTDH04 228.60m (C42)																KTDH04 229.80m (C43)		
Sample Point		C42-C1-3	C42-C1-4	C42-C1-5	C42-C1-6	C42-C1-7	C42-C1-8	C42-C1-9	C42-C1-10	C42-C1-11	C42-C1-12	C42-C1-13	C42-C1-14	C42-C1-15	C42-C1-16	C42-C1-17	C42-C1-18	C42-C1-20	C43-C2-1	C43-C2-2	C43-C2-3
Weight %	L.L.D. %																				
Zn	0.07	64.74	65.17	64.44	65.10	65.39	64.69	64.43	64.50	64.00	64.94	64.36	65.39	64.02	65.13	65.77	65.23	64.80	64.59	65.64	64.63
Fe	0.03	0.71	0.73	0.89	0.74	0.86	0.89	0.85	0.81	0.68	0.81	0.72	0.65	0.82	0.79	0.71	0.66	0.88	0.83	0.69	0.82
Mn	0.02	0.17	0.17	0.12	0.08	0.20	0.16	0.15	0.14	0.11	0.14	0.12	0.13	0.12	0.10	0.14	0.06	0.10	0.18	0.13	0.12
Cd	0.03	0.31	0.30	0.35	0.42	0.29	0.27	0.29	0.27	0.37	0.44	0.42	0.40	0.44	0.39	0.39	0.33	0.34	0.27	0.24	0.31
Cu	0.06	<0.06	<0.06	<0.06	<0.06	<0.06	<0.06	<0.06	0.07	<0.06	<0.06	<0.06	<0.06	<0.06	<0.06	<0.06	<0.06	0.10	0.84	0.47	0.49
Sn	0.03	<0.03	<0.03	<0.03	<0.03	<0.03	<0.03	<0.03	<0.03	<0.03	<0.03	<0.03	<0.03	<0.03	<0.03	<0.03	<0.03	0.04	0.04	<0.03	<0.03
In	0.06	<0.06	<0.06	<0.06	0.18	<0.06	<0.06	0.09	<0.06	<0.06	0.06	<0.06	<0.06	<0.06	<0.06	<0.06	<0.06	<0.06	<0.06	<0.06	<0.06
Ag	0.06	<0.06	<0.06	<0.06	<0.06	<0.06	0.07	<0.06	0.08	<0.06	<0.06	<0.06	<0.06	0.08	0.13	<0.06	<0.06	<0.06	<0.06	<0.06	<0.06
Ga	0.02	0.05	0.16	0.14	0.07	0.07	0.06	0.20	0.05	0.14	0.13	0.17	0.13	0.14	0.23	0.14	0.09	0.05	0.16	0.17	0.13
S	0.03	33.76	33.48	33.60	33.47	34.18	33.51	33.83	33.44	33.71	33.27	33.61	33.60	33.78	33.59	33.66	33.71	33.48	32.28	32.41	32.77
Total		99.74	100.00	99.53	100.06	100.99	99.64	99.83	99.35	99.01	99.78	99.40	100.29	99.40	100.34	100.81	100.07	99.79	99.17	99.75	99.28
Atomic %																					
Zn		48.02	48.34	47.92	48.32	47.88	48.08	47.72	48.09	47.74	48.35	47.92	48.38	47.62	48.18	48.44	48.27	48.14	48.65	49.18	48.46
Fe		0.62	0.64	0.77	0.64	0.74	0.77	0.74	0.70	0.59	0.71	0.63	0.56	0.72	0.68	0.61	0.57	0.77	0.73	0.61	0.72
Mn		0.15	0.15	0.10	0.07	0.18	0.14	0.13	0.13	0.10	0.12	0.10	0.12	0.11	0.09	0.12	0.06	0.09	0.16	0.12	0.11
Cd		0.13	0.13	0.15	0.18	0.12	0.11	0.12	0.12	0.16	0.19	0.18	0.17	0.19	0.17	0.17	0.14	0.15	0.12	0.10	0.14
Cu							0.03	0.02	0.06	0.02	0.00						0.04	0.08	0.65	0.36	0.38
Sn		0.00	0.00		0.01					0.01	0.01					0.01		0.01	0.01		
In			0.01		0.08	0.00		0.04		0.02	0.03	0.01				0.02		0.00		0.01	
Ag			0.00				0.03	0.02	0.03		0.00	0.01		0.03	0.06			0.00			
Ga		0.03	0.11	0.10	0.05	0.05	0.04	0.14	0.03	0.09	0.09	0.12	0.09	0.10	0.16	0.10	0.06	0.03	0.11	0.12	0.09
S		51.05	50.63	50.95	50.65	51.03	50.79	51.08	50.84	51.27	50.50	51.03	50.69	51.23	50.67	50.55	50.86	50.72	49.57	49.50	50.10
Total		100.00	100.00	100.00	100.00	100.00	100.00	100.00	100.00	100.00	100.00	100.00	100.00	100.00	100.00	100.00	100.00	100.00	100.00	100.00	100.00
FeS		1.26	1.29	1.58	1.30	1.50	1.57	1.50	1.43	1.21	1.43	1.29	1.13	1.47	1.39	1.23	1.16	1.56	1.45	1.21	1.44
MnS		0.30	0.30	0.21	0.15	0.36	0.28	0.26	0.26	0.20	0.25	0.21	0.24	0.23	0.17	0.24	0.11	0.18	0.33	0.23	0.22
CdS		0.27	0.26	0.31	0.37	0.25	0.23	0.26	0.24	0.33	0.38	0.37	0.34	0.39	0.34	0.34	0.28	0.30	0.23	0.20	0.27

Sample Name		KTDH04 229.80m (C43)																
Sample Point		C43-C2-4	C43-C2-5	C43-C2-6	C43-C2-8	C43-C2-9	C43-C2-10	C43-C2-11	C43-C2-12	C43-C2-13	C43-C2-14	C43-C2-15	C43-C2-16	C43-C2-17	C43-C2-18	C43-C2-19	C43-C2-20	C43-C2-21
Weight %	L.L.D. %																	
Zn	0.07	64.84	65.18	64.79	64.90	64.11	65.56	64.40	63.96	65.21	64.17	65.03	64.80	65.00	64.20	65.33	65.22	64.29
Fe	0.03	0.87	0.67	0.71	0.71	0.79	0.73	0.80	0.82	0.60	0.81	0.75	0.77	0.75	0.77	0.83	0.82	0.79
Mn	0.02	0.15	0.07	0.08	0.07	0.05	0.06	0.06	0.11	0.07	0.11	0.14	0.20	0.15	0.16	0.12	0.09	0.07
Cd	0.03	0.31	0.31	0.30	0.26	0.31	0.36	0.31	0.36	0.33	0.21	0.40	0.38	0.31	0.28	0.29	0.33	0.30
Cu	0.06	0.85	0.43	0.24	0.30	0.49	0.20	0.32	0.38	0.28	0.94	0.65	0.33	0.25	0.24	0.83	0.42	0.10
Sn	0.03	0.08	<0.03	<0.03	<0.03	<0.03	<0.03	<0.03	<0.03	0.04	<0.03	<0.03	<0.03	<0.03	0.05	<0.03	<0.03	<0.03
In	0.06	<0.06	<0.06	<0.06	<0.06	<0.06	<0.06	<0.06	<0.06	<0.06	<0.06	<0.06	0.09	0.08	<0.06	<0.06	<0.06	<0.06
Ag	0.06	<0.06	0.07	<0.06	<0.06	<0.06	<0.06	<0.06	<0.06	<0.06	<0.06	<0.06	<0.06	0.13	<0.06	<0.06	<0.06	<0.06
Ga	0.02	0.13	0.16	<0.02	0.35	<0.02	0.22	0.22	0.16	0.12	0.07	0.10	0.29	0.08	0.15	0.15	0.04	0.06
S	0.03	32.43	32.34	32.46	32.45	33.05	32.22	33.36	32.66	32.79	32.96	32.72	32.56	32.64	32.49	32.52	32.06	32.90
Total		99.65	99.22	98.58	99.04	98.80	99.35	99.47	98.44	99.44	99.27	99.79	99.41	99.38	98.33	100.08	98.98	98.50
Atomic %																		
Zn		48.62	49.09	48.96	48.89	48.13	49.37	48.01	48.30	48.85	48.03	48.60	48.64	48.79	48.60	48.77	49.29	48.43
Fe		0.76	0.59	0.63	0.63	0.69	0.65	0.70	0.73	0.53	0.71	0.65	0.68	0.66	0.68	0.73	0.72	0.69
Mn		0.13	0.06	0.07	0.06	0.04	0.05	0.05	0.10	0.06	0.10	0.12	0.17	0.13	0.15	0.11	0.08	0.06
Cd		0.13	0.13	0.13	0.11	0.14	0.16	0.14	0.16	0.15	0.09	0.17	0.17	0.14	0.12	0.13	0.15	0.13
Cu		0.66	0.34	0.19	0.23	0.38	0.15	0.24	0.30	0.21	0.72	0.50	0.25	0.19	0.19	0.64	0.33	0.08
Sn		0.03		0.01	0.00		0.00			0.02					0.02			
In													0.04	0.03				
Ag			0.03			0.02			0.02	0.03		0.02		0.06		0.02		0.02
Ga		0.09	0.12		0.25		0.16	0.15	0.11	0.09	0.05	0.07	0.20	0.05	0.10	0.11	0.03	0.04
S		49.58	49.65	50.01	49.83	50.59	49.47	50.71	50.29	50.08	50.30	49.86	49.84	49.95	50.14	49.51	49.40	50.54
Total		100.00	100.00	100.00	100.00	100.00	100.00	100.00	100.00	100.00	100.00	100.00	100.00	100.00	100.00	100.00	100.00	100.00
FeS		1.51	1.16	1.26	1.25	1.40	1.28	1.42	1.46	1.05	1.42	1.30	1.35	1.32	1.37	1.44	1.43	1.40
MnS		0.26	0.12	0.14	0.13	0.08	0.10	0.10	0.19	0.12	0.20	0.25	0.35	0.27	0.29	0.21	0.16	0.12
CdS		0.27	0.27	0.26	0.23	0.27	0.31	0.28	0.31	0.29	0.19	0.35	0.33	0.27	0.25	0.25	0.29	0.27

APPENDIX D

GALENA MINOR AND MAJOR ELEMENT

COMPOSITION

Sample Name		KTD194-12 86.55m (A09)									KTD194-12 109.35m (A11)				
Sample Point		A09-C1-1	A09-C1-2	A09-C1-5	A09-C1-10	A09-C1-11	A09-C1-12	A09-C1-16	A09-C1-26	A09-C1-28	A11-C1-6	A11-C1-8	A11-C1-9	A11-C1-11	A11-C1-12
Occurrence		overgrowth around pyrite	overgrowth around pyrite	overgrowth around pyrite	overgrowth around pyrite	overgrowth around pyrite	overgrowth around pyrite	overgrowth around pyrite	overgrowth around pyrite	overgrowth around pyrite	infill between quartz	infill between quartz	infill between quartz	infill between quartz	infill between quartz
Weight %	L.L.D. %														
Pb	0.08	84.81	86.86	84.04	86.11	86.64	85.28	84.75	85.94	84.25	85.19	86.02	85.92	86.00	85.66
Bi	0.07	0.61	0.67	0.68	0.56	0.85	0.39	0.21	0.28	0.67	0.16	0.17	0.26	0.14	<0.07
Cu	0.02	0.03	0.05	0.04	<0.02	<0.02	<0.02	<0.02	<0.02	0.03	<0.02	<0.02	0.06	<0.02	<0.02
Ag	0.02	0.22	0.16	0.09	0.09	0.22	0.07	<0.02	0.04	0.18	<0.02	<0.02	<0.02	<0.02	<0.02
Se	0.03	0.10	0.05	0.14	0.06	0.05	0.07	<0.03	<0.03	<0.03	<0.03	<0.03	<0.03	<0.03	<0.03
Sn	0.01	<0.01	0.03	0.02	<0.01	<0.01	<0.01	<0.01	0.02	<0.01	<0.01	<0.01	<0.01	<0.01	0.03
Sb	0.02	<0.02	<0.02	<0.02	<0.02	<0.02	<0.02	<0.02	<0.02	<0.02	<0.02	<0.02	<0.02	<0.02	<0.02
As	0.05	<0.05	<0.05	<0.05	<0.05	<0.05	<0.05	<0.05	<0.05	<0.05	<0.05	<0.05	<0.05	<0.05	<0.05
S	0.01	13.26	13.59	13.04	13.39	13.65	13.42	13.21	13.32	13.09	13.55	13.30	13.21	13.26	13.41
Total		99.03	101.40	98.04	100.21	101.42	99.22	98.17	99.60	98.21	98.90	99.49	99.44	99.39	99.09
Atomic %															
Pb		49.34	49.37	49.53	49.64	49.15	49.39	49.76	49.85	49.57	49.27	49.98	50.04	50.06	49.67
Bi		0.35	0.38	0.39	0.32	0.48	0.22	0.12	0.16	0.39	0.09	0.10	0.15	0.08	0.04
Cu		0.06	0.09	0.07					0.01	0.05			0.12		0.03
Ag		0.25	0.17	0.11	0.10	0.23	0.08		0.05	0.20					
Se		0.15	0.07	0.21	0.09	0.08	0.10			0.04	0.01				
Sn			0.03	0.02		0.00	0.00		0.02			0.01			0.03
Sb															
As															
S		49.86	49.89	49.67	49.85	50.05	50.21	50.12	49.91	49.74	50.62	49.91	49.69	49.86	50.24
Total		100.00	100.00	100.00	100.00	100.00	100.00	100.00	100.00	100.00	100.00	100.00	100.00	100.00	100.00

Sample Name		KTD194-12 109.35m (A11)								KTD194-12 135.60m (A16)					
Sample Point		A11-C1-13	A11-C1-14	A11-C1-15	A11-C1-16	A11-C1-17	A11-C1-18	A11-C1-19	A11-C1-20	A16-C1-3	A16-C1-4	A16-C1-5	A16-C1-6	A16-C1-7	A16-C1-18
Occurrence		infill between quartz	infill between quartz	infill between quartz	infill between quartz	infill between quartz	infill between quartz	infill between quartz	infill between quartz	inclusion in sphalerite	inclusion in sphalerite	inclusion in sphalerite	inclusion in sphalerite	inclusion in sphalerite	replaced by chalcopyrite
Weight %	L.L.D. %														
Pb	0.08	85.46	85.23	85.79	86.84	85.87	84.98	85.21	84.68	84.13	85.06	84.19	86.00	84.30	84.93
Bi	0.07	0.19	0.16	0.21	0.12	0.18	0.12	0.09	0.09	0.54	0.49	0.59	0.58	0.59	<0.07
Cu	0.02	<0.02	0.03	<0.02	0.02	<0.02	0.03	<0.02	<0.02	0.24	0.05	0.02	0.17	0.11	0.06
Ag	0.02	<0.02	<0.02	<0.02	<0.02	<0.02	<0.02	<0.02	<0.02	0.18	0.14	0.12	0.14	0.11	<0.02
Se	0.03	<0.03	<0.03	<0.03	<0.03	<0.03	<0.03	<0.03	<0.03	<0.03	<0.03	<0.03	<0.03	<0.03	<0.03
Sn	0.01	<0.01	<0.01	<0.01	<0.01	<0.01	<0.01	<0.01	<0.01	<0.01	0.01	<0.01	<0.01	<0.01	<0.01
Sb	0.02	<0.02	<0.02	<0.02	<0.02	<0.02	<0.02	<0.02	<0.02	<0.02	<0.02	<0.02	<0.02	<0.02	<0.02
As	0.05	<0.05	<0.05	<0.05	<0.05	<0.05	<0.05	<0.05	<0.05	<0.05	<0.05	<0.05	<0.05	<0.05	<0.05
S	0.01	13.15	13.30	13.26	13.48	13.39	13.28	13.33	13.34	13.33	13.44	13.15	13.44	13.43	13.27
Total		98.80	98.72	99.26	100.47	99.44	98.40	98.63	98.10	98.42	99.20	98.06	100.33	98.54	98.25
Atomic %															
Pb		50.09	49.71	49.96	49.87	49.76	49.70	49.69	49.53	48.94	49.20	49.52	49.37	48.95	49.71
Bi		0.11	0.09	0.12	0.07	0.10	0.07	0.05	0.05	0.31	0.28	0.34	0.33	0.34	0.01
Cu		0.02	0.06		0.04	0.03	0.06	0.03	0.03	0.46	0.09	0.05	0.31	0.22	0.11
Ag					0.00					0.20	0.16	0.13	0.15	0.12	
Se											0.02				
Sn							0.00				0.01		0.00		0.01
Sb															
As															
S		49.79	50.13	49.91	50.02	50.11	50.17	50.23	50.39	50.09	50.23	49.96	49.84	50.37	50.17
Total		100.00	100.00	100.00	100.00	100.00	100.00	100.00	100.00	100.00	100.00	100.00	100.00	100.00	100.00

Sample Name		KTD194-12 135.60m (A16)		KTDH04 85.30m (C11)										
Sample Point		A16-C1-19	A16-C1-20	C11-C1-3	C11-C1-4	C11-C1-7	C11-C1-10	C11-C1-15	C11-C1-16	C11-C1-22	C11-C1-23	C11-C1-24	C11-C1-29	C11-C1-30	C11-C1-33
Occurrence		replaced by chalcopyrite	replaced by chalcopyrite	replacing pyrite	replacing pyrite	replacing pyrite	replacing pyrite	replacing pyrite	replacing pyrite	replacing pyrite	replacing pyrite	replacing pyrite	replacing pyrite	replacing pyrite	replacing sphalerite
Weight %	L.L.D. %														
Pb	0.08	86.11	85.62	85.10	84.95	85.01	85.80	85.15	85.46	85.41	85.24	85.59	85.97	84.68	85.42
Bi	0.07	0.16	0.15	0.20	0.08	<0.07	<0.07	0.15	0.21	0.18	0.18	<0.07	0.12	0.22	<0.07
Cu	0.02	0.04	0.06	0.05	<0.02	<0.02	<0.02	<0.02	<0.02	<0.02	0.07	<0.02	<0.02	<0.02	<0.02
Ag	0.02	<0.02	<0.02	<0.02	<0.02	<0.02	<0.02	<0.02	<0.02	<0.02	<0.02	<0.02	<0.02	<0.02	<0.02
Se	0.03	<0.03	<0.03	<0.03	<0.03	<0.03	<0.03	<0.03	<0.03	<0.03	<0.03	<0.03	<0.03	<0.03	<0.03
Sn	0.01	0.03	<0.01	<0.01	<0.01	<0.01	<0.01	<0.01	<0.01	<0.01	<0.01	<0.01	0.01	0.02	<0.01
Sb	0.02	<0.02	<0.02	<0.02	<0.02	<0.02	<0.02	<0.02	<0.02	<0.02	<0.02	<0.02	<0.02	<0.02	<0.02
As	0.05	<0.05	<0.05	<0.05	<0.05	<0.05	<0.05	<0.05	<0.05	<0.05	<0.05	<0.05	<0.05	<0.05	<0.05
S	0.01	13.45	13.27	13.28	13.26	13.23	13.08	13.13	13.18	12.96	13.44	13.47	13.45	13.18	13.33
Total		99.78	99.10	98.62	98.29	98.24	98.88	98.43	98.85	98.56	98.92	99.06	99.55	98.09	98.76
Atomic %															
Pb		49.68	49.87	49.68	49.77	49.82	50.36	50.04	50.02	50.44	49.42	49.57	49.68	49.78	49.77
Bi		0.09	0.09	0.11	0.05	0.03	0.02	0.09	0.12	0.10	0.10		0.07	0.13	0.04
Cu		0.08	0.11	0.09		0.02	0.02	0.01	0.03		0.13		0.01	0.03	
Ag															
Se						0.03			0.00						
Sn		0.03		0.01								0.01	0.01	0.02	
Sb															
As															
S		50.12	49.93	50.10	50.19	50.10	49.61	49.86	49.83	49.46	50.35	50.42	50.23	50.05	50.19
Total		100.00	100.00	100.00	100.00	100.00	100.00	100.00	100.00	100.00	100.00	100.00	100.00	100.00	100.00

Sample Name		KTDH04 85.30m (C11)					KTDH04 92.05m (C15)								
Sample Point		C11-C1-35	C11-C1-36	C11-C1-38	C11-C1-39	C11-C1-40	C15-C1-4	C15-C1-5	C15-C1-6	C15-C1-7	C15-C1-8	C15-C1-9	C15-C1-10	C15-C1-11	C15-C1-12
Occurrence		replacing sphalerite	replacing sphalerite	replacing sphalerite	replacing sphalerite	replacing sphalerite	hosted in sphalerite	hosted in sphalerite	hosted in sphalerite	hosted in sphalerite	hosted in sphalerite	hosted in sphalerite	hosted in sphalerite	hosted in sphalerite	hosted in sphalerite
Weight %	L.L.D. %														
Pb	0.08	84.77	84.84	84.96	84.63	85.77	86.10	86.27	86.25	86.37	86.68	85.92	87.24	86.06	85.90
Bi	0.07	0.13	0.11	<0.07	0.15	<0.07	0.22	0.14	0.13	0.17	<0.07	0.17	0.09	0.13	0.21
Cu	0.02	<0.02	<0.02	<0.02	<0.02	0.06	<0.02	<0.02	<0.02	<0.02	<0.02	<0.02	<0.02	<0.02	<0.02
Ag	0.02	<0.02	<0.02	<0.02	<0.02	<0.02	<0.02	<0.02	<0.02	<0.02	<0.02	<0.02	<0.02	<0.02	<0.02
Se	0.03	<0.03	<0.03	<0.03	<0.03	<0.03	<0.03	<0.03	<0.03	<0.03	<0.03	<0.03	<0.03	<0.03	<0.03
Sn	0.01	<0.01	<0.01	<0.01	<0.01	<0.01	<0.01	0.03	0.01	0.03	0.31	<0.01	0.01	<0.01	<0.01
Sb	0.02	<0.02	<0.02	<0.02	<0.02	<0.02	<0.02	<0.02	<0.02	<0.02	<0.02	<0.02	<0.02	<0.02	<0.02
As	0.05	<0.05	<0.05	<0.05	<0.05	<0.05	<0.05	<0.05	<0.05	<0.05	<0.05	<0.05	<0.05	<0.05	<0.05
S	0.01	13.14	13.27	13.08	13.32	13.18	13.40	13.11	13.30	13.19	13.24	13.42	13.40	13.07	13.23
Total		98.04	98.22	98.04	98.10	99.00	99.72	99.54	99.69	99.76	100.23	99.50	100.74	99.26	99.34
Atomic %															
Pb		49.93	49.69	50.11	49.53	50.12	49.80	50.41	50.06	50.28	50.17	49.73	50.15	50.43	50.04
Bi		0.07	0.06	0.03	0.09	0.03	0.13	0.08	0.07	0.10	0.01	0.10	0.05	0.07	0.12
Cu			0.03	0.01	0.01	0.12	0.01	0.01					0.01		0.02
Ag															
Se															0.01
Sn		0.01						0.03	0.01	0.03	0.31		0.01	0.01	0.00
Sb															
As															
S		49.99	50.21	49.84	50.38	49.74	50.06	49.48	49.86	49.59	49.51	50.18	49.78	49.49	49.80
Total		100.00	100.00	100.00	100.00	100.00	100.00	100.00	100.00	100.00	100.00	100.00	100.00	100.00	100.00

Sample Name		KTDH04 92.05m (C15)					KTDH04 93.50m (C16)								
Sample Point		C15-C1-13	C15-C1-14	C15-C1-16	C15-C1-17	C15-C1-18	C16-C1-1	C16-C1-2	C16-C1-3	C16-C1-4	C16-C1-5	C16-C1-6	C16-C1-7	C16-C1-8	C16-C1-9
Occurrence		hosted in sphalerite	hosted in sphalerite	hosted in sphalerite	hosted in sphalerite	hosted in sphalerite	hosted in sphalerite	hosted in sphalerite	hosted in sphalerite	hosted in sphalerite	hosted in sphalerite	hosted in sphalerite	hosted in sphalerite	hosted in sphalerite	hosted in sphalerite
Weight %	L.L.D. %														
Pb	0.08	87.26	86.58	85.29	85.99	86.16	85.36	87.26	87.02	84.88	86.58	86.74	87.08	87.93	87.14
Bi	0.07	0.22	0.31	<0.07	0.11	<0.07	0.19	0.16	0.12	0.18	0.22	0.25	<0.07	0.32	0.13
Cu	0.02	<0.02	0.03	<0.02	<0.02	<0.02	<0.02	0.05	<0.02	<0.02	0.02	<0.02	<0.02	<0.02	<0.02
Ag	0.02	<0.02	<0.02	<0.02	<0.02	<0.02	<0.02	<0.02	<0.02	<0.02	<0.02	<0.02	<0.02	<0.02	<0.02
Se	0.03	<0.03	<0.03	<0.03	<0.03	<0.03	<0.03	<0.03	<0.03	<0.03	<0.03	<0.03	<0.03	<0.03	<0.03
Sn	0.01	<0.01	<0.01	0.01	0.01	0.04	<0.01	0.02	<0.01	<0.01	<0.01	<0.01	<0.01	0.01	<0.01
Sb	0.02	<0.02	<0.02	<0.02	<0.02	<0.02	<0.02	<0.02	<0.02	<0.02	<0.02	<0.02	<0.02	<0.02	<0.02
As	0.05	<0.05	<0.05	<0.05	<0.05	<0.05	<0.05	<0.05	<0.05	<0.05	<0.05	<0.05	<0.05	<0.05	<0.05
S	0.01	13.45	13.35	13.27	13.23	13.28	13.21	13.18	13.34	12.99	13.38	13.51	13.36	13.18	13.31
Total		100.93	100.27	98.57	99.34	99.48	98.77	100.67	100.47	98.05	100.19	100.49	100.44	101.45	100.58
Atomic %															
Pb		50.04	49.99	49.87	50.12	50.07	49.93	50.48	50.21	50.22	49.95	49.78	50.22	50.70	50.30
Bi		0.13	0.18		0.06	0.02	0.11	0.09	0.07	0.11	0.12	0.14		0.19	0.08
Cu			0.05			0.02	0.02	0.10			0.05		0.01		
Ag															
Se		0.01						0.04	0.02		0.02				
Sn				0.01	0.01	0.04		0.02						0.01	0.00
Sb															
As															
S		49.82	49.78	50.12	49.81	49.84	49.94	49.28	49.71	49.67	49.86	50.08	49.77	49.11	49.62
Total		100.00	100.00	100.00	100.00	100.00	100.00	100.00	100.00	100.00	100.00	100.00	100.00	100.00	100.00

Sample Name		KTDH04 93.50m (C16)										KTDH04 93.85m (C17)			
Sample Point		C16-C1-10	C16-C1-11	C16-C1-12	C16-C1-13	C16-C2-2	C16-C2-3	C16-C2-4	C16-C2-5	C16-C2-6	C16-C2-7	C17-C1-1	C17-C1-2	C17-C1-3	C17-C1-4
Occurrence		hosted in sphalerite	hosted in sphalerite	hosted in sphalerite	hosted in sphalerite	replaced by chalcopyrite	replaced by chalcopyrite	replaced by chalcopyrite	replaced by chalcopyrite	replaced by chalcopyrite	replaced by chalcopyrite	hosted in sphalerite	hosted in sphalerite	hosted in sphalerite	hosted in sphalerite
Weight %	L.L.D. %														
Pb	0.08	86.55	86.34	85.78	86.41	86.02	86.19	86.43	87.04	85.91	88.15	87.53	84.89	85.94	85.27
Bi	0.07	0.09	0.19	0.45	0.16	0.23	0.23	<0.07	0.16	<0.07	0.27	<0.07	0.30	0.07	0.18
Cu	0.02	<0.02	0.04	<0.02	0.05	0.03	<0.02	0.05	0.04	0.09	<0.02	0.04	<0.02	<0.02	0.03
Ag	0.02	<0.02	<0.02	<0.02	<0.02	<0.02	<0.02	<0.02	<0.02	<0.02	<0.02	<0.02	<0.02	<0.02	<0.02
Se	0.03	<0.03	<0.03	<0.03	<0.03	<0.03	<0.03	<0.03	<0.03	<0.03	0.15	0.27	0.07	0.03	<0.03
Sn	0.01	<0.01	0.01	0.01	<0.01	<0.01	<0.01	<0.01	0.03	<0.01	<0.01	<0.01	0.02	0.01	0.02
Sb	0.02	<0.02	<0.02	<0.02	<0.02	<0.02	<0.02	<0.02	<0.02	<0.02	<0.02	0.26	<0.02	<0.02	<0.02
As	0.05	<0.05	<0.05	<0.05	<0.05	<0.05	<0.05	<0.05	<0.05	<0.05	<0.05	<0.05	<0.05	<0.05	<0.05
S	0.01	13.25	13.31	13.23	13.26	13.00	13.28	13.13	13.38	13.44	13.38	13.35	13.35	13.28	13.11
Total		99.89	99.89	99.47	99.88	99.29	99.70	99.61	100.65	99.44	101.95	101.45	98.63	99.33	98.62
Atomic %															
Pb		50.24	50.00	49.96	50.12	50.49	50.03	50.41	50.08	49.63	50.30	50.00	49.45	49.99	50.06
Bi		0.05	0.11	0.26	0.09	0.14	0.13	0.02	0.09	0.02	0.15		0.17	0.04	0.10
Cu			0.07		0.09	0.06		0.10	0.07	0.18		0.07	0.00		0.07
Ag				0.00											
Se							0.02				0.23	0.41	0.11	0.05	
Sn		0.01	0.01	0.01			0.00		0.03				0.02	0.01	0.02
Sb												0.25			
As															
S		49.70	49.81	49.77	49.70	49.32	49.82	49.48	49.72	50.17	49.32	49.26	50.25	49.90	49.74
Total		100.00	100.00	100.00	100.00	100.00	100.00	100.00	100.00	100.00	100.00	100.00	100.00	100.00	100.00

Sample Name		KTDH04 93.85m (C17)				KTDH04 101.40m (C20)									
Sample Point		C17-C1-5	C17-C1-6	C17-C1-7	C17-C1-9	C20-C2-1	C20-C2-2	C20-C2-3	C20-C2-4	C20-C1-1	C20-C1-2	C20-C1-3	C20-C1-4	C20-C1-14	C20-C1-16
Occurrence		hosted in sphalerite	hosted in sphalerite	hosted in sphalerite	replaced by chalcopyrite	infill between quartz	infill between quartz	infill between quartz	inclusion in pyrite	hosted in sphalerite	hosted in sphalerite	hosted in sphalerite	hosted in sphalerite	replaced by chalcopyrite	replaced by chalcopyrite
Weight %	L.L.D. %														
Pb	0.08	84.81	85.31	85.76	85.16	84.64	85.21	86.14	85.20	85.57	85.97	85.80	85.04	86.24	85.63
Bi	0.07	0.15	0.10	0.13	0.14	0.30	0.13	0.27	0.17	0.17	0.09	0.11	<0.07	0.12	0.15
Cu	0.02	<0.02	<0.02	<0.02	0.05	0.02	<0.02	<0.02	<0.02	0.03	<0.02	<0.02	<0.02	0.11	<0.02
Ag	0.02	<0.02	<0.02	<0.02	<0.02	<0.02	<0.02	<0.02	<0.02	<0.02	<0.02	<0.02	<0.02	<0.02	<0.02
Se	0.03	0.05	<0.03	<0.03	<0.03	<0.03	<0.03	<0.03	<0.03	<0.03	<0.03	<0.03	<0.03	<0.03	<0.03
Sn	0.01	0.03	<0.01	<0.01	<0.01	<0.01	<0.01	<0.01	<0.01	<0.01	<0.01	<0.01	<0.01	<0.01	<0.01
Sb	0.02	<0.02	<0.02	<0.02	<0.02	<0.02	<0.02	<0.02	<0.02	<0.02	<0.02	<0.02	<0.02	<0.02	<0.02
As	0.05	<0.05	<0.05	<0.05	<0.05	<0.05	<0.05	<0.05	<0.05	<0.05	<0.05	<0.05	<0.05	<0.05	<0.05
S	0.01	13.30	13.18	13.33	13.25	13.30	13.38	13.30	13.20	13.28	13.16	13.26	13.41	13.24	13.12
Total		98.33	98.59	99.22	98.58	98.26	98.72	99.72	98.57	99.04	99.22	99.17	98.45	99.71	98.90
Atomic %															
Pb		49.58	50.00	49.86	49.78	49.51	49.59	49.96	49.92	49.84	50.23	50.00	49.51	50.05	50.19
Bi		0.08	0.06	0.07	0.08	0.17	0.07	0.16	0.10	0.10	0.05	0.06	0.04	0.07	0.09
Cu			0.02	0.00	0.09	0.04	0.02	0.03	0.02	0.05			0.00	0.20	0.02
Ag														0.01	
Se		0.07			0.02					0.03	0.03				
Sn		0.03			0.00	0.01			0.01					0.00	0.01
Sb															
As															
S		50.24	49.92	50.06	50.03	50.27	50.31	49.85	49.96	49.98	49.68	49.94	50.45	49.66	49.70
Total		100.00	100.00	100.00	100.00	100.00	100.00	100.00	100.00	100.00	100.00	100.00	100.00	100.00	100.00

Sample Name		KTDH04 101.40m (C20)											KTDH04 199.30m (C37)		
Sample Point		C20-C1-17	C20-C1-19	C20-C1-20	C20-C1-21	C20-C1-22	C20-C1-23	C20-C1-24	C20-C1-25	C20-C1-26	C20-C1-27	C20-C1-28	C37-C1-8	C37-C1-9	C37-C1-10
Occurrence		replaced by chalcopyrite	replaced by chalcopyrite	replaced by chalcopyrite	replaced by chalcopyrite	replaced by chalcopyrite	replaced by chalcopyrite	replaced by chalcopyrite	replaced by chalcopyrite	replaced by chalcopyrite	replaced by chalcopyrite	replaced by chalcopyrite	replaced by chalcopyrite	replaced by chalcopyrite	replaced by chalcopyrite
Weight %	L.L.D. %														
Pb	0.08	84.81	85.33	85.23	85.46	84.87	84.63	87.26	86.33	84.84	84.72	85.82	84.66	86.83	85.15
Bi	0.07	0.18	0.19	0.21	0.24	0.20	0.18	0.20	<0.07	0.11	<0.07	0.14	0.20	0.27	0.23
Cu	0.02	0.03	0.04	0.26	<0.02	0.05	0.09	0.03	0.87	0.25	<0.02	0.09	0.03	0.08	<0.02
Ag	0.02	<0.02	<0.02	<0.02	<0.02	<0.02	<0.02	<0.02	<0.02	<0.02	<0.02	<0.02	<0.02	<0.02	<0.02
Se	0.03	<0.03	<0.03	<0.03	<0.03	<0.03	<0.03	<0.03	<0.03	<0.03	<0.03	<0.03	0.09	0.03	0.05
Sn	0.01	<0.01	0.03	<0.01	<0.01	<0.01	<0.01	<0.01	<0.01	<0.01	0.02	<0.01	<0.01	<0.01	<0.01
Sb	0.02	<0.02	<0.02	<0.02	<0.02	<0.02	<0.02	<0.02	<0.02	<0.02	<0.02	<0.02	<0.02	<0.02	<0.02
As	0.05	<0.05	<0.05	<0.05	<0.05	<0.05	<0.05	<0.05	<0.05	<0.05	<0.05	<0.05	<0.05	<0.05	<0.05
S	0.01	13.33	13.19	13.32	13.29	13.15	13.27	13.58	13.47	13.15	13.27	13.32	13.14	13.47	13.21
Total		98.35	98.77	99.02	98.98	98.27	98.17	101.06	100.67	98.34	98.01	99.36	98.11	100.68	98.64
Atomic %															
Pb		49.55	49.92	49.45	49.80	49.86	49.53	49.79	48.98	49.71	49.68	49.81	49.78	49.77	49.82
Bi		0.11	0.11	0.12	0.14	0.11	0.11	0.11	0.03	0.06	0.02	0.08	0.11	0.15	0.13
Cu		0.05	0.07	0.48	0.03	0.10	0.17	0.06	1.61	0.47		0.16	0.05	0.15	0.02
Ag															
Se													0.14	0.05	0.07
Sn			0.03								0.02				
Sb															
As						0.01									
S		50.30	49.87	49.94	50.03	49.92	50.20	50.04	49.39	49.76	50.27	49.95	49.92	49.88	49.95
Total		100.00	100.00	100.00	100.00	100.00	100.00	100.00	100.00	100.00	100.00	100.00	100.00	100.00	100.00

Sample Name		KTDH04 199.30m (C37)						KTDH04 227.40m (C41)							
Sample Point		C37-C1-11	C37-C1-12	C37-C1-14	C37-C1-16	C37-C1-17	C37-C1-18	C41-C1-1	C41-C1-2	C41-C1-3	C41-C1-4	C41-C1-5	C41-C1-6	C41-C1-7	C41-C1-8
Occurrence		replaced by chalcopyrite	replaced by chalcopyrite	replaced by chalcopyrite	replaced by chalcopyrite	replaced by chalcopyrite	replaced by chalcopyrite	hosted in sphalerite	hosted in sphalerite	hosted in sphalerite	hosted in sphalerite	hosted in sphalerite	hosted in sphalerite	hosted in sphalerite	hosted in sphalerite
Weight %	L.L.D. %														
Pb	0.08	86.08	86.89	85.18	84.98	84.80	85.82	87.78	87.03	86.53	87.07	87.35	87.16	86.69	87.97
Bi	0.07	0.12	<0.07	0.27	0.24	0.26	<0.07	0.24	0.18	0.17	0.15	0.21	0.20	0.22	0.11
Cu	0.02	<0.02	<0.02	0.04	0.04	0.15	0.35	<0.02	<0.02	<0.02	<0.02	<0.02	<0.02	0.02	<0.02
Ag	0.02	0.04	<0.02	<0.02	<0.02	<0.02	<0.02	<0.02	<0.02	<0.02	<0.02	<0.02	<0.02	<0.02	<0.02
Se	0.03	0.03	<0.03	<0.03	<0.03	<0.03	<0.03	<0.03	<0.03	<0.03	<0.03	<0.03	<0.03	<0.03	<0.03
Sn	0.01	<0.01	<0.01	<0.01	<0.01	<0.01	<0.01	0.02	<0.01	<0.01	0.03	<0.01	<0.01	<0.01	0.01
Sb	0.02	<0.02	<0.02	<0.02	<0.02	<0.02	<0.02	<0.02	<0.02	<0.02	<0.02	<0.02	<0.02	<0.02	<0.02
As	0.05	<0.05	<0.05	<0.05	<0.05	<0.05	<0.05	<0.05	<0.05	<0.05	<0.05	<0.05	<0.05	<0.05	<0.05
S	0.01	13.25	13.30	13.18	13.25	13.15	13.23	13.16	13.32	13.32	13.34	13.30	13.40	13.40	13.41
Total		99.51	100.19	98.66	98.51	98.36	99.40	101.20	100.54	100.02	100.59	100.85	100.75	100.33	101.50
Atomic %															
Pb		50.06	50.24	49.90	49.70	49.73	49.75	50.70	50.22	50.08	50.19	50.34	50.12	49.94	50.34
Bi		0.07	0.03	0.15	0.14	0.15	0.02	0.14	0.10	0.10	0.09	0.12	0.11	0.13	0.06
Cu			0.02	0.07	0.08	0.28	0.65		0.00	0.02	0.02	0.00	0.00	0.04	0.02
Ag		0.04													
Se		0.05	0.04	0.01	0.02	0.03	0.02	0.03						0.02	
Sn						0.00		0.02			0.03	0.00			0.01
Sb															
As															
S		49.77	49.67	49.87	50.07	49.80	49.55	49.11	49.67	49.81	49.68	49.53	49.77	49.88	49.57
Total		100.00	100.00	100.00	100.00	100.00	100.00	100.00	100.00	100.00	100.00	100.00	100.00	100.00	100.00

Sample Name		KTDH04 227.40m (C41)													
Sample Point		C41-C1-9	C41-C1-10	C41-C1-11	C41-C1-12	C41-C1-13	C41-C1-14	C41-C1-15	C41-C1-16	C41-C1-17	C41-C1-18	C41-C1-19	C41-C1-20	C41-C1-21	C41-C1-22
Occurrence		hosted in sphalerite	hosted in sphalerite	hosted in sphalerite	hosted in sphalerite	hosted in sphalerite	hosted in sphalerite	hosted in sphalerite	hosted in sphalerite	hosted in sphalerite	hosted in sphalerite	hosted in sphalerite	hosted in sphalerite	hosted in sphalerite	replaced by chalcopyrite
Weight %	L.L.D. %														
Pb	0.08	84.88	87.39	86.25	87.20	86.82	86.72	87.54	86.75	87.49	87.93	87.29	87.19	87.53	86.22
Bi	0.07	0.19	0.28	0.27	0.28	<0.07	0.16	0.17	0.15	0.28	0.24	0.21	0.09	0.29	0.12
Cu	0.02	0.05	0.04	0.04	<0.02	<0.02	<0.02	<0.02	<0.02	0.03	0.04	<0.02	<0.02	0.02	0.04
Ag	0.02	<0.02	<0.02	<0.02	<0.02	<0.02	<0.02	<0.02	<0.02	<0.02	<0.02	<0.02	<0.02	<0.02	<0.02
Se	0.03	<0.03	<0.03	0.05	<0.03	<0.03	<0.03	<0.03	<0.03	<0.03	<0.03	<0.03	<0.03	<0.03	<0.03
Sn	0.01	<0.01	<0.01	<0.01	<0.01	<0.01	<0.01	<0.01	<0.01	<0.01	<0.01	<0.01	<0.01	<0.01	<0.01
Sb	0.02	<0.02	<0.02	<0.02	<0.02	<0.02	<0.02	<0.02	<0.02	<0.02	<0.02	<0.02	<0.02	<0.02	<0.02
As	0.05	<0.05	<0.05	<0.05	<0.05	<0.05	<0.05	<0.05	<0.05	<0.05	<0.05	<0.05	<0.05	<0.05	<0.05
S	0.01	13.15	13.46	13.36	13.13	13.26	13.13	13.40	13.40	13.37	13.23	13.26	13.37	13.28	13.21
Total		98.26	101.17	99.98	100.61	100.08	100.01	101.11	100.30	101.17	101.43	100.76	100.65	101.12	99.60
Atomic %															
Pb		49.87	50.00	49.82	50.61	50.31	50.49	50.22	49.99	50.21	50.59	50.39	50.19	50.38	50.18
Bi		0.11	0.16	0.16	0.16	0.04	0.09	0.09	0.09	0.16	0.14	0.12	0.05	0.17	0.07
Cu		0.09	0.07	0.08			0.01		0.00	0.06	0.07	0.01		0.04	0.08
Ag		0.01	0.00												
Se				0.08					0.04		0.02	0.02	0.01	0.01	
Sn											0.00		0.01		
Sb															
As													0.01		
S		49.91	49.77	49.87	49.23	49.66	49.41	49.68	49.89	49.58	49.19	49.46	49.73	49.40	49.67
Total		100.00	100.00	100.00	100.00	100.00	100.00	100.00	100.00	100.00	100.00	100.00	100.00	100.00	100.00

Sample Name		KTDH04 227.40m (C41)											KTDH04 229.80m (C43)		
Sample Point		C41-C1-23	C41-C1-24	C41-C1-25	C41-C1-26	C41-C1-27	C41-C1-28	C41-C1-29	C41-C1-30	C41-C1-31	C41-C1-32	C41-C1-33	C43-C1-1	C43-C1-2	C43-C1-3
Occurrence		replaced by chalcopyrite	replaced by chalcopyrite	replaced by chalcopyrite	replaced by chalcopyrite	replaced by chalcopyrite	replaced by chalcopyrite	replaced by chalcopyrite	replaced by chalcopyrite	replaced by chalcopyrite	replaced by chalcopyrite	replaced by chalcopyrite	hosted in sphalerite	hosted in sphalerite	hosted in sphalerite
Weight %	L.L.D. %														
Pb	0.08	86.27	87.50	87.19	86.99	85.65	86.37	85.11	86.67	86.39	86.64	85.81	85.04	86.06	86.30
Bi	0.07	0.17	0.21	0.25	0.30	0.14	0.07	0.10	0.08	0.33	<0.07	0.28	0.24	<0.07	0.13
Cu	0.02	<0.02	0.02	<0.02	<0.02	0.03	0.15	0.09	0.11	0.39	<0.02	<0.02	<0.02	0.03	<0.02
Ag	0.02	<0.02	<0.02	<0.02	<0.02	<0.02	<0.02	<0.02	<0.02	<0.02	<0.02	<0.02	<0.02	<0.02	<0.02
Se	0.03	0.04	<0.03	<0.03	<0.03	<0.03	<0.03	<0.03	<0.03	<0.03	<0.03	<0.03	<0.03	<0.03	<0.03
Sn	0.01	0.02	<0.01	<0.01	<0.01	0.01	<0.01	<0.01	<0.01	<0.01	<0.01	0.04	<0.01	<0.01	<0.01
Sb	0.02	<0.02	<0.02	<0.02	<0.02	<0.02	<0.02	<0.02	<0.02	<0.02	<0.02	<0.02	<0.02	<0.02	<0.02
As	0.05	<0.05	<0.05	<0.05	<0.05	<0.05	<0.05	<0.05	<0.05	<0.05	<0.05	<0.05	<0.05	<0.05	<0.05
S	0.01	13.16	13.29	13.30	13.29	13.15	13.20	13.23	13.30	13.36	13.30	13.15	13.12	12.96	13.14
Total		99.65	101.02	100.74	100.57	98.98	99.79	98.53	100.17	100.48	99.94	99.27	98.41	99.05	99.57
Atomic %															
Pb		50.26	50.40	50.29	50.24	50.13	50.14	49.76	50.08	49.56	50.18	50.14	49.98	50.64	50.37
Bi		0.10	0.12	0.14	0.17	0.08	0.04	0.06	0.05	0.19	0.00	0.16	0.14	0.01	0.07
Cu		0.03	0.04			0.06	0.28	0.17	0.21	0.72	0.03	0.03	0.00	0.06	0.01
Ag															
Se		0.06			0.01			0.04			0.01		0.04	0.02	
Sn		0.02			0.01	0.01	0.01	0.00		0.00		0.04			
Sb															
As															
S		49.54	49.45	49.56	49.57	49.72	49.53	49.96	49.66	49.53	49.78	49.63	49.84	49.27	49.54
Total		100.00	100.00	100.00	100.00	100.00	100.00	100.00	100.00	100.00	100.00	100.00	100.00	100.00	100.00

Sample Name		KTDH04 229.80m (C43)													
Sample Point		C43-C1-4	C43-C1-5	C43-C1-6	C43-C1-7	C43-C1-8	C43-C1-9	C43-C1-10	C43-C1-11	C43-C1-12	C43-C1-13	C43-C1-14	C43-C1-15	C43-C1-16	C43-C1-17
Occurrence		hosted in sphalerite	hosted in sphalerite	hosted in sphalerite	hosted in sphalerite	hosted in sphalerite	hosted in sphalerite	hosted in sphalerite	hosted in sphalerite	hosted in sphalerite	hosted in sphalerite	hosted in sphalerite	hosted in sphalerite	hosted in sphalerite	hosted in sphalerite
Weight %	L.L.D. %														
Pb	0.08	86.32	86.77	84.86	85.29	85.58	86.28	86.44	85.05	86.62	86.94	86.42	84.89	85.07	86.28
Bi	0.07	0.23	0.16	0.23	0.11	0.12	0.18	0.19	<0.07	<0.07	0.17	0.20	0.30	0.08	0.18
Cu	0.02	<0.02	<0.02	<0.02	<0.02	<0.02	<0.02	<0.02	<0.02	<0.02	<0.02	<0.02	0.02	0.02	<0.02
Ag	0.02	<0.02	<0.02	<0.02	<0.02	<0.02	<0.02	<0.02	<0.02	<0.02	<0.02	<0.02	<0.02	<0.02	<0.02
Se	0.03	<0.03	<0.03	<0.03	0.04	<0.03	<0.03	<0.03	<0.03	<0.03	<0.03	0.09	0.06	<0.03	<0.03
Sn	0.01	<0.01	<0.01	<0.01	0.02	<0.01	<0.01	<0.01	<0.01	<0.01	<0.01	<0.01	<0.01	<0.01	<0.01
Sb	0.02	<0.02	<0.02	<0.02	<0.02	<0.02	<0.02	<0.02	<0.02	<0.02	<0.02	<0.02	<0.02	<0.02	<0.02
As	0.05	<0.05	<0.05	<0.05	<0.05	<0.05	<0.05	<0.05	<0.05	<0.05	<0.05	<0.05	<0.05	<0.05	<0.05
S	0.01	12.94	13.11	13.07	12.99	12.95	13.22	13.17	13.13	13.30	13.18	13.17	12.96	13.04	13.14
Total		99.49	100.03	98.17	98.45	98.66	99.67	99.81	98.18	99.92	100.28	99.87	98.23	98.21	99.60
Atomic %															
Pb		50.72	50.55	50.03	50.32	50.51	50.21	50.33	50.03	50.18	50.46	50.27	50.19	50.19	50.34
Bi		0.13	0.09	0.14	0.06	0.07	0.10	0.11	0.02	0.04	0.10	0.11	0.18	0.05	0.10
Cu		0.01	0.02	0.03	0.01			0.01	0.02				0.04	0.04	0.02
Ag												0.01			
Se					0.06	0.01			0.00		0.03	0.13	0.09		
Sn		0.00			0.02	0.01								0.01	0.00
Sb															
As															
S		49.14	49.34	49.80	49.53	49.39	49.69	49.54	49.92	49.78	49.41	49.48	49.51	49.72	49.53
Total		100.00	100.00	100.00	100.00	100.00	100.00	100.00	100.00	100.00	100.00	100.00	100.00	100.00	100.00

Sample Name		KTDH04 229.80m (C43)								KTDH04 232.30m (C44)					
Sample Point		C43-C1-19	C43-C1-20	C43-C1-21	C43-C1-22	C43-C2-6	C43-C2-7	C43-C2-9	C43-C2-11	C44-C3-1	C44-C3-2	C44-C3-3	C44-C3-4	C44-C3-5	C44-C3-6
Occurrence		replaced by chalcopyrite	replaced by chalcopyrite	replaced by chalcopyrite	replaced by chalcopyrite	inclusion in chalcopyrite	inclusion in chalcopyrite	inclusion in chalcopyrite	inclusion in chalcopyrite	infill between anhydrite and gypsum	infill between anhydrite and gypsum	infill between anhydrite and gypsum	infill between anhydrite and gypsum	infill between anhydrite and gypsum	infill between anhydrite and gypsum
Weight %	L.L.D. %														
Pb	0.08	84.86	86.89	87.11	85.72	83.18	84.15	77.45	77.19	86.63	86.66	86.74	86.09	85.41	86.26
Bi	0.07	0.34	0.22	0.21	0.25	1.49	1.31	1.30	1.47	<0.07	0.11	0.16	0.13	0.14	0.11
Cu	0.02	0.10	0.08	<0.02	<0.02	0.79	1.49	4.14	4.49	<0.02	0.04	<0.02	<0.02	<0.02	0.03
Ag	0.02	<0.02	<0.02	<0.02	<0.02	0.46	0.54	0.48	0.51	<0.02	<0.02	<0.02	<0.02	<0.02	<0.02
Se	0.03	0.09	0.14	0.09	0.07	0.44	0.44	0.38	0.69	<0.03	<0.03	<0.03	<0.03	<0.03	<0.03
Sn	0.01	<0.01	<0.01	<0.01	0.01	<0.01	<0.01	<0.01	<0.01	<0.01	<0.01	<0.01	<0.01	<0.01	0.02
Sb	0.02	<0.02	<0.02	<0.02	<0.02	<0.02	<0.02	<0.02	<0.02	<0.02	<0.02	<0.02	<0.02	<0.02	<0.02
As	0.05	<0.05	<0.05	<0.05	<0.05	<0.05	<0.05	<0.05	<0.05	<0.05	<0.05	<0.05	<0.05	<0.05	<0.05
S	0.01	12.95	13.30	13.22	13.04	13.13	13.29	14.67	14.09	13.12	13.30	13.33	13.45	13.30	13.31
Total		98.33	100.64	100.64	99.09	99.48	101.21	98.43	98.43	99.75	100.11	100.23	99.67	98.86	99.73
Atomic %															
Pb		50.09	50.02	50.33	50.30	47.78	47.17	40.99	41.25	50.55	50.13	50.14	49.71	49.80	49.99
Bi		0.20	0.12	0.12	0.14	0.85	0.73	0.68	0.78	0.00	0.06	0.09	0.07	0.08	0.07
Cu		0.19	0.14	0.04	0.02	1.47	2.72	7.15	7.82	0.01	0.08		0.03		0.05
Ag		0.02				0.50	0.58	0.48	0.52						
Se		0.13	0.22	0.14	0.11	0.66	0.64	0.53	0.97		0.04			0.02	0.02
Sn		0.00	0.01		0.01						0.00		0.00		0.02
Sb															
As															
S		49.37	49.48	49.37	49.43	48.73	48.15	50.17	48.66	49.45	49.69	49.77	50.18	50.10	49.85
Total		100.00	100.00	100.00	100.00	100.00	100.00	100.00	100.00	100.00	100.00	100.00	100.00	100.00	100.00

Sample Name		KTDH04 232.30m (C44)													
Sample Point		C44-C3-7	C44-C3-8	C44-C3-9	C44-C3-10	C44-C3-11	C44-C3-12	C44-C3-13	C44-C3-14	C44-C3-15	C44-C3-16	C44-C3-17	C44-C3-18	C44-C3-19	C44-C3-20
Occurrence		infill between anhydrite and gypsum	infill between anhydrite and gypsum	infill between anhydrite and gypsum	infill between anhydrite and gypsum	infill between anhydrite and gypsum	infill between anhydrite and gypsum	infill between anhydrite and gypsum	infill between anhydrite and gypsum	infill between anhydrite and gypsum	infill between anhydrite and gypsum	infill between anhydrite and gypsum	infill between anhydrite and gypsum	infill between anhydrite and gypsum	infill between anhydrite and gypsum
Weight %	L.L.D. %														
Pb	0.08	86.02	86.35	86.20	85.79	85.29	86.07	85.86	86.72	86.34	85.52	86.41	86.31	86.28	86.89
Bi	0.07	0.14	0.18	<0.07	0.27	0.10	0.16	0.14	0.17	<0.07	0.19	0.17	0.13	0.23	0.08
Cu	0.02	<0.02	<0.02	<0.02	<0.02	<0.02	<0.02	<0.02	0.03	<0.02	0.04	<0.02	<0.02	<0.02	<0.02
Ag	0.02	<0.02	<0.02	<0.02	<0.02	<0.02	<0.02	<0.02	0.06	<0.02	<0.02	<0.02	<0.02	<0.02	<0.02
Se	0.03	<0.03	0.05	<0.03	<0.03	<0.03	<0.03	<0.03	<0.03	0.04	<0.03	<0.03	<0.03	<0.03	0.04
Sn	0.01	<0.01	<0.01	0.01	0.02	<0.01	<0.01	<0.01	<0.01	<0.01	0.03	<0.01	<0.01	<0.01	<0.01
Sb	0.02	<0.02	<0.02	<0.02	<0.02	<0.02	<0.02	<0.02	<0.02	<0.02	<0.02	<0.02	<0.02	<0.02	<0.02
As	0.05	<0.05	<0.05	<0.05	<0.05	<0.05	<0.05	<0.05	<0.05	<0.05	<0.05	<0.05	<0.05	<0.05	<0.05
S	0.01	13.40	13.23	13.33	13.19	13.34	13.50	13.28	13.48	13.41	13.44	13.34	13.43	13.42	13.39
Total		99.56	99.80	99.54	99.27	98.72	99.73	99.27	100.46	99.79	99.22	99.92	99.87	99.93	100.40
Atomic %															
Pb		49.78	50.17	50.01	50.08	49.70	49.62	49.98	49.79	49.85	49.51	50.01	49.83	49.81	50.06
Bi		0.08	0.10		0.16	0.06	0.09	0.08	0.10	0.03	0.11	0.10	0.07	0.13	0.04
Cu		0.01				0.02	0.02		0.05	0.03	0.08			0.02	
Ag									0.07						
Se			0.07			0.03		0.00		0.05					0.07
Sn			0.00	0.01	0.02		0.00				0.03				0.00
Sb															
As															
S		50.12	49.66	49.97	49.74	50.20	50.27	49.94	50.00	50.04	50.27	49.89	50.10	50.04	49.83
Total		100.00	100.00	100.00	100.00	100.00	100.00	100.00	100.00	100.00	100.00	100.00	100.00	100.00	100.00

Sample Name		KTDH04 232.30m (C44)												
Sample Point		C44-C3-21	C44-C3-22	C44-C3-23	C44-C1-1	C44-C1-2	C44-C1-3	C44-C1-4	C44-C1-5	C44-C2-1	C44-C2-3	C44-C2-4	C44-C2-5	C44-C2-6	C44-C2-7
Occurrence		infill between anhydrite and gypsum	infill between anhydrite and gypsum	infill between anhydrite and gypsum	replaced by chalcopyrite	replaced by chalcopyrite	replaced by chalcopyrite	replaced by chalcopyrite	replaced by chalcopyrite	replaced by chalcopyrite	replaced by chalcopyrite	replaced by chalcopyrite	replaced by chalcopyrite	replaced by chalcopyrite	replaced by chalcopyrite
Weight %	L.L.D. %														
Pb	0.08	86.87	86.55	86.09	87.29	86.91	87.41	86.57	85.68	86.27	85.99	86.13	86.61	86.86	86.18
Bi	0.07	0.22	0.14	<0.07	0.12	0.24	<0.07	0.12	0.11	0.14	0.09	0.15	0.32	0.18	0.18
Cu	0.02	0.04	<0.02	<0.02	<0.02	<0.02	<0.02	<0.02	<0.02	<0.02	0.02	0.03	<0.02	0.03	<0.02
Ag	0.02	<0.02	<0.02	<0.02	<0.02	<0.02	<0.02	<0.02	<0.02	<0.02	<0.02	<0.02	<0.02	<0.02	<0.02
Se	0.03	<0.03	0.05	<0.03	<0.03	<0.03	<0.03	<0.03	<0.03	<0.03	<0.03	<0.03	<0.03	<0.03	<0.03
Sn	0.01	<0.01	<0.01	<0.01	0.02	<0.01	<0.01	<0.01	<0.01	<0.01	<0.01	<0.01	<0.01	<0.01	<0.01
Sb	0.02	<0.02	<0.02	<0.02	<0.02	<0.02	<0.02	<0.02	<0.02	<0.02	<0.02	<0.02	<0.02	<0.02	<0.02
As	0.05	<0.05	<0.05	<0.05	<0.05	<0.05	<0.05	<0.05	<0.05	<0.05	<0.05	<0.05	<0.05	<0.05	<0.05
S	0.01	13.38	13.39	13.62	13.71	13.45	13.56	13.40	13.41	13.43	13.42	13.35	13.45	13.43	13.43
Total		100.51	100.12	99.71	101.13	100.60	100.98	100.08	99.19	99.84	99.52	99.66	100.38	100.50	99.80
Atomic %															
Pb		50.02	49.94	49.41	49.57	49.94	49.92	49.97	49.66	49.80	49.74	49.90	49.81	49.94	49.77
Bi		0.13	0.08	0.04	0.07	0.14	0.04	0.07	0.06	0.08	0.05	0.08	0.18	0.10	0.10
Cu		0.07		0.04	0.03				0.02	0.03	0.04	0.06	0.03	0.05	
Ag															
Se			0.07	0.01					0.04						
Sn					0.01						0.00		0.01		
Sb															
As															
S		49.78	49.91	50.51	50.31	49.93	50.05	49.96	50.22	50.09	50.16	49.96	49.97	49.90	50.13
Total		100.00	100.00	100.00	100.00	100.00	100.00	100.00	100.00	100.00	100.00	100.00	100.00	100.00	100.00

Sample Name		KTDH04 232.30m (C44)					
Sample Point		C44-C2-8	C44-C2-9	C44-C2-10	C44-C2-11	C44-C2-12	C44-C2-13
Occurrence		inclusion in chalcopyrite	inclusion in chalcopyrite	inclusion in chalcopyrite	inclusion in chalcopyrite	inclusion in chalcopyrite	inclusion in chalcopyrite
Weight %	L.L.D. %						
Pb	0.08	86.54	85.47	85.89	87.08	86.88	86.31
Bi	0.07	0.21	0.30	<0.07	0.21	0.21	0.14
Cu	0.02	0.55	0.47	0.46	0.80	1.02	0.52
Ag	0.02	<0.02	<0.02	<0.02	<0.02	<0.02	<0.02
Se	0.03	<0.03	<0.03	<0.03	<0.03	<0.03	<0.03
Sn	0.01	<0.01	<0.01	<0.01	<0.01	<0.01	0.01
Sb	0.02	<0.02	<0.02	<0.02	<0.02	<0.02	<0.02
As	0.05	<0.05	<0.05	<0.05	<0.05	<0.05	<0.05
S	0.01	13.58	13.28	13.36	13.58	13.62	13.47
Total		100.87	99.53	99.71	101.68	101.73	100.44
Atomic %							
Pb		49.07	49.37	49.43	49.00	48.68	49.26
Bi		0.12	0.17	0.02	0.12	0.12	0.08
Cu		1.01	0.89	0.86	1.47	1.86	0.97
Ag							
Se		0.04		0.01	0.03	0.02	0.01
Sn							0.01
Sb							
As							
S		49.76	49.57	49.69	49.38	49.32	49.67
Total		100.00	100.00	100.00	100.00	100.00	100.00

APPENDIX E

FLUID INCLUSION MICROTHERMOMETRY DATA

Sample ID	Depth from present-day surface (m)	Elevation from present-day mean sea level (m)	Sample type	FIA number	T_f	T_m	Salinity	T_h
KTDH24 6.50 m (F01)	6.1	275.9	vein	1Qp1	-53.8	-5.4	8.4	267.6
KTDH24 6.50 m (F01)	6.1	275.9	vein	1Qp1	-51.0	-5.4	8.4	261.2
KTDH24 6.50 m (F01)	6.1	275.9	vein	1Qp1	-52.7	-5.4	8.4	246.4
KTDH24 6.50 m (F01)	6.1	275.9	vein	1Qp1	-53.5	-5.4	8.4	256.1
KTDH24 6.50 m (F01)	6.1	275.9	vein	1Qp2	-54.9	-3.1	5.1	248.2
KTDH24 6.50 m (F01)	6.1	275.9	vein	1Qp2	-57.0	-3.3	5.4	207.8
KTDH24 6.50 m (F01)	6.1	275.9	vein	1Qp2		-3.1	5.1	240.3
KTDH24 6.50 m (F01)	6.1	275.9	vein	1Qp2	-57.9	-3.5	5.7	243.6
KTDH24 6.50 m (F01)	6.1	275.9	vein	1Qp2	-57.9	-3.5	5.7	242.0
KTDH24 6.50 m (F01)	6.1	275.9	vein	1Qp2	-58.4	-3.5	5.7	240.8
KTDH24 6.50 m (F01)	6.1	275.9	vein	1Qp2	-58.4	-3.5	5.7	242.0
KTDH24 9.20 m (F02)	8.6	273.3	vein	1Qd1	-53.2	-3.7	6.0	221.1
KTDH24 9.20 m (F02)	8.6	273.3	vein	1Qd1	-60.7	-3.6	5.9	237.9
KTDH24 9.20 m (F02)	8.6	273.3	vein	1Qd1	-30.1	-3.6	5.9	202.9
KTDH24 9.20 m (F02)	8.6	273.3	vein	1Qd2	-56.4	-3.4	5.6	221.4
KTDH24 9.20 m (F02)	8.6	273.3	vein	1Qd2	-58.2	-3.8	6.2	219.4
KTDH24 9.20 m (F02)	8.6	273.3	vein	1Qd2	-57.4	-3.5	5.7	207.4
KTDH24 9.20 m (F02)	8.6	273.3	vein	1Qd3	-55.7	-3.3	3.4	219.0
KTDH24 9.20 m (F02)	8.6	273.3	vein	1Qd3	-56.9	-3.3	3.4	204.0
KTDH24 9.20 m (F02)	8.6	273.3	vein	1Qd3		-3.3	3.4	241.5
KTDH24 9.20 m (F02)	8.6	273.3	vein	1Qd3	-57.2	-3.3	3.4	226.8
KTDH24 9.20 m (F02)	8.6	273.3	vein	1Qd4	-41.9	-3.9	6.3	222.3
KTDH24 9.20 m (F02)	8.6	273.3	vein	1Qd4	-50.7	-3.8	6.2	233.5
KTDH24 9.20 m (F02)	8.6	273.3	vein	1Qd4		-3.7	6.0	262.6
KTDH24 18.70 m (F05)	17.6	264.4	vein	1Qd5	-41.6	-3.6	5.86	272.2
KTDH24 18.70 m (F05)	17.6	264.4	vein	1Qd5	-43.5	-3.1	5.11	275.3
KTDH24 18.70 m (F05)	17.6	264.4	vein	1Qd5	-45.9	-3.1	5.11	275.7
KTDH24 18.70 m (F05)	17.6	264.4	vein	1Qd5	-45.1	-3.8	6.16	278.7
KTDH24 18.70 m (F05)	17.6	264.4	vein	1Qd6	-46.7	-3.4	5.56	240.6
KTDH24 18.70 m (F05)	17.6	264.4	vein	1Qd6	-55.2	-3.1	5.11	227.2
KTDH24 18.70 m (F05)	17.6	264.4	vein	1Qd7		-3.7	6.01	256.1
KTDH24 18.70 m (F05)	17.6	264.4	vein	1Qd7	-65.6	-3.7	6.01	254.6
KTDH23 29.25 m (J01)	24.8	256.1	vein	2Qp12	-42.4	-2.7	4.49	247.1
KTDH23 29.25 m (J01)	24.8	256.1	vein	2Qp12	-42.9	-2.7	4.49	237.2
KTDH23 29.25 m (J01)	24.8	256.1	vein	2Qp12	-40.7	-2.7	4.49	238.9
KTDH23 29.25 m (J01)	24.8	256.1	vein	2Qp12	-43.5	-2.7	4.49	253.8
KTDH23 29.25 m (J01)	24.8	256.1	vein	2Qp12	-42.2	-2.8	4.65	279.9
KTDH23 29.25 m (J01)	24.8	256.1	vein	2Qd1	-44.4	-3.0	4.96	261.0
KTDH23 29.25 m (J01)	24.8	256.1	vein	2Qd1	-44.8	-3.0	4.96	256.5
KTDH23 29.25 m (J01)	24.8	256.1	vein	2Qd2	-44.8	-3.0	4.96	267.5
KTDH23 29.25 m (J01)	24.8	256.1	vein	2Qd2	-44.0	-3.0	4.96	262.9
KTDH23 49.80 m (J03)	42.2	238.7	vein	2Qp4	-39.1	-2.9	4.8	267.7
KTDH23 49.80 m (J03)	42.2	238.7	vein	2Qp4	-40.1	-3.0	5.0	266.7
KTDH23 49.80 m (J03)	42.2	238.7	vein	2Qp4	-39.0	-3.0	5.0	264.2
KTDH23 49.80 m (J03)	42.2	238.7	vein	2Qp5	-51.1	-3.0	5.0	261.0
KTDH23 49.80 m (J03)	42.2	238.7	vein	2Qp5		-4.1	6.6	270.8
KTDH23 53.50 m (J05)	45.4	235.6	vein	2Qp6	-56.9	-2.4	4.0	262.4
KTDH23 53.50 m (J05)	45.4	235.6	vein	2Qp6	-63.7	-4.0	6.5	254.8
KTDH23 53.50 m (J05)	45.4	235.6	vein	2Qp7	-62.7	-3.9	6.3	279.6
KTDH23 53.50 m (J05)	45.4	235.6	vein	2Qp7	-60.8	-3.9	6.3	280.8
KTDH23 53.50 m (J05)	45.4	235.6	vein	2Qp7	-61.0	-3.8	6.2	253.3
KTDH23 53.50 m (J05)	45.4	235.6	vein	2Qp7	-58.7	-2.7	4.5	266.7
KTDH23 53.50 m (J05)	45.4	235.6	vein	2Qp7	-45.1	-3.8	6.2	330.4
KTDH23 53.50 m (J05)	45.4	235.6	vein	2Qp7	-51.9	-3.8	6.2	329.3
KTDH23 53.50 m (J05)	45.4	235.6	vein	2Qp7	-59.8	-3.5	5.7	280.9
KTDH23 53.50 m (J05)	45.4	235.6	vein	2Qp8	-47.9	-3.9	6.3	266.7
KTDH23 53.50 m (J05)	45.4	235.6	vein	2Qp8	-59.5	-5.2	8.1	262.8
KTDH23 54.55 m (J08)	46.3	234.7	vein	2Qp9		-4.3	6.9	309.7
KTDH23 54.55 m (J08)	46.3	234.7	vein	2Qp9		-4.1	6.6	303.5

KTDH23 54.55 m (J08)	46.3	234.7	vein	2Qp9	-56.2	-4.0	6.5	297.8
KTDH23 54.55 m (J08)	46.3	234.7	vein	2Qp9	-62.2	-4.1	6.6	305.5
KTDH23 54.55 m (J08)	46.3	234.7	vein	2Qp10	-61.0	-4.2	6.7	306.2
KTDH23 54.55 m (J08)	46.3	234.7	vein	2Qp10		-4.1	6.6	311.0
KTDH23 54.55 m (J08)	46.3	234.7	vein	2Qp11	-51.1	-4.1	6.6	262.1
KTDH23 54.55 m (J08)	46.3	234.7	vein	2Qp11	-54.8	-4.1	6.6	263.8
KTDH23 54.55 m (J08)	46.3	234.7	vein	2Qp11	-61.9	-4.1	6.6	266.4
KTDH04 18.40 m (C02)	18.4	207.1	hbx	2Qp1	-41.0	-3.0	5.0	281.4
KTDH04 18.40 m (C02)	18.4	207.1	hbx	2Qp1	-43.2	-3.0	5.0	283.1
KTDH04 18.40 m (C02)	18.4	207.1	hbx	2Qp1	-40.9	-3.0	5.0	283.9
KTDH04 18.40 m (C02)	18.4	207.1	hbx	2Qp2	-42.5	-3.0	5.0	301.4
KTDH04 18.40 m (C02)	18.4	207.1	hbx	2Qp2	-44.1	-3.1	5.1	301.8
KTDH04 18.40 m (C02)	18.4	207.1	hbx	2Qp2	-43.1	-3.1	5.1	302.8
KTDH04 18.40 m (C02)	18.4	207.1	hbx	2Qp2		-3.0	5.0	315.4
KTDH04 18.40 m (C02)	18.4	207.1	hbx	2Qp2		-3.0	5.0	313.3
KTDH04 18.40 m (C02)	18.4	207.1	hbx	2Qp3	-44.5	-4.1	6.6	304.4
KTDH04 18.40 m (C02)	18.4	207.1	hbx	2Qp3	-37.0	-3.9	6.3	318.8
KTDH04 18.40 m (C02)	18.4	207.1	hbx	2Qp3	-44.7	-4.1	6.6	320.1
KTDH23 108.30 m (J16)	91.9	189.1	vein	4Qp17	-44.1	-3.4	5.6	296.3
KTDH23 108.30 m (J16)	91.9	189.1	vein	4Qp17	-56.1	-3.8	6.2	265.4
KTDH23 108.30 m (J16)	91.9	189.1	vein	4Qp18		-3.9	6.3	272.1
KTDH23 108.30 m (J16)	91.9	189.1	vein	4Qp18	-63.9	-3.9	6.3	266.7
KTDH23 108.30 m (J16)	91.9	189.1	vein	4Qp18	-62.7	-3.9	6.3	257.6
KTDH23 108.30 m (J16)	91.9	189.1	vein	4Qp18	-64.4	-3.9	6.3	259.2
KTDH23 108.30 m (J16)	91.9	189.1	vein	4Qp18	-63.4	-3.9	6.3	259.3
KTDH23 108.30 m (J16)	91.9	189.1	vein	4Qp18	-63.9	-3.9	6.3	254.8
KTDH23 108.30 m (J16)	91.9	189.1	vein	4Qp19	-55.9	-3.5	5.7	272.6
KTDH23 108.30 m (J16)	91.9	189.1	vein	4Qp19	-47.3	-3.6	5.9	271.2
KTDH23 108.30 m (J16)	91.9	189.1	vein	4Qp19	-59.2	-3.3	5.4	275.0
KTDH23 108.30 m (J16)	91.9	189.1	vein	4Qp19	-60.0	-3.3	5.4	281.3
KTDH23 108.30 m (J16)	91.9	189.1	vein	4Qp19	-59.7	-3.4	5.6	304.3
KTDH23 108.30 m (J16)	91.9	189.1	vein	4Qp19	-54.8	-3.2	5.3	266.9
KTDH23 108.30 m (J16)	91.9	189.1	vein	4Qp19	-60.0	-3.5	5.7	277.3
KTD194-12 110.45 m (A13)	99.1	165.9	vein	4Sp1	-54.8	-3.1	5.1	275.6
KTD194-12 110.45 m (A13)	99.1	165.9	vein	4Sp1	-53.5	-3.1	5.1	274.7
KTD194-12 110.45 m (A13)	99.1	165.9	vein	4Sp1	-49.3	-3.1	5.1	279.8
KTD194-12 110.45 m (A13)	99.1	165.9	vein	4Sp1	-50.5	-3.1	5.1	270.3
KTD194-12 110.45 m (A13)	99.1	165.9	vein	4Sp1		-3.1	5.1	275.0
KTD194-12 110.45 m (A13)	99.1	165.9	vein	4Qp1	-58.7	-3.5	5.7	319.5
KTD194-12 110.45 m (A13)	99.1	165.9	vein	4Qp1		-3.3	5.4	324.1
KTD194-12 110.45 m (A13)	99.1	165.9	vein	4Qp2	-53.5	-3.0	5.0	315.8
KTD194-12 110.45 m (A13)	99.1	165.9	vein	4Qp2		-3.5	5.7	317.4
KTD194-12 110.45 m (A13)	99.1	165.9	vein	4Qp2	-59.3	-3.5	5.7	305.5
KTD194-12 110.45 m (A13)	99.1	165.9	vein	4Qp2	-55.4	-3.2	5.3	304.4
KTD194-12 110.45 m (A13)	99.1	165.9	vein	4Qp3	-50.8	-3.8	6.2	360.3
KTD194-12 110.45 m (A13)	99.1	165.9	vein	4Qp3		-3.2	5.3	321.8
KTDH23 156.00 m (J21)	132.5	148.4	vein	4Qp20	-40.4	-3.1	5.1	290.5
KTDH23 156.00 m (J21)	132.5	148.4	vein	4Qp20	-40.4	-3.1	5.1	285.9
KTDH23 156.00 m (J21)	132.5	148.4	vein	4Qp20	-57.4	-3.1	5.1	291.7
KTDH23 156.00 m (J21)	132.5	148.4	vein	4Qp21	-57.2	-3.4	5.6	317.5
KTDH23 156.00 m (J21)	132.5	148.4	vein	4Qp21		-3.4	5.6	316.4
KTDH23 156.00 m (J21)	132.5	148.4	vein	4Qp22	-58.4	-3.4	5.6	310.4
KTDH23 156.00 m (J21)	132.5	148.4	vein	4Qp22	-58.2	-3.3	5.4	301.9
KTDH23 156.00 m (J21)	132.5	148.4	vein	4Qp22	-59.0	-3.4	5.6	300.7
KTDH23 156.00 m (J21)	132.5	148.4	vein	4Qp22	-55.7	-3.2	5.3	298.1
KTDH23 156.00 m (J21)	132.5	148.4	vein	4Qp22	-58.2	-3.3	5.4	306.6
KTDH23 156.00 m (J21)	132.5	148.4	vein	4Qp22	-76.4	-3.3	5.4	305.3
KTDH23 156.00 m (J21)	132.5	148.4	vein	4Qp22		-3.3	5.4	308.0
KTDH04 84.40 m (C10)	84.4	141.1	vein	4Qp4	-57.2	-3.4	5.6	335.4
KTDH04 84.40 m (C10)	84.4	141.1	vein	4Qp4	-53.8	-3.2	5.3	306.8
KTDH04 84.40 m (C10)	84.4	141.1	vein	4Qp4	-57.0	-3.4	5.6	323.1
KTDH04 84.40 m (C10)	84.4	141.1	vein	4Qp4	-51.1	-3.4	5.6	340.4
KTDH04 84.40 m (C10)	84.4	141.1	vein	4Qp5	-57.4	-4.0	6.5	308.7
KTDH04 84.40 m (C10)	84.4	141.1	vein	4Qp5		-3.3	5.4	305.0
KTDH04 84.40 m (C10)	84.4	141.1	vein	4Qp5	-46.4	-3.1	5.1	302.8

KTDH04 84.40 m (C10)	84.4	141.1	vein	4Qp5		-3.6	5.9	303.2
KTDH04 84.40 m (C10)	84.4	141.1	vein	4Qp6	-57.9	-6.0	9.2	257.1
KTDH04 84.40 m (C10)	84.4	141.1	vein	4Qp6		-3.4	5.6	277.9
KTDH04 84.40 m (C10)	84.4	141.1	vein	4Qp6	-48.8	-3.3	5.4	258.3
KTDH04 84.40 m (C10)	84.4	141.1	vein	4Qp6	-58.4	-3.4	5.6	299.0
KTDH04 84.40 m (C10)	84.4	141.1	vein	4Qp6	-53.0	-4.2	6.7	261.7
KTDH04 84.40 m (C10)	84.4	141.1	vein	4Qp6	-54.3	-3.2	5.3	285.1
KTDH04 84.40 m (C10)	84.4	141.1	vein	4Qp6	-54.5	-3.4	5.6	258.7
KTDH04 84.40 m (C10)	84.4	141.1	vein	4Qp6	-54.9	-3.4	5.6	255.8
KTDH04 84.40 m (C10)	84.4	141.1	vein	4Qp6	-58.5	-3.4	5.6	262.4
KTDH04 84.40 m (C10)	84.4	141.1	vein	4Qp6	-57.2	-3.3	5.4	254.1
KTDH04 84.40 m (C10)	84.4	141.1	vein	4Qp6		-3.4	5.6	256.4
KTDH04 84.40 m (C10)	84.4	141.1	vein	4Qp7	-58.2	-3.4	5.6	270.2
KTDH04 84.40 m (C10)	84.4	141.1	vein	4Qp7		-2.8	4.7	266.5
KTDH04 84.40 m (C10)	84.4	141.1	vein	4Qp7	-52.1	-3.4	5.6	274.1
KTDH04 84.40 m (C10)	84.4	141.1	vein	4Qp7	-57.7	-3.4	5.6	270.5
KTDH04 84.40 m (C10)	84.4	141.1	vein	4Qp7	-58.2	-3.4	5.6	270.4
KTDH04 84.40 m (C10)	84.4	141.1	vein	4Qp7		-3.4	5.6	269.5
KTDH04 84.40 m (C10)	84.4	141.1	vein	4Qp7		-3.4	5.6	268.3
KTDH04 93.50 m (C16)	93.5	132.0	hbx	4Sp2	-56.1	-3.9	6.3	282.0
KTDH04 93.50 m (C16)	93.5	132.0	hbx	4Sp2	-48.9	-3.1	5.1	272.7
KTDH04 93.50 m (C16)	93.5	132.0	hbx	4Sp2	-47.4	-3.2	5.3	271.4
KTDH04 93.50 m (C16)	93.5	132.0	hbx	4Sp2	-45.7	-3.2	5.3	265.0
KTDH04 93.50 m (C16)	93.5	132.0	hbx	4Sp2	-47.7	-3.2	5.3	278.0
KTDH04 93.85 m (C17)	93.9	131.7	hbx	4Sp3	-51.6	-3.9	6.3	253.0
KTDH04 93.85 m (C17)	93.9	131.7	hbx	4Sp3		-3.9	6.3	276.2
KTDH04 93.85 m (C17)	93.9	131.7	hbx	4Sp3		-3.9	6.3	276.7
KTDH04 93.85 m (C17)	93.9	131.7	hbx	4Sp3		-4.0	6.5	253.7
KTDH04 93.85 m (C17)	93.9	131.7	hbx	4Qd1	-39.6	-3.4	5.6	301.2
KTDH04 93.85 m (C17)	93.9	131.7	hbx	4Qd1	-39.6	-3.4	5.6	295.1
KTDH04 93.85 m (C17)	93.9	131.7	hbx	4Qd1	-39.4	-3.4	5.6	294.5
KTDH04 93.85 m (C17)	93.9	131.7	hbx	4Qd1	-39.7	-3.3	5.4	283.1
KTDH04 93.85 m (C17)	93.9	131.7	hbx	4Qd1	-39.6	-3.4	5.6	311.5
KTDH04 93.85 m (C17)	93.9	131.7	hbx	4Qd1	-39.9	-3.4	5.6	309.2
KTDH04 93.85 m (C17)	93.9	131.7	hbx	4Qd1	-42.8	-3.5	5.7	311.2
KTDH04 93.85 m (C17)	93.9	131.7	hbx	4Qd1		-3.5	5.7	303.5
KTDH04 93.85 m (C17)	93.9	131.7	hbx	4Qd1		-4.0	6.5	335.1
KTDH04 101.40 m (C20)	101.4	124.1	hbx	4Sp4	-51.6	-3.9	6.3	301.4
KTDH04 101.40 m (C20)	101.4	124.1	hbx	4Sp4	-49.1	-4.1	6.6	296.5
KTDH04 101.40 m (C20)	101.4	124.1	hbx	4Sp4	-53.3	-4.0	6.5	307.4
KTDH04 101.40 m (C20)	101.4	124.1	hbx	4Sp4	-53.5	-4.0	6.5	292.5
KTDH04 101.40 m (C20)	101.4	124.1	hbx	4Sp4	-47.0	-3.9	6.3	307.5
KTDH04 101.40 m (C20)	101.4	124.1	hbx	4Sp4	-54.1	-3.9	6.3	307.7
KTDH04 101.40 m (C20)	101.4	124.1	hbx	4Sp4	-54.1	-4.0	6.5	295.3
KTDH04 101.40 m (C20)	101.4	124.1	hbx	4Sp4	-48.8	-4.3	6.9	306.0
KTDH04 101.40 m (C20)	101.4	124.1	hbx	4Sp4	-53.3	-3.8	6.2	304.3
KTDH04 101.40 m (C20)	101.4	124.1	hbx	4Sp4	-54.5	-4.6	7.3	304.4
KTDH04 101.40 m (C20)	101.4	124.1	hbx	4Sp4	-53.7	-4.0	6.5	300.3
KTDH04 101.40 m (C20)	101.4	124.1	hbx	4Sp4	-49.7	-3.9	6.3	295.2
KTDH04 101.40 m (C20)	101.4	124.1	hbx	4Sp4	-54.8	-3.9	6.3	304.4
KTDH04 101.40 m (C20)	101.4	124.1	hbx	4Sp4	-52.7	-4.0	6.5	293.9
KTDH04 101.40 m (C20)	101.4	124.1	hbx	4Sp4	-54.8	-4.0	6.5	290.0
KTDH04 101.40 m (C20)	101.4	124.1	hbx	4Sp4	-47.7	-4.6	7.3	306.1
KTDH04 101.40 m (C20)	101.4	124.1	hbx	4Sp4	-51.1	-3.8	6.2	296.5
KTDH04 114.80 m (C28)	114.8	110.7	hbx	4Sp5	-40.3	-3.9	6.3	303.8
KTDH04 114.80 m (C28)	114.8	110.7	hbx	4Sp5	-61.0	-4.0	6.5	366.8
KTDH04 114.80 m (C28)	114.8	110.7	hbx	4Sp5	-55.9	-4.0	6.5	302.4
KTDH04 114.80 m (C28)	114.8	110.7	hbx	4Sp5	-55.4	-4.1	6.6	347.0
KTDH04 114.80 m (C28)	114.8	110.7	hbx	4Sp5	-53.8	-4.1	6.6	360.9
KTDH04 114.80 m (C28)	114.8	110.7	hbx	4Sp5	-58.4	-3.6	5.9	292.5
KTDH04 114.80 m (C28)	114.8	110.7	hbx	4Sp5	-58.9	-4.1	6.6	292.6
KTDH04 114.80 m (C28)	114.8	110.7	hbx	4Sp5	-60.2	-4.0	6.5	294.5
KTDH04 114.80 m (C28)	114.8	110.7	hbx	4Sp5		-4.1	6.6	304.3
KTDH04 114.80 m (C28)	114.8	110.7	hbx	4Sp5	-58.5	-3.7	6.0	293.3
KTDH04 114.80 m (C28)	114.8	110.7	hbx	4Sp5	-57.5	-3.7	6.0	313.4

KTDH04 114.80 m (C28)	114.8	110.7	hbx	4Sp5	-56.2	-3.7	6.0	296.3
KTDH04 114.80 m (C28)	114.8	110.7	hbx	4Sp5	-58.5	-3.7	6.0	296.8
KTDH04 114.80 m (C28)	114.8	110.7	hbx	4Sp5	-62.0	-4.1	6.6	304.1
KTDH04 114.80 m (C28)	114.8	110.7	hbx	4Sp5	-60.2	-4.1	6.6	305.5
KTDH04 114.80 m (C28)	114.8	110.7	hbx	4Qp8	-66.5	-4.1	6.6	299.8
KTDH04 114.80 m (C28)	114.8	110.7	hbx	4Qp8	-64.7	-4.5	7.2	314.5
KTDH04 114.80 m (C28)	114.8	110.7	hbx	4Qp8	-66.8	-4.1	6.6	295.6
KTDH04 114.80 m (C28)	114.8	110.7	hbx	4Qp8	-63.7	-4.1	6.6	311.0
KTDH04 114.80 m (C28)	114.8	110.7	hbx	4Qp8	-63.7	-4.2	6.7	312.6
KTDH04 117.90 m (C29)	117.9	107.6	hbx	4Qp9	-38.1	-2.9	4.8	291.5
KTDH04 117.90 m (C29)	117.9	107.6	hbx	4Qp9	-37.4	-2.9	4.8	284.3
KTDH04 117.90 m (C29)	117.9	107.6	hbx	4Qp10	-54.6	-3.0	5.0	292.9
KTDH04 117.90 m (C29)	117.9	107.6	hbx	4Qp10	-56.2	-3.0	5.0	293.0
KTDH04 117.90 m (C29)	117.9	107.6	hbx	4Qp10	-55.6	-3.1	5.1	294.5
KTDH04 117.90 m (C29)	117.9	107.6	hbx	4Qp10	-55.9	-3.0	5.0	294.0
KTDH04 117.90 m (C29)	117.9	107.6	hbx	4Qp11	-56.1	-3.0	5.0	264.8
KTDH04 117.90 m (C29)	117.9	107.6	hbx	4Qp11	-56.7	-3.1	5.1	270.1
KTDH04 117.90 m (C29)	117.9	107.6	hbx	4Qp12	-57.4	-3.8	6.2	288.3
KTDH04 117.90 m (C29)	117.9	107.6	hbx	4Qp12	-59.3	-3.9	6.3	286.8
KTDH04 169.20 m (C33)	169.2	56.3	vein	4Sp6	-50.8	-3.8	6.2	303.4
KTDH04 169.20 m (C33)	169.2	56.3	vein	4Sp6	-52.7	-3.8	6.2	300.1
KTDH04 169.20 m (C33)	169.2	56.3	vein	4Sp6	-53.7	-4.1	6.6	298.0
KTDH04 169.20 m (C33)	169.2	56.3	vein	4Sp6		-4.1	6.6	302.6
KTDH04 169.20 m (C33)	169.2	56.3	vein	4Sp7	-50.3	-3.3	5.4	285.1
KTDH04 169.20 m (C33)	169.2	56.3	vein	4Sp7	-49.9	-3.5	5.7	290.4
KTDH04 169.20 m (C33)	169.2	56.3	vein	4Sp7	-51.1	-3.4	5.6	343.1
KTDH04 169.20 m (C33)	169.2	56.3	vein	4Sp7		-3.3	5.4	287.9
KTDH04 169.20 m (C33)	169.2	56.3	vein	4Sp7		-3.5	5.7	290.7
KTDH04 169.20 m (C33)	169.2	56.3	vein	4Qp13	-40.6	-3.6	5.9	294.3
KTDH04 169.20 m (C33)	169.2	56.3	vein	4Qp13	-40.4	-3.6	5.9	293.9
KTDH04 169.20 m (C33)	169.2	56.3	vein	4Qp13	-38.9	-3.3	5.4	296.0
KTDH04 169.20 m (C33)	169.2	56.3	vein	4Qp13	-40.4	-3.6	5.9	292.3
KTDH04 169.20 m (C33)	169.2	56.3	vein	4Qp13	-41.7	-3.6	5.9	294.6
KTDH04 169.20 m (C33)	169.2	56.3	vein	4Qp13	-40.6	-3.6	5.9	294.8
KTDH04 169.20 m (C33)	169.2	56.3	vein	4Qp13	-40.0	-3.3	5.4	293.8
KTDH04 169.20 m (C33)	169.2	56.3	vein	4Qp14	-41.7	-3.6	5.9	308.6
KTDH04 169.20 m (C33)	169.2	56.3	vein	4Qp14	-42.0	-3.4	5.6	331.1
KTDH04 169.20 m (C33)	169.2	56.3	vein	4Qp14	-42.0	-3.4	5.6	280.3
KTDH04 169.20 m (C33)	169.2	56.3	vein	4Qp14	-40.6	-3.4	5.6	294.8
KTDH04 169.20 m (C33)	169.2	56.3	vein	4Qp14	-57.7	-4.1	6.6	297.6
KTDH04 169.20 m (C33)	169.2	56.3	vein	4Qp15	-41.7	-3.7	6.0	292.0
KTDH04 169.20 m (C33)	169.2	56.3	vein	4Qp15	-41.7	-3.4	5.6	296.8
KTDH04 169.20 m (C33)	169.2	56.3	vein	4Qp16	-57.2	-3.4	5.6	299.7
KTDH04 169.20 m (C33)	169.2	56.3	vein	4Qp16	-57.2	-3.6	5.9	295.3
KTDH04 169.20 m (C33)	169.2	56.3	vein	4Qp16	-55.1	-2.9	4.8	297.6
KTDH04 169.20 m (C33)	169.2	56.3	vein	4Qp16	-57.7	-3.4	5.6	301.0
KTDH04 169.20 m (C33)	169.2	56.3	vein	4Qp16	-55.7	-3.5	5.7	299.9
KTDH04 169.20 m (C33)	169.2	56.3	vein	4Qp16	-54.0	-3.6	5.9	299.2
KTDH04 169.20 m (C33)	169.2	56.3	vein	4Qp16	-56.6	-3.5	5.7	296.2
KTDH04 169.20 m (C33)	169.2	56.3	vein	4Qp16		-3.5	5.7	299.3
KTDH04 169.20 m (C33)	169.2	56.3	vein	4Qp16	-55.9	-3.4	5.6	295.9
KTDH04 169.20 m (C33)	169.2	56.3	vein	4Qp16	-52.7	-3.2	5.3	294.8
KTDH04 169.20 m (C33)	169.2	56.3	vein	4Qd2		-3.3	5.4	295.7
KTDH04 169.20 m (C33)	169.2	56.3	vein	4Qd2		-3.3	5.4	295.7
KTDH04 169.20 m (C33)	169.2	56.3	vein	4Qd2	-58.9	-3.3	5.4	292.3
KTDH04 169.20 m (C33)	169.2	56.3	vein	4Qd2		-3.3	5.4	294.5
KTDH04 228.60m (C42)	228.6	-3.1	vein	6Ao1	-58.5	-1.6	2.74	277.9
KTDH04 228.60m (C42)	228.6	-3.1	vein	6Ao2	-47.8	-1.6	2.74	208.3
KTDH04 228.60m (C42)	228.6	-3.1	vein	6Ao3	-45.5	-1.6	2.74	269.7
KTDH04 228.60m (C42)	228.6	-3.1	vein	6Ao4	-51.3	-2.1	3.55	195.9
KTDH04 229.80 m (C43)	229.8	-4.3	hbx	6Sp1	-52.4	-3.0	5.0	282.7
KTDH04 229.80 m (C43)	229.8	-4.3	hbx	6Sp1	-47.4	-3.1	5.1	277.6
KTDH04 229.80 m (C43)	229.8	-4.3	hbx	6Sp1	-50.3	-2.8	4.7	306.5
KTDH04 229.80 m (C43)	229.8	-4.3	hbx	6Sp1	-46.8	-2.8	4.7	300.8
KTDH04 229.80 m (C43)	229.8	-4.3	hbx	6Sp1	-48.8	-2.9	4.8	295.3

KTDH04 229.80 m (C43)	229.8	-4.3	hbx	6Sp1	-49.1	-2.8	4.7	309.2
KTDH04 229.80 m (C43)	229.8	-4.3	hbx	6Sp2	-47.9	-3.0	5.0	276.0
KTDH04 229.80 m (C43)	229.8	-4.3	hbx	6Sp2	-49.7	-3.1	5.1	282.9
KTDH04 229.80 m (C43)	229.8	-4.3	hbx	6Sp2	-50.5	-3.1	5.1	275.1
KTDH04 229.80 m (C43)	229.8	-4.3	hbx	6Sp2	-50.5	-3.1	5.1	282.9
KTDH04 229.80 m (C43)	229.8	-4.3	hbx	6Sp2		-3.1	5.1	284.5
KTDH04 229.80 m (C43)	229.8	-4.3	hbx	6Sp2	-47.4	-3.1	5.1	274.1
KTDH04 229.80 m (C43)	229.8	-4.3	hbx	6Sp2		-3.1	5.1	283.8
KTDH04 229.80 m (C43)	229.8	-4.3	hbx	6Sp2	-47.3	-3.1	5.1	274.3
KTDH04 229.80 m (C43)	229.8	-4.3	hbx	6Sp2	-47.4	-3.1	5.1	284.7
KTDH04 229.80 m (C43)	229.8	-4.3	hbx	6Sp2	-47.4	-3.0	5.0	271.6
KTDH04 229.80 m (C43-1)	229.8	-4.3	hbx	6Sp4	-52.5	-3.1	5.11	284.4
KTDH04 229.80 m (C43-1)	229.8	-4.3	hbx	6Sp4	-60.0	-3.1	5.11	278.2
KTDH04 229.80 m (C43-1)	229.8	-4.3	hbx	6Sp5	-59.5	-3.1	5.11	263.1
KTDH04 229.80 m (C43-1)	229.8	-4.3	hbx	6Sp5	-58.9	-3.5	5.71	289.6
KTDH04 229.80 m (C43-1)	229.8	-4.3	hbx	6Sp6	-28.7	-2.8	4.65	261.0
KTDH04 229.80 m (C43-1)	229.8	-4.3	hbx	6Sp6	-32.2	-2.8	4.65	274.6
KTDH04 229.80 m (C43-1)	229.8	-4.3	hbx	6Sp6	-20.8	-3.0	4.96	272.5
KTDH04 229.80 m (C43-1)	229.8	-4.3	hbx	6Sp6	-58.3	-2.8	4.65	275.3
KTDH04 229.80 m (C43-1)	229.8	-4.3	hbx	6Sp6	-60.8	-2.8	4.65	270.5
KTDH04 229.80 m (C43-1)	229.8	-4.3	hbx	6Sp6		-2.8	4.65	271.5
KTDH04 229.80 m (C43-1)	229.8	-4.3	hbx	6Sp6	-51.1	-3.1	5.11	268.0
KTDH04 229.80 m (C43-1)	229.8	-4.3	hbx	6Sp7	-54.3	-2.8	4.65	253.2
KTDH04 229.80 m (C43-1)	229.8	-4.3	hbx	6Sp7	-58.9	-3.0	4.96	241.1
KTDH04 232.30 m (C44)	232.3	-6.8	hbx	6Sp3	-36.5	-2.6	4.3	292.3
KTDH04 232.30 m (C44)	232.3	-6.8	hbx	6Sp3		-2.7	4.5	279.0
KTDH04 232.30 m (C44)	232.3	-6.8	hbx	6Sp3	-44.2	-2.8	4.7	287.0
KTDH04 232.30 m (C44)	232.3	-6.8	hbx	6Sp3	-44.8	-2.8	4.7	334.2
KTDH04 232.30 m (C44)	232.3	-6.8	hbx	6Sp3	-44.2	-2.7	4.5	289.6
KTDH04 232.30 m (C44)	232.3	-6.8	hbx	6Sp3		-2.5	4.2	284.3
KTDH04 232.30 m (C44)	232.3	-6.8	hbx	6Sp3		-2.8	4.7	282.8
KTDH04 232.30 m (C44-1)	232.3	-6.8	hbx	6Sp8		-2.8	4.65	282.8
KTDH04 232.30 m (C44-1)	232.3	-6.8	hbx	6Sp8	-57.9	-2.8	4.65	284.7
KTDH04 232.30 m (C44-1)	232.3	-6.8	hbx	6Sp8		-2.8	4.65	280.1
KTDH04 232.30 m (C44-1)	232.3	-6.8	hbx	6Sp8		-2.8	4.65	290.7
KTDH04 232.30 m (C44-1)	232.3	-6.8	hbx	6Sp8		-2.8	4.65	280.8
KTDH04 232.30 m (C44-1)	232.3	-6.8	hbx	6Sp8	-28.3	-2.9	4.80	281.8
KTDH04 232.30 m (C44-1)	232.3	-6.8	hbx	6Sp8	-55.2	-2.8	4.65	279.7
KTDH04 232.30 m (C44-1)	232.3	-6.8	hbx	6Sp8	-40.7	-2.7	4.49	297.4
KTDH04 232.30 m (C44-1)	232.3	-6.8	hbx	6Sp8		-2.8	4.65	283.7
KTDH04 232.30 m (C44-1)	232.3	-6.8	hbx	6Sp8		-2.9	4.80	274.9
KTDH04 232.30 m (C44-1)	232.3	-6.8	hbx	6Sp8	-65.4	-2.8	4.65	272.5
KTDH04 232.30 m (C44-1)	232.3	-6.8	hbx	6Sp8	-60.2	-2.8	4.65	268.2
KTDH04 232.30 m (C44-1)	232.3	-6.8	hbx	6Sp8		-2.8	4.65	288.2
KTDH04 232.30 m (C44-1)	232.3	-6.8	hbx	6Sp8		-2.8	4.65	285.9
KTDH04 232.30 m (C44-1)	232.3	-6.8	hbx	6Sp9	-40.9	-3.2	5.26	262.4
KTDH04 232.30 m (C44-1)	232.3	-6.8	hbx	6Sp9	-53.3	-2.8	4.65	282.2
KTDH04 232.30 m (C44-1)	232.3	-6.8	hbx	6Sp9		-2.8	4.65	292.6
KTDH04 232.30 m (C44-1)	232.3	-6.8	hbx	6Sp10		-2.8	4.65	296.4
KTDH04 232.30 m (C44-1)	232.3	-6.8	hbx	6Sp10	-52.7	-2.8	4.65	284.0
KTDH04 239.70m (C45)	239.7	-14.2	vein	6Ao6	-72.4	-2.8	4.65	317.6
KTDH04 239.70m (C45)	239.7	-14.2	vein	6Ao6	-67.2	-2.1	3.55	174.7

Note: Samples are arranged according to mineralization stage and decreasing elevation from the present-day mean sea level.

Explanation: hbx – matrix of hydrothermal breccia, FIA number: 1st number – mineralization stage, 1st letter – Q for quartz, A for anhydrite and S for sphalerite, 2nd letter – p for primary fluid inclusion, d for pseudosecondary fluid inclusion and o for solitary primary fluid inclusion, 2nd number – number of fluid inclusion assemblage, T_m – ice melting temperature, T_h – homogenization temperature.

APPENDIX F

DEBYE-HUCKEL COEFFICIENTS, IONIC CHARGE AND ION SIZE PARAMETER

Debye-Huckel Coefficients (A and B)	250 °C	300 °C	Reference
A in $kg^{1/2}mole^{-1/2}$	0.9785	1.2555	Helgeson et al. (1981) in
B in $kg^{1/2}mole^{-1}cm^{-1}$ x 10^{8}	0.3792	0.3965	Henley et al (1984a)

	Ionic charge (z_i)	Ion size parameter ($å_i$) in 10^{-8} cm	Reference
Na^+	1	4	Truesdell and Jones (1974)
K^+	1	3	in Henley et al (1984a)
Ca^{2+}	2	6	
Cl^-	1	3.5	
H_2S	0	0	
HS^-	1	4	
SO_4^{2-}	2	4	
HSO_4^-	1	4	
H_2	0	0	

APPENDIX G

FREE ENERGIES OF FORMATION OF MINERALS AND AQUEOUS SPECIES AT THE SATURATED VAPOR PRESSURE OF PURE WATER

$\Delta G°_f$	250 °C	300 °C	Reference
Quartz	-869.0	-872.4	Helgeson et al. (1981) in Henley et al (1984c)
K-feldspar	-3810.0	-3827.5	
Muscovite	-5680.6	-5706.1	
Kaolinite	-3853.5	-3872.3	
H^+	0	0	
K^+	-307.5	-312.5	
H_2O	-258.2	-264.0	

APPENDIX H

EQUILIBRIUM CONSTANTS (LOG K VALUES) FOR SOME HYDROLYTIC AND REDOX REACTIONS

Reaction	250 °C	300 °C	References
$2H_2S + O_{2(g)} = S_{2(g)} + 2H_2O$	30.06	27.21	Helgeson et al. (1978), Robie et al. (1978) and Fisher and Barnes (1972) in Henley et al (1984d)
$H_2S_{(aq)} = HS^- + H^+$	-7.60	-8.05	
$HS^- + 2O_2 = SO_4^{2-} + H^+$	63.90	55.38	
$HSO_4^- = H^+ + SO_4^{2-}$	-5.27	-6.08	
$H_2O_{(l)} = H_2 + \frac{1}{2}O_2$	-20.23	-17.81	
$H_2O_{(l)} = H^+ + OH^-$	-11.08	-11.28	
$\frac{1}{2}H_2 = H^+ + e^-$	0	0	
$H_2S + 2O_2 = 2H^+ + SO_4^{2-}$	56.3	-47.33	
$Au + H_2S(aq) + HS^- = Au(HS)_2^- + \frac{1}{2}H_2(g)$	-1.56	-1.35	Shenberger and Barnes (1989)
$Au + 2Cl^- + H^+ = AuCl_2^- + \frac{1}{2}H_2$	-6.5	-4.5	Helgeson, H.C (1969) in Seward (1993)